University of Nottingham
UK | CHINA | MALAYSIA

MELT-PROCESSING OF NOVEL BIORESORBABLE POLYMER NANOCOMPOSITES FOR HEALTHCARE

Magdalena Maria Patel, MSc Eng

Thesis submitted to the University of Nottingham
for the degree of Doctor of Philosophy

June 2019

Declaration

Except where specific reference has been made to other sources, the work presented in this thesis is the original work of the author. It has not been submitted, in whole, or in part, for any other degree or professional qualification.

Signed Magdalena Patel Date 31/05/2019

Magdalena Maria Patel

“I have frequently been questioned, especially by women, of how I could reconcile family life with a scientific career. Well, it has not been easy.”

Maria Skłodowska-Curie, two-time Nobel Prize winner and a mother of two daughters, including Irène Joliot-Curie also a Nobel Prize winner

Abstract

The load bearing capacity of biodegradable polymeric medical devices remains limited; an improvement in mechanical properties is desirable to widen the range of applications. Incorporation of nanoparticles via melt compounding is a route to improving mechanical properties, but appropriate processing routes are required to ensure the best outcome, achieving an optimum dispersion while minimising process-induced degradation. Various nanomaterials have been investigated for polylactic acid (PLA) reinforcement for orthopaedic applications; hydroxyapatite (HA), the main inorganic constituent of bone, is one of the most promising bioresorbable nanofillers.

The principal focus of this work is the optimised processing of novel bioresorbable materials using scalable compounding techniques. The materials consist of: Resomer LR706S poly(L-co-D,L-lactide) (LR706S) PLA matrix from Evonik; novel nanoparticles of hydroxyapatite (HANP) with rod or platelet morphology, synthesised via a hydrothermal counter-flow process; dispersant coatings added in-situ onto HANP plates. The molecular dispersants consist of either purchased neat dodecenylsuccinic anhydride (DDSA) or bespoke short chained PLA with isosorbide head groups polymerised via a standard ring-opening route involving lactide, a tin catalyst and isosorbide initiator.

Nanocomposites were processed in a laboratory scale twin-screw recirculating extruder HAAKE Minilab II, produced by Thermo Scientific, fitted with co-rotating conical screws. The materials were compounded in various conditions in order to establish processing parameters that provide an agreeable compromise between particles mixing and minimising the effect of polymer degradation. The produced materials were assessed by GPC, TGA, DSC, TEM, microCT, rheometry and flexural mechanical measurements. Three preferred compositions were selected to go forward to scaled-up manufacturing, using commercial processing facilities.

Performed experiments showed that, beyond drying the polymer and fillers, drying of the bottled N_2 (N_{2D}) was essential to maintain high molecular weight of PLA, which in turn yielded high wall shear stress half-life time during compounding. The highest range of molecular weights was reported for HANP rod composites in N_{2D} with the greatest M_w at 2.5 wt%. Additionally, molecular weight decreased with increasing amount of filler, regardless of the type of HANP.

DSC measurements revealed that glass transition temperatures (T_g) for respective HANP rod and plate nanocomposites compounded in N_{2D} were practically identical but higher than for the nanocomposites produced in Air. Furthermore, T_g of the nanocomposites was greater than the one measured for neat PLA and large changes of molecular weight were required (over 70% when compared to neat LR706S) to reflect it in the glass transition temperature of the material.

The temperature at 5% weight loss for the compounded materials, measured in the TGA, was greater than for neat LR706S, and for HANP plates it was higher than for rods.

Flexural properties were tested via three-point bending of miniature specimens and showed that modulus was independent of molecular weight over the considered range, while bending strength showed a small decrease with lowering M_w. The flexural strength and modulus were found to be higher for HANP plate nanocomposites compounded in N_{2D} than mixed in Air, with the highest values shown for 10 wt% HANP rods in N_{2D}.

TEM image analysis was carried out with a semi-quantitative approach and revealed superior dispersion in 2.5 wt% HANP rod nanocomposites mixed in N_{2D} when compared to other materials. This was confirmed by microCT measurements.

Finally, the developed novel nanocomposites were successfully used in the production of demonstrator resorbable proximal pins and tensile bars by applying the optimised processes at scale on industrial equipment.

Acknowledgements

First of all, I would like to express my deepest gratitude to Dr Andrew Parsons, Dr Davide De Focatiis and Prof David Grant for their guidance, knowledge, encouragement, relentless support and the reading of my thesis, I could not dream of better PhD supervisors. I would also like to thank my project colleagues, Dr Gabriel Choong for training me on all the processing equipment and pointing me in the right direction when required, Dr Michael Ward for being a great lab partner and friend, Dr Kirsty Walton and Dr Miquel Gimeno-Fabra for producing the particles for my research and sharing their expertise. I would like to extend my thanks to all the knowledgeable researchers and technicians at the Faculty of Engineering and Medical Sciences, who I met during samples characterisation, for their expertise, support and cheerfulness.

I would like to acknowledge EPSRC for the funding of our project BENcH (reference: EP/J017272/1) and IOM3, the UoN Graduate School and MeDe Innovation for financial support for my international research trips and conference attendances.

On a private note, I would like to express special thanks to Dr Rupesh Patel - my husband, for taking care of our son, cooking, cleaning, his immense patience, love and support at all times, research advice, helping me with MatLab coding, falling asleep alongside the noise of a clicking keyboard, reading my work and introducing me to his friends and lunch time Chinese poker. You kept me sane on this challenging journey! Thank you also to my loving mum and parents in-law for all their help, childcare, cooking, prayers, hugs and phone calls. I am grateful for my family in Poland and the UK for always being there for me and believing in me. I would like to thank all of my friends, particularly to Dr Uresha Patel and Dr Lorelei Gherman for sharing this girly journey at the edge of science and to Magda, Karolina, Natalia and Kasia for replying to me at the latest hour and always being kind to me.

This work would not be possible if not help from you all.

Finally, Milan my son, thank you for coming to my life, being an ace at the nursery and letting me write. This thesis is dedicated to you and hopefully betterment of your future.

Thank You for directing my path to Nottingham, so I could become who I am, meet the right people and finish the commenced work. *"Life is like a box of chocolates. You never know what you're gonna get."* - F. Gump.

Contents

List of Figures

List of Tables

Nomenclature

Abbreviations

is8PLA	Isosorbide ended 8 mer unit linear PLA (600 Da)
is8PLAHA	Is8PLA coated HANP plates
is16PLA	Isosorbide ended 16 mer unit linear PLA (1200 Da)
is16PLAHA	Is16PLA coated HANP plates
is16PLAHApp	Is16PLAHA produced at Promethean Particles
is24PLA	Isosorbide ended 24 mer unit linear PLA (1800 Da)
is24PLAHA	Is24PLA coated HANP plates
microCT	X-ray microcomputer tomography
nHA	HA nanoparticles
pH	Potential of hydrogen
starPLA	Branched 6-armed, 7 mer units per arm, PLA (3 kDa)
starPLAHA	StarPLA coated HANP plates

2003D	PLA Ingeo 2003D from NatureWorks
Air	Ambient air
BTE	Bone tissue engineering
C^3C_{18}-mmt	Octadecylammonium cation modified montmorillonite
CM	Compression moulding
ED	Exponential decay
DDSA	Dodecenyl succinic anhydride
DDSAHA	DDSA coated HANP plates
DSC	Differential scanning calorimetry
F-F	Flory-Fox equation
GPC	Gel permeation chromatography
HA	Hydroxyapatite
HANP	Novel hydroxyapatite nanoparticles (for this study)
HDDSA	Pre-hydrolysed DDSA
HEPA	High-efficiency particulate absorber
IM	Injection moulding
IV	Intrinsic viscosity
L/D	Length-to-diameter ratio for the screw of an extruder

LLA-g-nHA	HA nanoparticles grafted with L-lactide
LR706S	PLA Resomer LR706S from Evonik
MA	Simple moving average
MD	Mechanical degradation
MWNT	Multi-walled carbon nanotube
N_2	Bottled nitrogen
N_{2D}	N_2 in line dried with a liquid nitrogen moisture trap
P1, P2	MiniLab pressure sensors
PCL	Polycaprolactone
PD	Particle dispersion
PDI	Polydispersity index
PDLA	Poly(D-lactic acid)
PDLLA	Poly(D,L-lactic acid)
PGA	Poly(glycolic acid)
PLA	Poly(lactic acid)
PLGA	Poly(DL-lactide-co-glycolide)
PLLA	Poly(L-lactic acid)
PS	Polystyrene no 430102 from Aldrich
RMI	Relative modification index
ROP	Ring-opening polymerization
SEM	Scanning electron microscopy
SME	Specific mixing energy
TD	Thermal degradation
TEM	Transmission electron microscopy
TGA	Thermogravimetric analysis
THF	Tetrahydrofuran
UoN	The University of Nottingham

Symbols

a	Mark–Houwink exponent
b	Transition speed constant
c	Transition slope constant
d	Die slit diameter
dx	Elemental length in the MiniLab channel
h	Thickness of a minibar specimen
h_{ML}	Height of the MiniLab back flow channel
l	Span length of a minibar specimen
l_{sa}	Square side length of a free space on TEM image
l_{ML}	Length of the MiniLab back flow channel
m	Extruder throughput
m_{ash}	Mass of LR706S ash residue
m_{HA}	HA mass
m_{f}	Residual sample mass after TGA
m_{o}	The original mass of the sample
m_{PLA}	PLA mass
n	Power law index
n_{s}	Screw rotation speed
t	Time
$t_{1/2}$	Wall shear stress half-life time
$t_{5\%}$	Temperature at 5% weight loss
$t_{5\%P}$	Temperature at 5% weight loss of polymeric part only
t_{deg}	Elapsed degradation time
t_{trans}	Transition time at 170 °C
t_{ML}	Total experiment time in the MiniLab
t_{R}	Mixing and recirculation time in the MiniLab
v	Velocity in the MiniLab back flow channel
w_{ML}	Width in the MiniLab back flow channel
$wt\%_{HA}$	HA weight percentage
y	Vertical distance in the MiniLab channel

A	Mean life time
C	Flow consistency index
D	Degradation shift factor
E	Flexural modulus
E_a	Activation energy for LR706S
E_{mix}	Mixing energy
F	The force required for a minibar deformation
F_f	Volumetric flow factor
K	Characteristic material constant
L	Capillary die length
M_i	Molar mass
M_n	Number average molecular weight
M_p	Molecular weight of the highest peak
M_v	Viscosity averaged molecular weight
M_w	Weight average molecular weight
M_w^*	Theoretical weight average molecular weight
M_{w0}	Weight average molecular weight of neat LR706S
N	Number of recirculation times in the MiniLab
N_i	Number of moles of each polymer species
Q	Volumetric flow rate
Q_{rel}	Relative volumetric flow rate
R	Universal gas constant
T	Torque
T_g	Glass transition temperature
T_g^∞	Glass transition temperature at the infinite M_n
T_m	Melting temperature
T_t	Test temperature
T_D	Reference degradation temperature
T_{ML}	Chamber temperature in the MiniLab
V_L	Recirculating loop volume in the MiniLab
V_{ML}	Maximum filling volume of the MiniLab
X_D	D-lactide concentration

a_D	Degradation shift factor
a_l	PLA melt thermal coefficient of expansion at 150 °C
ε	Strain
η	Viscosity
η_0	Viscosity at zero shear rate
η_∞	Viscosity at infinite shear rate
η_{rel}	Relative viscosity
$\dot{\gamma}$	Shear rate
$\dot{\gamma}_{rel}$	Relative shear rate
λ	Relaxation time
λ_0	Relaxation time of the undegraded polymer at 170 °C
λ_{deg}	Relaxation time of the degraded polymer at T_t
λ_D	Decay rate
ρ	Density
ρ_{HA}	HA density
ρ_{PLA150}	PLA density at 150 °C
ρ_{PLA210}	PLA density at 210 °C
σ	Stress
σ_f	Flexural (bending) strength
τ	Shear stress
τ_{ap}	Apparent shear stress
τ_w	Wall shear stress
τ_{w0}	Wall shear stress at $t_R = 0$
$\o$	Screw outer diameter in an extruder

ΔP	Pressure difference between P1 and P2 in the MiniLab
ΔP_C	Pressure difference for capillary die
ΔP_0	Pressure difference for orifice die

1. Motivation and Thesis Overview

1.1. Introduction

Continuous technological development is enabling substantial progress in medicine, which consequently is extending the length of our lives. However, this increase in life expectancy places greater stress on medical innovation as wellbeing should be ensured throughout our lifetime. The increasing demands and expectations on biomedical engineering can be met by advances in pharmacy, medical devices, implants and tissue engineering. Our current aging population requires medical support in numerous healthcare areas which results in further research in biomaterials science to provide novel materials for medical applications [1, 2] in cardiovascular, neural and orthopaedic technologies [3]. This thesis will focus on bioresorbable polymeric nanocomposites [4, 5] for orthopaedic applications [6, 7].

The majority of implants used in orthopaedic surgeries are produced from metals, which often have to be removed in a second operation once their supporting function is fulfilled, e.g. bone screws and plates. This additional surgery has several adverse effects, such as increasing the risk of infection for patients [8]. Metal implants frequently cause inflammatory reactions and require premature removal, thereby disturbing healing and recovery [9]. Recently, a regenerative bone tissue engineering (BTE) approach has been advanced instead of replacement methods, in order to avoid the highlighted issues. Non-degradable implants are successfully being replaced by implants made from biocompatible and biodegradable polymers of synthetic or natural origin. This can limit problems with inflammatory reactions and no secondary surgery is required [10].

Another major drawback of metallic implants is stress shielding during healing. This causes the growth of bone structure that does not possess the ability to support weight once the implant is removed. Presently available degradable polymeric implants can prevent some issues with stress shielding [11]. However, they remain limited in their load bearing capability and require improvements of their mechanical properties in order to overcome this limitation [9].

As a result of the highlighted issues, one of the key areas of focus for BTE is the fabrication of bioresorbable materials that are able to function for a targeted period of time under load-bearing conditions. This would allow them to support damaged bones during healing and to replace lost bone stock [12]. Appropriate selection of biomaterials: their geometry, type of reinforcement inclusions and their size distribution, porosity and ability to release biomolecules at a desired rate, plays a critical role in the development of biomedical composites for medical devices [13].

The key requirements for ideal bone support and replacement materials are:

- Biocompatibility – support of normal cellular activity without any immune response or toxic effects during resorption [14],
- Mechanical properties – uniform stress distribution and strength on a par with bone properties, thereby providing temporary support to the defect region [13],
- Porosity – controlled volume and pore size to enable tissue in-growth and support of the fractured bone [13],
- Biodegradability – degradation rate matching growth of new tissue [15],
- Osteoinductivity and/or osteoconductivity – stimulation of new bone formation [15, 16],
- Surface properties – appropriate chemical and topographical properties for influencing cellular adhesion and new bone formation [17].

Biodegradable nanocomposite materials can fulfil the majority of the requirements mentioned above by combining the characteristics of biodegradable polymers (e.g. saturated aliphatic polyesters like poly(lactic acid)) and bioactive inorganic ceramics (e.g. hydroxyapatite nanoparticles). They have the potential to deliver appropriate mechanical and bioactive properties, degradation control and bioactivity by the volume fraction, size, shape and arrangement of inclusions. However, good nanoparticle dispersion throughout the polymer matrix has thus far only been achieved at a laboratory scale [18]. Therefore commercially available resorbable polymeric devices are produced only with macrosized filler e.g. Ligafix 30, an anterior cruciate ligament interference screw (SBM, France) composed of 30% tricalcium phosphate and 70% of Poly-D,L-lactic Acid [19]. Additionally, currently developed nanocomposite materials for orthopaedic applications are still less stiff (modulus below 7 GPa) than cortical bone (7-25 GPa) [13, 20].

The long-term goal of this area of research is to develop a customisable bioresorbable material that can be fabricated at short notice, that is weight-bearing over longer timescales, that allows for sufficient vascular infiltration and bone ingrowth and that can be coupled with infection management [17]. BTE has been evolving rapidly to match those demands by utilising various biocompatible polymers and ceramics. However, fully resorbable nanocomposites for orthopaedic implants remains an unrealised goal. Further investigation is required to enable the transfer of laboratory results into the manufacture of commercial articles, and this is one of the main aims of this project [21].

1.1.1. Overview of the BENcH project

The BENcH project (Integrated Molecular Design of Melt-processable Bioresorbable Engineering Nanocomposites for Healthcare) was an EPSRC-funded interdisciplinary project supported by several industrial collaborators [22]. The main challenge for the research team involved the design and manufacture of novel resorbable polymer nanocomposite materials for healthcare, which could be used in applications from bone fracture fixation to drug delivery. Integrated methodologies were utilised in forming composite systems consisting of medical-grade degradable polymer and novel nanoparticles with dedicated molecular dispersants. The developed nanocomposites were used in the production of demonstrator resorbable implants by applying the optimised processes at scale on industrial equipment.

The project addressed different aspects of the orthopaedics field including: replacement of lost bone stock, support of damaged bones during healing and potentially targeted delivery of active ingredients. Requirements for those areas differ significantly due to the nature of bone structure, shown in Figure 1.1. Cancellous bone (spongy bone core that contains bone marrow) has relatively low mechanical demands in comparison to cortical bone (Young's modulus of 1 GPa and 17 GPa respectively), also known as compact bone, which forms the dense outer part of bone [23]. The market has been largely saturated with a wide range of materials for non-load-bearing bone repair [17]. Therefore, the principal focus of the project was in the production of materials for mechanically demanding applications requiring sufficient strength to support bone over the healing period, appropriate stiffness to avoid bone atrophy and the ability to be tolerated by the body.

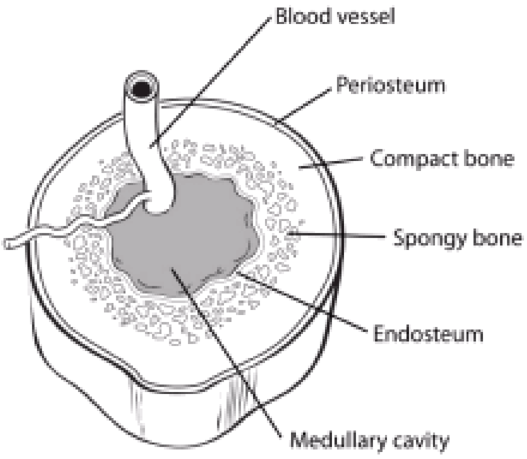

Figure 1.1. Bone cross section. Adapted from Cancer.org [24].

Key challenges, and the BENcH project aims, concentrated on scalable particle synthesis, controlling and tailoring process degradation, melt compounding of the bioresorbable poly(lactic acid) (PLA) nanocomposites and establishing scalable manufacturing methods to produce proof-of-concept, next generation medical devices.

PLA composites with inorganic, nanosized fillers are not a new concept. They have received a lot of recent attention because of their biocompatibility and enhanced mechanical properties, which have the potential to mimic the properties of bone in orthopaedic applications [25]. The novelty of the project is in the use of tailored dispersants coupled to hydroxyapatite (HA) nanofillers. Together these give potential for producing fully resorbable PLA nanocomposites, where the filler is appropriately dispersed via melt compounding. Melt compounding is a commonly used and scalable industrial process. The applied HA reinforcement may also act as a pH buffer in the composite to control the degradation caused by the acidic decomposition products of PLA [9].

To fulfil the aforesaid expectations, the BENcH project had an interdisciplinary team of researchers working in parallel:

- Stream 1 – nanoparticle and dispersant synthesis and scaleup completed by Walton [26];
- Stream 2 – rheological study, performed by Choong et al. [27], [28], *in vitro* hydrolytic degradation and mechanical properties characterisation of the produced materials carried out by Ward [29];
- Stream 3 – nanocomposite manufacture, quantification, process conditions optimisation and scaleup.

This dissertation falls primarily within Stream 3.

1.2. Aims and objectives of this thesis

The aim of this PhD was to produce novel bioresorbable HA-PLA nanocomposites for healthcare applications, via melt processing. Research has previously been carried out on HA-PLA nanocomposites, however findings reported in the literature are limited to only laboratory scale experiments. These provide insufficient explanation regarding the effect of processing conditions on the properties of the materials and the particles' dispersion. The novelty of the current work was in the use of HA nanofillers coupled to tailored dispersants that together enable production of a PLA nanocomposite via direct melt compounding, which is a scalable process.

Appropriate nanoparticles dispersion and the controlling of process degradation is necessary for obtaining a composite with improved and uniform mechanical properties. Therefore, efficient compounding of the nanoparticles with PLA, via polymer melt mixing with the filler in an extruder, is needed to ensure the required dispersion. Optimisation of the processing parameters e.g. temperature, rotational speed of the screws during compounding, recirculation time and calculation of the volumetric flow rate are all essential for achieving a desired dispersion of nanoparticles and for minimising process-induced degradation.

Furthermore, the shape of HA nanoparticles, their weight percentage in the composite and the type of dispersant have a profound effect on the properties of the obtained material. Therefore, initially, an assessment of the degradation of pure PLA during processing was needed to understand its role in the composite degradation during melt compounding. Calculation of the volumetric flow of the material within the recirculating compounder was necessary to relate the processing parameters to the dispersion effectiveness and enable process scalability.

Development of characterisation protocols was required to analyse and quantify particle dispersion and to link the specific dispersion with the melt compounding parameters and mechanical properties of the processed materials. Through extensive experimental work, the selected nanocomposites were produced with established scalable processing conditions to manufacture proof of concept orthopaedic medical devices.

The core activities for this work included:

- Process conditions optimisation for extrusion and injection moulding (effect of molecular weight and polymer structure, thermal degradation during processing, effect of additives, flow effects);

- Melt compounding of biodegradable resorbable PLA nanocomposites (effects of different particle shapes, coatings and loading on processing);
- Dispersion characterisation of the produced nanocomposites and association with mechanical properties;
- Development of characterisation protocols – monitoring degradation (gel permeation chromatography), dispersion quantification (transmission electron microscopy, microcomputed tomography) and macroscopic dispersion measures (e.g. thermogravimetric analysis, differential scanning calorimetry);
- Material production for delivery of demonstrator products with industrial partners (Evonik Industries AG, TESco Associates).

1.3. Outline

This thesis describes the production of novel bioresorbable HA-PLA nanocomposites for healthcare applications via melt processing and consists of eight chapters.

A review of the literature relating to the thesis in presented in Chapter 2. An overview of composites, predominantly nanocomposites, is provided followed by a brief summary of biomaterials for medical applications, with an emphasis on bioresorbable HA-PLA nanocomposites similar to those produced in this work. Previous experimental characterisation of thermal, mechanical and rheological properties of PLA and HA-PLA nanocomposites and of similar systems are reported, with attention to melt processing conditions. An overview of nanoparticle dispersion quantification methods for nanoscale images is also provided.

Chapter 3 describes the materials, namely medical grade PLA and novel HA nanofillers, safety procedures for nanoparticles handling, the utilised melt processing equipment and procedures for the manufacturing of nanocomposites. The methodology and specimen preparation for characterisation techniques used in later chapters are also summarised.

Chapter 4 reports on melt compounding analysis: laboratory scale extrusion limitations and reproducibility followed by the influence of processing parameters, types and amount of nanosized HA filler on the PLA matrix and particle mixing. Wall shear stress half-life time and mixing energy were compared to evaluate the changing properties of materials during compounding. A generally applicable set of processing parameters was identified to enable mixing of all types of novel HA nanoparticles with PLA in ambient air and inert atmospheres. Capillary rheology measurements of polystyrene and PLA were compared through a Carreau model and power-law model with their flow in the back-flow channel of the recirculating extruder used to approximate the number of recirculations during compounding for the polymers and nanocomposites.

Chapter 5 examines the effects of the addition of different HA nanoparticles and using changing melt compounding parameters on the molar mass, thermal and mechanical properties of the materials. The molecular weight of PLA, before and after processing in air, N_2 and dried N_2 are reported together with the molecular weight of all the processed nanocomposites, to identify evidence for matrix degradation. Molecular weight was compared with wall shear stress half-life time to indicate the materials with improved particle dispersion. A rheological model was also applied to separate the shear and temperature related degradation effects of melt processing. The glass transition temperature and degradation temperature (at 5% weight loss) were compared to assess thermal stability of the filled and unfilled PLA in air and inert atmospheres. They were linked with molecular weight measurements in order to evaluate degradation caused by the presence of HA. The flexural mechanical properties of the materials were also linked with the molecular weight and combined with previous findings to seek correlations between the results.

Chapter 6 reports and discusses the weight residue remaining after nanocomposites burn off in air; a method used as a verification of the filler weight fraction. The influence of run-to-run variations on the HANP content deviation is discussed. The morphology of HA-PLA nanocomposites was characterised using transmission electron microscopy and microcomputed tomography to observe and quantify particle dispersion.

Chapter 7 focuses on scalable manufacturing, the utilisation of larger extruders and methodology optimisation for compounding of pelletised stock of the developed nanocomposites. The demonstrator resorbable device and tensile bars were injection moulded at scale on industrial equipment. Characterisation techniques applied in the previous chapters were also used for the produced samples to confirm their molar mass, thermal and mechanical properties and HA nanoparticles dispersion. The influence of subsequent processing steps on the properties of the materials and final products is discussed.

Chapter 8 presents the conclusions of this work and proposes recommendations for future work.

Appendix provides short video footage of scale up melt processing activities carried out at Evonik Industries AG.

2. Literature Review

The following literature review is focused on poly(lactic acid) and hydroxyapatite reinforced PLA nanocomposites for biomedical applications, in particular their properties and melt processing.

Firstly, the concept of composites is briefly introduced with emphasis on nanocomposites as materials with nanosized filler. A review of a range of matrices with various nanofillers is presented and PLA nanocomposites are introduced as example of biodegradable materials with particular attention to manufacturing of HA-PLA nanocomposites. Next, biomaterials for medical applications are discussed with emphasis applied to the degradable bioesters, especially PLA and in particular HA reinforced PLA nanocomposites for orthopaedic devices. Properties of PLA are compared with the nanocomposite to highlight the change in material response due to the presence of HA nanofillers. Several HA-PLA nanocomposite systems are reviewed to show the influence of HA nanoparticles (nHA) on the material thermal stability, limiting degradation, mechanical reinforcement and rheological response. Melt processing of PLA and its nanocomposites filled with nHA is reviewed with focus on the equipment and methods to summarise favourable processing parameters to minimise materials degradation and maximise particle dispersion. Finally, the last section is concerned with quantifying the dispersion of nanoparticles on transmission electron microscopy micrographs. This is followed by some closing remarks and a summary of the presented literature review.

2.1. Composites

A composite is a material comprising of two or more phases or constituents, where a reinforcement (often the discontinuous phase) is dispersed in a matrix (continuous phase) [30]. Composites can be natural, for example, wood (cellulose fibres in lignin) and bone (collagen reinforced with HA), or artificial [31], for example, chipboard (wood waste embedded in resin glue) and concrete (sand and stones in cement). The most widely studied composites are synthetic composites based on a polymeric matrix reinforced with various fibres, e.g. thermoplastics with glass fibres used in the manufacture of internal bus panels and seats [32], or with mineral fillers, such as polypropylene mixed with talc for domestic appliances [33]. Nanocomposites are a special case of composites where interface interactions between phases are maximised due to the large available surface area of the nanosized filler [34].

2.1.1. Nanocomposites overview

Nanoparticles are often classified via their number of nano-scale dimensions (i.e. less than 100 nm) [34]:

(i) one-dimensional - rod, needle or tube e.g. magnesium hydroxide needles [35].
(ii) two dimensional - platelet structures e.g. layered silicates [36].
(iii) sphere-like three-dimensional structures e.g. zinc oxide [37].

2.1.1.1. Nanocomposites

The greater surface area of the reinforcement in nanomaterials leads to a potential improvement in stress transfer. Additionally, as a result of the smaller dimensions of the filler, the size of flaws becomes smaller and the composites become stronger [31]. Finally, less material is required for effective reinforcement therefore the produced materials have densities comparable to pristine polymer. For these reasons, nanomaterials have become an attractive option for high end niche applications in the automotive industry, aerospace and healthcare.

Polymers reinforced with carbon nanotubes are an example of composites filled with one-dimensional nanoparticles which are both conductive and have excellent mechanical properties [38]. As an example, polycarbonate filled with carbon nanotubes is a candidate material for the production of conductive packaging for sensitive electronics capable of dissipating static charge [39].

Naturally occurring montmorillonites are extensively investigated two dimensional nanoparticles. After surface modification they readily exfoliate in the polymers improving mechanical and thermal properties, e.g. polyimide - clay nanocomposites [40] which, when compared to the original polymer, can be utilised in applications at higher temperatures such as the material for engine covers [41].

Carbon black is a well know additive [42], representing three-dimensional nanoparticles, which is extensively used for elastomers reinforcement, particularly rubbers [43]. It increases the strength, stiffness and wear resistance of rubber, all of which are essential properties for vehicle tyres, and is also utilised in applications where improved static charge dissipation is required [44].

2.1.1.2. PLA nanocomposites

Due to increasing everyday usage of petroleum-based polymers creating undegradable waste there is a great demand for development of green materials with nontoxic components allowing for composting. Research efforts in biodegradable polymers have focused on a family of polyesters, especially PLA due to commercial availability, melt processability on the existing equipment and good properties of the final product [45]. The application of PLA ranges from agriculture through to disposable cutlery and biodegradable packaging, and to medical devices. PLA nanocomposites are expected to have improved mechanical properties in comparison to the neat polymer, hence various nanomaterials have been investigated for PLA reinforcement. These include, but are not limited to, organic clays, minerals, silicates and carbon nanotubes.

PLA modification with naturally occurring silicates additionally offers improved gas barrier properties which are of particular interest to the food packaging industry to preserve freshness. In a study by Sinha Ray et al. [46], the testing of PLA-organically modified layered silicate nanocomposites, prepared by melt extrusion of PLA and montmorillonite modified with octadecylammonium cation (C^3C_{18}-mmt), is reported. Benefits from this nanocomposite include: increased strength, decreased gas permeability and higher modulus in the solid and melt state. When comparing PLA/4 wt% C^3C_{18}-mmt with PLA in solid state, experimental data showed increases of 56% (86 MPa to 137 MPa) in flexural strength, increases of 15% (4.8 GPa to 5.5 GPa) in flexural modulus, increases of

47% in storage modulus, and reductions of 12% in oxygen gas permeability. The incorporated nanoparticles enhanced the material properties even at only 4 wt% and intensified the rate of degradation. Over a 60-day period, under compost, the neat PLA had ~60% residual weight, whereas the PLA/4 wt% C^3C_{18}-mmt had fully degraded which is exceptionally beneficial for removal of packaging waste.

Batch to batch variations in the produced nanocomposites cause varying degradation rate and mechanical properties between the manufactured products. Scale up and production of a successful nanocomposite on a large scale eliminates the variation in properties seen between small batches, however such scale up can be limited due to cost of the materials or their shelf life. Therefore, production of a masterbatch, a concentrated uniform composite premix diluted further during subsequent processing, was considered as another method to uniform properties of produced items. This technique was utilised by Villmow et al. [47] for extrusion of multi-walled carbon nanotube (MWNT) PLA composites. It was proven that compounding temperature, screw profile and rotation speed all affect dispersion quality within the composite. Application of a masterbatch with a high dispersion index resulted in diluted composites with similar high MWNT dispersion, while composites produced from inferior masterbatches contained primary agglomerates. Therefore, masterbatch quality is crucial for further processing.

Another factor influencing PLA nanocomposite degradation is the degree of dispersion of the reinforcing particles, which can be aided with surfactants, and the content of hydrophilic groups in the discontinuous phase which causes faster degradation [10]. Armentano et al. [48] reported a 70% weight loss of poly(DL-lactide-co-glycolide) (PLGA) and PLGA films with single wall carbon nanotubes including carboxyl groups in biological fluid taking 22 days and 18 days respectively, i.e. 18% faster degradation.

PLA modification with inorganic nanofillers like hydroxyapatite improves mechanical and gas barrier properties in a similar way to clays. HA is a naturally occurring mineral with applications ranging from the preserving of antique canvas and paper from acidic deterioration [49], through to bone cements [50], and to commercially available enamel restoring toothpastes. HA reinforced PLA materials for biomedical applications and the nanocomposite constituents will be further discussed in the subsequent section.

2.2. Biomaterials for medical applications

The minimal requirements for biomaterials are: nontoxicity, efficacy, serialisability and biocompatibility. Implanted materials can induce a foreign body reaction, which is a natural body defence response, causing implant rejection or encapsulation. Consequently, research efforts in biodegradable polymers for medical devices have focused on polyesters [51, 52] as they do not require long lasting biocompatibility or repeat operations for removal.

The following biodegradable polyesters attracted significant attention: poly(glycolic acid) (PGA), poly(lactic acid) [2], polycaprolactone (PCL) [53], poly(p-dioxanone) [11], poly(3-hydroxybutyrate), polyethylene oxide [54] and their co-polymers, all of which share promising and comparably good properties for the fixation of tissue. Such polyesters started to be used in medicine as (i) devices for tissue fixation, e.g. bone plates [55] ligament screws [56] and suture anchors [53, 57]; (ii) drug delivery systems (by controlling the diffusion of active ingredients) [58, 59]; and (iii) wound treatments [60, 61] like surgical staples, sutures or artificial skin [62]. However, each of these bioabsorbable products on their own have some shortcomings which limit their usage [63].

2.2.1. Biodegradable poly(lactic acid)

Out of all the biodegradable polyesters, PLA is receiving the greatest attention because, in addition to its biomedical applicability, it has increasing commercial availability. As PLA degradation rate is comparable to bone healing rate, i.e. the time taken for total polymer degradation is similar to the timescales involved in bone remodelling, it has been applied mainly in the orthopaedic field [53]. Numerically, for bone healing, soft callus formation generally occurs in the first 4-6 weeks, adequate strength is seen to be gained within 3-6 months and bone remodelling is completed within several months to several years [64]; naturally all timescales are dependent on the age and health of the patient. In comparison, amorphous PLA maintains its strength up to 12 weeks, this is followed by gradual degradation [55] and absorbs in vivo within 12-16 months [18].

2.2.1.1. PLA origins

PLA marked its place in the world of polymers in 1932 when Carothers pioneered the manufacture of this aliphatic polyester from lactic acid. However, the original product had low molecular weight and poor mechanical properties. In 1954 DuPont patented higher molecular weight PLA but its predisposition to hydrolytic degradation, common to all aliphatic polyesters studied at that time, halted this research. Ethicon resumed work in this area, and in 1972, introduced high-strength fibres for biocompatible resorbable sutures made from copolymers of lactic acid and glycolic acids. However, until the late 1980s, the high production cost of aliphatic polyesters limited their application exclusively to medical products [65].

The technology to produce PLA on a commercial scale was developed by a newly established company, Cargill Dow LLC, in 1997. They patented a low-cost continuous process for the production of lactic acid-based polymers in the melt. The Cargill process is described in detail by Henton et al. [66], along with further information regarding the bacterial fermentation process of lactic acid production, and Cargill’s method life cycle analysis with green chemistry principles.

2.2.1.2. Synthesis

PLA is a chiral polymer which can be synthesised from optically active D- or L-enantiomers of lactic acid (2-hydroxy propionic acid). The molecular structure of PLA is shown in Figure 2.1. The relative amounts of the two enantiomers and their distribution determine many properties of the polymer. PLA tends to be crystalline opaque white material with L-content greater than 90% or totally amorphous and transparent polymer with lower stereopurity [67].

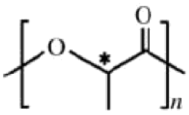

Figure 2.1. Structural repeat unit of PLA with the chiral carbon atom marked by *. Adapted from Jiang et al. [67].

Poly(L-lactic acid) (PLLA) crystalizes in three different structural conformations – α, β and ϒ, which develop under different temperature and pressure dependent processing conditions. Additional information regarding PLA crystallinity and complex thermodynamic changes occurring during crystallisation, relevant for modifying polymer properties, can be found in Fambri and Migliaresi [68].

Commercially available high molecular weight PLA resins, greater than ~100 kg.mol^{-1} (1 g.mol^{-1} = 1 Da) are typically copolymers of PLLA and poly(D-lactic acid) (PDLA) or poly(D,L-lactic acid) (PDLLA) and are produced via the lactide ring-opening polymerization (ROP) route [69]. ROP process, illustrated in Figure 2.2, starts with lactic acid, derived from renewable resources, followed by condensation to the low molecular weight PLA pre-polymer that is catalytically converted to a mixture of lactide stereoisomers. Next, lactides undergo a ring opening reaction using a catalyst to form the polymer chain [66].

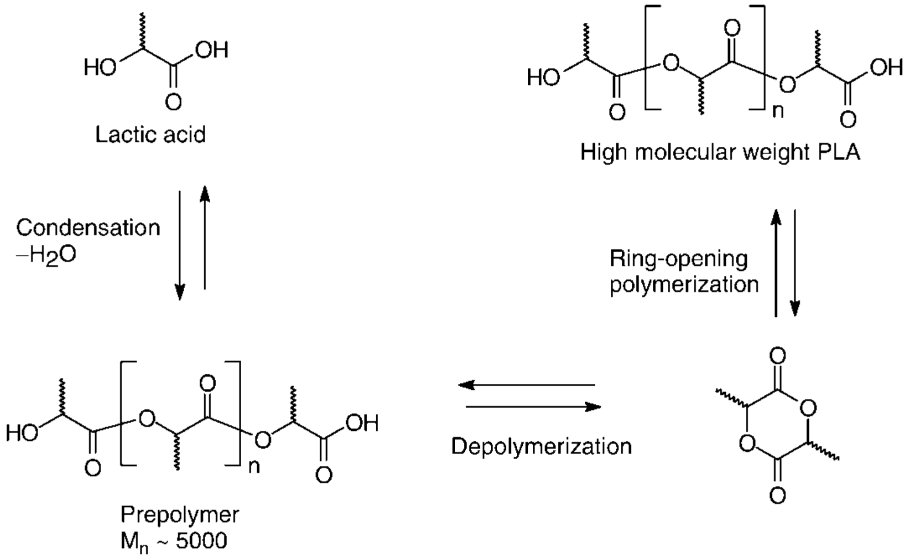

Figure 2.2. Production of PLA from lactic acid via lactide ROP. Adapted from Henton et al. [66].

2.2.1.3. Bone fixation devices

Many commercially available PLA products have been employed in the medical field [2, 51], such as: ligament and tendon reconstruction fibres, stents for vascular and urological surgeries, meshes for guided bone regeneration, bone mini plates for facial restorations, pins, screws, rods, suture anchors, meniscus arrows, rivets for the skull, lumbar interbody cage devices [51, 53, 57] and injectable microspheres in temporary fillings in facial reconstructive and cosmetic surgeries [70]. Figure 2.3 illustrates examples of PLA bone fixation devices produced by Gunze and Conmed.

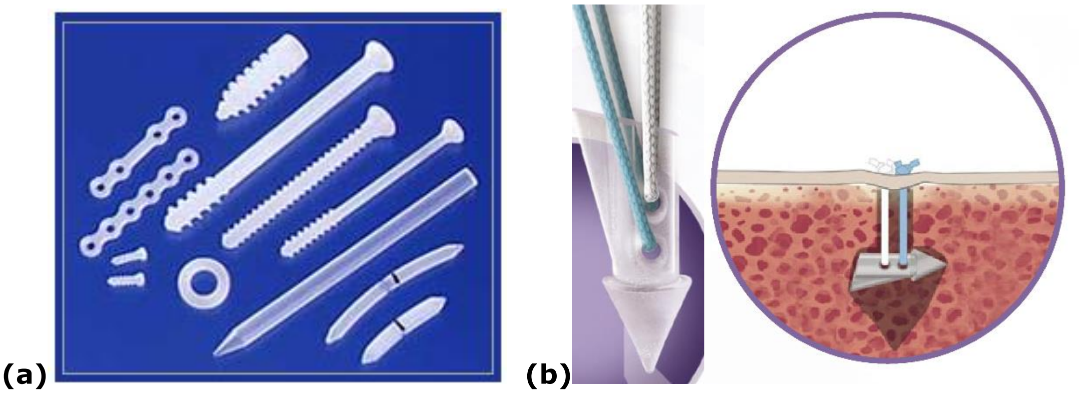

Figure 2.3. PLA bone fixation devices: (a) GRAND FIX - plates, screws, rods and spacers, adapted from Gunze [71], (b) Impact - PLA suture anchor for shoulder reconstruction, adapted from Conmed [72].

As shown above, PLA bone fixation devices were successfully commercialised and utilised in surgical procedures. Nevertheless, the size of PLA devices is limited due to bulk degradation of the polymer [73] which produces poor results for fixation under load. Bulk degradation is a process by which both the inside of the material and the surface degrade equally with initial loss of the molecular weight of PLA without total mass loss [52]. The polymer mass remains while the product degrades thus causing loss in mechanical properties while blocking tissue ingrowth. Subsequently the macroscopic structure of the polymer deteriorates, which then leads to a major mass loss at the end of the degradation process [11]. Formation of acidic products from degradation has an autocatalytic effect on the hydrolysis reaction thereby increasing degradation rate [74]. Burst of acidic decomposition products can cause an inflammatory response, illustrated in Figure 2.4. It is therefore important to match the degradation rate of any biomedical device with the rate of tissue regeneration. Figure 2.5 compares changes to mechanical properties of implant and tissue during tissue regeneration.

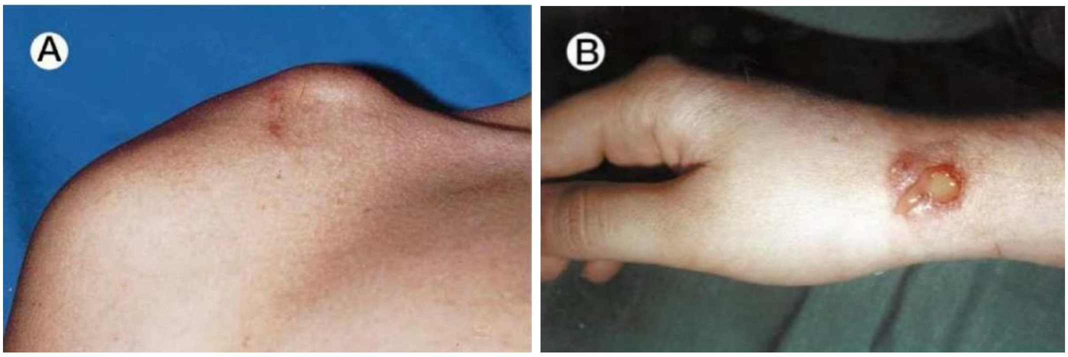

Figure 2.4. Example of a burst release of degradation material causing local inflammatory reaction (A) in shoulder fixture (B) screw in the wrist. Adapted from Parsons [75].

The toughness of PLA used for bone fixation can be improved by self-reinforcing with PLA fibres or drawing, which increases average orientation and crystallinity. Experimental data from TÖrmälä et al. [54] indicates that bending stiffness of PLLA can be increased from 113-142 MPa unreinforced to 300 MPa self-reinforced, with fibres with a draw ratio of 12. The increased stiffness was found to be dependent on draw ratio e.g. fibres with a draw ratio of 4 provided only 200 MPa of stiffness.

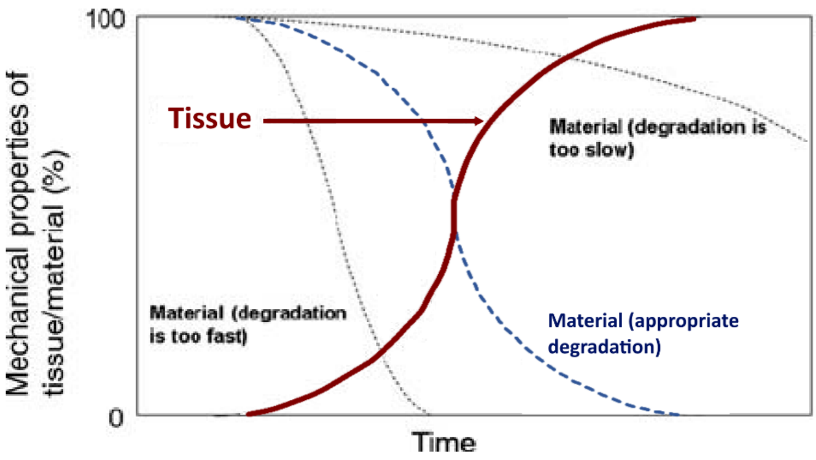

Figure 2.5. Estimation of applicable range of mechanical properties for bioresorbable medical device during tissue regeneration. Adapted from Suzuki and Ikada [53].

However, this strength adjustment is complex as the healing rate is dependent on the patient and on the extent of the tissue damage. Additionally, degradation products like oligomers, monomers, additives, residues of polymerisation initiators and catalysts are also of concern as they may cause toxic effects in the body. These compounds are released continuously in the body therefore their amount is limited within the established regulations, and safety of their metabolites must be considered. Another concern is the method of sterilisation used for biodegradable medical devices. PLA is sensitive to radiation which causes its degradation, and therefore it is usually sterilised by toxic ethylene oxide requiring extensive degassing [53].

Mechanical limitations of PLA devices causing poor results for fixation under load can be mitigated by inclusion of filler e.g. HA.

2.2.2. Resorbable hydroxyapatite

Hydroxyapatite, HA ($Ca_{10}(PO_4)_6(OH)_2$) is the main inorganic component of bone [76] and is used as a dental and orthopaedic material. Advantages of incorporating HA in PLA include (i) improvements of mechanical properties in comparison to the neat polymer, (ii) generation of nanotopography imitating the structure of bone [77], (iii) formation of a biologically active surface which provides a bonding interface with tissues [18] and (iv) potentially neutralization of acidic degradation products of PLA [9].

However, lack of adhesion between HA and PLA was shown in [78] and a key to the improvement of the interfacial adhesion and mechanical properties of the nanocomposites is through modification of the HA surface. This was illustrated in studies by Qiu et al. [78] and Hong et al. [79] where nHA was successfully grafted with L-lactide via extensive mixing in heated solvent, discussed further in Section 2.5.3. For additional information on various other surface modifications of nHA, for example with several carboxylic acids and silanes, for materials for biomedical applications, the reader is referred to a paper by Šupová [4].

2.2.3. HA-PLA biocomposites

HA-PLA composites for medical applications are of high interest as they combine the osteoconductivity and bone bonding ability of hydroxyapatite [2] with the biodegradability and easy processing of polylactic acid [45].

HA-PLA composites can be obtained via: solvent mixing [80-83], sintering [84], forging [85, 86], in situ polymerization [87] and melt compounding [9, 20, 88-91]. However, the most common technologies for processing PLA based nanomaterials are extrusion and injection moulding discussed further in Section 2.4.

HA-PLA nanocomposites were studied by various research groups with examples of the work shown below. Mathieu et al. [80] produced 5–30 wt% nHA-PLLA via solvent mixing, sintering and twin screw extrusion under nitrogen, examples of scanning electron microscopy (SEM) images are shown in Figure 2.6. The composites obtained via melt compounding had homogenous filler dispersion and exhibited a 36.8% higher modulus at 10 wt% HA, approx. 0.52 GPa, in comparison to compounds mixed in a solvent (chloroform), approx. 0.38 GPa.

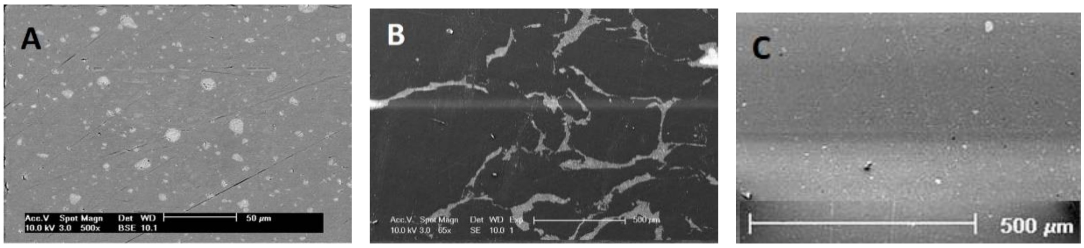

Figure 2.6. SEM images of 5 wt% HA-PLLA produced by (A) solvent mixing, (B) sintering and (C) extrusion. Scale bar 50 µm in (A) and 500 µm in (B) and (C). Adapted from Mathieu et al. [80].

Wilberforce et al. [20] produced nano and micro HA-PLLA composites also via melt mixing in a twin extruder. BSE-SEM images of the obtained 10-30 wt% HA-PLLA nanocomposites are shown in Figure 2.7.

Delabarde et al. [88] compounded PLLA with 0.5-10 wt% nHA in a twin screw co-rotating extruder to investigate effects of accelerated ageing on the nanocomposite films submerged in aqueous NaOH at 50 °C; examples of their SEM images are shown in Figure 2.8.

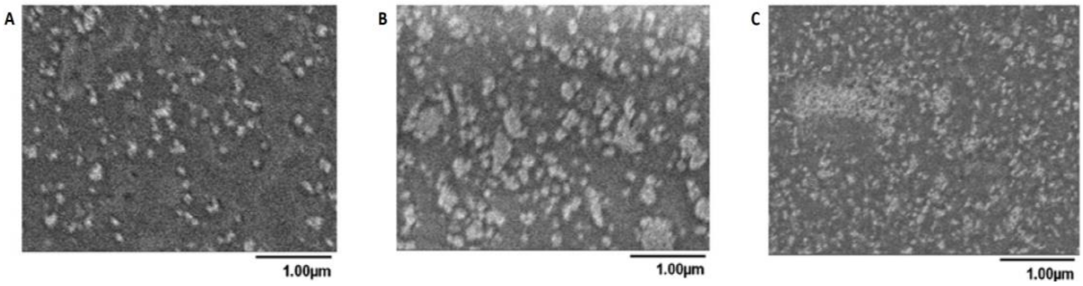

Figure 2.7. BSE-SEM images of freeze fractured HA-PLLA nanocomposites at: (A) 10 wt%, (B) 20 wt%, (C) 30 wt%. Adapted from Wilberforce et al. [20].

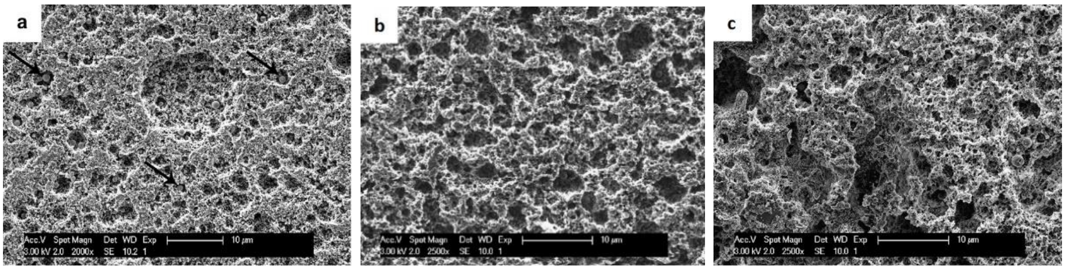

Figure 2.8. SEM images of amorphous PLLA-10 wt% nHA after (a) 1 week, (b) 3 weeks and (c) 5 weeks of ageing. Scale bar 10 µm. Adapted from Delabarde et al. [88].

All the melt processed materials were produced on a laboratory scale. The majority of these were from semicrystaline PLLA [9, 20, 80, 88-90] of relatively low average molecular weight (M_w) for the utilised polymer packaging grades [9, 89, 90] with the highest M_w of 218 kg.mol^{-1} [9]. For the medical grade PLA [20, 80, 88, 91], the highest M_w was 350 kg.mol^{-1} [20]. The compounded HA nanofiller ranged from custom synthesised particles [9, 20, 80, 91] to commercially available products [88-90].

Previous research in the area of extruded HA-PLA nanocomposites, introduced above, provides a reasonable starting point for optimising processing of novel HA nanofillers with high molecular weight, medical grade, amorphous PLA via melt compounding, dedicated for scale-up, focused on in this work. Melt compounding parameters applied in the relevant research will be further discussed in Section 2.4.1.2.

2.3. Thermal properties

2.3.1. Transition temperatures and melt density of PLA

The glass transition temperature (T_g) and the melting temperature (T_m) of PLA are dependent on both the molecular weight and the isomeric purity of the resin. Decreasing the amount of PLLA relative to PDLA reduces the order in the polymer causing a decrease of the T_g and T_m from 50-70 °C and 170-190 °C respectively for isotactic PLLA, to 34 °C and 155 °C for syndiotactic PLA. In contrast, equimolar blending of pure PLLA with PDLA increases T_m for the PLA stereocomplex to 230 °C. A rise in both T_g and T_m is also caused by increasing the molecular weight of PLA, which is shown in Figure 2.9 [68]. Additionally, Dorgan et al. [92] demonstrated, via differential scanning calorimetry of commercial grade branched and linear PLAs with comparably high molecular weights, that different architectures have indistinguishable melting and glass transition temperatures.

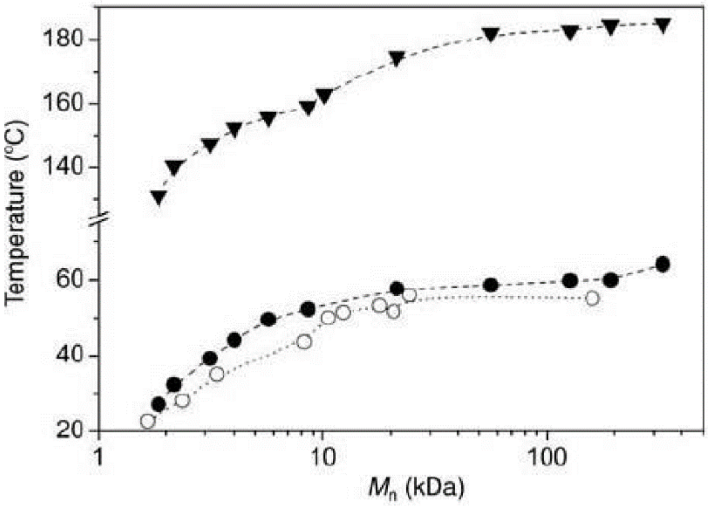

Figure 2.9. Increase of glass transition temperature of PDLLA (o) and PLLA (•) and melting temperature of PLLA (▼) with increasing molecular weight. Adapted from Fambri et al. [68].

The transition temperatures, T_g and T_m, are important in establishing operating temperatures for processing. Articles requiring good thermal stability could be produced from highly crystalline PLA by injection moulding, whereas more amorphous resins with a higher content of PDLA could be used for extrusion [69].

The physical characteristics of PLA, such as density, heat capacity, mechanical and rheological properties, are greatly dependent on T_m and T_g. Amorphous PLA transitions from a glassy state to a rubbery state above T_g (~58 °C) and will behave like a viscous fluid upon further heating. However, below T_g, amorphous PLA becomes a glass that is susceptible to creep. Once PLA is cooled to room temperature, and below, it behaves as a brittle polymer [66].

2.3.2. PLA thermal stability and degradation

Polymer degradation is an irreversible process changing the molecular structure of a material. Starting from the manufacture of the polymer up to product decomposition, polymer degradation results in a loss of properties and fragmentation. The process is affected by environmental and processing conditions over a period of time. Although polymer degradation can be affected by numerous factors this section focuses on thermal degradation of PLA during processing.

Thermal degradation usually alters the physical and optical properties of polymers, resulting in, for example: a change in colour, a decrease in molecular weight, a reduction in ductility, embrittlement and chalking (erosion of the top layer of the polymer causing a powdery residue). Various mechanisms are responsible for thermally induced changes such as depolymerisation and chain scission. Thermal degradation of polymers is also related to their melting temperature regime and their structural composition [10].

Degradation of polymers can be assessed by various methods. These include gel permeation chromatography, which measures molecular weight via hydrodynamic volume; scanning electron microscopy or atomic force microscopy, which enables observation of visual changes; X-ray diffraction, which monitors changes in the crystal structure; and electrochemical impedance spectroscopy, which enables surface energy measurements [10]. Also, rheological measurements can reflect the loss in molecular weight of PLA in the molten state [28, 93].

PLA has rather poor thermal stability: the temperature for maximum rate of decomposition ranges from 240 °C to 370 °C [94]. The exact figure is strongly dependent on the structure of the polymer chain end-groups, the molecular weight, macromolecular architecture and sample purity. The upper limit of thermal resistance of PLLA has been studied by Libiszowski et al. [94] who measured the onset temperature of thermal degradation as 337 °C and the temperature of maximum degradation rate as 376 °C.

PLA degradation at higher melt processing temperatures during manufacturing causes an undesired loss of weight and molecular weight reduction of the polymer in final products. Taubner et al. [95] reported that processing of dried PLLA with number average molecular weight (M_n) initially of 40 kg.mol^{-1} in a twin-screw extruder with screw rotation speeds of 120 rpm and 20 rpm at 210 °C caused the M_n to drop to 33.6 kg.mol^{-1} and 30.2 kg.mol^{-1} respectively and at 240 °C the M_n values decreased severely to 25.6 kg.mol^{-1} and 13.6 kg.mol^{-1} respectively. Faster screw speed led to reduced degradation which may be due to shorter residence time; numerically, when the speed was increased from 20 rpm to 120 rpm the residence time decreased from 7 min to under 2 min).

Thermal degradation mechanisms for this polyester are complex and can be mostly attributed to: hydrolysis by water residue in the polymer, unzipping depolymerisation and intra- and inter-molecular transesterification forming decomposition products e.g. cyclic lactide oligomers. Various transesterification degradation reactions of PLA were summarised by Lim et al. [69]. Kopinke et al. [96] proposed that above 200 °C, PLA can degrade through intra- and inter-molecular ester exchange, cis-elimination, radical and concerted non-radical reactions, resulting in the formation of acetaldehyde, methylketene, carbon monoxide and dioxide. Other important factors that should be also taken into consideration to control the thermal degradation process of the polymer include residues of the polymerisation catalyst, chain-end structures, depolymerisation catalysts, stereoisomeric composition, racemization and copolymerisation [97]. Lee et al. [98] reported experiments on thermal degradation dependency on chain-end structures and observed an increase from ~260 °C to ~450 °C in the temperature to complete weight loss when using OH- and Cl-terminated polylactides respectively.

2.3.3. Thermal stability of HA-PLA nanocomposites

Inclusion of nHA in PLA changes the temperature at 5% weight loss ($t_{5\%}$) of the polymer. Wan et al. [81] demonstrated an increase in $t_{5\%}$ with increasing amounts of particles for HA-PLA nanocomposites produced via mixing in preheated dimethylformamide at 60 °C and subsequent freeze drying. Numerically, when compared to PLA only, for the nanocomposite with 10 wt% nHA, $t_{5\%}$ increased by 4.9 °C which increased by a further 8.3 °C for 20 wt% nHA. Liu et al. [90], in their study on microinjection moulded 5 wt% nHA-PLA, showed 2 °C decrease in $t_{5\%}$ for the microinjection moulded sample when compared with conventionally injection moulded material. This infers a decrease of molecular weight due to increased shearing, however M_n was not provided to validate this assumption.

2.4. Melt processing of PLA and the nanocomposites

PLA resins and composites can be converted into a wide range of products via melt processing, which involves heating the polymer above T_m (or softening temperature for amorphous PLA) to enable shaping, followed by cooling to stabilize the dimensions.

Properties of PLA can be adapted for different fabrication processes, such as extrusion, injection moulding, stretch blow moulding, thermoforming, film and sheet casting, foaming, fibre spinning and electrospinning. Controlling polymer branching, molecular weight distribution and content of D-isomer enables tailoring of PLA for specific applications.

One common drawback of industrial processing of PLA in the molten state is the aforementioned degradation discussed in Section 2.3.2, causing lactide formation, which then fumes and fouls the equipment. This can be minimised by stabilising the polymer with additives and a catalyst [66], and by elevating the temperature of the processing equipment to reduce lactide condensation. All thermal processing operations are expected to influence the degradation of PLA to some degree [69].

The importance of adequate drying of PLA before further processing cannot be understated. Moisture residue combined with the temperature and manufacturing time contributes greatly to the molecular weight drop of the polymer via hydrolysis. Henton et al. [66] reported that amorphous PLA significantly reduces its M_w from ~300 kg.mol^{-1} to ~5 kg.mol^{-1} during a month when exposed to 60 °C and 80% relative humidity, respectively. PLA is a hygroscopic thermoplastic which readily absorbs moisture from the atmosphere. Therefore, it is generally packed in dry air, preferably under vacuum, and stored in sealed containers. Commercially available PLA is dried by the manufacturer to moisture levels below 400 ppm before shipping, and is followed subsequently by drying, directly before processing, to 200 ppm or even 50 ppm to ensure a reasonable safety margin. Generally, PLA handling before processing should be minimalized and performed in a dry air atmosphere. Ideally the polymer should be conveyed directly from the dryer to the processing equipment. Most manufacturers recommend drying crystalline PLA at 65 °C to 87 °C, and amorphous PLA at lower temperature, in vacuum ovens purged with dry air or using dehumidified air with a dew point of -40 °C [99].

The most common technologies for processing thermoplastics materials, including PLA and its nanocomposites, are extrusion and injection moulding. Therefore, this section focuses on these two techniques.

2.4.1. Extrusion

For extrusion, the optimal quantity of PDLA in PLA is in the range of 4-8 wt%, which does not allow PLLA crystallisation during processing. This decrease of isomeric purity also depresses the T_m of PLA, which expands the processing window and reduces thermal and hydrolytic degradation. The temperature during extrusion must be greater than T_m to enable homogenous melting, but low enough to limit thermal degradation. Usually the processing temperature is set between 40 °C and 50 °C above T_m to ensure complete melting of PLA [100].

2.4.1.1. Mixing with a single screw extruder

Figure 2.10 illustrates the construction of an extruder, which consists of the following parts: (i) a feed section which conveys the received polymer pellets into the screw; (ii) a transition section, also known as the melting or compression section, where the decreasing flight depth compresses the polymer; (iii) a metering section with constant shallow flight depth which pumps out the required amount of molten polymer. The length-to-diameter ratio (L/D) describes the proportion of flight length to the outer diameter of the screw and controls the shear and residence time of the melt. Thus screws with large L/D provide better mixing, greater shear heating and longer melt residence time in the extruder. Commercially available PLA can be processed with conventional extruders, used for other thermoplastics, with an L/D of 24-30 [69]. Particularly useful is low-shear equipment used for extruding polyethylene terephthalate, with an L/D of 20 [101], as it provides gentle mixing thereby minimising degradation of PLA. Compression ratio is another important screw factor which is obtained from the ratio of the flight depth in the feed section to the flight depth in the metering section. The bigger the compression ratio, the greater the shear heating provided by the screw. PLA is usually processed within a compression ratio of 2-3 [69].

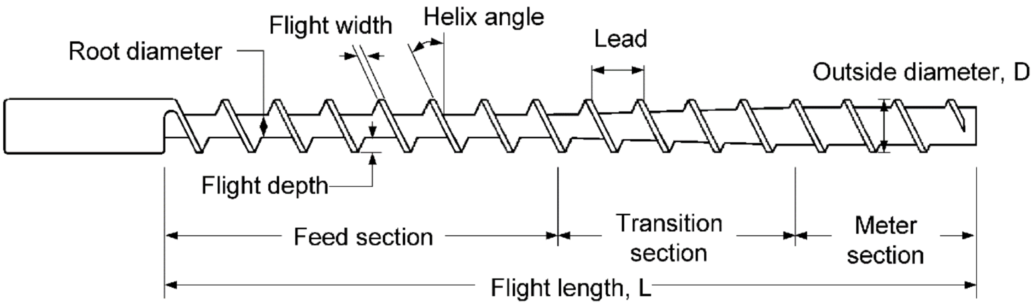

Figure 2.10. Representative construction of a single-screw extruder. Adapted from Lim et al. [69].

The extruder screw is driven by a motor which transports PLA pellets from the feeding zone, fed there via the hopper, through further sections of the barrel. Friction occurring during this process produces most of the heat required to melt the polymer. However, heater bands are also wrapped around the extruder barrel to provide uniform temperature distribution, usually within the range of 200-210 °C, to ensure even melting of PLA thereby achieving optimal viscosity for processing i.e. 500-1000 Pa.s at shear rates of 10-50 s^{-1} for a molecular weight of ~100 $kg.mol^{-1}$. Rheological properties of PLA must be taken into consideration during extrusion [100].

2.4.1.2. Compounding in a twin-screw extruder

The conventional single screw extruders are usually unable to provide sufficient mixing to break up and disperse filler agglomerates in the polymer melt. A twin-screw extruder typically achieves better particle dispersion in the matrix [69] by exerting greater shearing. This section will focus mainly on reviewing the processing aspects of twin-screw extrusion of PLA nanocomposites filled with hydroxyapatites. Attempts were made by various research groups to produce uniformly dispersed nanocomposites via a range of different extruders with examples of the work shown below.

Mathieu et al. [80] ground pre-dried PLLA pellets in liquid nitrogen down to 1 mm and mixed them with pre-dried 5 wt% nHA in glass vials. Further mixing was performed in a Micro 5 Compounder with two conical co-rotating screws at two temperatures 200 °C and 205 °C and at 3 different speeds for 1-4 minutes under nitrogen (to minimise oxidative degradation of the polymer). Optimum compounding conditions were achieved at a temperature of 205 °C and a speed of 100 rpm. The composites obtained via this process were observed to have homogenous filler dispersion.

Wilberforce et al. [20] also utilised a small twin screw extruder (HAAKE II microcompounder, Thermofisher Scientific) for optimised melt mixing of PLLA with 10-30 wt% of nano and micro sized HA. They successfully compounded materials at 200 °C with a speed of 125 rpm for 15 minutes.

Delabarde et al. [88] conducted melt compounding tests within an operating regime similar to the experiments performed by Mathieu et al. [80], using a DSM Micro 5 compounder with co-rotating screws to mix PLLA with 0.5-10 wt% nHA at 200 °C and with a screw speed of 110 rpm to obtain compression moulded films.

2.4.2. Injection moulding

Injection moulding enables the conversion of molten polymer into articles of a complex shape requiring high dimensional precision. Figure 2.11 illustrates the construction of an injection moulding machine, which consist of: a mould, operating under high pressure, and a reciprocating extruder plasticising and conveying the polymer melt.

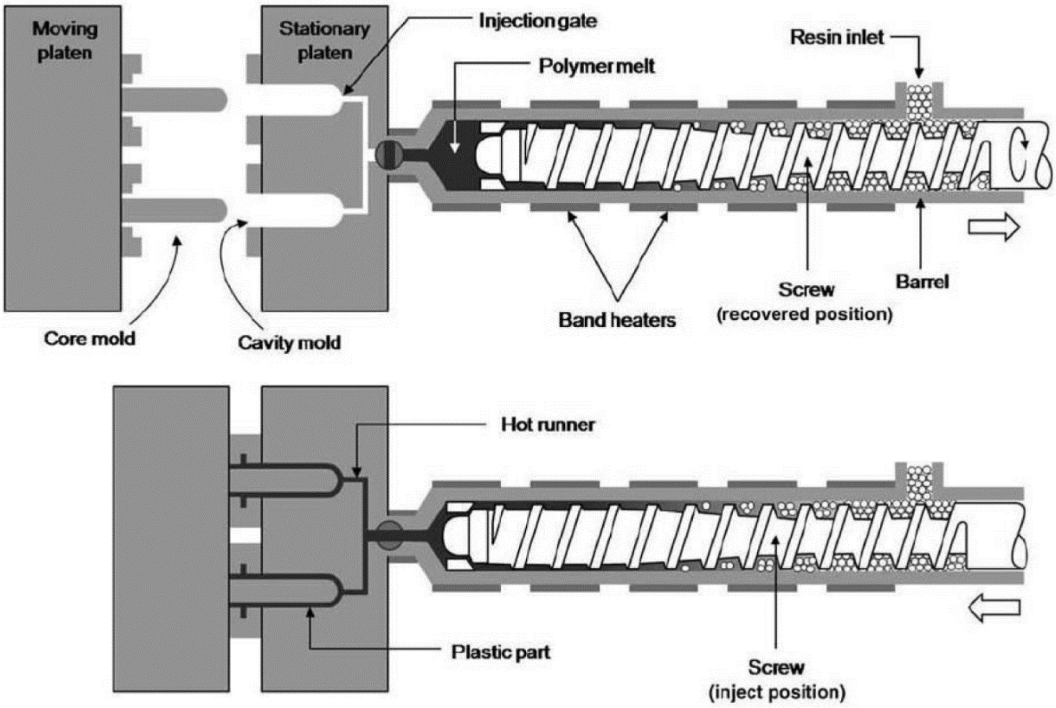

Figure 2.11. Injection moulding machine with a reciprocating screw. Top: backward screw rotation accumulating polymer melt in the front of the barrel. Bottom: once the moulds are clamped the screw moves forward injecting molten polymer into the mould via the hot runner. Adapted from Lim et al. [100].

This extruding unit contains a reciprocating screw that can move axially within the barrel to build up the pressure necessary for the injection and compression of the molten polymer into the mould. Most injection moulding machines for PLA are two-stage systems integrating a reciprocating screw extruder with a shooting pot. The extruder feeds the plasticized polymer into the shooting pot under relatively low pressure which rises once the plunger injects the melt from the shooting pot to the mould via a hot runner. The screw can continue rotating through the majority of the cycle which enables uniform melt quality and more consistent shot size, reducing cycle time [100]. A typical injection moulding cycle is illustrated in Figure 2.12.

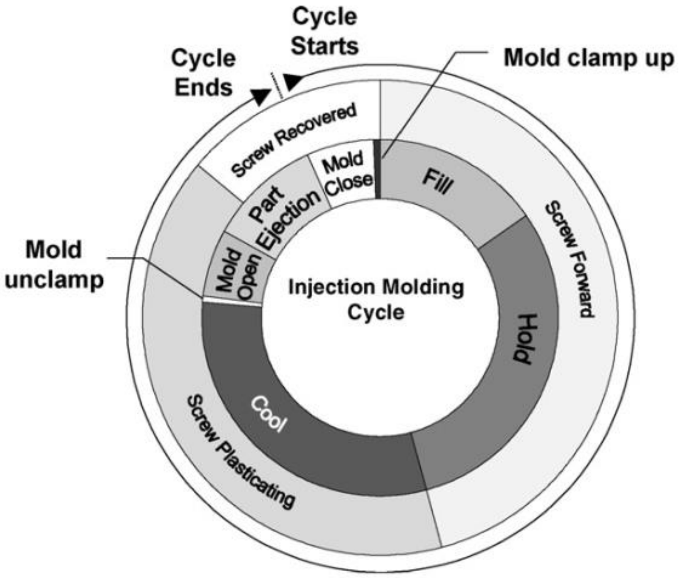

Figure 2.12. Injection moulding cycle. Adapted from Lim et al. [69].

Cycle time is often minimised to maximise the production throughput, which is achieved via:

(i) Reduction of operational time of non-process events like mould opening, part ejection and mould closing [69]. Typically up to 95% of the cycle time is taken by cooling of polymer in the mould [102, 103].

(ii) Another method involves transferring partially cooled elements and then cooling further outside of the injection mould on chilled surfaces. However, this is not a feasible method for production of PLA medical devices, where dimensional control is vital, due to increased part shrinkage during further cooling without applied hold pressure. PLA products undergoing isobaric cooling in the mould at 24 °C have an expected shrinkage strain of 0.004 [101].

(iii) Lowering the mould temperature enhances heat removal from the polymer which also reduces the cycle time. However, lactide condenses on cold tooling surfaces, which limits the minimum mould temperature to 25-30 °C. Deposition of the lactide layers can be also decreased by polishing moulds and increasing injection speed during fill [69]. Typical injection speeds for biopolymers range from 0.013 $m.s^{-1}$ to 0.051 $m.s^{-1}$ [101].

During injection moulding the molten polymer is shaped in a mould under pressure while it is cooling. Quenching of molten PLA at high cooling rate will produce a highly amorphous polymer which is more brittle under ambient conditions. A study on the fracture toughness of quenched PLA was undertaken in Park et al. [104]; results indicated a toughness of approx. 4.2 $MPa.m^{0.5}$ and 3.2 $MPa.m^{0.5}$ in static and dynamic loading conditions respectively. Surgical orthopaedic fixtures require mechanical properties matching at least those of cancellous bone (compressive strength between 2-20 MPa and elastic modulus between 0.1-2 GPa) and ideally reaching the lower range of strength for cortical bone (compressive strength 100-200 MPa and elastic modulus 7-25 GPa) [13, 20]. Cancellous bone properties could be achieved and exceeded by using crystalline PLA [100]. High levels of crystallinity may be obtained during fast cooling via rapid crystallisation of PLA containing less than 1% of PDLA. To achieve this nucleating agents are often added to resins to enhance the development of crystallinity during the cooling cycle [66]. In a study by Kolstad [105] talc was used as a nucleating agent in poly(91% L-lactide-co-9% meso-lactide) and results showed, at 90 °C, a crystallisation half-time reduction of 32% when increasing talc levels from 2 wt% to 6 wt%. Another option to increase the crystallinity of PLA is annealing of the injection moulded articles at temperatures greater than T_g but below T_m. Thermal processing history of PLA can be observed via differential scanning calorimetry measurements.

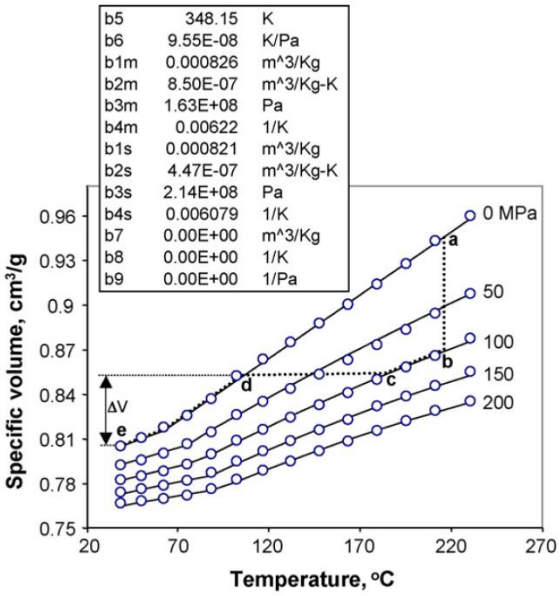

Figure 2.13. Pressure-volume-temperature plot for PLA 7000D manufactured by NatureWorks LLC. Adapted from Lim et al. [69].

The diagram presented in Figure 2.13 illustrates the fill, hold and cool events occurring during injection moulding of PLA. The process of injection moulding consists of an isothermal injection of polymer into a mould (trace ab in Figure 2.13) where it undergoes isobaric cooling (trace bc), followed by isochoric cooling once the gate temperature drops below T_g (trace cd). The article is then ejected and continues isobaric cooling to room temperature outside the mould (trace de). The injection moulding steps have influence on the shrinkage of the manufactured PLA articles, which is minimalized by applying increased pressure during isobaric cooling. However, large hold pressure leads to forming "flash" on the injected article due to excessive material flow into the mould parting line [69].

2.5. Mechanical and rheological properties

2.5.1. Properties of PLA

Viscometry of dilute polymer solutions enables the determination of polymer molecular weight. Solution viscosity of PLA in solvent is often used for molecular weight evaluation despite the fact that is not a directly applicable property for the melt processed polymer. Melt rheology links the molecular structure of PLA with dynamic properties such as viscosity.

Melts of low molecular weight PLA behave similarly to Newtonian fluids under applied shear, whereas high molecular weight PLA becomes a pseudoplastic non-Newtonian fluid [69].

During processing, polymers undergo shear deformation and therefore their viscosity can be described as the resistance of material to flow. With increasing viscosity, the applied force required to deform the fluid increases as well [93].

Semicrystalline PLA usually has a higher shear viscosity than amorphous PLA, with the same molecular weight, under identical processing conditions due to differences in polymer chain structure, such as molecular geometry, flexibility and the intermolecular forces. The partially organised pattern of molecules in semicrystalline PLA, in comparison to the entirely random order in amorphous PLA, provides a greater resistance to flow as a result of reduced polymer chain flexibility and stronger intermolecular forces [106]. Furthermore, with an increasing shear rate the viscosity of the melt decreases significantly, and the molten polymer shows shear-thinning behaviour. Viscoelastic properties of PLA melts can be characterised by the zero-shear viscosity (η_0) which is strongly affected by the molecular weight [69]. This η_0 value is attained at the limit of low shear rate and can be obtained from dynamic experiments. However, interpretation of the melt rheology of PLA is not always consistent mainly due to difficulties with measurement of absolute PLA molecular weight and added complications arising from the array of optical copolymers examined [66].

Dorgan et al. [92] reported an increase of η_0 and shear thinning in PLA after incorporating star-shaped polymer chain architectures obtained through multi-armed initiators. Their polymer chain length can be described by the span molecular weight, which is defined as the longest linear chain span found across the polymer molecule. For star polymers the maximum span is the length of two star arms. It has been confirmed experimentally that the η_0 of monodisperse star polymers depends only on the span molecular weight. Dorgan demonstrated that architectural modifications of the polymer caused changes in flow properties, enhancing PLA's applicability for melt processing. An example comparing the complex viscosity of a four-arm tetrol-initiated PLA star and a diol-initiated linear PLA, having identical molecular weight and composition, can be found in Figure 2.14. Characteristics expected of branched materials are seen: a higher η_0 and a lower viscosity at high shear rates for star materials.

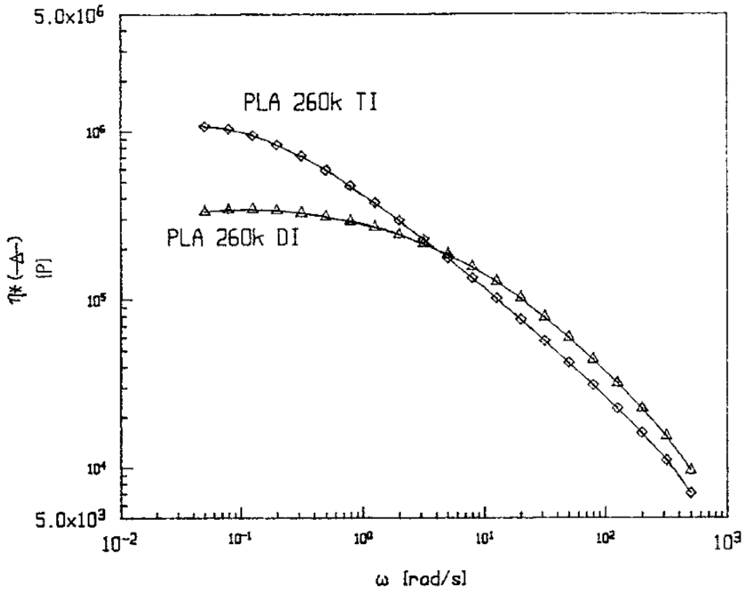

Figure 2.14. Flow curves for star (TI) and linear (DI) PLA both having nominal M_w of 260 kg.mol^{-1}. Adapted from Dorgan et al. [92].

Factors such as: molecular weight distribution of the polymer, degree and type of branching, isomeric composition, melt stability and shear rate, affect the flow characteristics of PLA and must therefore be taken into consideration during both (i) modelling and optimisation of processing operations and (ii) tooling design [66]. The rheological parameters of the polymer melt are also influenced by processing conditions, e.g. increasing temperature during extrusion causes a decrease of melt viscosity.

PLA mechanical properties are also affected by the molecular weight, the chain architecture, and the degree of crystallinity [93]. Overall, PLA exhibits good mechanical properties, with tensile strengths ranging from 50 MPa to 70 MPa, modulus of elasticity values from 3 GPa to 4 GPa, elongation at break between 2% and 5%, flexural modulus of 4-5 GPa and flexural strength of 100 MPa [107]. As a result of these properties it could replace many thermoplastics in processing applications e.g. thermoformed polystyrene dairy containers, blown-extruded polyethylene cling films and blow-mouldable polyethylene terephthalate bottles. However, the low elongation at break limits some of its uses. It is also worth noting that although amorphous PLA is brittle at room temperature, it has good strength and stiffness.

The mechanical properties of PLA can be adjusted to suit application by several approaches. To modify the strength, these include: (i) blending with other polymers, e.g. PCL/PLLA blend (in solution) with composition ratio 80:20, which decreases tensile strength to 22 MPa while increasing elongation at break to 11% (ii) copolymerisation, e.g. addition of 10 wt% of PLLA-PCL copolymer to 80:20 PCL/PLA blend, which modifies tensile strength to 19 MPa and elongation at break to 31% [108], and (iii) plasticization, e.g. with 20 wt% of tributyl citrate which decreases tensile strength to 7.1 MPa and increases elongation at break to 350% [107]. Crystallisation of PLLA considerably improves the mechanical properties of the polymer and it can be encouraged via several manufacturing methods such as: (i) annealing – thermally inducing crystallisation, e.g. annealing PLLA with M_w ~50 kg.mol^{-1} at 105 °C increased crystallinity from 9 to 52%, flexural strength from 100 to 113 MPa, and Izod impact resistance (notched) from 2.5 to 7 kJ.m^{-2} (ii) freezing in mechanical orientation, e.g. drawing PLLA film in biaxial orientation with stretching of 2-6 times in both directions at temperature above T_g (70-90 °C) increases tensile strength to 100-200 MPa and elongation at break to 50-150% [107], and (iii) nucleation via incorporating a filler during extrusion, e.g. addition of 6 wt% talc to PLLA reduces the crystallization half-time from 3 min at 110 °C to 25 s [69].

2.5.2. Polymer reinforcement with micro and nanoparticles

Wilberforce et al. [20] produced nano and micro HA-PLLA composites via twin screw extrusion. The HA size variation influenced the dynamic mechanical properties of the compounded composites. Consequently, it was established that the storage modulus of the nanocomposites was higher than that for the microcomposites, e.g. for 30 wt% of nano and micro HA-PLLA composites, the modulus reached 6.7 GPa and 5.6 GPa respectively, and approached the lower range of values displayed by cortical bone (7-8 GPa) in dry conditions. The storage modulus values for nHA-PLLA composites were higher as there was more nHA per unit volume to reinforce the polymer chains and their surface area is greater, which may be promoting a more effective stiffening of the PLLA.

McManus et al. [82] obtained 30-50 wt% nano and micro HA-PLA via solvent mixing. When compared with neat PLA, bending modulus increased for both the conventional composites and the nanocomposites by factors of 2.5-9.5 and 2.7-16.3, respectively. When comparing micro- and nanosized fillers the greatest difference in bending modulus was shown for 40 wt% HA-PLA where the modulus for the nanomaterial was 3.6 times greater than for the composite with a micro sized filler.

The effects of a bimodal distribution of micro-HA (5 μm) and nHA (100 nm) particles on the flexural properties of melt compounded HA-PLLA composites were investigated by Takayama et al. [109]. The materials contained 10 wt% HA, which for the bimodal nanocomposite consisted of 5 wt% micro-HA and 5 wt% nHA. The bending properties were effectively improved for the material with bimodal distribution showing approximately 40% increase in modulus in comparison to composites with monomodal distribution. As expected, flexural strength was the lowest for the nanocomposite, approximately 40% lower than that for the microcomposite. The highest strength was again seen for the bimodal material which was approximately 8% higher than the microcomposite.

2.5.3. Effect of nHA reinforcement of PLA

Addition of nanoparticles to polymers is expected to significantly improve mechanical properties of the polymer, for example stiffness, over those of the neat matrix and conventional microcomposites [82], mainly due to the large surface area of nanofillers [110]. Mechanical properties of nanocomposites also depend on factors such as the initial molecular weight and crystallinity of PLA, polymer degradation in relation to processing conditions, nHA morphology, loading content, degree of dispersion in the matrix and interfacial adhesion [81]. Examples of work on changing mechanical properties for nHA-PLA are provided below.

Wan et al. [81] produced 10-30 wt% nanocomposites via solution intercalation of custom synthesised plate-like nHA and commercially available PLA. The greatest tensile strength and modulus were obtained for 20 wt% nHA-PLA which increased by 33% and 21% respectively when compared with neat PLA. The decrease of mechanical properties for higher nHA content was attributed to nanoparticle agglomeration.

Mathieu et al. [80] claimed to obtain a minimal increase in tensile modulus for melt compounded 5-10 wt% nHA-PLLA when compared with only extruded polymer. However, the change in modulus is not clear on the provided graphical results due to the error size.

Liu et al. [89] compared mechanical properties of PDLA, PLLA and 1:1 PDLA/PLLA blends with their 2 wt% HA nanocomposites produced by melt compounding. At 20 °C the storage modulus for 2 wt% nHA-PDLA/PLLA was 5% higher than for PDLA/PLLA blend, while no significant difference was observed in the tensile strength and elongation. Tensile strength for 2 wt% nHA-PLLA decreased by 7% when compared with PLLA only and no difference was shown in their elongation.

Delabarde et al. [88] melt compounded PLLA with 0.5-10 wt% nHA to produce compression moulded films which were conditioned at 200 °C and quenched in cold water for amorphous structure. An increase in the rate of mass loss during ageing in 0.01M NaOH at 50 °C was observed in the presence of nHA, in comparison with films produced only with PLLA. In one case, numerical data indicated a 100% increase in mass loss over a 5-week period from 1.5% (PLLA amorphous) to 3% (10 wt% nHA- PLLA amorphous). However, the decrease in tensile strength and strain to failure within the aging time was less pronounced for nanocomposites than in the unmodified films since the nHA acted as a reinforcement. Over a 5-week period, the yield stress for amorphous PLLA decreased by a factor of 6.5 (approx. from 52 MPa to 8 MPa), whereas for 10 wt% nHA- PLLA amorphous the factor was 1.25 (approx. from 50 MPa to 40 MPa).

Qiu et al. [78] compared properties of PLLA (M_n 179 kg.mol^{-1}) nanocomposites, produced via melt compounding and compression moulded into samples followed by annealing, with 5-30 wt% needle-like nHA grafted with L-lactide (LLA-g-nHA) and nHA needle-like filler without surface modification. The tensile strength for 5-15 wt% LLA-g-nHA/PLLA increased 8-12% when compared with PLLA only (61 MPa), while the tensile strength of 20 wt% LLA-g-nHA/PLLA was comparable with the 5 wt% nanocomposite and further decreased to 2% below the strength of neat polymer with addition of 30 wt% particles. For 5-20 wt% unmodified nHA-PLLA nanocomposite the tensile strength only decreased by 6-34% when compared with pure PLLA. The tensile modulus for LLA-g-nHA nanocomposites with the same filler content range increased almost linearly by 9-76% when compared with PLLA only (1.65 GPa). For nanocomposites with unmodified nHA, tensile modulus initially increased by 9% for 5 wt% nHA and subsequently decreased down to 9% below the modulus of neat polymer for 20 wt% nHA.

Hong et al. [111] also grafted nHA with L-lactide and prepared nanocomposites with PLLA (M_w 300 kg.mol^{-1}), produced via solvent mixing and compression moulded into samples, with 2-20 wt% unmodified nHA and LLA-g-nHA. Half of the specimens prepared from each nanocomposite were then annealed. Tensile strength of the nanocomposites, as moulded, with unmodified nHA decreased with increasing amounts of filler by 3-22% when compared to neat PLLA (60 MPa), while addition of LLA-g-nHA did not alter the strength of the materials. Annealing increased tensile strength of neat PLLA (by 17% to 70.5 MPa) and both LLA-g-nHA and unmodified nHA nanocomposites. The strength for the annealed nHA-PLLA decreased with increasing amounts of filler when compared to annealed PLLA; this decrease occurred at a greater rate in relation to these nanocomposites as moulded. The strength decreased by 4-33% for annealed nHA-PLLA, and for 20 wt% nHA, to a level similar to that of unannealed sample. Tensile strength of the annealed nanocomposites with grafted particles increased by 6% at 4 wt% LLA-g-nHA, when compared with annealed PLLA, followed by a decrease in strength with increased particle loading, which at 10-20 wt%

LLA-g-nHA, decreased to a level obtained for PLLA as moulded. On the other hand, tensile modulus was unaffected by the type of the nanocomposite, i.e. unmodified or grafted nHA. The modulus of the materials as moulded increased with increasing amounts of filler by 21-64% when compared with PLLA (1.9 GPa). For the annealed materials the modulus increased by 10-23% with increasing amount of HA when compared with annealed PLLA (3.1 GPa). Bending modulus of the nanocomposites as moulded was also compared and was reported to increase with the amount of particles, and for materials with LLA-g-nHA it increased by 16-69% when compared to PLLA only (3.2 GPa). For composites with unmodified nHA the increase was to a lesser extent at 6-47%. The bending strength of annealed nanocomposites with grafted particles, in similar fashion to the tensile strength of these annealed materials, increased by 5% at 4 wt% LLA-g-nHA when compared with annealed PLLA (121 MPa). This was followed by a decrease of strength to 40% the strength of annealed PLLA for 20 wt% LLA-g-nHA. For unmodified nHA-PLLA the bending strength decreased more rapidly by 2-50%.

Melt processability of nanocomposites can be evaluated via melt rheology which also determines strength of interactions between the particles and polymer matrix and material structure (filler dispersion) which influence mechanical properties [46]. Typically, addition of particles to a polymer melt causes viscosity to increase, for example modified layered nanoclays in PLA [46, 112, 113], in line with Einstein's theory about the viscosity of liquids for dilute dispersions [114]. However, at high shear rates, well dispersed nanocomposites exhibit shear thinning of the melt due to shear alignment of filler e.g. PLA nanocomposites with increasing amounts of intercalated clay plates of C^3C_{18}-mmt [46] or percolated fibrous sepiolite [115]. This shear thinning happens at a greater extent with larger amounts of particles yet without decreasing molecular weight of the polymer matrix. Similar melt behaviour was found for PLA nanocomposites with SiO_2 grafted with lactide [116, 117] and unmodified nHA-PCL, the latter one with lower shear thinning response [118]. Additionally, Pluta [119] reported that melt mixing PLA with fixed amounts of organoclay but for a longer period of time also increased the filler network formation, similarly seen when increasing the amount of nanoparticles in the composite, nevertheless at a cost of decreasing molecular weight of the matrix despite compounding under dried N_2 (to limit hydrolytic and oxidative degradation of the polymer). For additional information on linear rheology of nanocomposites the reader is referred to a paper by Song et al. [114].

2.6. Quantifying nanoparticles dispersion

The distribution of nanoparticles in composites has previously been investigated via various imaging techniques ranging from optical microscopy [47], SEM [80, 89, 120] and X-ray microcomputer tomography (microCT) [9, 121] for detection of macro and micro sized agglomeration, followed by transmission electron microscopy (TEM) [88, 109, 113, 122] to observe dispersion of the nanofiller. There are several image analysis approaches developed for dispersion/agglomeration estimation on micrographs of composites, with examples described below, which ideally should be implemented programmatically with pixel by pixel particles edge detection [123, 124] to eliminate subjectivity during thresholding for image binarization.

Built on previous ideas of mean inter-particle distance which are insensitive to agglomeration, Khare et al. [125] focused on particle free areas to estimate nanocomposite dispersion by simply fitting on the micrograph the largest possible square (aligned with the image edges) without including any particles. If the type and amount of filler in the system is unchanged but the size of particle free square increases, increased agglomeration is indicated due to ineffective mixing as shown in Figure 2.15. A reduction in the particle free area occurs as a result of improved dispersion and increased amounts of the filler in the nanocomposite.

The opposite idea is to focus on the area occupied by the particles to produce histograms with particle areas to estimate particle dispersion based on the size of detected agglomerates [39]. However, on its own, this approach is insensitive to particle distribution.

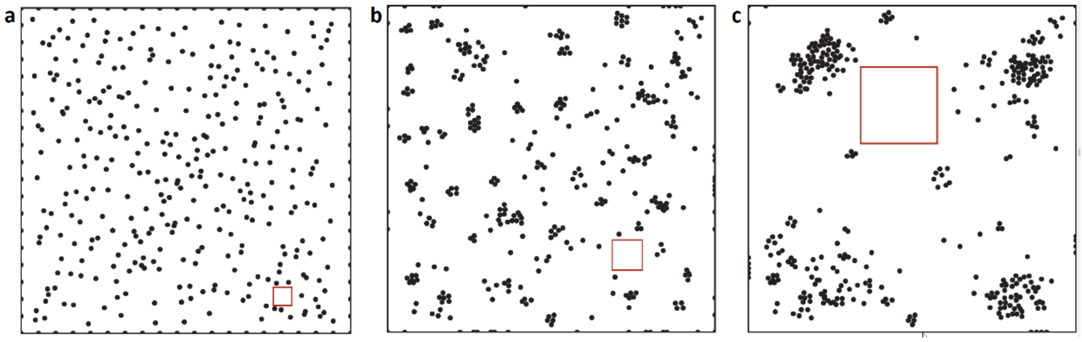

Figure 2.15. Estimation of nanocomposite dispersion on micrographs, with (a) randomly distributed (b) clustered and (c) agglomerated filler, by finding the largest possible square of free space without encapsulating particles. Adapted from Khare et al. [125].

A third approach includes populating the micrograph with arrays of lines, at least two parallel lines in any direction for anisotropic materials and two perpendicular lines, or even better a grid of lines, for isotropic nanocomposite, as shown in Figure 2.16. Intersections between the imposed lines and the nanoparticles were used to obtain a Dispersion Quantity metric based on the mean of the particle free-path distance and its standard deviation; for calculation details see Luo et al. [36].

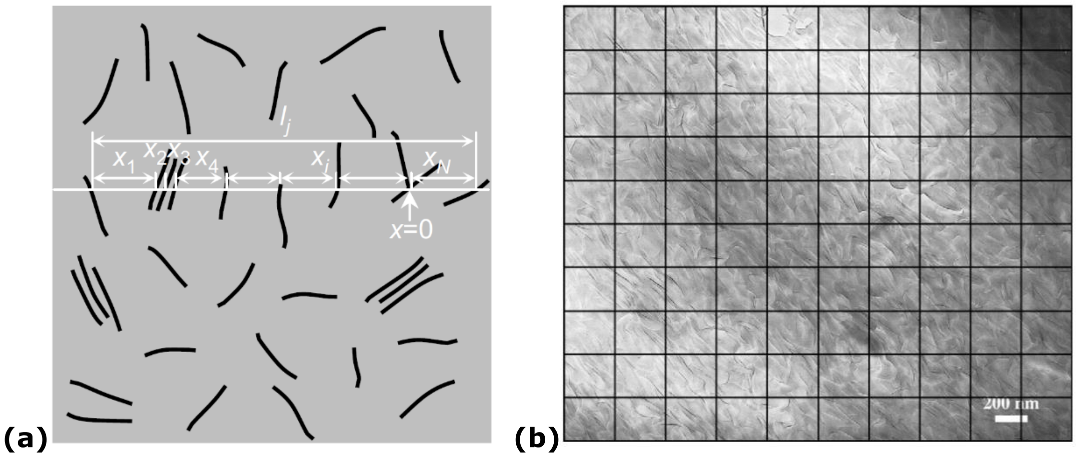

Figure 2.16. Estimation of distances between nanoparticles on micrographs by applying (a) parallel lines or (b) grid. Adapted from Luo et al. [36].

A more sophisticated technique employs Delaunay triangulation based on covering the image with a network of triangles where each vertex is placed at a geometric centre of a particle or agglomerate. For well dispersed systems the area of the micrograph would be populated with triangles of similar surface area, while for nanocomposites with uneven distribution the size of the triangles would vary significantly as shown in Figure 2.17. Taylor et al. [126] used the mean triangle area and its standard deviation to obtain an Area Disorder metric which ranged from zero to one. Intuitively, the Area Disorder increases for poor dispersions and decreases for well dispersed systems. This method is particularly useful for comparing dispersion of materials with different nanoparticle morphology and varying agglomeration, as the triangulation is based on the geometric centre of each detected shape.

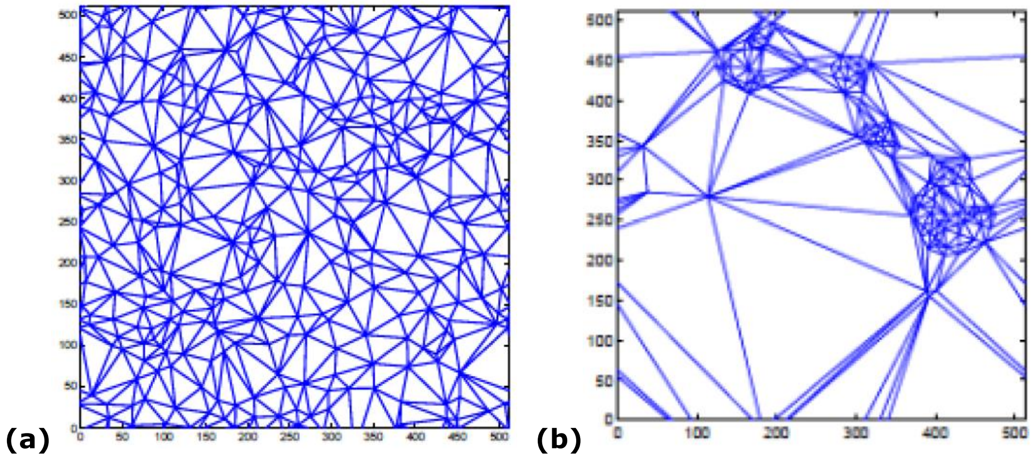

Figure 2.17. Image triangulation of micrographs for (a) well and (b) poorly dispersed materials, with the same nanoparticle content, with triangle vertexes at the geometric centre of each detected shape. Adapted from Taylor et al. [126].

However, in practice quantification of dispersion on nanocomposite images has proven difficult to apply in an automated manner. The acquired TEM micrographs of biodegradable materials frequently have multiple points of varying brightness and contrast due to beam sensitivity of the sample, which persists even upon using TEM with a less powerful electron gun and lowering accelerating voltage, causing nanosized sections to locally warp in the field of view. Similarly, striations originating from the ultramicrotome knife, used for precision cutting of the sample, can cause image shading distortions [122] which are difficult to eliminate. Therefore, few PLA nanocomposites research groups have attempted quantitative analysis of the acquired TEM micrographs due to inherent image uniformity issues which additionally challenge automation of the process despite commercially available image analysis software.

2.7. Summary

This literature overview regarding the processing of biodegradable polyesters and their nanocomposites focused on progress in melt compounding of bioresorbable nHA-PLA materials, for orthopaedic applications, their properties and characterisation. Challenges in optimisation of melt processing of high molecular weight PLA with nHA were highlighted, including polymer degradation, effects of filler morphology, coatings and dispersion, to provide foundations for the development of a scalable manufacturing route.

Until now nHA-PLA have not been produced at scale, from high molecular weight medical grade polymer and large uniform batches of tailored nanoparticles, to deliver feedstock for manufacturing of internal orthopaedic devices. One of the aims of this thesis is to build on pre-existing nHA-PLA research by understanding the influence of processing conditions on properties of the nanocomposites obtained at the laboratory scale and to transfer this knowledge into material production for delivery of demonstrator implants.

3. Methodology

3.1. Materials

3.1.1. Polymers

Two polymer matrix materials were used in this study at various stages; polystyrene (PS) and polylactic acid. The polystyrene was no. 430102 from Aldrich. Two grades of PLA were used: Ingeo 2003D (2003D) from NatureWorks and Resomer LR706S (LR706S) from Evonik Industries AG which were amorphous. The 430102 grade of PS from Aldrich is a hard yet brittle thermoplastic with high transparency dedicated for extrusion or injection moulding of packaging containers and disposable cutlery. The 2003D PLA is a crop-derived transparent biopolymer designed for extrusion of food packaging and cutlery. The LR706S PLA is a synthetic, transparent, high molecular weight biodegradable polymer intended for medical device applications. Table 3.1 presents the properties of these polymers, including: weight average molecular weight M_w, intrinsic viscosity IV, optical isomer composition with chiral enantiomers provided in the D, L convention, density ρ, melting and glass transition temperatures, T_m and T_g respectively, and recommended drying conditions, provided by the manufacturers and obtained from literature.

Table 3.1. Properties of polymers used in this study.

	PS	2003D	LR706S
M_w [kg.mol^{-1}] ($^*CH_2Cl_2$)	192	130* [127]	446* [127]
IV [dl.g^{-1}] (25°C, $CHCl_3$)	-	1.3 [128, 129]	4
Enantiomers	-	L:D 95:5 [130]	L:D,L 70:30
ρ [g.cm^{-3}]	1.04-1.07 [129]	1.24	1.248 [129]
T_g [°C]	100 [129]	59 [130]	59.8 [28]
T_m [°C]	240 [129]	150-158 [130]	-
Drying	-	Vacuum oven 50 °C, >5 h	Vacuum oven 50 °C, >5 h

3.1.2. Hydroxyapatite nanoparticles

Novel hydroxyapatite nanoparticle (HANP) fillers used in this work were developed at the University of Nottingham (UoN) in a laboratory scale counter-current hydrothermal reactor [131]. To produce the particles, a stream of heated and pressurised ammonium phosphate solution is mixed with a room temperature stream of calcium nitrate tetrahydrate solution under controlled conditions. Instant nucleation of HA occurs at the mixing point [76, 132]. The aqueous suspension of HANP that is obtained can be freeze-dried to provide ceramic powder suitable for compounding. Depending on the pH of the solutions in the reactor, HANP can be produced in rod (pH ~10) or plate (pH ~8) shape[1], as shown on SEM and TEM images in Figure 3.1.

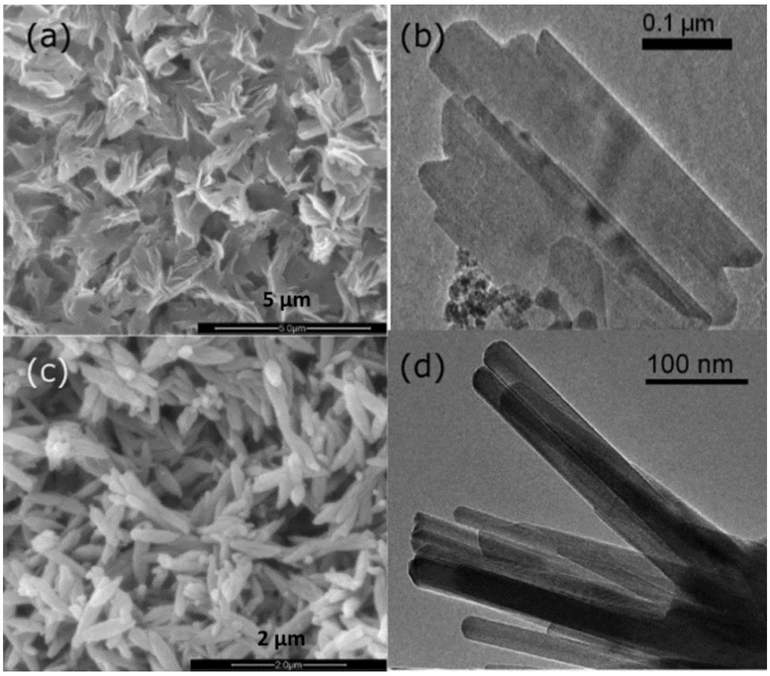

Figure 3.1. (a) SEM and (b) TEM image of HANP plates, and (c) SEM and (d) TEM image of HANP rods. Adapted from Lester et al. [76].

HANP are polydisperse and Lester et al. [76] provided only maximum dimensions of: 2 µm by 2 µm and 80 nm for plates and diameters up to 40 nm for rods with maximum length, up to 1.3 µm, estimated from

---

[1] HANP plates and rods were manufactured by a team of Prof E. H. Lester and Dr M. Gimeno-Fabra at UoN and given for the benefit of project BENcH to explore the influence of HANP reinforcement on PLA. HANP plates and rods allocated for scale up activities were purchased from Promethean Particles and produced in a larger reactor following the manufacturing route described above.

Figure 3.1(c). The volume and surface area of a single cuboid plate and cylindrical rod were calculated with aforesaid dimensions and converted to cm. Representations of the shape proportions are shown in Figure 3.2.

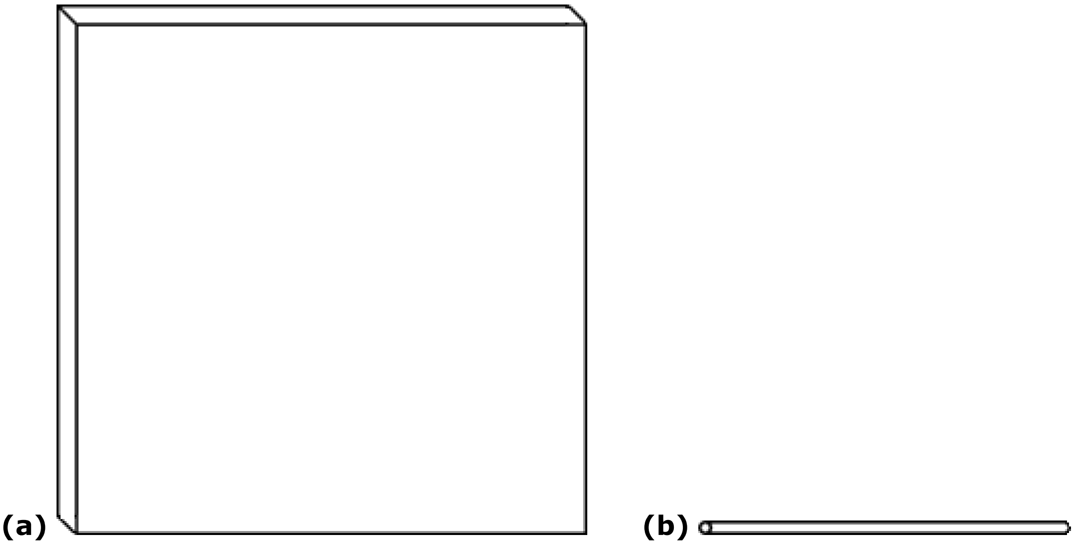

Figure 3.2. Comparison of maximum dimensions, at a scale of 35.000:1, for HANP (a) plate and (b) rod.

The number of times in which a cuboid plate and cylindrical rod volume would occur in one cm^3 was multiplied by their respective surface area. The specific surface area was calculated, using a HA density of 3.156 g.cm^3 [20], which for HANP rods was estimated at being nearly 4 times greater than that for HANP plates (at least 32 m^2.g^{-1} and 9 m^2.g^{-1} respectively). Based on those values, Table 3.2 provides a comparison of the theoretical surface area for HANP rod and plate for nanocomposites at identical particle loading.

Table 3.2. Examples of theoretical HANP surface area in 5 g of HANP-PLA nanocomposite samples.

HANP [wt%]	HANP [v%]	Surface area [m^2.g^{-1}]	
		HANP rod	HANP plate
2.5	1	4	1.13
5	2	8	2.25
10	4	16	4.50

Brunauer-Emmett-Teller measurements for specific surface area and pycnometry for bulk density were not performed as they do not account for material agglomeration and also due to consideration of equipment contamination with nanoparticles during sample decompression.

3.1.3. HANP coated with dispersants

As hydrolytic degradation tests of HA-PLA nanocomposites show loss of tensile strength due to lack of adhesion between the filler and matrix [78] a key to the improvement of interfacial adhesion is modification of the HA surface [79]. Enhancing matrix-reinforcement interactions enables efficient compounding of the nanoparticles with polymer to ensure the necessary dispersion during melt processing [26].

The HANP plates used in this work can be coated in the reactor *in situ.* Tailored novel dispersants are added to the room temperature stream by incorporating an organic solvent and the oligomers become grafted onto the surface of the HANP [133]. The produced coated HANP are polydisperse, see TEM images in Figure 3.3, with average dimensions of 300 × 115 × 20 nm [26]. All the modified HANP shown on SEM and TEM images in Figure 3.3 had plate-like shapes, demonstrating that the coating process and the dispersants had little or no effect on the original HANP morphology. The HANP rods could not be coated in the reactor due to basic pH required to produce rods shape which affected dispersants attachment [134]. Coating level, confirmed by thermogravimetric analysis, varies due to the polymer chain length and concentration of the dispersant in the solution (which was adjusted to limit excess polymer formation in the final HANP product and prevent blockages within the continuous flow rig) [26].

Table 3.3 summarises coated HANP plates[2] used in this research with applied three different groups of dispersants based on: (a) head group functionalized polyolefins i.e. dodecenyl succinic anhydride (DDSA) dissolved in ethanol [133], (b) short chain linear polylactides with an isosorbide head group and (c) branched chain polylactides produced using sorbitol, the last two dissolved in acetone [26]. The isosorbide

---

[2] DDSAHA were produced by a team of Prof E. H. Lester and Dr M. Gimeno-Fabra, and is8PLAHA, is16PLAHA, is24PLAHA and starPLAHA were manufactured by a team of Prof D. J. Irvine and Dr K. Walton at UoN and given for the benefit of project BENcH to explore influence of coating on HANP dispersion in PLA.

ended linear PLA coatings have three different chain lengths which consist of 8, 16 and 24 lactic acid mer units (abbreviated as is8PLA, is16PLA and is24PLA respectively) corresponding to molecular weights of 600 g.mol^{-1}, 1200 g.mol^{-1} and 1800 kg.mol^{-1}, respectively (without the head group) [26]. The branched PLA dispersant have six-armed star like polymer morphology with chain length of 7 lactic acid mer units per arm (starPLA) with overall molecular weight of 3000 g.mol^{-1} [26]. Coating level varies due to the polymer chain length and concentration of the dispersant in the solution (which was adjusted to limit excess polymer formation in the final HANP product and prevent blockages within the continuous flow rig) [26].

The coated HA nanoplates synthesised in the counter-current hydrothermal reactor [131] were extracted from the obtained product suspension via adding organic solvent, toluene for DDSA coated HANP [133] and acetone for polylactide coated HANP [26], in the proportion of 1:6 by volume. The organic and aqueous phases were separated and coated HANP from the organic solution were centrifuged and washed twice with distilled water, to remove excess of unbound dispersant (residue visible in the right bottom corner of the SEM image of is24PLAHA in Figure 3.3), followed by freeze drying.

Table 3.3. HANP plates coated with various dispersants: (a) DDSA, (b) linear polylactides and (c) branched polylactides; produced at: (1) UoN or (2) Promethean Particles as a larger batch for scale up activities.

Coated HANP	Name	Coating [wt%]
DDSA coated plates^{1a}	DDSAHA	12 [133]
is8PLA coated plates^{1b}	is8PLAHA	50 [134]
is16PLA coated plates^{1b}	is16PLAHA	30 [134]
is24PLA coated plates^{1b}	is24PLAHA	55 [134]
starPLA coated plates^{1c}	starPLAHA	35 [134]
is16PLA coated plates^{2b}	is16PLAHApp	48 [134]

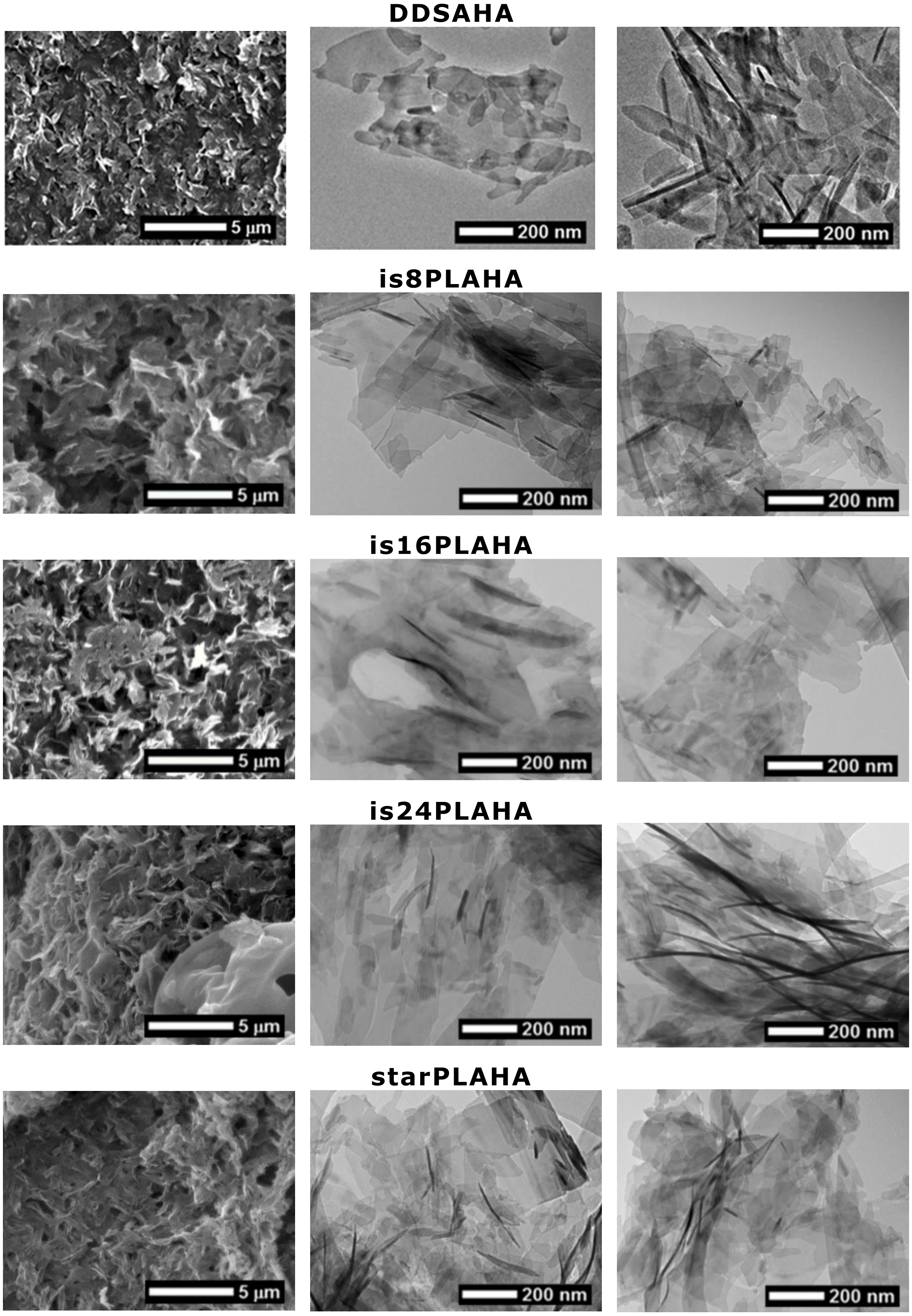

Figure 3.3. SEM (left) and TEM (centre and right) micrographs of: DDSAHA adapted from Gimeno-Fabra et al. [133], is8PLAHA, is16PLAHA, is24PLAHA and starPLAHA adapted from Walton [134].

3.1.3.1. Particles for the nanocomposites scale-up

The is16PLAHApp were produced using Promethean Particles facilities, in a larger reactor following the manufacturing route described in Section 3.1.3 for polylactide coated HANP, and allocated for scale up activities.

As trial runs with is16PLAHApp (with coating level of 55% [26]) gave yellowed nanocomposite, which indicates remaining residue of unbound polylactide with HANP that was confirmed via optical observation of microsized polymeric lumps, particles were washed again with tetrahydrofuran (THF) [134]. The method being: adding of 50 ml of THF to 5 g of is16PLAHApp and sonicating for 10 min, centrifuging the suspension, decanting the solvent and HANP freeze drying, which gave a refined product without visible unbound PLA (coating level of 48%, confirmed by thermogravimetric analysis) [134].

3.2. Processing methods

3.2.1. Handling of HA nanoparticles

There are currently no Work Place Exposure Limits in UK specifically for nanoparticles [135]. However, exposure to dry nanoparticle powders could be harmful by inhalation and may lead to inflammation due to oxidative stress, possibly causing a respiratory condition, and must be treated with care [136, 137]. Therefore, particle drying was carried out in tall tempered glass vials in: (i) a dedicated oven with disabled convection and ventilation or (ii) a vacuum oven with controllable gradual vacuuming and decompression rate, to avoid particle agitation and spread with air flow. Weighing and mixing actions involving HANP were performed in a dry anaerobic glove box where any potential spillage would be contained in a sealed environment. Prepared polymer/nanoparticle mixtures were transported in sealed glass vials. Materials were introduced to the extruder under an extraction cone with an applied high-efficiency particulate absorber (HEPA) filter. Additional personal protection was used in the form of disposable gloves and a face mask with positive pressure air flow and filter. Additionally, a handheld vacuum device with HEPA filter was provided in case of any particle spillage. Any tools which had been in contact with HANP were cleaned under the extraction cone with wet wipes, which were then sealed in a bag for disposal.

3.2.2. Melt compounding

Melt processing was performed using a twin-screw recirculating extruder HAAKE MiniLab II (MiniLab), produced by Thermo Scientific, fitted with co-rotating conical screws. Transportation, melting, pressure build up and mixing are simultaneous processes taking place in the barrel of the compounder. A gas inlet point placed at the bottom of the barrel, shown in Figure 3.4(a), allows for compounding under inert gas. Two pressure transducers in the recirculation channel provide pressure difference (ΔP) measurements that can be used to determine the wall shear stress (τ_w). The chamber temperature (T_{ML}), screw rotation speed (n_s) and torque (T) can be pre-set in the Thermo Haake PolyLab Monitor software. Data is collected over the total experiment time (t_{ML}) including materials loading, mixing and extrusion. The system has the following alarm thresholds: temperature 360 °C, screw rotation speed 360 rpm, torque 5.5 Nm and pressure 210 bar. Figure 3.4(b) provides an image of the mixing chamber of the MiniLab with the co-rotating screws in place. The extruder has a maximum filling volume of 7 ml and a recirculating loop volume (V_L) of 5 ml, marked on Figure 3.4(b) with red arrows. The back flow channel volume is 1.5 ml [138]. Samples can be extruded through a die via a pneumatically controlled bypass valve in the form of a tape or rod depending on the shape of the applied die. The system also allows for direct extrusion of the compounded material via an adaptor die to the barrel of a compatible MiniJet injection moulder.

3.2.2.1. Processing procedures and parameters

Prior to compounding in Air and N_2, PLA was dried at 50 °C in a vacuum oven for a minimum of 8 h and HANP were used directly from a dry anaerobic glove box where they were stored after freeze drying at the end of the manufacturing process. For compounding in N_{2D} all the materials were dried in an oven including: uncoated HANP at 300 °C with disabled convection and ventilation for a minimum of 8 h, coated HANP at 50 °C in a vacuum oven for 3 h and PLA as previously stated.

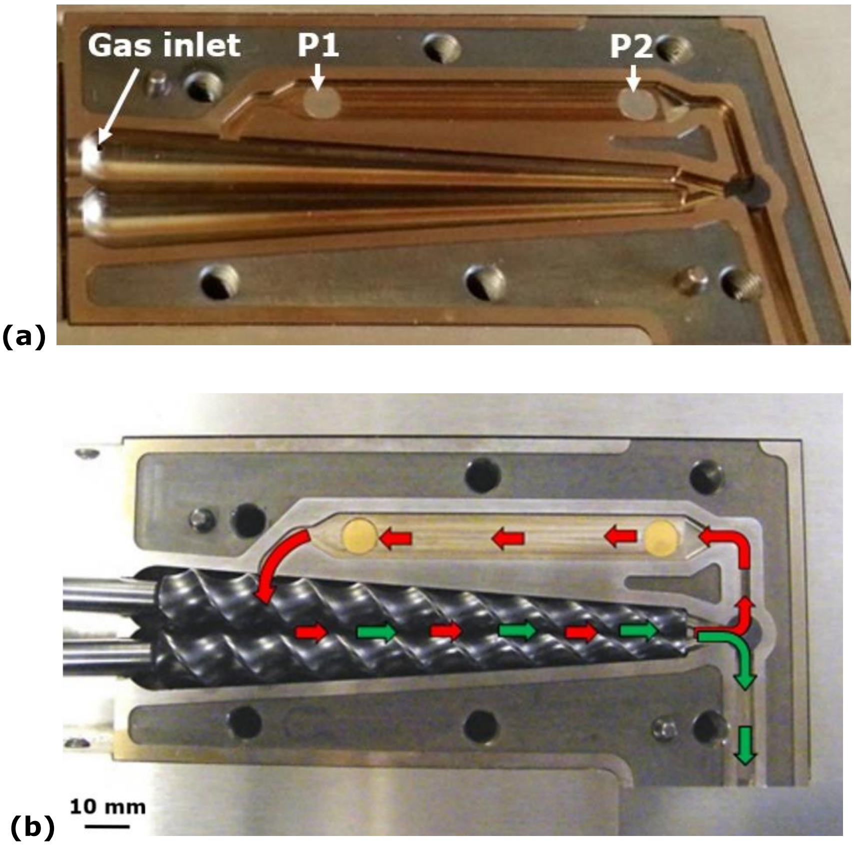

Figure 3.4. Open barrel of HAAKE MiniLab II compounder; (a) with gas inlet port and two pressure transducers (P1, P2) marked, (b) with inserted co-rotating screws, red arrows showing recirculation in the back flow channel and green arrows indicating extrusion.

LR706S and HANP were fed manually into the MiniLab in 3-4 gradual loadings over 3-4 min. PLA or polymer/nanoparticle mixtures were filled from a glass vial via the funnel slowly, to prevent overflow, and pushed through the feeding pipe into the extruder chamber with T-bar plunger with a copper end. Pressure was applied on the T-bar plunger steadily, to avoid overloading pressure sensors and reaching alarm thresholds, and was exerted by hand only. Material filled into the compounder was recirculated via an integrated back-flow channel.

Melt was mixed at 210 °C with a n_s of 50 rpm for 15 min in ambient air (Air) or in bottled nitrogen (N_2), at 1 bar and a flow rate of 0.3 $l.min^{-1}$, which was in-line dried with a liquid nitrogen moisture trap (N_{2D}) to remove residual water, as shown in Figure 3.5.

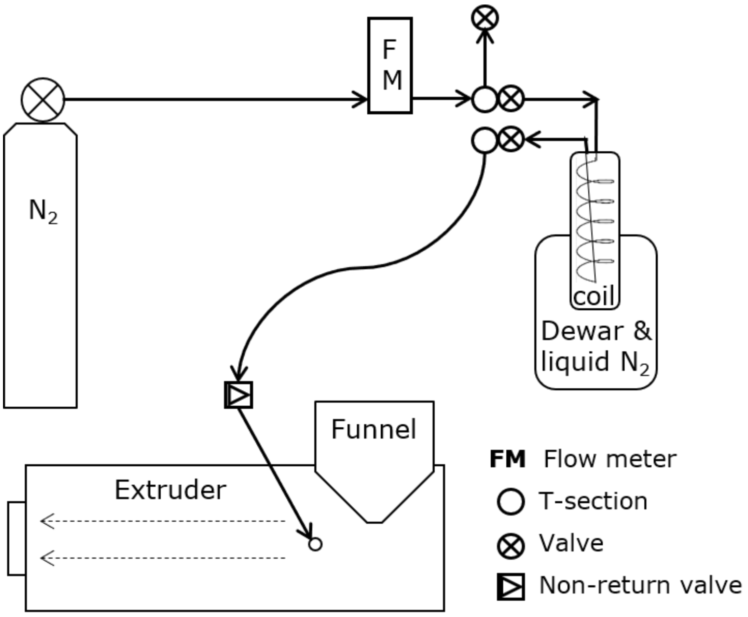

Figure 3.5. Flow diagram of N_2 drying setup and connection to MiniLab.

These compounding conditions were chosen as tests carried out at lower temperatures were unsuccessful as alarm thresholds were reached for the pressure sensors. A n_s of 50 rpm and recirculation time of 15 min were preferred to minimise matrix degradation due to applied shear yet to provide sufficient mixing for the nanocomposites. Further details regarding establishing the compounding method are discussed throughout Section 4.4 analysing influence of processing parameters on HA-PLA melt compounding.

The Thermo Haake software records T_{ML}, n_s, T and ΔP data during material recirculation. An example of those measurements is shown in Figure 3.6 where: (i) materials loading ended at 3.5 min with the maximum peak for T and ΔP, (ii) followed by 15 min of mixing and recirculation through the back flow channel and (iii) finished with extrusion marked with sudden decrease of T and ΔP due to opening of the bypass valve.

Collected data allows for the calculation of mixing energy E_{mix} (in J) [121]:

$$E_{mix} = \int_0^{t_R} n_s \, 2\pi \, T \, dt_R \tag{3.1}$$

where t_R is the mixing and recirculation time (in min). E_{mix} will be used to calculate specific mechanical energy as a comparison parameter between different extruders during scale-up activities, as shown later in Section 7.4.

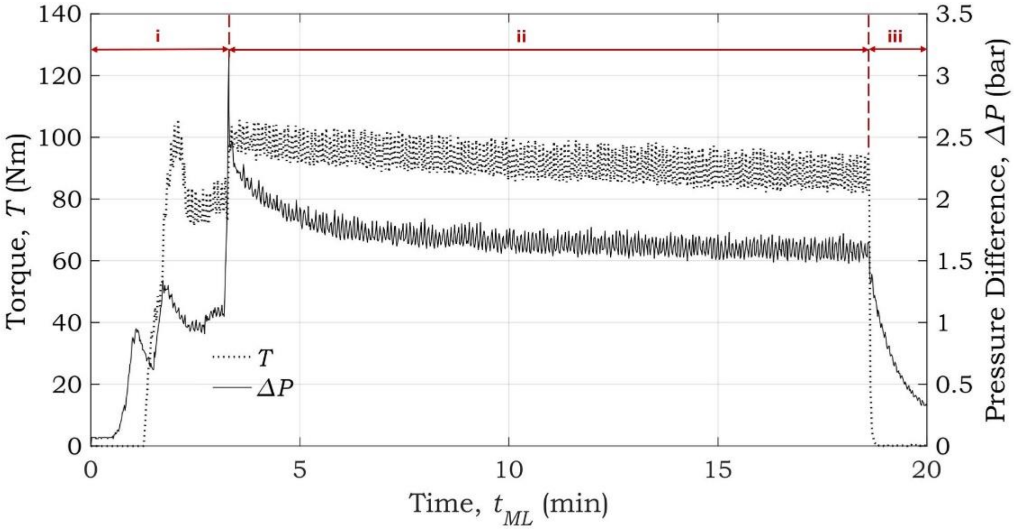

Figure 3.6. Raw data collected during compounding in MiniLab of 2.5 wt% uncoated HANP plates in LR706S in N_{2D} at 210 °C and 50 rpm, where (i) marks material loading stage, (ii) mixing during recirculation and (iii) bypass valve opening and extrusion.

3.2.2.2. Recirculating extruder analysis

The back-flow channel acts as a rheological slit capillary die of known dimensions with two pressure sensors, P1 and P2, as shown in Figure 3.4. This allows for the measurement of ΔP which can be used to compute rheological information concerning the flow behaviour of the material. By considering force equilibrium on an element of fluid in a uniform rectangular channel, illustrated in Figure 3.7, referring to the back-flow channel, wall shear stress (in Pa) was defined [139] as:

$$\tau_w = \frac{h_{ML}\,\Delta P}{2\,l_{ML}} \tag{3.2}$$

where MiniLab back flow channel height h_{ML}=1.5 mm and length (between P1 and P2) l_{ML}=64 mm. The channel geometry also allows for calculation of the apparent shear stress τ_{ap}:

$$\tau_{ap} = \frac{h_{ML}\, w_{ML}\, \Delta P}{2\, (h_{ML} + w_{ML})\, l_{ML}} \quad \textbf{(3.3)}$$

where MiniLab back flow channel width w_{ML}=10 mm, and the relative shear rate $\dot{\gamma}_{rel}$ [139]:

$$\dot{\gamma}_{rel} = \frac{6\, Q_{rel}}{w_{ML}\, h_{ML}^2} \quad \textbf{(3.4)}$$

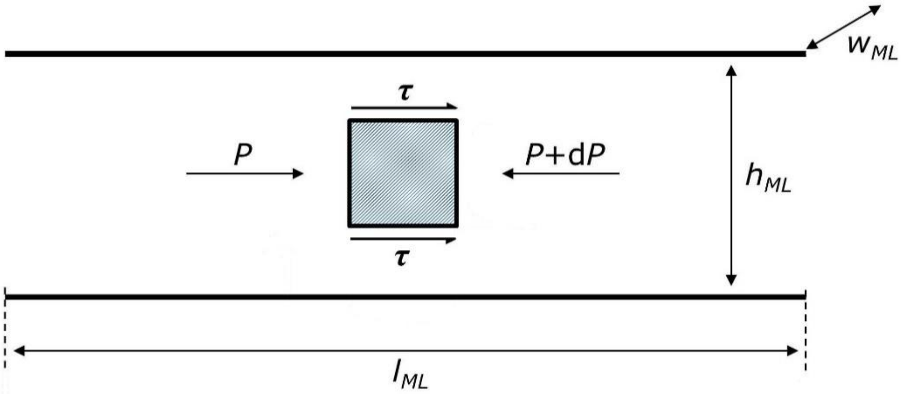

Figure 3.7. Forces acting on an element of fluid in a rectangular channel.

Q_{rel}, see Equation (3.5), is the relative volumetric flow rate [138], correlated with set n_s by the volumetric flow factor F_f =8.10^{-7} m^3 obtained for the MiniLab experimentally and provided by the equipment producer.

$$Q_{rel} = \frac{n_s}{60}\, F_f \quad \textbf{(3.5)}$$

As viscosity η is defined as the ratio of the shear stress τ to the shear rate $\dot{\gamma}$ [93]:

$$\eta = \frac{\tau}{\dot{\gamma}} \quad \textbf{(3.6)}$$

substituting Equations (3.3) and (3.4) into Equation (3.6) gives relative viscosity η_{rel}. The correlation between n_s and Q_{rel} is not absolute hence $\dot{\gamma}_{rel}$ and η_{rel} obtained in MiniLab are only relative values at any given temperature.

To obtain flow curves from rheometry test in capillary mode in the MiniLab, different n_s are set and ΔP is then measured between pressure sensors of the back-flow channel over approx. 40 s for a given temperature. One measurement point obtained in the capillary mode, e.g. Figure 3.8, is equivalent to a standard recirculation test in MiniLab, e.g. Figure 3.6, carried out with constant n_s but over longer period of time. The example of the capillary mode measurements, shown in Figure 3.8, presents the results of a rheometry test performed in MiniLab with PS (which thermal degradation is less pronounced than for PLA). The acquired data, when verified with viscosity measurements carried out in a capillary rheometer, enables determination of the actual volumetric flow rate Q in the back-flow channel, which will be discussed in Section 4.8 providing better correlation between n_s and Q.

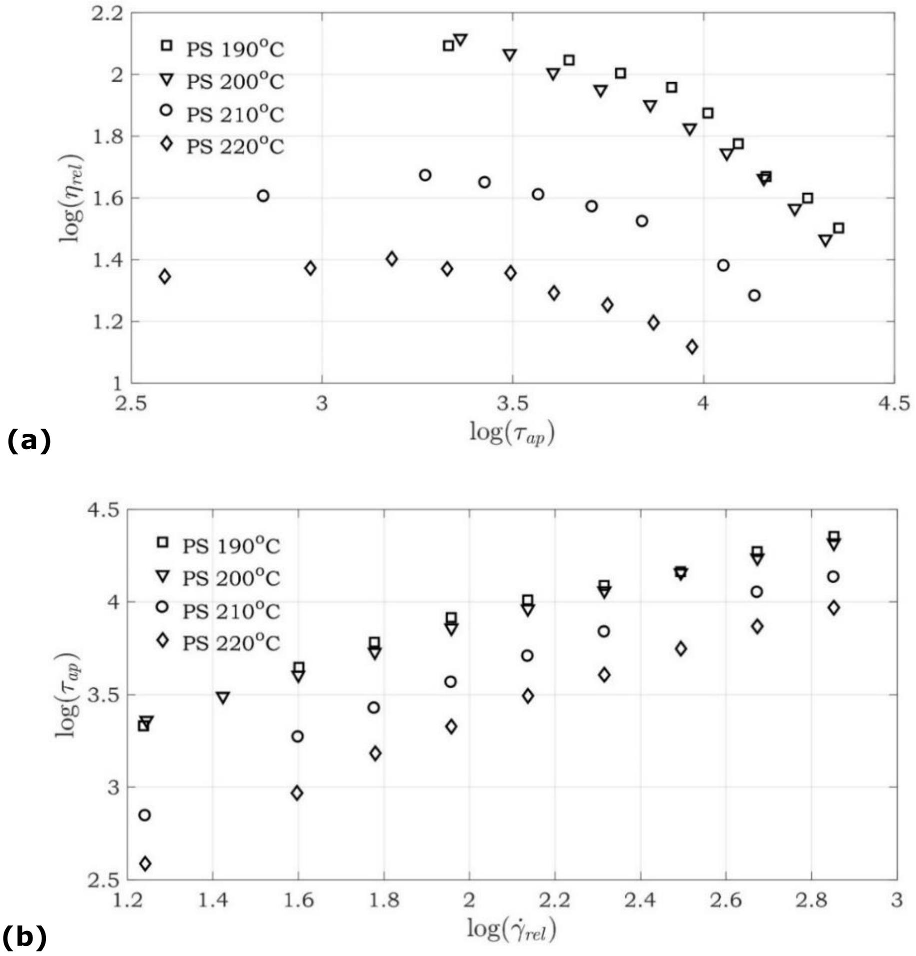

Figure 3.8. PS relative viscosity measurements from capillary mode in MiniLab. (A) log(η_{rel}) as a function of log(τ_{ap}). (B) log(τ_{ap}) as a function of log($\dot{\gamma}_{rel}$).

3.2.3. Injection moulding

The HAAKE MiniJet injection moulding machine, see Figure 3.9, is a small piston injection moulding (IM) system produced by Thermo Scientific requiring only approx. 5 g of material. It can be fitted with a range of moulds, including a custom Ø25 mm 1 mm thick disc mould.

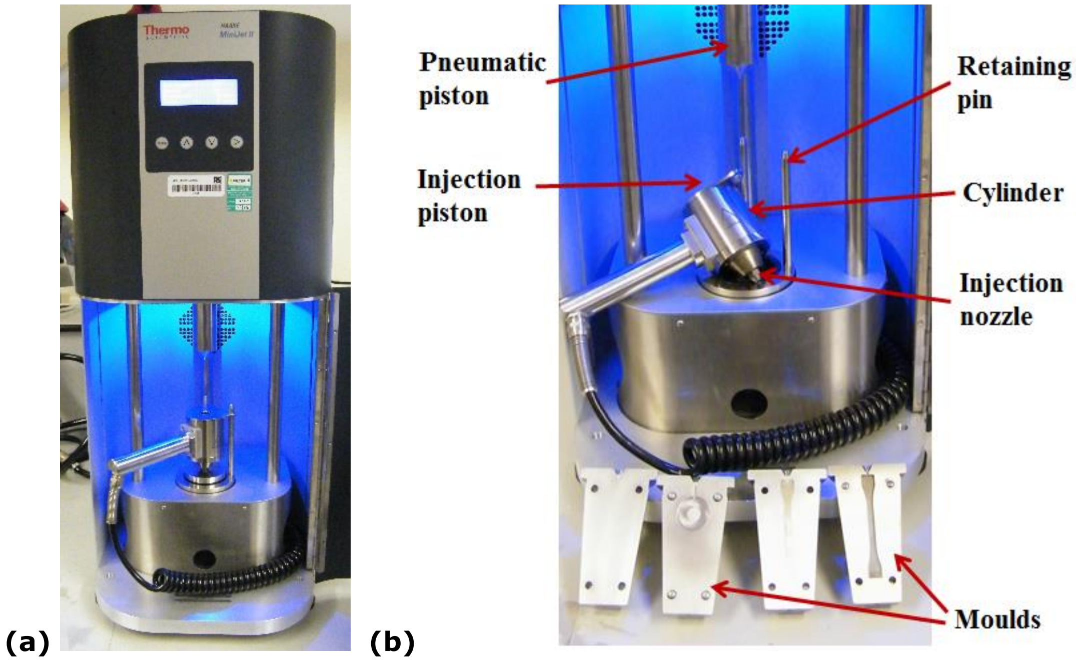

Figure 3.9. (a) Opened Haake MiniJet injection moulder and (b) system description with available moulds.

Through the use of a special die it was possible to transfer compounded materials directly from the MiniLab to the MiniJet, to produce specimens for further characterisation; see Figure 3.10 for injection mounding cycle. Melt was injected from the barrel at 205 °C, for 5 s, with an injection piston at 800 bar, into a mould at a temperature of 45 °C. This was followed by a 15 s hold at 800 bar to allow for sample freezing below T_g during cooling [140]. The sample was then manually removed from the mould which was immediately reinserted in the MiniLab and allowed to heat up for 30 s before starting the next injection cycle.

This MiniLab to MiniJet melt transfer was used to emulate the industrial continuous injection moulding process without an intermediate cooling stage. However, due to residual IM stress within the samples produced for Ward [29] for further mechanical testing, the injection moulding step was subsequently removed and replaced with compression moulding.

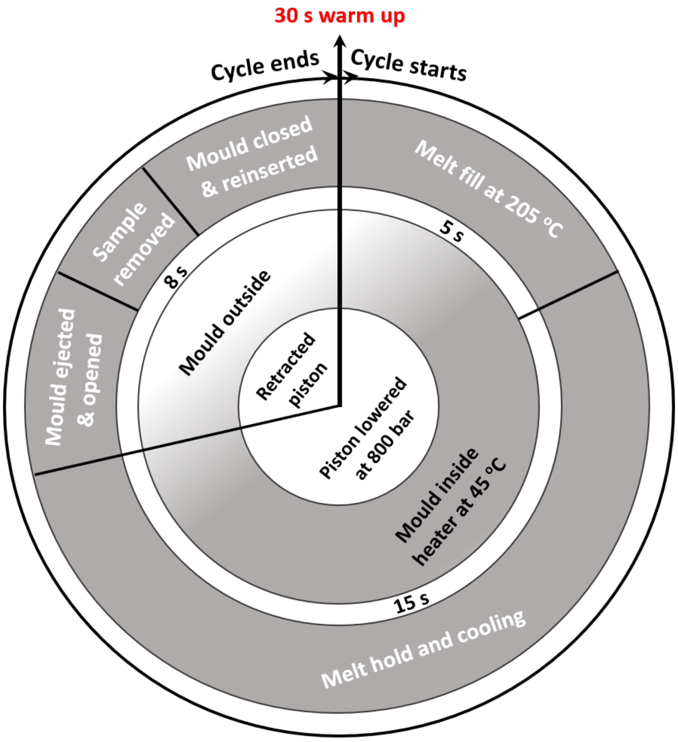

Figure 3.10. MiniJet injection moulding cycle.

3.2.4. Compression moulding

Extruded materials from the compounder were compression moulded (CM) at 170 °C for 15 min using a Daniels hand operated hydraulic heated press with in-house flash moulds [141] to produce isotropic Ø25 mm and Ø8 mm discs with 0.5 mm thickness. The applied moulds can produce multiple samples with thickness dictated by the mould thickness as shown in Figure 3.11(a). Flash moulds conduct the heat to the material and distribute the exerted pressure over the surface of the mould. Pressure forces are not applied straight onto the specimens, as the excess melt is directed away from the cavity to form flash, leaving hot material to form to shape in the cavity.

The moulding stack, shown in Figure 3.11(b), consisted of: a lower and upper stainless steel sheet followed by disposable aluminium foil sheets encapsulating the stainless steel flash mould with the required cavities. The aluminium foils were applied for easy sample release when separating moulded materials from the stainless steel sheets. The moulds and aluminium foils were cleaned with acetone prior to moulding. Extrudate tapes were cut into 2 × 5 mm pieces and inserted into the mould cavities with 10 wt% excess and placed in the moulding stack which was positioned between the preheated press platens. Prior to moulding, all materials were dried at 50 °C in a vacuum oven for a minimum of 8 h.

The moulding cycle consisted of: a 10 min warm up with gradual lowering of press platens, a 3 min pressure cycling from 0 to 40 bar to release any air trapped between PLA or nanocomposite fragments, a 2 min hold at 40 bar, followed by cooling until ~50 °C (below PLA T_g) for 6 min with a stream of water passed through cooling channels in the platens. The cooled samples were then removed from the mould.

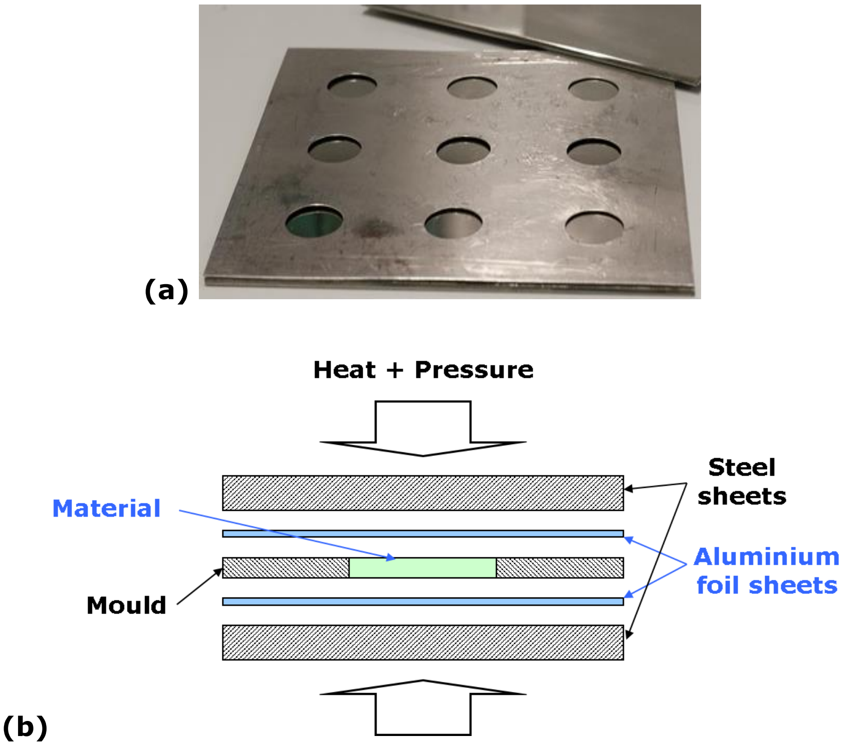

Figure 3.11. (a) Multiple specimens mould capable of producing discs of Ø25 mm and 0.5 mm thickness; (b) a schematic diagram of the moulding stack.

3.2.5. Thermogravimetric analysis

Thermogravimetric analysis (TGA) tests were performed using a Thermal Analysis Instruments TGA Discovery to confirm the HANP content and thermal stability for all the nanocomposite specimens.

TGA platinum pans were washed with tap water to remove ash residue from previous tests and burned off with a pure butane blow torch until they glowed orange for 10 s to remove any water or sample residue. Each sample, for which mass ranged between 9 mg and 13 mg, was placed on a tared pan and inserted into the TGA auto sampler. Clean bottled air was used as a purge gas, flowing at 40 ml.min^{-1}, over nitrogen as PLA burn off in nitrogen was incomplete as evidenced by substantial black tarry charring. Materials were held in the furnace at ambient temperature for 10 min to equilibrate them to the ambient conditions, followed by heating up at 5 $°\text{C.min}^{-1}$ up to 500 °C and were subsequently held isothermally at 500 °C for 20 min. Three repeats were carried out for each nanocomposite by separately burning off three samples from the same batch. Measurements were acquired by TRIOS software by Thermal Analysis Instruments and exported to Excel for analysis.

HANP weight percentage was calculated after subtracting the mass of LR706S ash residue (m_{ash}) from the residual sample mass after burn off (m_f). Firstly, m_{ash} was obtained by averaging results of six LR706S burn off test for increased accuracy due to small final mass. Subsequently HANP weight percentage was calculated using:

$$\text{HANP wt\%} = \frac{m_f - m_{ash}}{m_o} \tag{3.7}$$

where m_o is the original mass of the sample before the burn off test.

It is worth noting that the TGA technique was also used to monitor polymer degradation and stability once filled with various HANP, with respect to neat LR706S, by comparing the temperature at 5% weight loss which indicates degradation onset [142].

3.2.6. Chromatography

Polymer molecular weights were analysed using gel permeation chromatography (GPC), using THF as eluent and calibrated with polystyrene standards. GPC is a type of size exclusion chromatography, where dissolved polymer is passed through a column with packing containing pores of different sizes. Separation of polymer chains by molecule size occurs by trapping smaller molecules in the pores of the adsorbent [143].

Materials were dried in a vacuum oven at 50 °C for at least 8 h prior to dissolving in THF in the proportion of 1 mg of material per 1 ml of solvent. After 4 h solutions were shaken in vials by hand for 10 s and transferred with a glass syringe and a polytetrafluoroethylene 0.45 µm filter into 1.5 ml GPC sample vials. Measurements were performed using an Agilent Technologies 1260 Infinity GPC system. Three repeats were carried out on each sample.

M_n, M_w, and polydispersity index (PDI) were used to describe the total molecular weight of LR706S and the nanocomposites. M_n and M_w are described by the following expressions:

$$M_n = \frac{\sum N_i M_i}{\sum_i N_i} \tag{3.8}$$

where N_i is the number of moles of each polymer species of molar mass M_i, and

$$M_w = \frac{\sum N_i M_i^2}{\sum_i N_i M_i} \tag{3.9}$$

Additionally, PDI can be calculated from:

$$\mathrm{PDI} = \frac{M_w}{M_n} \tag{3.10}$$

Analysis of the results, an example of which is provided in Figure 3.12, was performed using the dedicated Astra software. Molecular weight differentiated with respect to polymer species residence time in the column was divided into (1) the total peak containing: (2) main peak from 10 min to 16.5 min with majority of the molecules and (3) peak with short chained species from 16.5 min to 18.9 min, which were then all converted into molecular weights in kg.mol^{-1}. A summary of results from fractions of peak 2 and 3 with total values from the full spread in peak 1 provides complete evaluation of molecular weights for a given specimen, where M_p marks molecular weight of the highest peak. However, in this study molecular weight values from the main peak (2) were only taken into consideration as the total M_n and PDI were highly sensitive to the amount of the short chained specimens from the peak (3), as shown in Figure 3.12(b), which was contained in a small percentage of the total peak area. This approach was found in other PLA research where only the main peak area was regarded [89, 144].

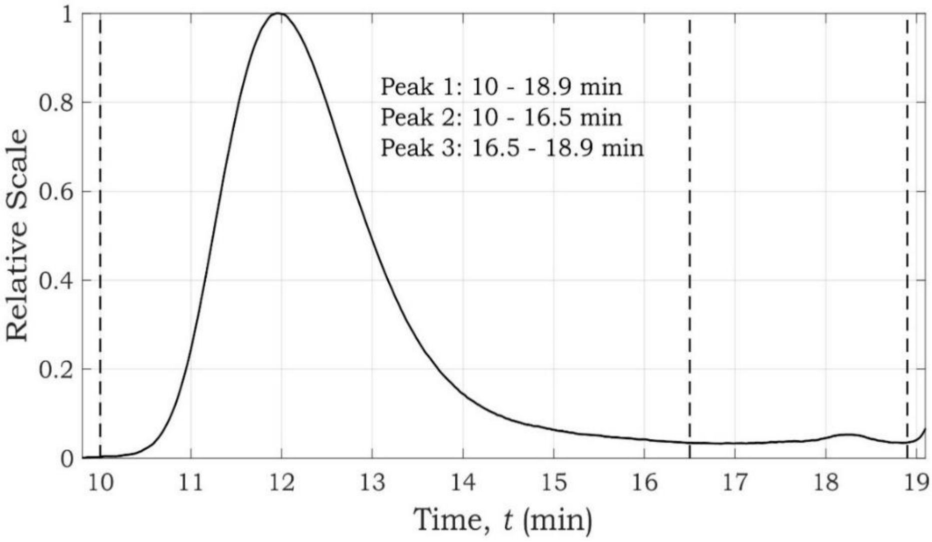

(a)

Peak Results	Peak 1	Peak 2	Peak 3
Peak Area [%]	100.00	93.32	6.68
M_n [kg.mol^{-1}]	10.61	115.40	0.78
M_p [kg.mol^{-1}]	424.70	424.70	1.39
M_w [kg.mol^{-1}]	354.80	380.10	1.12
PDI (M_w/M_n)	33.44	3.29	1.44

(b)

Figure 3.12. Example GPC analysis with Astra software showing (a) molecular weight differentiated with respect to polymer species residence time in the column separated into: the total peak 1 containing main peak 2 and peak 3 with short chained species; (b) conversion into molecular weights.

3.2.7. Differential scanning calorimetry

A preliminary differential scanning calorimetry (DSC) analysis was performed to explore the influence of (i) addition of HANP in LR706S and

(ii) decrease of polymer matrix molecular weight due to thermal degradation, on T_g.

Calorimetric scans were carried out using a Thermal Analysis Instruments DSC2500 Discovery with N_2 as a purge gas at 50 ml.min^{-1} for sample and 325 ml.min^{-1} for base. Samples were sealed in standard hermetic aluminium pans and heated from room temperature to 220 °C at a rate of 10 °C.min^{-1}, followed by cooling to 20 °C at 25 °C.min^{-1}, and a second heating up to 220 °C at 10 °C.min^{-1}. Specimens, with mass ranging between 2.5 mg and 5 mg, were tested in the DSC chamber against an empty reference pan. Three repeats were carried out for each material by separately carrying out heat/cool/heat cycle for three samples from the same batch. The initial heating cycle was carried out to erase sample thermal history whilst the secondary heating cycle was used for determining the T_g of material with a defined thermal history. Measurements were acquired by TRIOS software by Thermal Analysis Instruments which was also used to analyse results. A plot of normalised heat flow against temperature was produced and T_g was established by finding the peak of the temperature derivative of the curve, as illustrated in Figure 3.13.

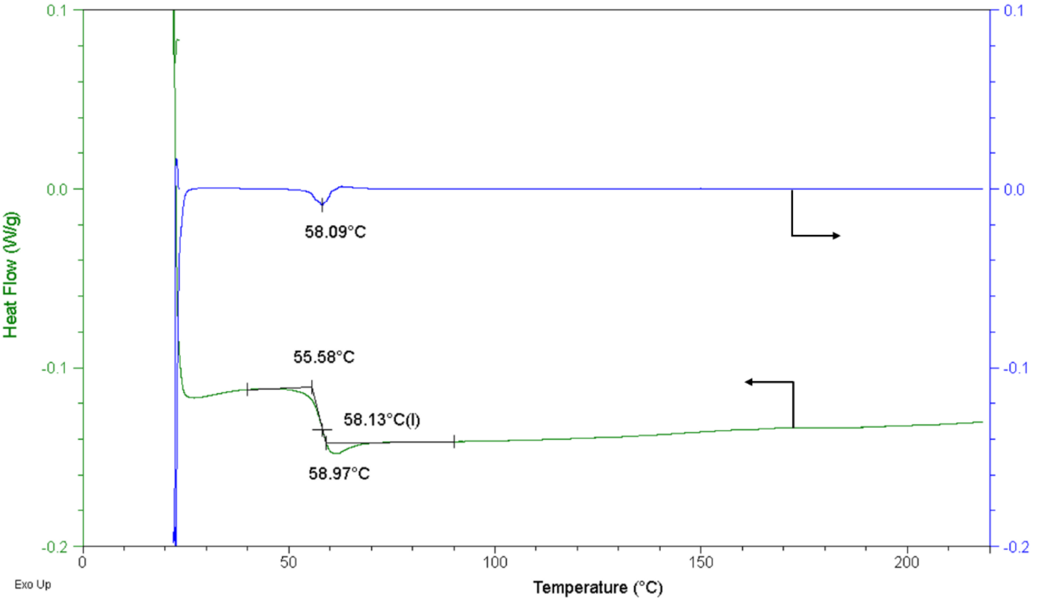

Figure 3.13. Determination of T_g using the peak of derivative heat flow compared with the inflection step change of heat flow as a function of temperature.

This method was applied as it is less user dependant than finding T_g by determining the inflection of the heat flow-temperature curve between the three tangent lines where data limits are selected by the user.

3.2.8. Capillary rheometry

Measurements were carried out with a twin bore Malvern Instruments Rosand RH10 rheometer, using a capillary die with length of L = 32 mm in the left-hand bore and an orifice die with essentially 0 mm length in the right-hand bore, all illustrated in Figure 3.14. This set of tungsten carbide dies, both with slit diameter of d = 2 mm, was used to perform the Bagley correction of viscosity via directly measuring the die entrance pressure drop to correct τ_w [145]:

$$\tau_w = \frac{d\,(\Delta P_L - \Delta P_0)}{4\,\mathrm{L}} \tag{3.11}$$

where ΔP_L is pressure difference for capillary die and ΔP_0 is pressure difference for orifice die.

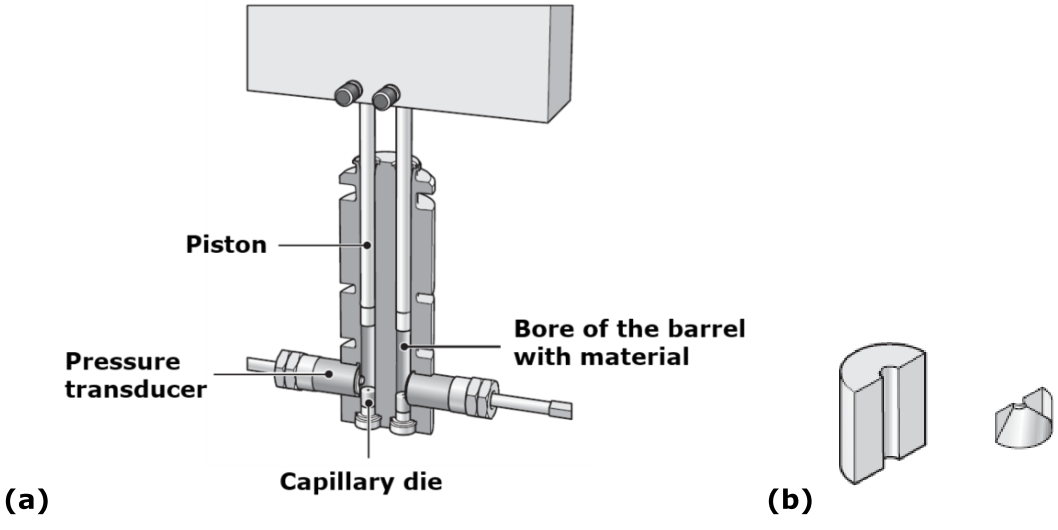

Figure 3.14. (a) Components schematic of the Rosand capillary rheometer and (b) cross section of the capillary and orifice die, adapted from Malvern [146].

The rheometer measures the viscosity of a sample by testing the same material in both bores which are temperature controlled. Pistons inside of the barrels are forcing material at identical defined speed through the dies which are held at the bores bottom by retention nuts. Pressure transducers measure the change of pressure directly above the dies.

PLA was dried prior to rheometric tests at 50 °C in a vacuum oven for a minimum of 8 h, PS was used directly as it is not hygroscopic. Each sample was loaded and preheated in the barrels up to 5 min. Two measurement pre-tests were carried out over 5 min to compress the polymer granules in the bores and remove air voids. Once the melt flow reached equilibrium the first data point was acquired, usually around 12 min from loading the material. Each test was performed with a fresh polymer sample after cleaning the rheometer components between the measurements.

The constant shear rate test was carried out to investigate the relationship between τ_w and $\dot{\gamma}$. The test consists of several speed stages where each applies a constant $\dot{\gamma}$. Viscosity is derived from the measured pressure, the piston speed and the die geometry. Rate-controlled measurements were executed for PLA at 210 °C and PS at 200 °C and 210 °C by applying a logarithmic $\dot{\gamma}$ ramp up in 9 steps ranging from 2 s^{-1} to 289 s^{-1}, illustrated in Figure 3.15.

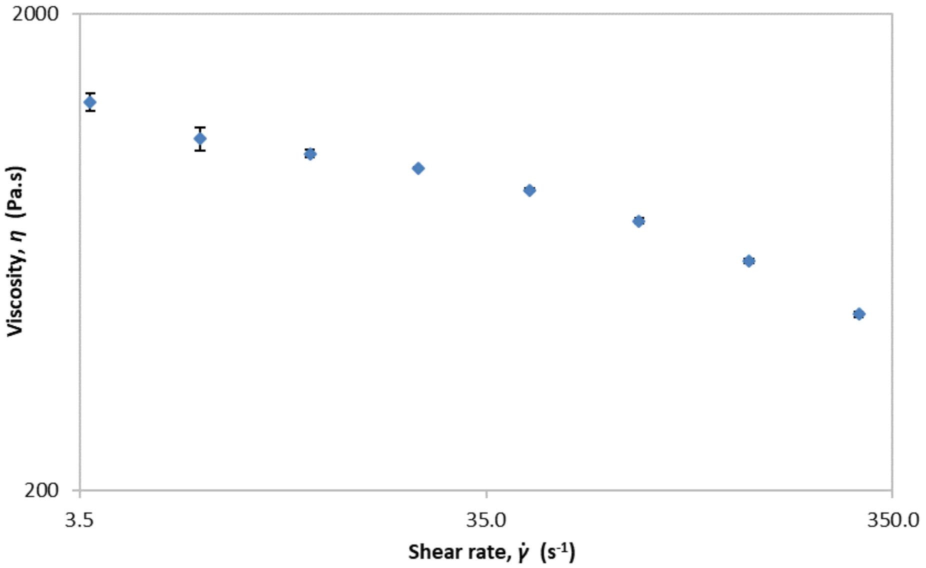

Figure 3.15. Example of constant shear rate test in capillary rheometer for 2003D at 210 °C.

A low speed degradation test was also performed by applying a single constant low $\dot{\gamma}$ for a specified length of time to investigate sample viscosity degradation at defined temperature. The following measurements were performed at 210 °C for: (i) 2003D: at $\dot{\gamma}$ of 18 s^{-1} for

15 min, (ii) LR706S: at $\dot{\gamma}$ of 30 s^{-1} for 15 min, example shown in Figure 3.16.

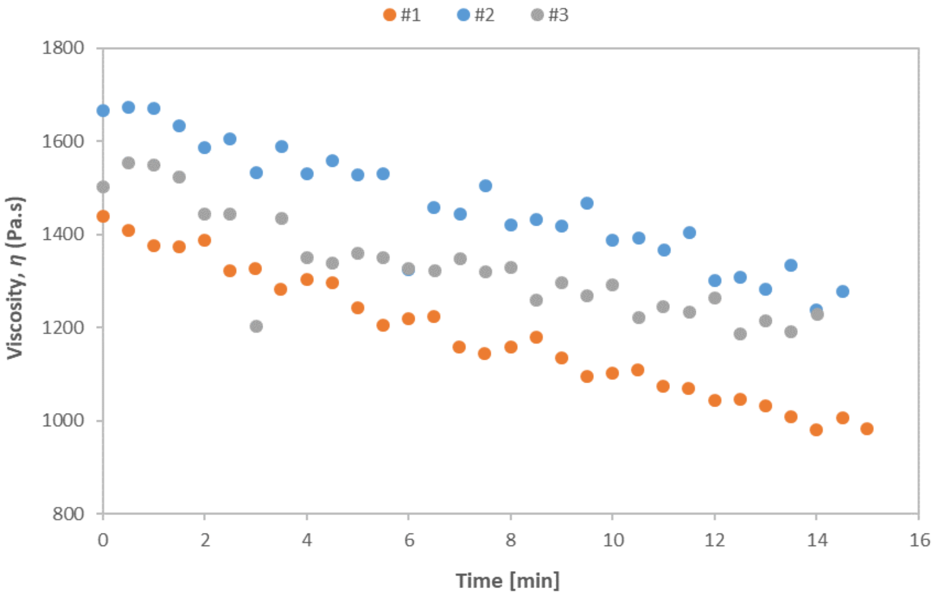

Figure 3.16. Example data from 3 runs of a low speed degradation test in the capillary rheometer for 2003D at 210 °C and at a constant shear rate of 18 s^{-1}.

3.2.9. Ultramicrotomy and Transmission Electron Microscopy

Ultramictrotomy sections, with thickness of 90 nm, were cut with a freshly prepared sharp glass knife at room temperature using either a manual RMC PT-PC PowerTome or an automatic Reichert-Jung Ultracut with a speed of 0.8 $mm.s^{-1}$. The extrudate block face was firstly trimmed with a blade into a trapeze shape with a height of ~2 mm. This was followed by directly mounting the trimmed extrudate in the ultramicrotome sample holder using a chuck, without embedding the material in a resin. Specimens were secured firmly in the holder to prevent any movement during cutting and reduce vibrations in the setup enabling consistent slice thickness; see Figure 3.17(a) for diagram of an ultramicrotome cutting sample. Note that the cutting surface was perpendicular to the extrusion direction. Sections were collected from the knife block dry with an eyelash tool, as illustrated in Figure 3.17(b), and supported on copper locket grids. The floating of sections on water for ease of collection and confirming section thickness based on colour refraction was not possible as PLA is hygroscopic. Sporadic knife macro-striation marks and marginal thickness variations within the sections were negligible as images were acquired at nanoscale.

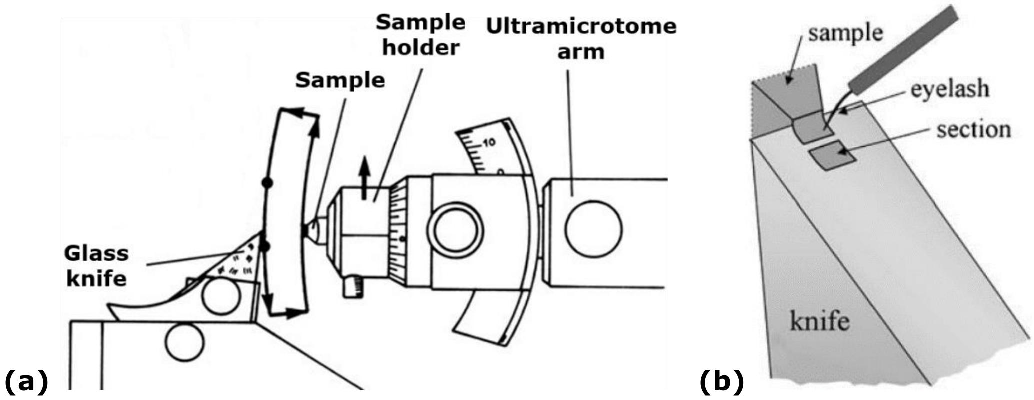

Figure 3.17. Diagram of (a) part of the ultramicrotome with arrows marking advance of the arm towards the knife to cut the sample, adapted from Efimov et al. [147] and (b) sample cut by a glass knife with sections collected with an eyelash tool, adapted from Michler [148].

TEM was utilised to investigate the nanocomposite morphology directly after extrusion. The instrument used for acquiring images was a FEI TECNAI G2 BioTWIN with tungsten filament gun at an accelerating voltage of 120 kV and 100 kV.

3.2.10. Microcomputed Tomography and image rendering

The microCT scans were performed using a XRadia/Zeiss VersaXRM-410 with source voltage 40 kV, lens magnification 10, field of view 2 mm by 2 mm and resolution of 1 µm. Images were provided as DICOM files. Samples used for the measurements were either 5 mm x 5 mm x 1 mm pieces cut out from IM discs or CM Ø8 mm discs with 0.5 mm thickness, produced as per methods described in Section 3.2.3 and 3.2.4 respectively.

Materialise Interactive Medical Image Control System (Mimics) software for 3D image processing was used to model nanocomposites from a slice-by-slice stack of 2D microCT scans. Firstly, a mean filter of 2 was applied, which is a type of spatial filter, to decrease noise in the images stack by reducing the amount of intensity variations. Secondly, two separate 3D masks were applied to determine LR706S matrix and HANP filler, which were then rendered with opening filter via dilation of the previously eroded entities for further morphological noise removal. Finally, extracted masks were transferred from Mimics to 3-matic - computer aided design software, which was employed for compiling a 3D model, exported as a 3D PDF file, and sample analysis to calculate volume percentage of matrix and particle. Detected HANP was treated as filler agglomeration and it was assumed that the reminder of nanoparticles below scan resolution were well dispersed. Fraction of the detected in microCT scan HANP volume percentage to total HANP volume percentage, calculated from TGA measurements, provides a measure for particles agglomeration in the nanocomposite.

3.2.11. Mechanical testing fixture and specimen preparation

The compression moulded isotropic Ø25 mm disc specimens, manufactured as per methods described in Section 3.2.4, were used to produce minibars. Discs were sectioned into small pieces using a custom cutting tool which used two single bevel blades separated by spacers [149], illustrated in Figure 3.18(a). The spacers determined the sample width of 2 mm. The strips cut from the discs were then sectioned into small bars of approximately 8 mm in length, shown in Figure 3.18(b), with a razor blade. Bar dimensions were measured using a micrometre and a scanner (HP Scanjet G4010 with optical scanning resolution up to 4800 dpi) for thickness and width, respectively.

Mechanical tests were carried out using a custom in-house miniature 3-point bending rig [149], shown in Figure 3.19, with specimen sizes of 8 x 2 x 0.5 mm. The rectangular samples were modelled as perfect beams where their flexural strength was calculated as the maximum stress experienced during specimen deformation:

$$\sigma = \frac{3\,F\,l}{2\,h^3} \tag{3.12}$$

where σ is the stress, F is the force required to deform a sample, l the span length and h the thickness of the specimen. All tests were performed to failure at a fixed strain rate of 0.1 s^{-1}.

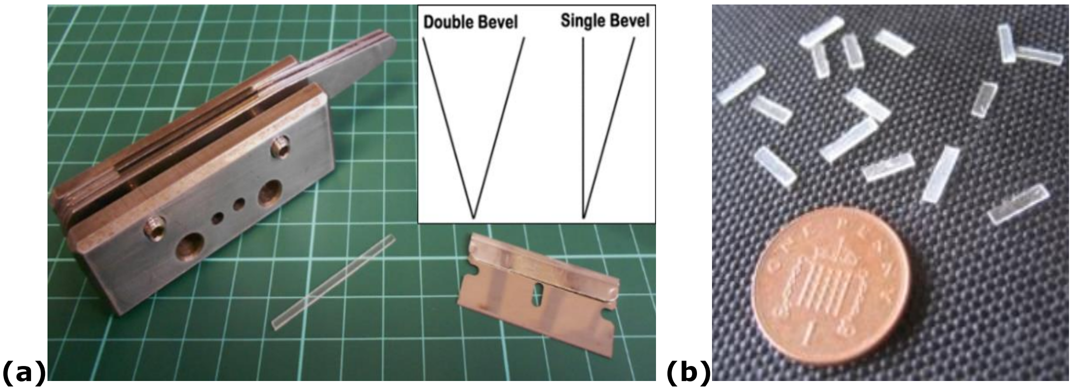

Figure 3.18. (a) Custom single bevel tool for cutting polymers into thin strips for sectioning with a single blade into (b) minibars.

3-point bending based on ASTM D790, ISO 178 was selected due to both its basic set up and it being comparable to the loading which the final products will experience if implanted in the body as fracture plates. The reduced testing dimensions are easily scalable [149]; however, increased measurement error is possible due to inaccuracies in the radius of curvature of the loading pin versus sample size [150]. This effect will therefore need to be considered for testing of actual medical devices. Although the material would be affected by water presence, which occurs *in vivo*, to remove the effects of moisture uptake and allow for focus on matrix reinforcement with HANP, specimens were tested in a dry environment.

The flexural modulus, flexural strength and the strain at maximum stress (marked with a dotted line on the right in Figure 3.20) can be obtained from the flexural testing of the polymer and nanocomposites. The flexural modulus (E) is calculated from the linear slope within the elastic region of material testing which is typically within the region of 0% - 1% strain (ε) – up to the left dotted line marked in Figure 3.20. Once the sample begins to experience plastic deformation a reduction in σ with increasing ε will be observed.

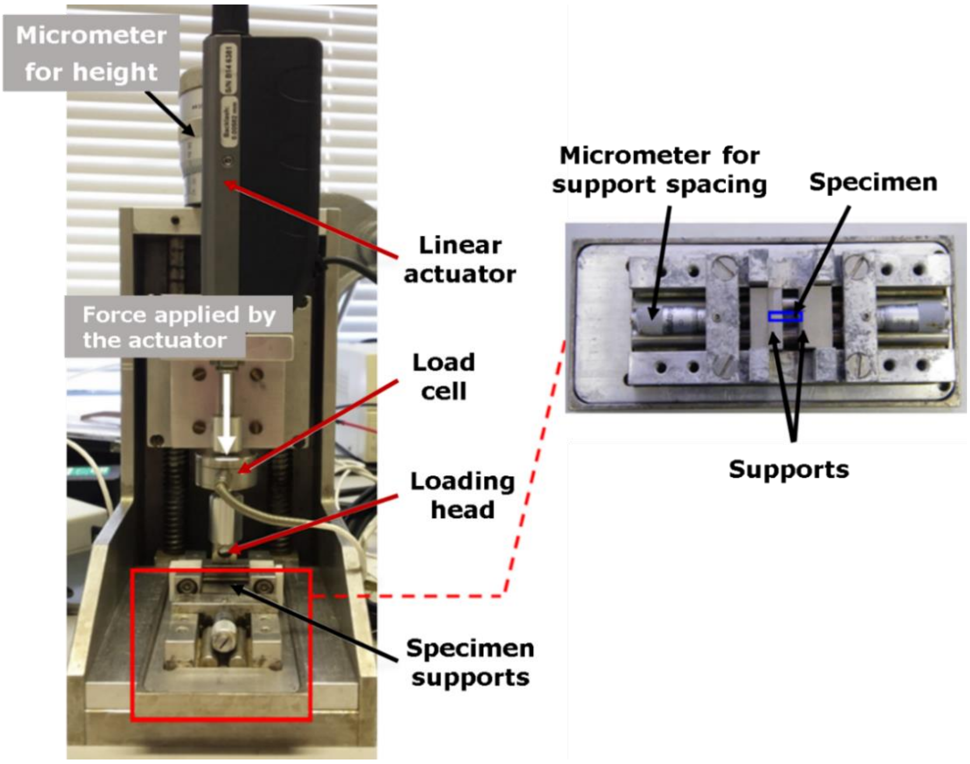

Figure 3.19. 3-point bending test fixture with loading cell for minibars.

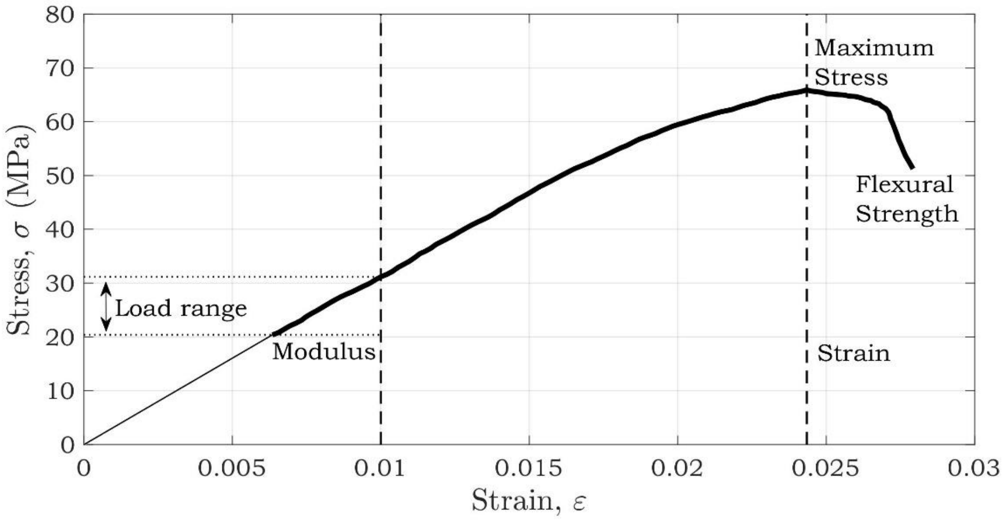

Figure 3.20. Stress versus strain graph obtained from measurements on the 3-point bending rig. Modulus is calculated from the linear region up to 0.01 ε, marked with a dotted line on the left, and the Maximum Stress point, which strain was marked with the right dotted line, is the yield.

For LR706S the modulus was calculated from the region between 0.6% and 1% ε. Alterations were made for nanocomposites which experienced plastic deformation or breakage at ε lower than 0.6% and flexural modulus was calculated, using equation (3.13), from a visually assessed linear slope region of the stress-strain curve.

$$E = \frac{\Delta\sigma}{\Delta\varepsilon} \tag{3.13}$$

4. Melt compounding analysis

This chapter describes melt mixing that was performed in the MiniLab, to produce HANP-LR706S nanocomposites. The processing equipment and methods were presented in Sections 3.2.2 and 3.2.2.1. The objective was to conduct various experiments to minimise the effect of degradation by adjusting processing parameters to maximise particle dispersion and eventually mechanical properties for the produced materials. Wall shear stress and mixing energy measurements acquired during compounding were analysed to evaluate the influence of (i) processing parameters and (ii) the amount and type of HANP, on polymer matrix and particles dispersion. Finally, the relation between pressure difference in the MiniLab and the volumetric flow rate was calculated through capillary rheometry measurements and the number of times material is recirculating in the extruder was estimated.

4.1. Trend line fitting and data filtering

An exponential decay was fitted with 95% confidence bounds to τ_w, illustrated in Figure 4.1(a-b), to quantify matrix degradation, by means of its effect on the wall shear stress, during melt compounding. Note that wall shear stress drops over time, due to mixing effects as well as due to degradation; in this chapter only the term degradation is used but the influence of mixing effects is also implied. Exponential decay can be described by the following equation:

$$\tau_w(t_R) = \tau_{w0}\ e^{-\lambda_D\ t_R} \tag{4.1}$$

where τ_{w0} is τ_w at t_R = 0 and λ_D is the decay rate, which relates to a characteristic timescale of the process, A, in the following way:

$$\lambda_D = \frac{1}{A} \tag{4.2}$$

Therefore Equation (4.1) can also be written as:

$$\tau_w(t_R) = \tau_{w0}\ e^{-t_R\,/\,A} \tag{4.3}$$

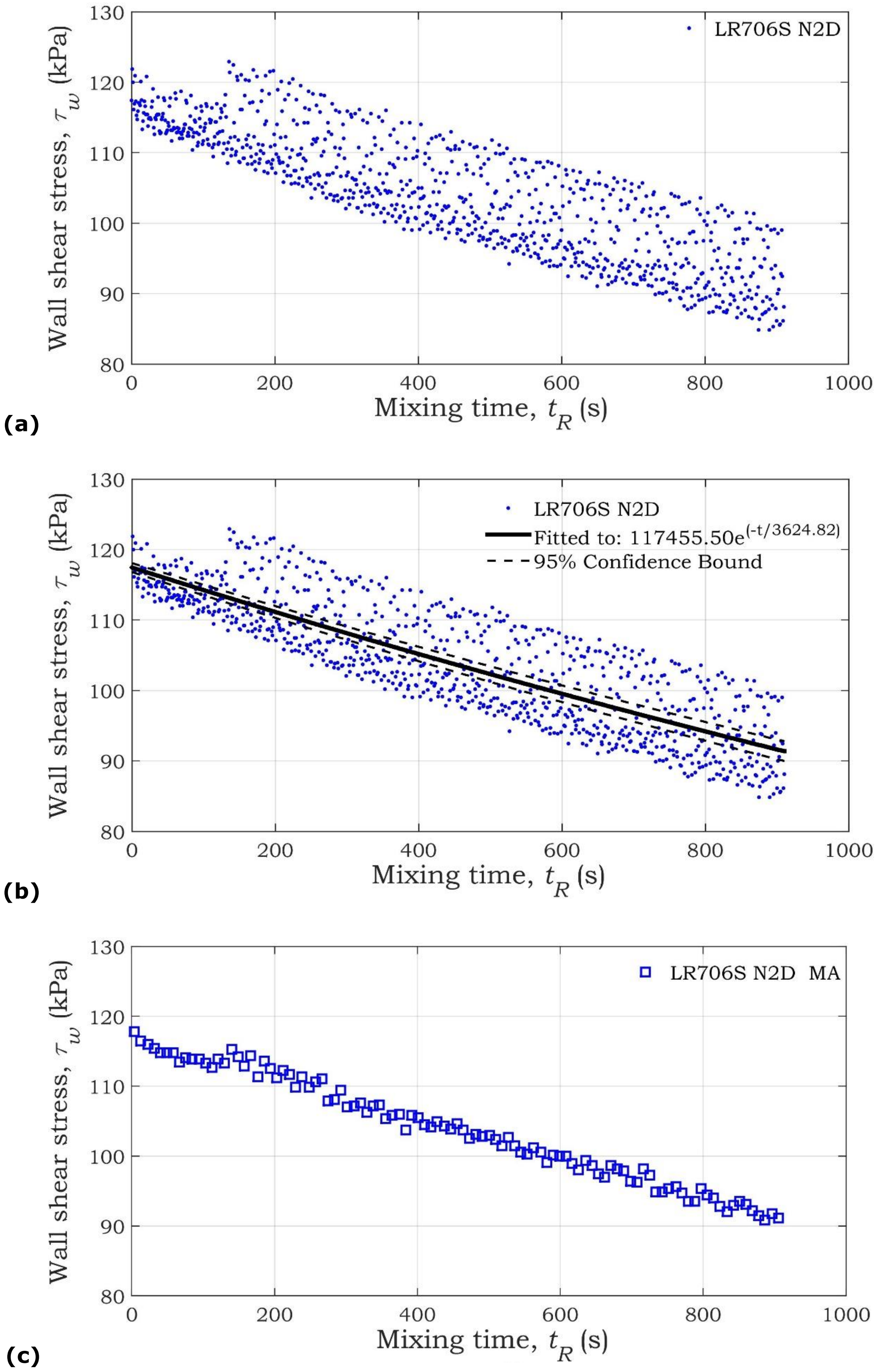

Figure 4.1. (a) Wall shear stress for recirculation of LR706S in N_{2D} at 210 °C and 50 rpm, (b) data fitted with exponential decay (ED) and (c) filtered with moving average (MA) of five points.

When the base of the exponential is chosen to be 2, instead of e, then the scaling time is the half-life, $t_{1/2}$:

$$\tau_w(t_R) = \tau_{w0}\ 2^{-t_R\,/\,t_{1/2}} \tag{4.4}$$

Therefore, the time required for the decaying τ_w to fall to half of its initial value can be described as:

$$t_{1/2} = \frac{\ln(2)}{\lambda_D} = \ln(2)\,A \tag{4.5}$$

The raw data was filtered with a simple moving average of nine points (recorded during period of 8 s) to aid visualisation of the acquired measurements, as shown in Figure 4.1(c).

4.2. Compounding limitations

To minimise matrix thermal degradation [144, 151], all melt compounding was performed at the lowest achievable temperature of 210 °C. Reducing the temperature below this threshold was not possible as increased melt viscosity caused the MiniLab emergency stop due to pressure sensors alarm limits being exceeded. The influence of a combination of polymer thermal, mechanical, oxidative and hydrolytic degradation [152] can be observed through decreasing τ_w values over t_R. The degradation and the effects from mixing are also reflected in variations of τ_{w0}, $t_{1/2}$ and E_{mix} for melt processing under different conditions. The larger the magnitude of $t_{1/2}$ the smaller the rate of decay of τ_w which indicates less matrix degradation which is also associated with higher τ_{w0}. The higher n_s was used to mix the materials within t_R the larger the magnitude of E_{mix} which is also influenced by other processing parameters, e.g. compounding under inert gas (moisture content).

PLA swelling caused by increased temperature was also taken into consideration to not exceed the MiniLab maximum filling volume (V_{ML}) during compounding. PLA density at 210 °C (ρ_{PLA210}) was calculated with the following equation [153]:

$$\rho_{PLA210} = \frac{\rho_{PLA150}}{1 + \alpha_l(210^oC - 150^oC)} \quad \textbf{(4.6)}$$

where, PLA density at 150 °C is ρ_{PLA150} = 1.1452 g.cm^{-3} [153] and PLA melt thermal coefficient of expansion at 150 °C is a_l = 0.00074 °C^{-1} [153].

V_{ML} can be described as:

$$V_{ML} = \frac{m_{HA}}{\rho_{HA}} + \frac{m_{PLA}}{\rho_{PLA210}} \quad \textbf{(4.7)}$$

where, HA density is ρ_{HA} = 3.156 g.cm^{-3} [20], m_{HA} is the mass of HA and m_{PLA} is the mass of PLA. From a nanocomposite weight percentage calculation we obtain m_{PLA}:

$$m_{PLA} = \frac{m_{HA}(100 - wt\%_{HA})}{wt\%_{HA}} \quad \textbf{(4.8)}$$

where $wt\%_{HA}$ is the desired HA weight percentage.

By substituting Equation (4.7) into (4.8) we obtain m_{HA}:

$$m_{HA} = \frac{V_{ML}\, \rho_{HA}\, wt\%_{HA}\, \rho_{PLA210}}{(wt\%_{HA}\, \rho_{PLA210}) + \rho_{HA}(100 - wt\%_{HA})} \quad \textbf{(4.9)}$$

Equations (4.8) and (4.9) allow for calculation of the required m_{PLA} and m_{HA} to obtain the desired $wt\%_{HA}$ within the MiniLab maximum filling volume to avoid overfilling of the extruder. For example to produce 2.5 wt% HANP rod nanocomposite, 7.553 g of LR70S and 0.194 g of HANP rod was required.

For melt compounding of HANP with LR706S, throughout this thesis, nominal values of particle wt% in nanocomposites are provided as those calculated to obtain the desired HANP concentration. However, the actual achieved particle wt% in the nanocomposites was confirmed via thermogravimetric measurements and discussed in detail, together with compliance variability between the calculated and measured HANP content, in Section 6.1.1.

4.3. Compounding reproducibility

Due to the high cost of LR706S and the restricted amount of HANP, experiments were designed to maximise data from a limited number of tests and most of the nanocomposites were produced in a single run. Experimental reproducibility was demonstrated via PLA recirculation tests and HANP-LR706S compounding experiments, illustrated in Figure 4.2 and Figure 4.3, which are numerically compared in Table 4.1.

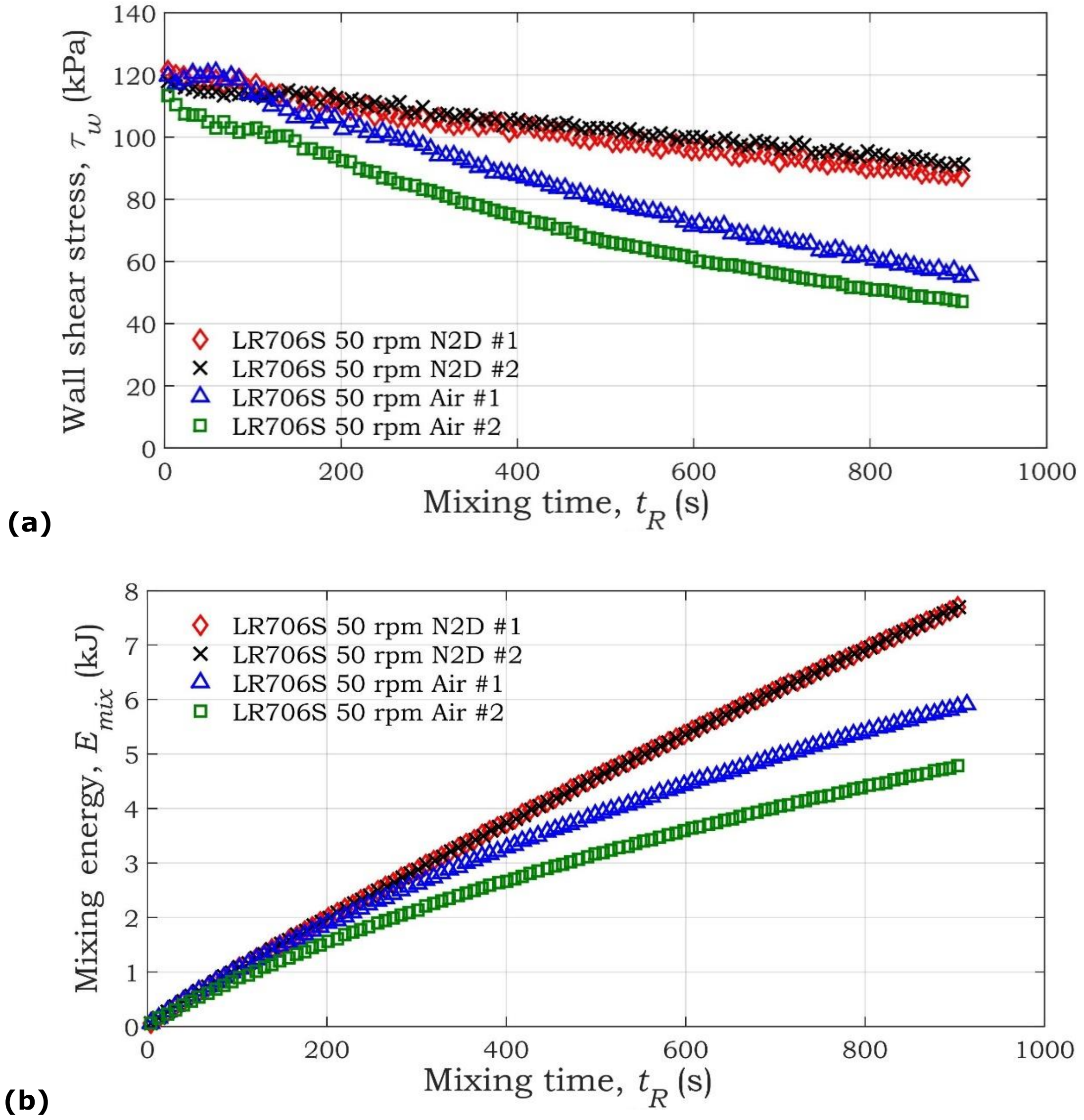

Figure 4.2. Repeated experiments of LR706S recirculation in Air and N_{2D} at 210 °C and 50 rpm for 15 min presented as (a) τ_w and (b) E_{mix}.

For the two repeats of LR706S recirculation in N_{2D}, where the plots in Figure 4.2 appear very similar, the numerical difference in τ_{w0}, $t_{1/2}$ and

E_{mix} was 1.3%, 21.1% and 0.2% respectively. Therefore, despite an almost identical E_{mix} used to mix the polymer in N_{2D} and similar τ_{w0}, the difference in $t_{1/2}$ was found to be the greatest from all compared tests. Variation in τ_{w0}, $t_{1/2}$ and E_{mix} for the two LR706S recirculation tests in Air was 10.1%, 10.7% and 18.7% respectively. These tests displayed the smallest difference in $t_{1/2}$ indicating similar degradation of the polymer.

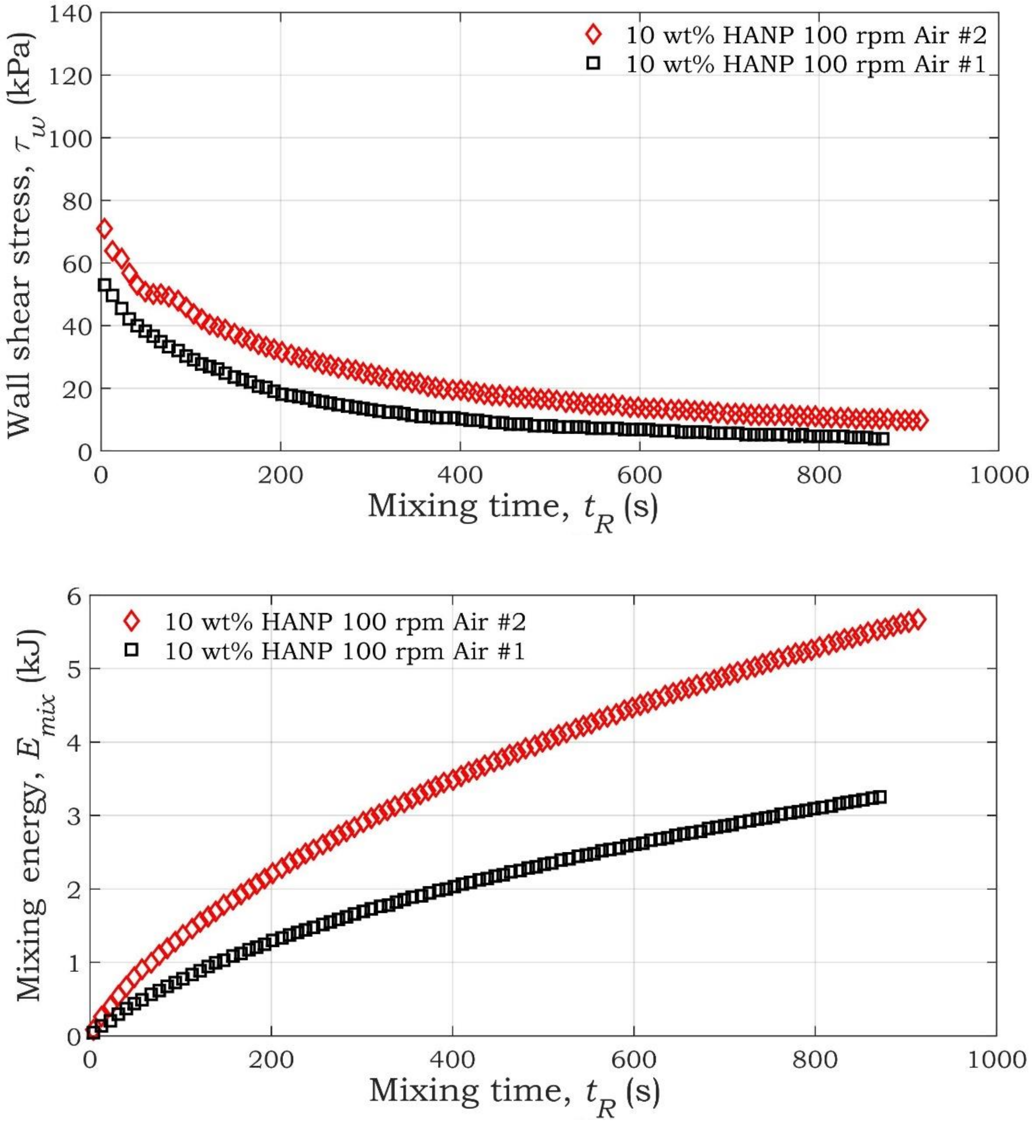

Figure 4.3. Repeated compounding of 10 wt% HANP plates with LR706S in Air at 210 °C and 100 rpm for 15 min presented as (a) τ_w and (b) E_{mix}.

For the compounding of 10 wt% HANP-LR706S, shown in Figure 4.3, the difference in τ_{w0}, $t_{1/2}$ and E_{mix} was 21.6%, 32.8% and 41.8% respectively, showing the greatest difference in E_{mix}. These results indicate that despite the same melt compounding conditions, experiments have inherent run-to-run variation likely due to manual handling. A difference of 0.81 wt% (9%) HANP was found between the two nominal 10 wt% HANP plate nanocomposites (for details see Table 6.5 in Section 6.1.1.4) and this particle variation caused additional vertical shift of the compounding curves. Repeatability can also be observed for overlapping t_R periods later in this chapter, in Figure 4.7 and Figure 4.8, where the influence of mixing time is illustrated.

Table 4.1. Experimental reproducibility for LR706S recirculation and compounding of 10 wt% HANP-LR706S nanocomposites carried out at 210 °C and various n_s for 15 min in Air and N_{2D}. Exponential decay was fitted with 95% confidence bounds.

Gas	Run	Material	HANP [wt%]	n_s [rpm]	τ_{w0} [kPa]	$t_{1/2}$ [s]	E_{mix} [kJ] at t_R = 10 min
N_{2D}	**#1**	LR706S	-	50	119.0 ±0.7	1983 ±69	5.39
N_{2D}	**#2**	LR706S	-	50	117.5 ±0.6	2513 ±96	5.37
Air	**#1**	LR706S	-	50	124.3 ±0.8	782 ±13	4.43
Air	**#2**	LR706S	-	50	111.8 ±0.5	698 ±7	3.60
Air	**#1**	HANP plate	10	100	45.4 ±0.5	185 ±3	2.61
Air	**#2**	HANP plate	10	100	57.9 ±0.6	275 ±4	4.47

The main cause behind the observed run-to-run variations was thought to be human input. The MiniLab was fed manually in 3 to 4 rounds due to the small volume of the feeding tube. As a result, loading overpressure occasionally occurred leading to small amounts of melt moving into free space behind the screws. Moreover, some of the coated HANP had a large static charge which persisted despite active earthing within the MiniLab and trials using a Milty Zerostat Anti-Static Gun. This static caused small portions of particles to deposit on surfaces near the feeding tube in an uncontrollable manner. The extruder was utilised in recirculation to aid the screw mixing process hence any loading differences would lead to batch-to-batch variations influencing τ_{w0}, $t_{1/2}$ and E_{mix} during melt compounding. Becoming more proficient at loading materials into the

MiniLab improved processing repeatability and the compliance between the theoretical and measured HANP content in the majority of the produced nanocomposites, discussed further in Section 6.1.1.

4.4. Influence of processing parameters on polymer matrix and particle dispersion

Neat LR706S was mixed in the twin-screw extruder under various conditions to assess PLA degradation during compounding and study the role of the matrix on the behaviour of the filled materials.

HANP-LR706S nanocomposites were compounded in the MiniLab, following particle handling procedures described in Section 3.2.1, with varying mixing parameters to explore optimal conditions for particle dispersion and minimise polymer matrix degradation. The influence of HANP on PLA, in comparison to LR706S melt only, was observed during compounding.

4.4.1. Screw speed

Various screw speeds were used for polymer recirculation to explore optimum mixing conditions firstly in Air and followed by tests carried out in N_2 which are summarised in Table 4.2. Finally, a range of wt% uncoated and coated HANP were mixed with LR706S at comparable screw speeds in Air and N_2 to optimise compounding conditions, summarised in Table 4.3.

4.4.1.1. PLA

In principle, for polymers with high thermal stability recirculated in the MiniLab, ΔP is greater with greater n_s, hence τ_{w0} is also higher for greater n_s. Additionally, polymers with high molecular weight, like LR706S, have higher melt viscosity causing greater ΔP and τ_w during mixing which gradually decreases over recirculation time due to polymer degradation. For LR706S recirculated in Air at 50 rpm and 100 rpm, illustrated in Figure 4.4, E_{mix} increased with higher n_s while τ_{w0} and $t_{1/2}$ decreased. This implies greater mechanical and hydrolytic degradation due to increased shear and moisture present in ambient air.

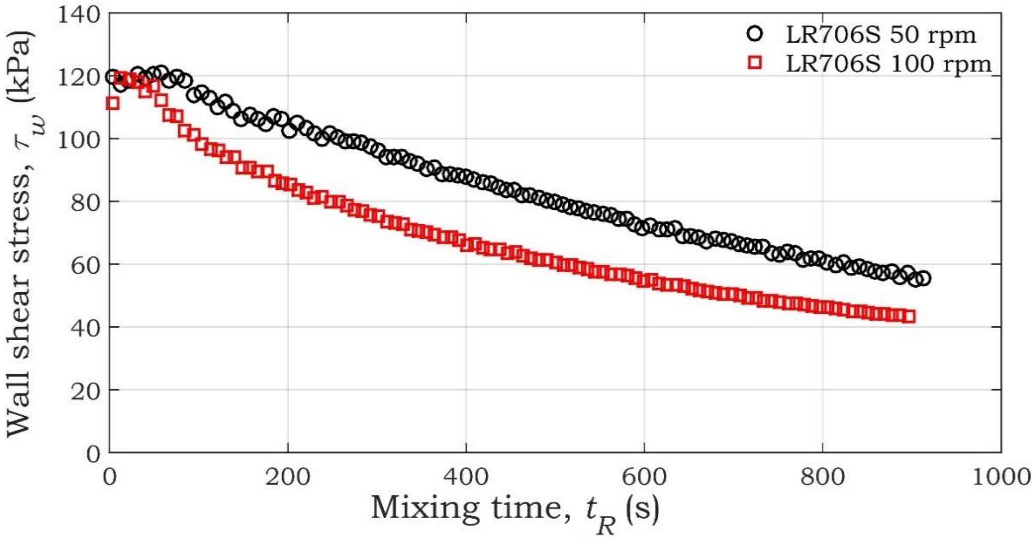

(a)

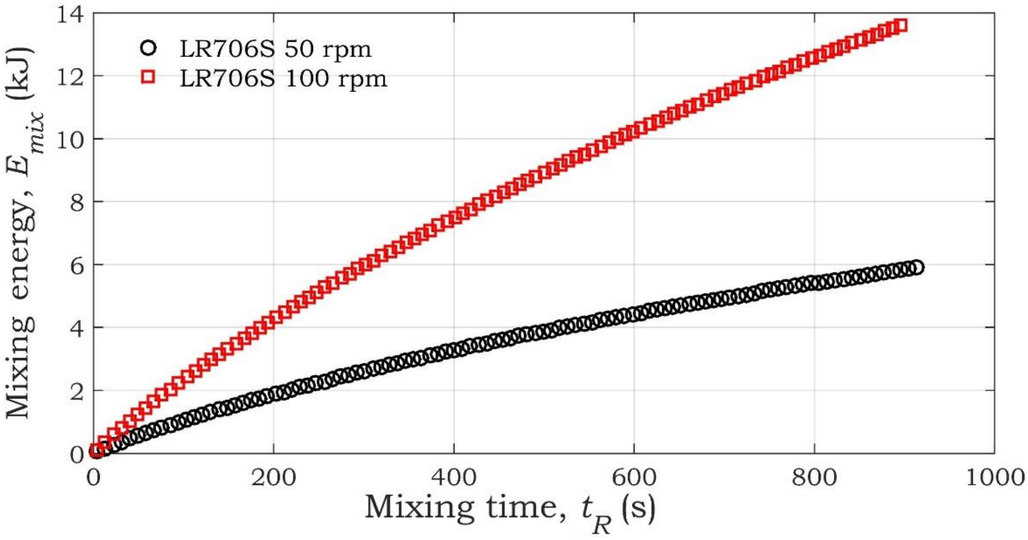

(b)

Figure 4.4. Recirculation of LR706S in Air at 210 °C for 15 min at 50 rpm and 100 rpm presented as (a) τ_w and (b) E_{mix}.

In contrast, for similar experiments carried out in nitrogen at 50 rpm, 100 rpm and 150 rpm, shown in Figure 4.5, E_{mix}, τ_{w0} and $t_{1/2}$ increased with n_s which infers less matrix decomposition during melt processing despite more mechanical force induced through sheering, with the exception of $t_{1/2}$ in the 150 rpm test. It was observed that $t_{1/2}$ increased by 25.8% for N_2 recirculation when increasing n_s from 50 rpm to 100 rpm, while it decreased by 13.8% when further increasing n_s to 150 rpm. This suggests that shear above 100 rpm caused mechanical degradation of the polymer which could not be compensated by the beneficial influence of inert gas. It was therefore hypothesized that melt processing under N_2 limits thermo-oxidative and hydrolytic degradation of PLA [151, 154], witnessed by the longer $t_{1/2}$ values in comparison to those from experiments undertaken in Air. This is in line with PLA degradation studies by Witzke [153] which suggest hydrolysis is the dominant degradation mechanism during melt processing in Air.

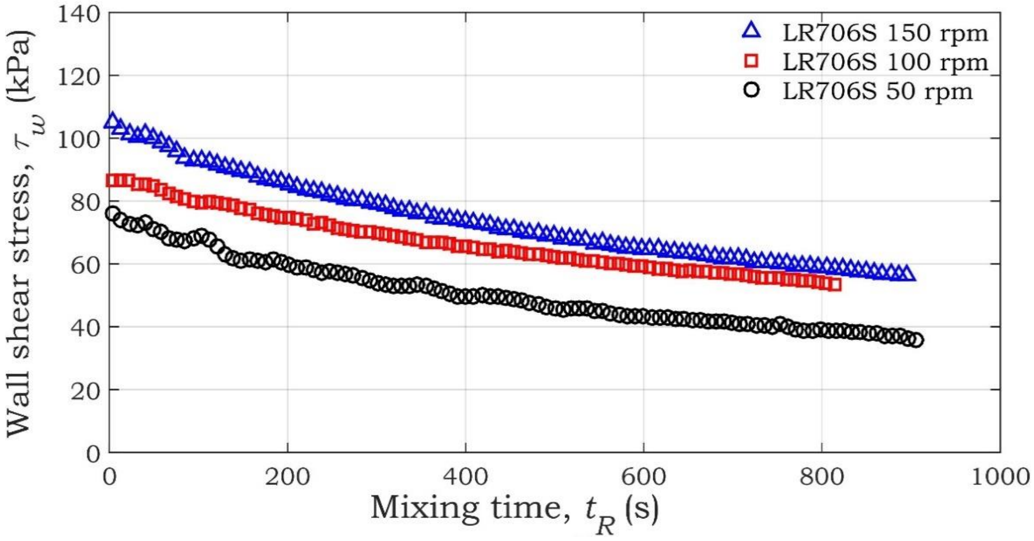

(a)

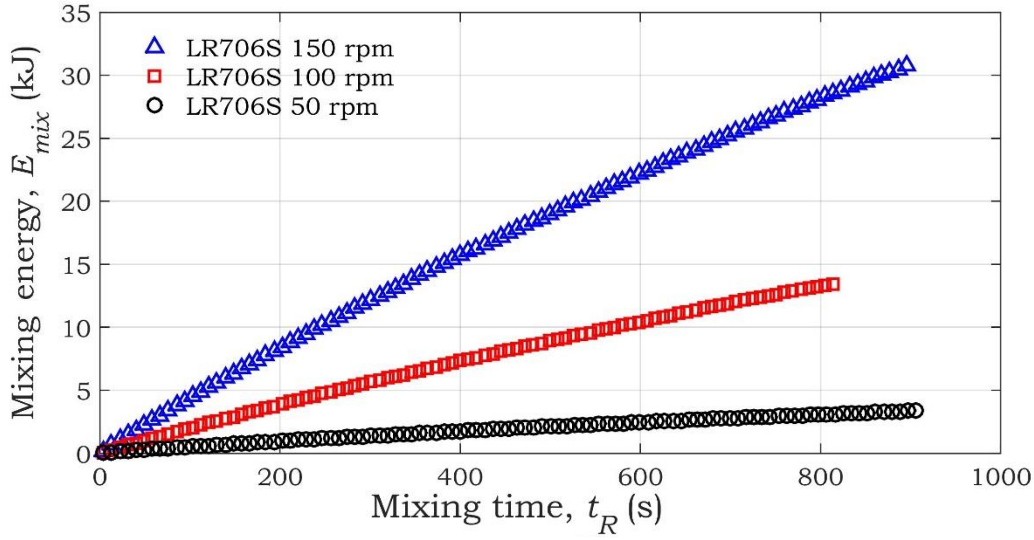

(b)

Figure 4.5. Recirculation of LR706S in N_2 at 210 °C for ~15 min at 50 rpm, 100 rpm and 150 rpm presented as (a) τ_w and (b) E_{mix}.

The $t_{1/2}$ summarised in Table 4.2 suggests that the least degradation occurred during recirculation of LR706S in N_2 at 100 rpm which was mixed with a E_{mix} over 4 times larger, after 10 min, than that at 50 rpm. This reveals that LR706S would need to be recirculated in N_2 at 50 rpm for a longer period to achieve the same E_{mix} as for 100 rpm, however that would cause substantial polymer matrix degradation due to the smaller

$t_{1/2}$. E_{mix} increased for experiments in both Air and N_2 by at least 50% for each 50 rpm increase in n_s. This indicates that better mixing properties are achievable using higher screw speeds, however, they are compromised by mechanical degradation of PLA inferred by the decreased $t_{1/2}$ for the N_2 test at 150 rpm and the Air test at 100 rpm. Higher τ_{w0} with increasing n_s for the N_2 tests suggests that the presence of inert gas limits mechanical degradation induced through polymer shearing. However, note that all τ_{w0} values for PLA experiments conducted in N_2 were lower when compared with corresponding Air tests, i.e. 42.5% and 24.5% lower at 50 rpm and 100 rpm respectively, which could be attributed to moisture content in the bottled gas discussed further in Section 4.4.3.1.

Through analysing $t_{1/2}$ and τ_{w0} values provided in Table 4.2, a compromise set of parameters for the mixing of LR706S in the MiniLab was established: 50 rpm in Air and 100 rpm in N_2.

Table 4.2. Recirculation of LR706S in Air and N_2 at 210 °C for t_R of ~15 min at various n_s.

Gas	n_s [rpm]	τ_{w0} [kPa]	$t_{1/2}$ [s]	E_{mix} [kJ] at t_R=10 min
Air	**50**	124.3±0.8	782±13	4.43
Air	**100**	112.4±1.0	580±11	10.24
N_2	**50**	71.4±0.3	859±9	2.46
N_2	**100**	84.8±0.2	1157±11	10.45
N_2	**150**	99.4±0.3	997±11	22.24

4.4.1.2. Nanocomposites

For neat LR706S mixed in Air, τ_{w0} and $t_{1/2}$ decreased with increasing n_s (see Table 4.2) inferring polymer degradation due to increased shear. In contrast, for HANP-LR706S recirculated in Air, τ_{w0}, $t_{1/2}$ and E_{mix} increased with higher n_s, which is shown in Figure 4.6, e.g. for 5 wt% HANP-LR706S the aforementioned values increased by 10.4%, 25.9% and 72.7% respectively when increasing n_s from 50 rpm to 100 rpm. This would suggest a limiting of mechanical degradation due to inclusion of HANP. However, τ_{w0}, $t_{1/2}$ and E_{mix} are objectively lower for the abovementioned nanocomposites than for LR706S only at particular screw speeds, see Table 4.2. For example for 10 wt% HANP-LR706S at 100 rpm τ_{w0}, $t_{1/2}$ and E_{mix} are 37.1%, 44.9% and 42.1% lower respectively than for LR706S at 100 rpm. Additionally, in Figure 4.6, for 10 wt% HANP-LR706S for n_s raised from 50 rpm up to 100 rpm τ_{w0} increased by 42%, E_{mix} by 79.1% while $t_{1/2}$ only by 3.4%. It was therefore hypothesized that presence of nanoparticle aggregates in polymer matrix due to incomplete dispersion creates additional shear which causes greater degradation of PLA.

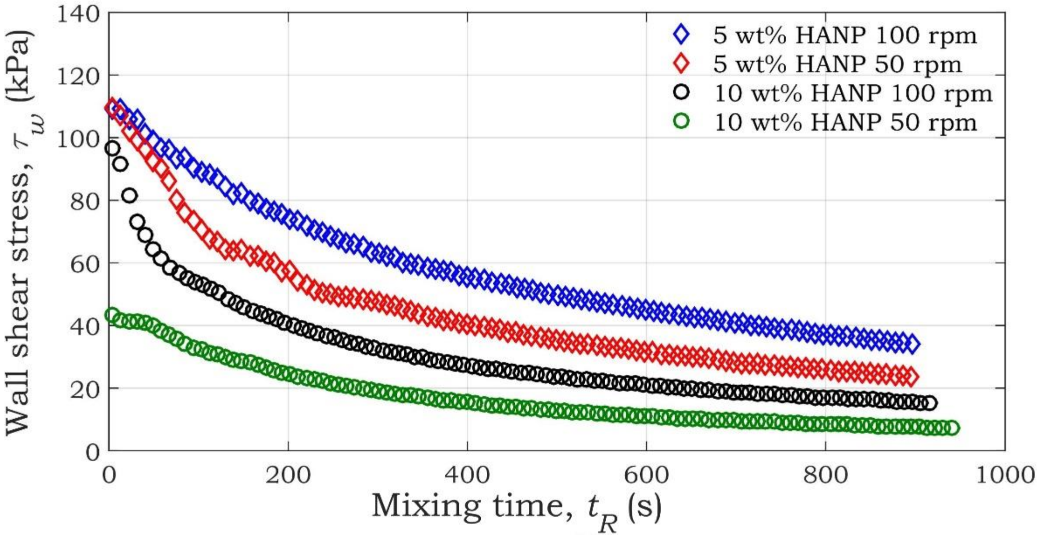

(a)

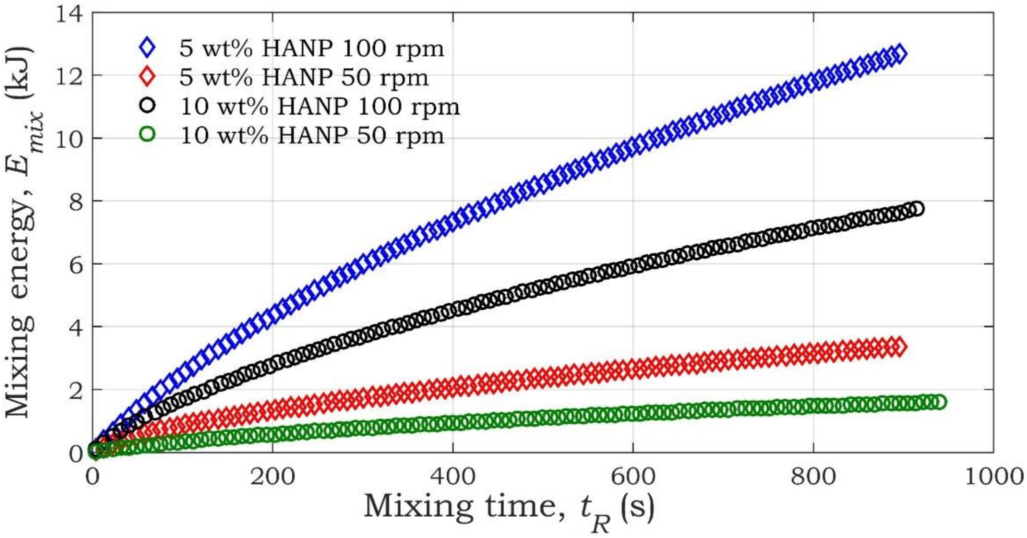

(b)

Figure 4.6. Compounding of plate HANP with LR706S in Air at 210 °C for ~15 min at 50 rpm and 100 rpm presented as (a) τ_w and (b) E_{mix}.

For similar experiments carried out in N_2 with coated and uncoated HANP, τ_{w0}, $t_{1/2}$ and E_{mix} increased when increasing n_s from 50 rpm to 100 rpm, e.g. for 2.8 wt% DDSAHA they increased by 10.5%, 38% and 73.2% respectively. This infers less matrix decomposition with added HANP during melt processing despite more mechanical force induced through shearing. For nanocomposites produced with a n_s of 150 rpm, $t_{1/2}$ reduced e.g. for 2.5 wt% HANP it decreased by 32.4% when compared with 100 rpm test. This suggests that compounding of HANP and LR706S with shear above 100 rpm caused more mechanical degradation of the polymer which could not be compensated for by the beneficial influence of inert gas and addition of HANP. However, it must be mentioned that τ_{w0} and $t_{1/2}$ values for nanocomposites compounded in N_2 were higher when compared with recirculation of neat LR706S in N_2 regardless of screw speed, which could be attributed to the desiccating effect of added particles discussed further in Section 4.4.3.2.

Table 4.3. Compounding of plate HANP and DDSAHA with LR706S in Air and N_2 at 210 °C for ~15 min at 50 - 150 rpm.

Gas	HANP type	HANP [wt%]	n_s [rpm]	τ_{w0} [kPa]	$t_{1/2}$ [s]	E_{mix} [kJ] at t_R = 10 min
N_2	HANP plate	**2.5**	150	135.7 ±1.1	1161 ±35	26.83
N_2	HANP plate	**2.5**	100	133.8 ±0.9	1717 ±56	16.29
N_2	HANP plate	**2.5**	50	121.1 ±0.7	1735 ±52	5.11
N_2	DDSAHA	**2.8**	150	135.9 ±0.9	1880 ±65	30.87
N_2	DDSAHA	**2.8**	100	134.7 ±0.8	2325 ±89	17.53
N_2	DDSAHA	**2.8**	50	120.6 ±0.8	1441 ±44	4.70
Air	HANP plate	**5**	100	101.7 ±0.7	504 ±7	9.72
Air	HANP plate	**5**	50	91.2 ±1.1	374 ±8	2.65
Air	HANP plate	**10**	100	70.7 ±1.1	320 ±8	5.93
Air	HANP plate	**10**	50	41.0 ±0.3	309 ±4	1.24

The $t_{1/2}$ summarised in Table 4.3 suggests that the least degradation occurred during compounding of 2.8 wt% DDSAHA in N_2 at 100 rpm which was mixed with a E_{mix} over 4 times larger, after 10 min, than that at 50 rpm. However, the influence of the increased E_{mix} with raised n_s, for the N_2 tests at 150 rpm, caused mechanical degradation of polymer matrix.

Higher τ_{w0} with increasing n_s for N_2 and Air compounding tests suggests that pressure in the extruder increases with greater mixing of particles with polymer melt. However, note that all τ_{w0} and $t_{1/2}$ values for compounding in Air were lower when compared with corresponding N_2 tests, which again can be linked to use of inert gas and the desiccating effect of added particles limiting degradation of PLA in bottled N_2.

Through analysing $t_{1/2}$ and τ_{w0} values provided in Table 4.3, applicable n_s for compounding of HANP with LR706S in the MiniLab was established to be 100 rpm in both Air and N_2. However, the chosen screw speed for subsequent compounding runs was 50 rpm as this allows for the loading and processing of a variety of nanocomposites without exceeding the MiniLab pressure sensors alarm limits. Without this constraint, the following could be achievable: (i) a decrease in processing temperature by at least 5 °C to minimise thermal degradation of the polymer, (ii) an increase in n_s to 100 rpm for better mixing, and as a result (iii) a decrease in recirculation time.

4.4.2. Mixing time

LR706S was recirculated in the MiniLab for various lengths of time to find optimal conditions which would aid screw mixing and not cause substantial matrix degradation due to prolonged residence in the extruder at an elevated temperature. Firstly, experiments were carried out in Air at 100 rpm for 4 – 27 min, illustrated in Figure 4.7, followed by tests conducted in N_2 at 150 rpm for 10 min and 15 min, all of which are summarised in Table 4.4. Finally, 5.6 wt% DDSAHA was compounded with LR706S in N_{2D} to explore optimal mixing time when compromising between particle dispersion and PLA degradation. Those experiments were conducted at 50 rpm for 5 – 15 min, shown in Figure 4.8 and summarised in Table 4.5.

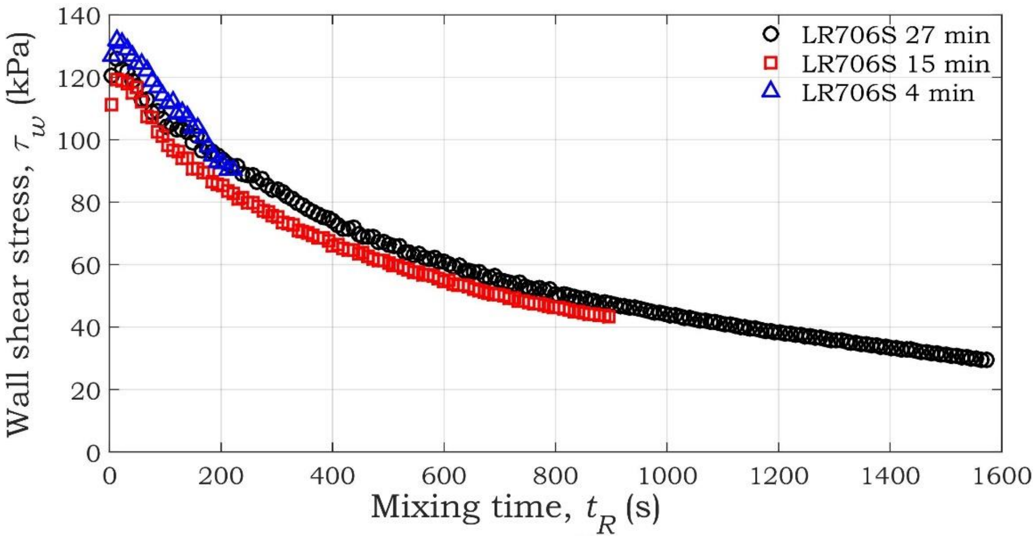

(a)

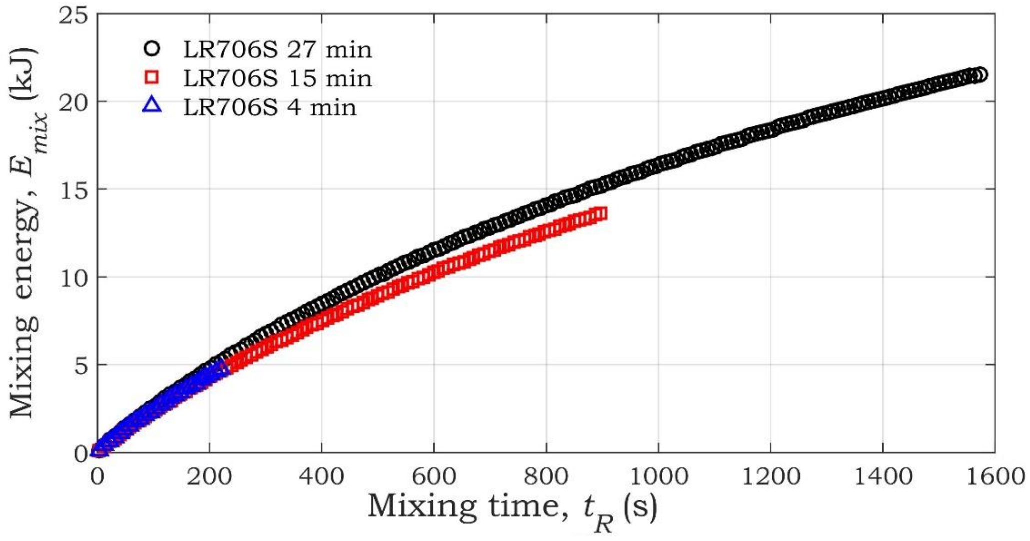

(b)

Figure 4.7. Recirculation of LR706S in Air at 210 °C and 100 rpm for 4 min, 15 min and 27 min presented as (a) τ_w and (b) E_{mix}.

All tests carried out for LR706S and nanocomposites were nominally identical for respective n_s with exception of mixing duration. However, slight random fluctuations of τ_{w0} and E_{mix} for the overlapping time periods were found. This run-to-run variation is inherent due to manual handling and the values remain comparable within the same order of magnitude. The analysis of $t_{1/2}$ variations revealed a decrease of $t_{1/2}$ with recirculation time for shorter runs due to greater uncertainty in fitting a model to less data. This is most likely due to the initial transient period after sample loading which had the greatest effect on short time experiments while during longer recirculation this effect was less prominent. Hence only $t_{1/2}$ for the longest tests was compared: for LR706S recirculated for 27 min at

100 rpm in Air, $t_{1/2}$ was 722 s, in N_2 for 15 min at 150 rpm it was 997 s, while for 5.6 wt% DDSAHA compounded for 15 min at 50 rpm in N_{2D}, $t_{1/2}$ was 729 s, which in average gives 816 s.

Figure 4.7(b) reveals an E_{mix} increase of 64.2% for LR706S recirculated in Air at 100 rpm for 15 min when compared to the 4 min test. Increasing the recirculation time to 27 min resulted in a further 13.2% increase in E_{mix}. A lower E_{mix} increase of 31.7% was recorded for PLA melt mixing in N_2 at 150 rpm when the recirculation time was changed from 10 min to 15 min as shown in Table 4.4.

Table 4.4. Recirculation of LR706S in Air and N_2 at 210 °C for 4 - 27 min at various n_s.

Gas	n_s [rpm]	t_R [min]	τ_{w0} [kPa]	$t_{1/2}$ [s]	E_{mix} [kJ] at t_R = 5 min	E_{mix} [kJ] at t_R = final
Air	100	**27**	114.3 ±0.6	722 ±7	6.74	21.64
Air	100	**15**	112.4 ±1.0	580 ±11	5.96	13.66
Air	100	**4**	135.4 ±2.0	383 ±25	-	4.88
N_2	150	**15**	99.4 ±0.3	997 ±11	12.13	30.93
N_2	150	**10**	96.9 ±0.4	856 ±13	11.47	21.12

Graphical results for the compounding of nanocomposites, shown in Figure 4.8, again appear similar in the overlapping time periods, with an E_{mix} increase of 25.7% when comparing the 5 min and 10 min test. This further increased by 25.8% for experiment conducted for 15 min; refer to Table 4.5 for numerical results. For the overlapping time periods a difference in τ_{w0} and E_{mix} was found which suggests a potential variation in the amount of HANP between the runs. This variation in HANP is later confirmed in Table 6.7 in Section 6.1.1.4.

As an increase in $t_{1/2}$ with the mixing time was expected to occur due to improved fitting of an exponential decay to more τ_w data from longer runs, an optimum mixing time was chosen based on the hypothesis that longer t_R in the MiniLab gives particles the opportunity to mix better with

PLA despite causing increased matrix degradation. This was later reflected in the improved flexural properties of the 5.6 wt% DDSAHA-LR706S compounded for 15 min, shown in Figure 5.33 in Section 5.3.1.3, when compared with the nanocomposite mixed for less time and with LR706S mixed for 15 min. By additionally reviewing compounding conditions applied by Wilberforce et al. [20], who also utilised the MiniLab for compounding of nHA with high molecular weight PLA, it was decided that 15 min for t_R will be an agreeable compromise between particle mixing with LR706S and limiting matrix degradation.

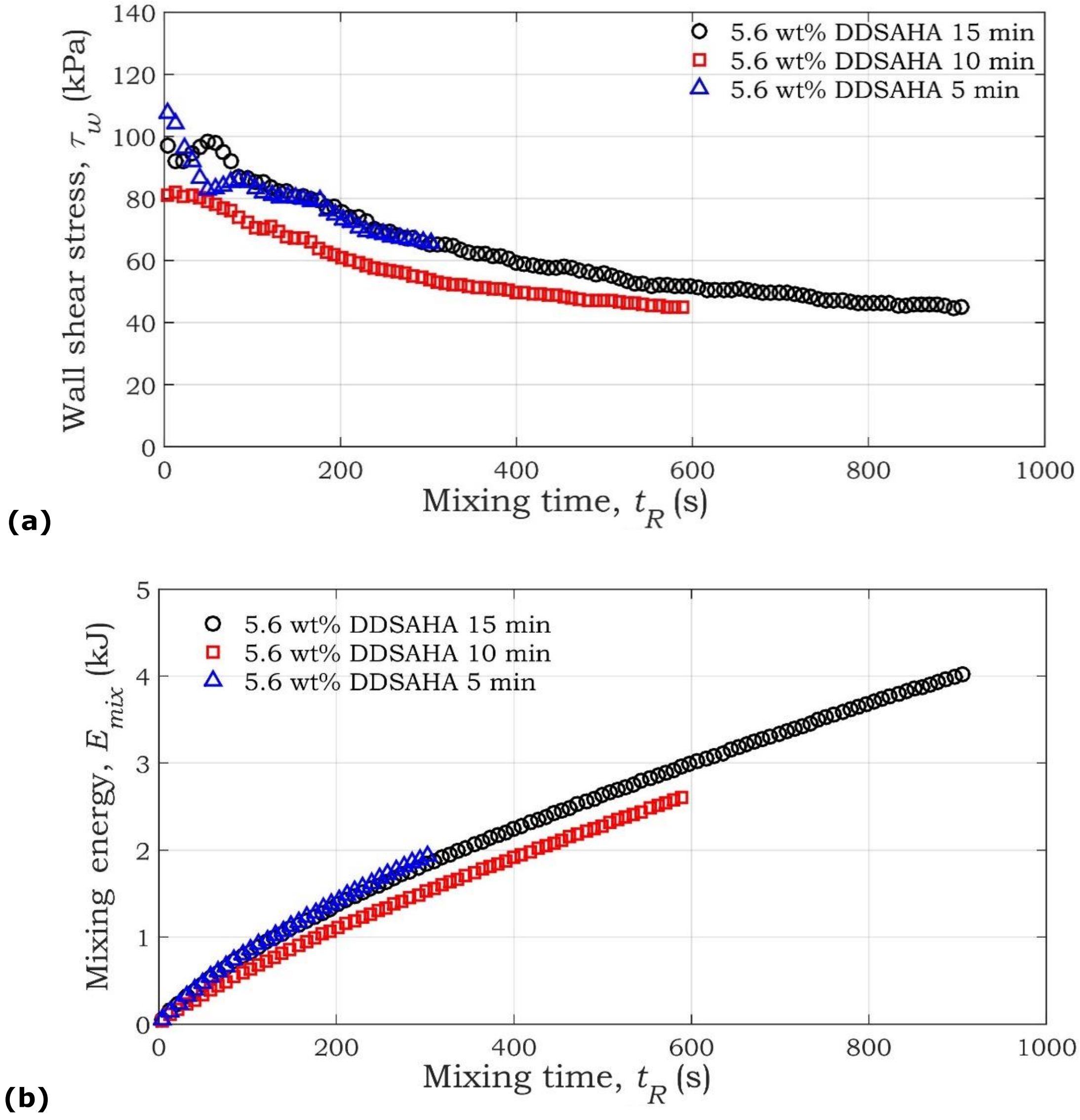

Figure 4.8. Compounding of 5.6 wt% DDSAHA and LR706S in N_{2D} at 210 °C and 50 rpm for 5 - 15 min presented as (a) τ_w and (b) E_{mix}.

Table 4.5. Comparison of 5.6 wt% DDSAHA compounding with LR706S in N_{2D} at 210 °C and 50 rpm for 5 - 15 min.

Gas	HANP type	HANP [wt%]	t_R [min]	τ_{w0} [kPa]	$t_{1/2}$ [s]	E_{mix} [kJ] at t_R = 5min	E_{mix} [kJ] at t_R = final
N_{2D}	DDSAHA	5.6	**5**	97.2 ±1.2	499 ±26	1.92	1.97
N_{2D}	DDSAHA	5.6	**10**	80.2 ±0.5	606 ±11	1.52	2.65
N_{2D}	DDSAHA	5.6	**15**	92.9 ±0.7	729 ±13	1.83	4.05

4.4.3. Mixing under inert gas

4.4.3.1. PS and PLA

PS was processed in the MiniLab in Air and N_{2D}, shown in Figure 4.9, to investigate the influence of inert gas on this thermoplastic polymer which is fairly stable during melt compounding; recirculation data is summarised in Table 4.6. Due to its lower molecular weight, PS has a substantially lower τ_{w0} when compared with PLA, shown in Figure 4.10, however its $t_{1/2}$ is much longer: around 3 times longer than LR706S in Air and 29 times longer than in N_{2D}. This confirms superior thermal stability of PS in comparison to PLA though mixing under N_{2D} still had beneficial effects on PS as $t_{1/2}$ increased by 95.5% when compared with mixing in Air.

LR706S was recirculated at 210 °C and 50 rpm for 15 min in Air, N_2 and N_{2D} to investigate the influence of gas on the mixing process, see Figure 4.10. It was expected that experiments in N_2 will improve mixing parameters in comparison to Air, however E_{mix} and τ_{w0} decreased substantially by 44.5% and 42.5% respectively despite a 9% increase in $t_{1/2}$, as shown in Table 4.7.

Figure 4.10 illustrates the importance of carefully drying nitrogen when it is used as an inert gas for melt processing of PLA. This prevents an excessive decrease in molecular weight caused by the presence of water, which can be a significant contaminant in bottled gas, and as a result considerably mitigates the reduction in τ_w during compounding [155].

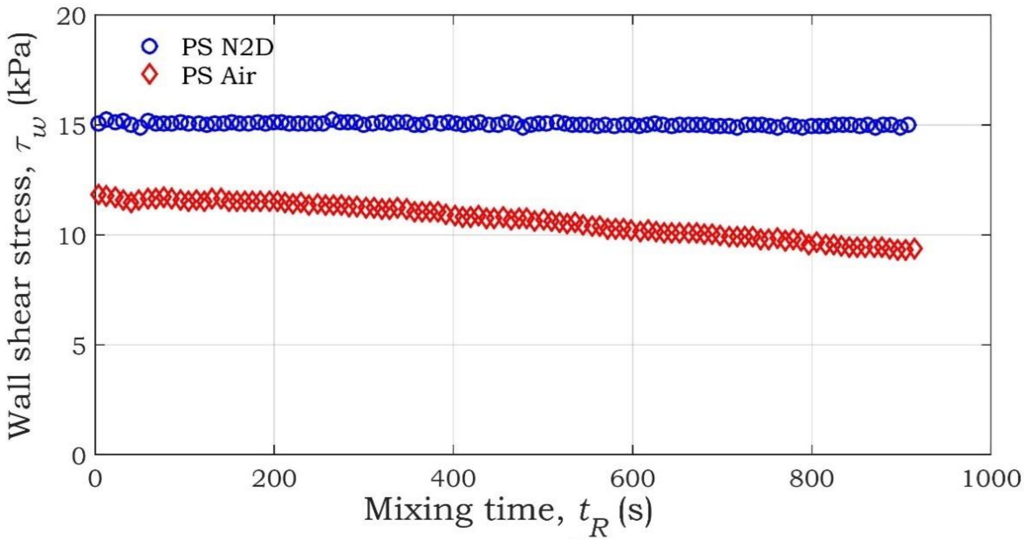

(a)

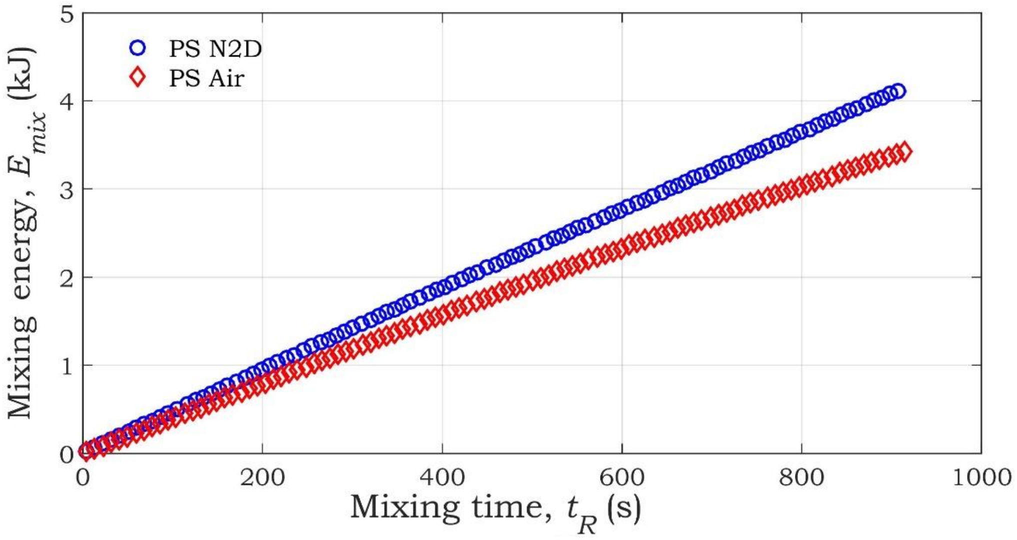

(b)

Figure 4.9. Recirculation of PS at 210 °C and 100 rpm for 15 min in Air and N_{2D} presented as (a) τ_w and (b) E_{mix}. Data filtered with moving average of nine points.

The $t_{1/2}$ for mixing in Air was the smallest, inferring faster degradation causing greater reduction in molecular weight. After recirculation in N_2 that had not been dried, the final τ_w was much lower than for either N_{2D} (58% less) or Air (35% less). The slight increase in $t_{1/2}$ implied that mixing under inert gas decreased thermo-oxidative degradation however the significant decrease of E_{mix} and τ_{w0} suggests moisture in N_2 caused hydrolytic degradation which was even greater than that in Air. It was expected that ppm moisture content in N_2 would be removed while passing through the gas inlet of the hot MiniLab chamber, however the above results indicate otherwise.

Table 4.6. Comparison of PS recirculation at 210 °C and 100 rpm for 15 min in Air and N_{2D}.

Gas	Polymer	τ_{w0} [kPa]	$t_{1/2}$ [s]	E_{mix} [kJ] at t_R = 10 min
N_{2D}	PS	15.1±0.01	58308±6555	2.77
Air	PS	12.0±0.01	2598±21	2.33

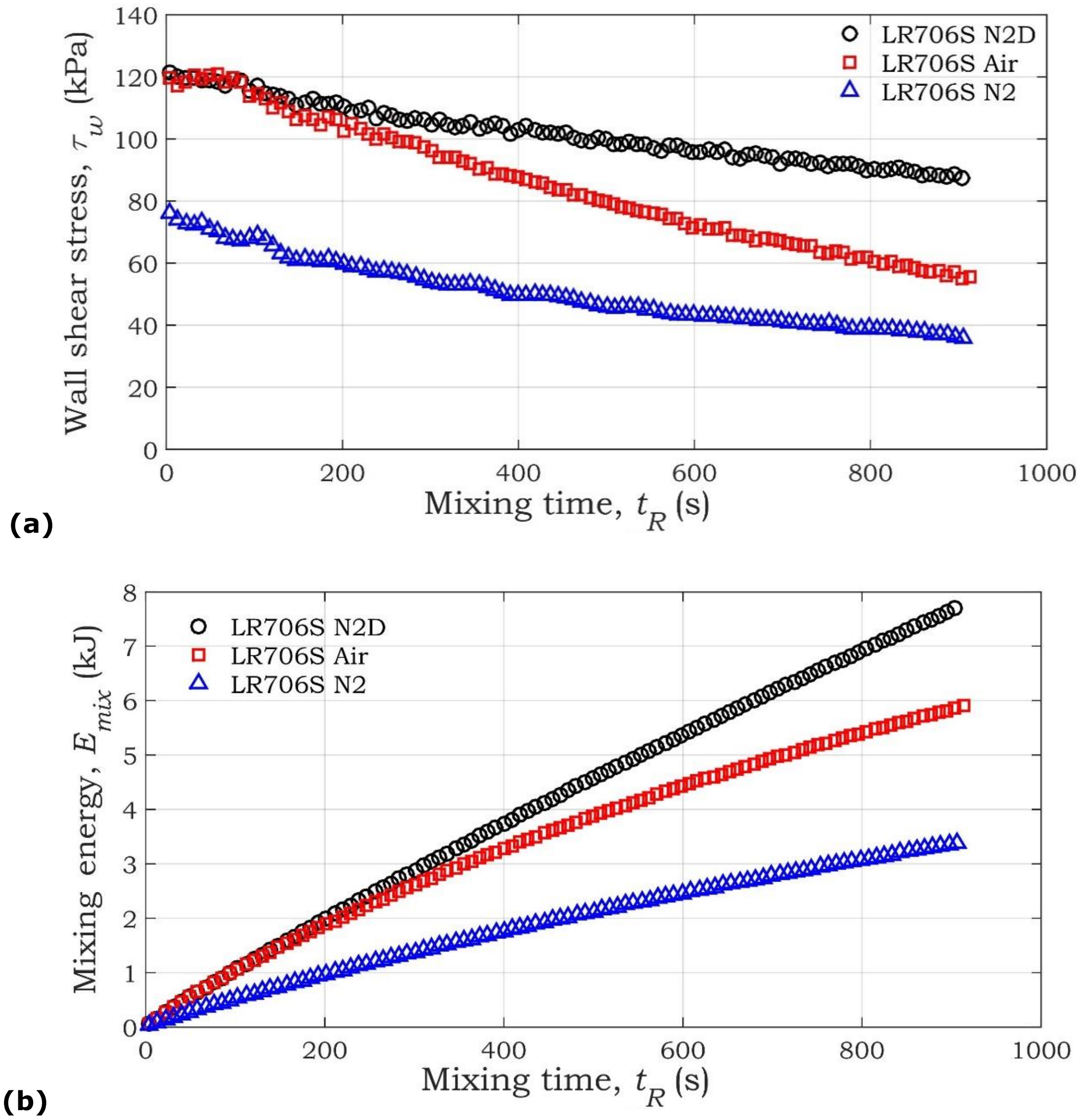

Figure 4.10. Recirculation of LR706S at 210 °C and 50 rpm for 15 min in Air, N_2 and N_{2D} presented as (a) τ_w and (b) E_{mix}.

Therefore, N_2 was in-line dried with a liquid nitrogen moisture trap, where gas was passed through a coil immersed in a dewar with liquid N_2 to remove any residual water by freezing. This gas drying process improved mixing parameters as $t_{1/2}$ and E_{mix} increased by 60.5% and

17.8% respectively for N_{2D} in comparison with recirculation in Air and τ_{w0} remained within the same order of magnitude. Thus, it was proved that even residual moisture content in the processing gas can cause severe hydrolytic degradation of PLA as displayed by substantially decreased $t_{1/2}$ values. These findings are in line with those from other studies, for example [144], which suggest that the removal of moisture and oxygen during melt processing determines the extent of PLA degradation.

Table 4.7. Comparison of LR706S recirculation at 210 °C and 50 rpm for 15 min in Air, N_2 and N_{2D}.

Gas	Polymer	τ_{w0} [kPa]	$t_{1/2}$ [s]	E_{mix} [kJ] at t_R = 10 min
N_{2D}	LR706S	119.0±0.7	1983±69	5.39
Air	LR706S	124.3±0.8	782±13	4.43
N_2	LR706S	71.4±0.3	859±9	2.46

4.4.3.2. Nanocomposites

Subsequently, HANP was mixed with LR706S at 210 °C and 50 rpm for 15 min in Air, N_2 and N_{2D} to investigate the influence of gas on the compounding process, see Figure 4.11. Based on LR706S recirculation in the MiniLab in various gas atmospheres, shown in Figure 4.10, it was expected that compounding in N_{2D} will improve $t_{1/2}$ in comparison to compounding in N_2 and Air, as demonstrated through an array of experiments summarised in Table 4.8. The general trend for the equivalent tests carried out in Air, N_2 and N_{2D} shown that τ_{w0} remained in the same order of magnitude and $t_{1/2}$ and E_{mix} increased, with the lowest values for tests in Air and the highest value for tests in N_{2D}.

Unlike findings from the recirculation of neat LR706S in N_2, for nanocomposites mixed under N_2, E_{mix} and τ_{w0} increased in comparison to values from experiments conducted in Air, e.g. for 2.5 wt% HANP plates they increased by 20.7% and 29.6% respectively, see Figure 4.11. For all compounding experiments $t_{1/2}$ was the greatest for tests carried out under in-line dried N_2 when compared with the Air runs, as illustrated in Figure 4.12, e.g. for 3.6 wt% is16PLAHA $t_{1/2}$ increased by 66.8% for the N_{2D} run.

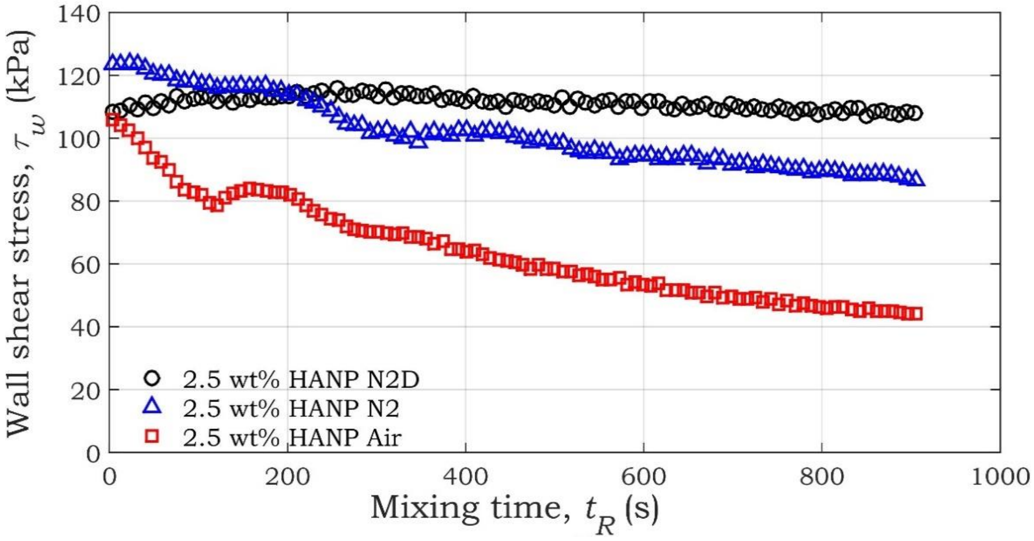

(a)

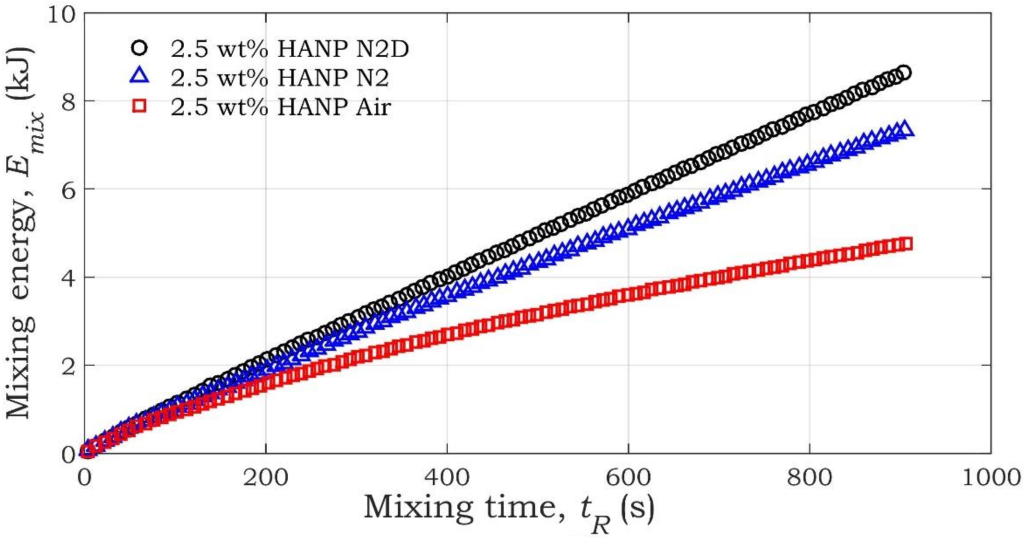

(b)

Figure 4.11. Compounding of 2.5 wt% plate HANP and LR706S at 210 °C and 50 rpm for 15 min in Air, N_2 and N_{2D} presented as (a) τ_w and (b) E_{mix}.

The greatest increase in $t_{1/2}$ for experiments conducted in N_{2D} was observed for 2.5 wt% HANP plates and rods, when compared to compounding in Air, which increased 21- and 19-fold respectively. This infers a decrease of hydrolytic degradation of PLA through moisture removal with N_{2D} and desiccating effects from the addition of dried HANP. Subsequently, a N_2 drying process was applied for final compounding experiments, including scale-up activities, as it was demonstrated that tests conducted under N_{2D} caused the least polymer degradation. This was evidenced by increased melt viscosity, which was witnessed by sharkskin extrudates, for all materials compounded under N_{2D}, shown in Figure 4.13. This elastic surface instability, caused by extrusion at high shear rate of very viscous melt [156, 157], is undesirable in commercial extrudate products but does not have a major impact on the production of injection moulded parts.

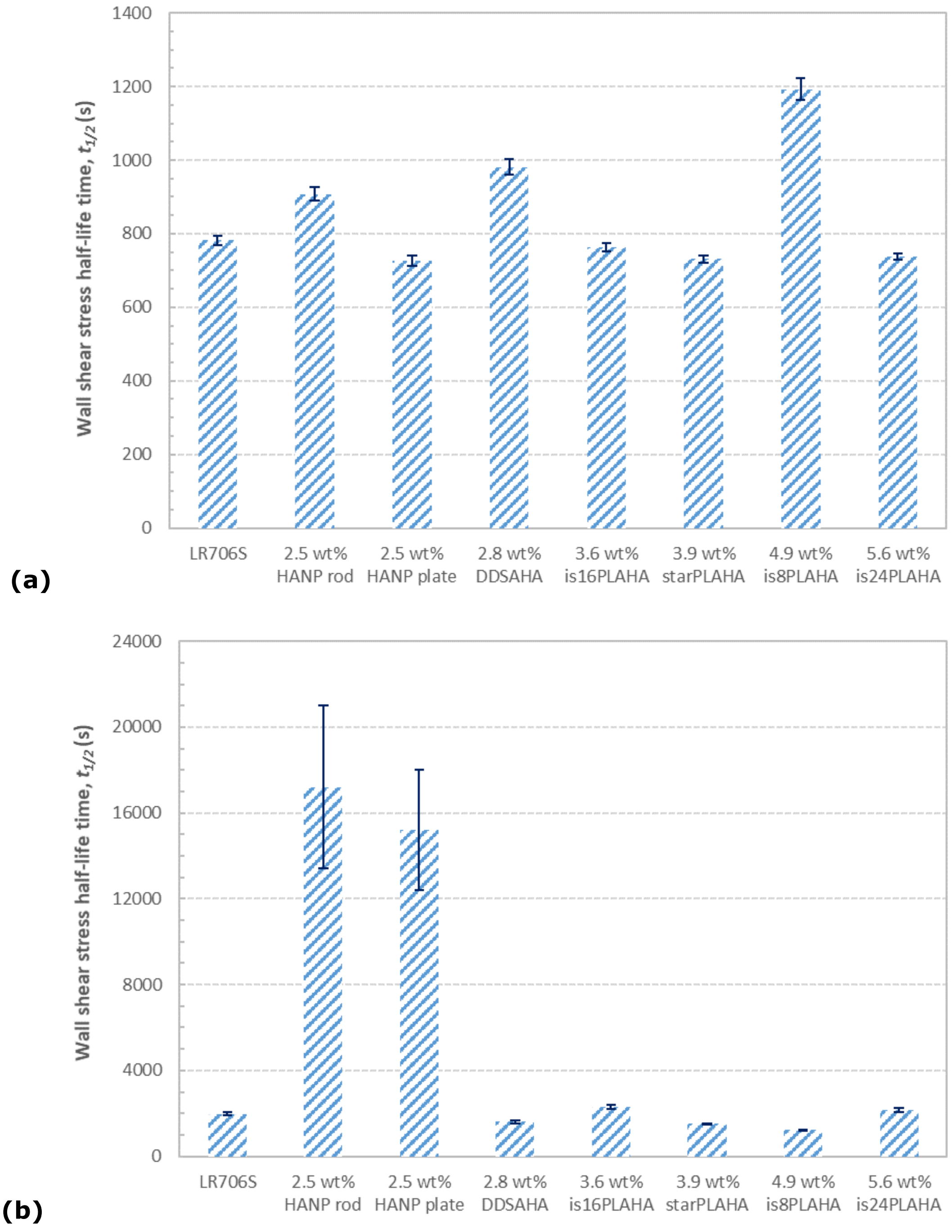

Figure 4.12. Wall shear stress half-life time for compounding of 2.5 wt% HANP-LR706S, for coated particles equivalent to 2.5 wt% of uncoated HANP plus coating, in (a) Air and (b) N_{2D}.

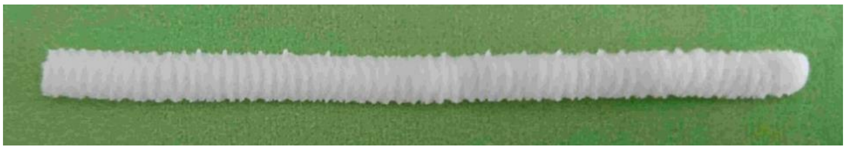

Figure 4.13. Extrudate of HANP plate nanocomposite compounded in the MiniLab under N_{2D}.

Table 4.8. Summary of various HANP compounded with LR706S at 210 °C and 50 rpm for 15 min in Air, N_2 and N_{2D}.

Gas	Material	HANP [wt%]	τ_{w0} [kPa]	$t_{1/2}$ [s]	E_{mix} [kJ] at t_R = 10 min
N_{2D}	LR706S	**-**	119.0±0.7	1983±69	5.39
Air	LR706S	**-**	124.3±0.8	782±13	4.43
N_{2D}	HANP rod	**2.5**	114.7±0.7	17209±3801	5.77
Air	HANP rod	**2.5**	116.1±0.8	908±19	4.25
N_{2D}	HANP plate	**2.5**	113.6±0.6	15212±2818	5.89
N_2	HANP plate	**2.5**	121.1±0.7	1735±52	5.11
Air	HANP plate	**2.5**	96.1±0.7	727±14	3.60
N_{2D}	DDSAHA	**2.8**	104.8±0.8	1601±56	4.06
N_2	DDSAHA	**2.8**	120.6±0.8	1441±44	4.70
Air	DDSAHA	**2.8**	122.7±0.8	981±21	4.71
N_{2D}	is16PLAHA	**3.6**	111.7±0.7	2296±95	5.08
Air	is16PLAHA	**3.6**	105.3±0.5	763±10	3.57
N_{2D}	starPLAHA	**3.9**	109.4±0.7	1504±46	4.30
Air	starPLAHA	**3.9**	106.2±0.6	731±10	3.98
N_{2D}	is8PLAHA	**4.9**	109.6±0.8	1218±33	4.47
Air	is8PLAHA	**4.9**	115.6±0.8	1193±29	4.37
N_{2D}	is24PLAHA	**5.6**	104.1±0.8	2169±96	4.65
Air	is24PLAHA	**5.6**	98.8±0.5	737±9	3.51

4.5. Influence of HANP coating

The importance of coating novel dispersants onto nanoparticles *in situ* in the hydrothermal synthesis rig was demonstrated in a comparative experiment where 2.5 wt% uncoated HANP plates and 0.28 wt% pre-hydrolysed DDSA (HDDSA), equivalent in composition to the 2.8 wt%

DDSAHA, were added separately to the PLA in the compounder. This control experiment, illustrated in Figure 4.14 with recirculation data summarised in Table 4.9, displayed the same significant decrease in τ_{w0}, $t_{1/2}$ and E_{mix} observed with the addition of uncoated HANP on their own [140]. The increase in $t_{1/2}$ observed for 2.8 wt% DDSAHA relative to its control infers that the dispersant coating was initially adhered to the HANP particles but also promotes HANP dispersion.

The influence of other dispersants can be found in Section 4.6 in Table 4.10.

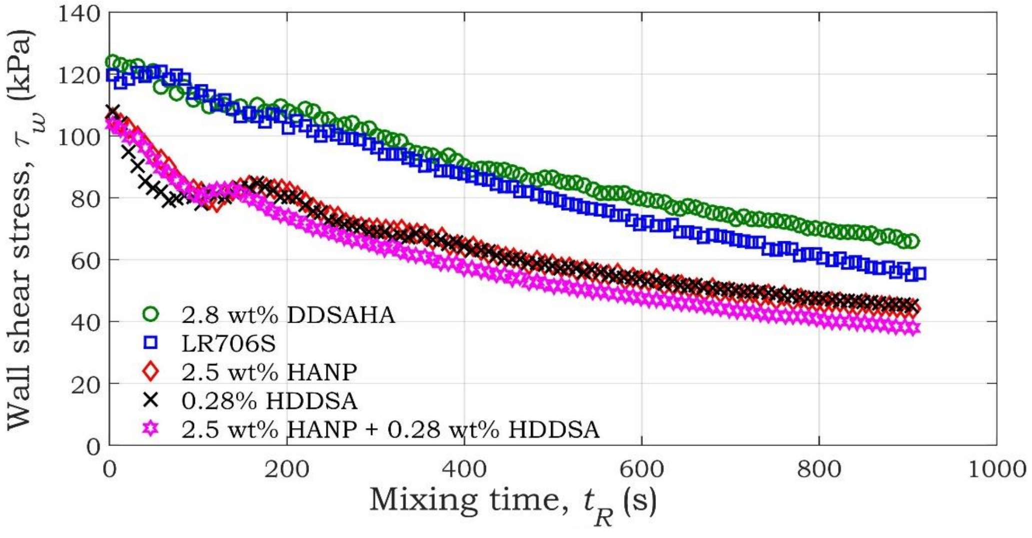

(a)

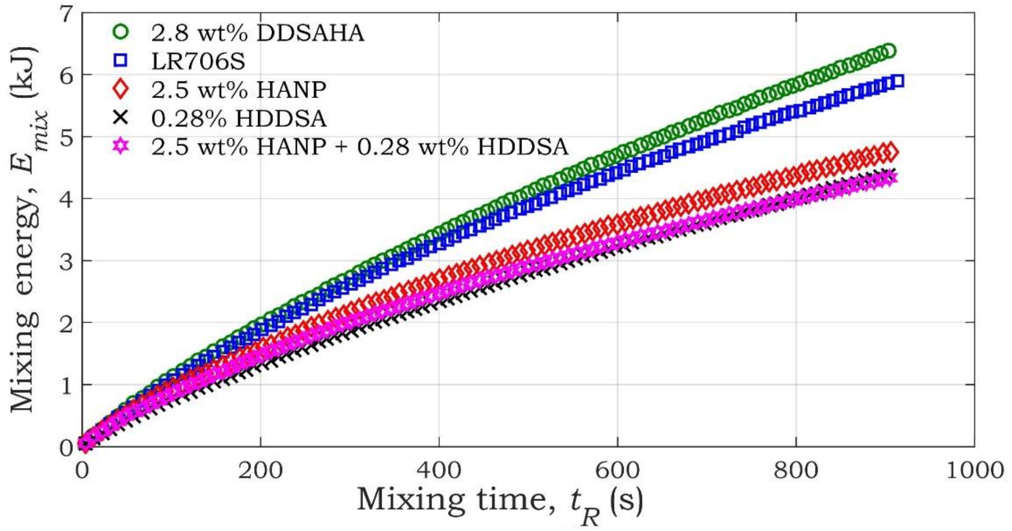

(b)

Figure 4.14. Difference in mixing of LR706S with DDSAHA coated during particle synthesis versus mixing of HANP and HDDSA during compounding in Air at 210 °C and 50 rpm for 15 min presented as (a) τ_w and (b) E_{mix}.

Table 4.9. Summary of compounding of DDSAHA-LR706S and its constituents in Air at 210 °C and 50 rpm for 15 min.

Gas	Material	HANP [wt%]	τ_{w0} [kPa]	$t_{1/2}$ [s]	E_{mix} [kJ] at t_R = 10 min
Air	LR706S	-	124.3 ±0.8	782 ±13	4.43
Air	HANP plate	**2.5**	96.1 ±0.7	727 ±14	3.60
Air	HDDSA	**0.28**	91.7 ±0.7	805 ±17	3.23
Air	HANP plate + HDDSA	**2.5+0.28**	94.6 ±0.7	613 ±9	3.29
Air	DDSAHA	**2.8**	122.7 ±0.8	981 ±21	4.71

4.6. Effect of HANP loading content

Preliminary compounding experiments were carried out in Air at 210 °C and 50 rpm for 15 min with 1-20 wt% uncoated HANP plates (within the amount range of nHA processed by Wilberforce et al. [20] and Delabarde et al. [88]), illustrated in Figure 4.15, and 2.5 wt% HANP rods and coated HANP. They were followed by tests conducted in N_{2D}, with the same mixing parameters, with a range of uncoated and coated HANP with varying wt%, examples of which are illustrated in Figure 4.16. Correlation of $t_{1/2}$ with the HANP loading content is shown in Figure 4.17. For coated HANP in pairs of the same particle type, a low value for wt% is equivalent to 2.5 wt% uncoated HANP, and a high value is equal to 5 wt% plus coating. The complete array of experiments was summarised in Table 4.10 to evaluate the effect of HANP addition on the polymer matrix properties during compounding.

Figure 4.15 shows the measurements of τ_w and E_{mix} as a function of recirculation time for up to 20 wt% of uncoated HANP plates. The addition of an increasing amount of uncoated HANP plates to LR706S caused a significant decrease of τ_{w0}, $t_{1/2}$ and E_{mix}. Only for 1 wt% HANP plates was $t_{1/2}$ greater, by 16.5%, than that for neat LR706S in Air while τ_{w0} and E_{mix} remained in the same order of magnitude. Similarly, for 2.8 wt% DDSAHA mixed with LR706S in Air, $t_{1/2}$ was longer by 20.3% when compared with PLA only, see Table 4.7 and Table 4.10 for exact values.

In contrast, for 5.6 wt% DDSAHA, $t_{1/2}$ shorted by 42.5% relative to that measured for the neat polymer. It was therefore hypothesized that small quantities of HANP disperse in the polymer matrix aiding melt properties of LR706S in Air. In contrast, above 1 wt% HANP plates and 2.5 wt% coated HANP it was presumed aggregates create additional shear and increase melt moisture which accelerates degradation of PLA.

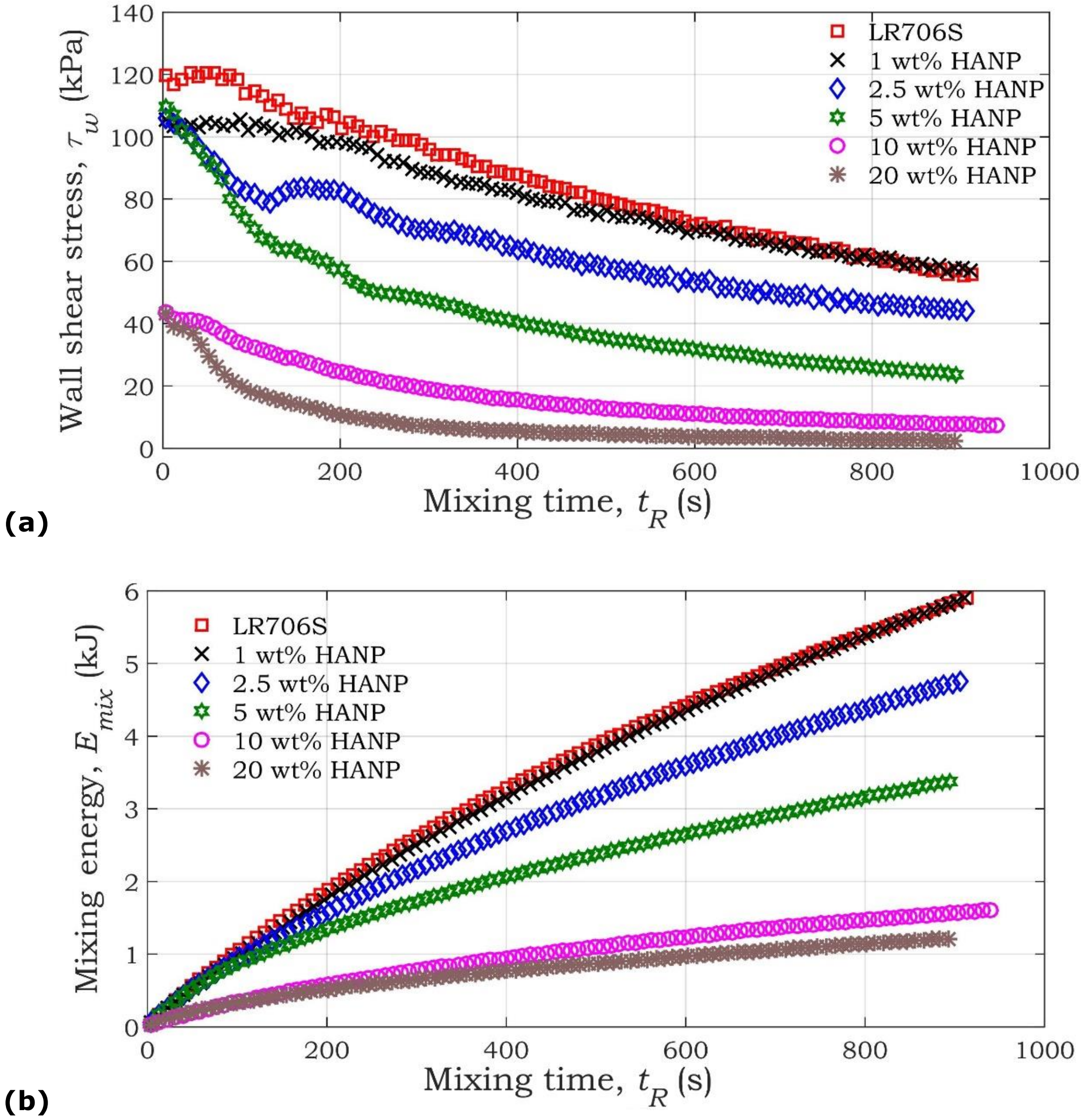

Figure 4.15. Compounding of 1 - 20 wt% plate HANP with LR706S in Air at 210 °C and 50 rpm for ~15 min presented as (a) τ_w and (b) E_{mix}.

Figure 4.16 shows measurements of τ_w and E_{mix} when compounding in N_{2D} for a selection of nanocomposites from Table 4.10. The addition of 7.2 wt% is16PLAHA to LR706S in comparison to 3.6 wt% is16PLAHA leads to a significant decrease in $t_{1/2}$. Numerically, $t_{1/2}$ reduced by 57.7%

after increasing the amount of HANP, which is probably indicative of inferior HANP dispersion or more prominent degradation of the particle coating causing further degradation of LR706S. The same figure illustrates also recirculation of up to 10 wt% HANP rods, where 2.5 wt% and 5 wt% appear very similar. However, analysing the numerical values provided in Table 4.10 reveals that actually with a greater amount of rods, τ_{w0} increased and $t_{1/2}$ decreased while E_{mix} remained comparable: τ_{w0} increased by 4% and $t_{1/2}$ decreased by 66.9% when the amount of rods changed from 2.5 wt% to 5 wt%, and τ_{w0} raised by an additional 3.9% while $t_{1/2}$ declined further by 37.9% for 10 wt% rods.

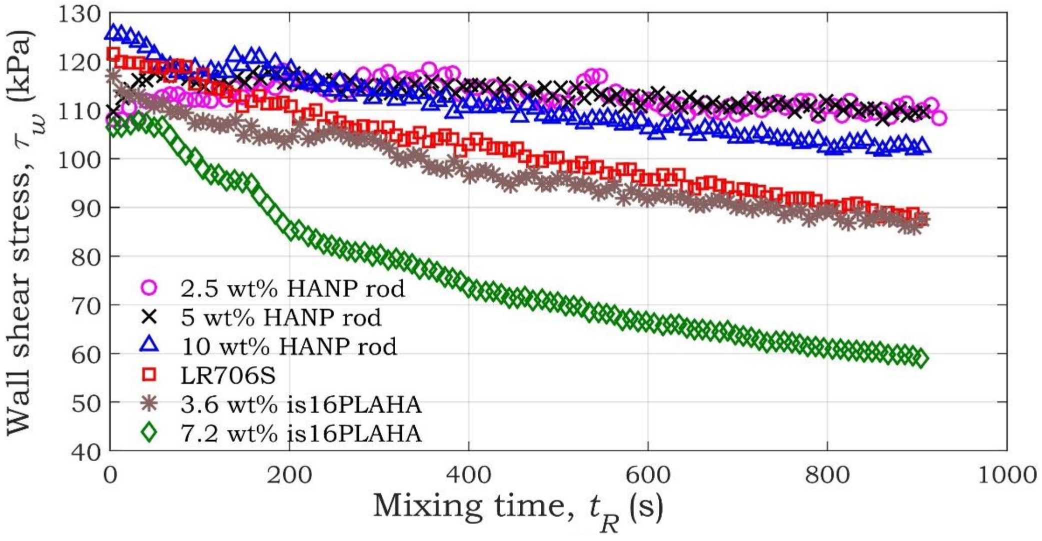

(a)

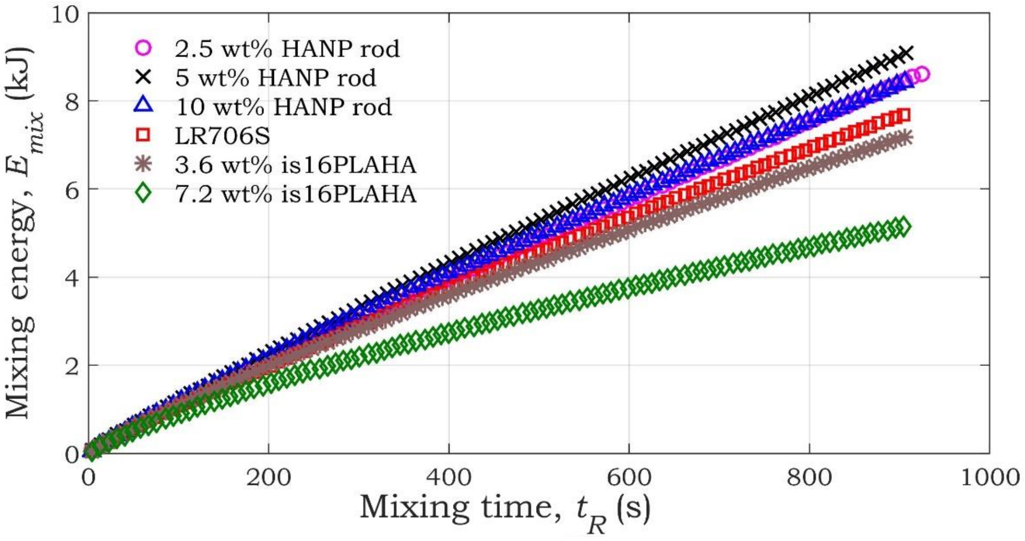

(b)

Figure 4.16. Compounding of rod HANP and is16PLAHA with LR706S in N_{2D} at 210 °C and 50 rpm for 15 min presented as (a) τ_w, with ordinate range between 40-130 kPa for improved clarity, and (b) E_{mix}.

Table 4.10. Summary of increasing loading content of various HANP compounded with LR706S at 210 °C and 50 rpm for 15 min in Air and N_{2D}. For all coated HANP lower wt% is equivalent to 2.5 wt% HANP and higher value to 5 wt%.

Gas	Material	HANP [wt%]	τ_{w0} [kPa]	$t_{1/2}$ [s]	E_{mix} [kJ] at t_R = 10 min
Air	LR706S	**-**	124.3±0.8	782±13	4.43
Air	HANP plate	**1**	110.3±0.8	936±20	4.36
Air	HANP plate	**2.5**	96.1±0.7	727±14	3.60
Air	HANP plate	**5**	91.2±1.1	374±8	2.65
Air	HANP plate	**10**	41.0±0.3	309±4	1.24
Air	HANP plate	**20**	38.9±0.7	122±3	0.97
Air	DDSAHA	**2.8**	122.7±0.8	981±21	4.71
Air	DDSAHA	**5.6**	86.9±0.7	450±6	2.49
N_{2D}	LR706S	**-**	119.0±0.7	1983±69	5.39
N_{2D}	HANP rod	**2.5**	114.7±0.7	17209±3801	5.77
N_{2D}	HANP rod	**5**	117.0±0.6	9766±1187	6.24
N_{2D}	HANP rod	**10**	121.9±0.7	3236±161	5.85
N_{2D}	HANP plate	**2.5**	113.6±0.6	15212±2818	5.89
N_{2D}	HANP plate	**5**	113.4±0.7	1756±55	5.04
N_{2D}	HANP plate	**10**	107.9±0.9	1145±34	4.56
N_{2D}	is16PLAHA	**3.6**	111.7±0.7	2296±95	5.08
N_{2D}	is16PLAHA	**7.2**	103.3±0.7	971±20	3.76
N_{2D}	is24PLAHA	**5.6**	104.1±0.8	2169±96	4.65
N_{2D}	is24PLAHA	**11.1**	86.0±0.7	735±15	3.02
N_{2D}	DDSAHA	**2.8**	104.8±0.8	1601±56	4.06
N_{2D}	DDSAHA	**5.6**	92.9±0.7	729±13	3.00
N_{2D}	starPLAHA	**3.85**	109.4±0.7	1504±46	4.30
N_{2D}	starPLAHA	**7.7**	99.1±0.8	620±12	3.08

Nevertheless, $t_{1/2}$ and E_{mix} for all rod HANP-LR706S in N_{2D} were greater when compared with respective wt% of uncoated and coated HANP. This infers that rods dispersed better than other HANP in the polymer matrix and improved its $t_{1/2}$, as shown in Figure 4.17.

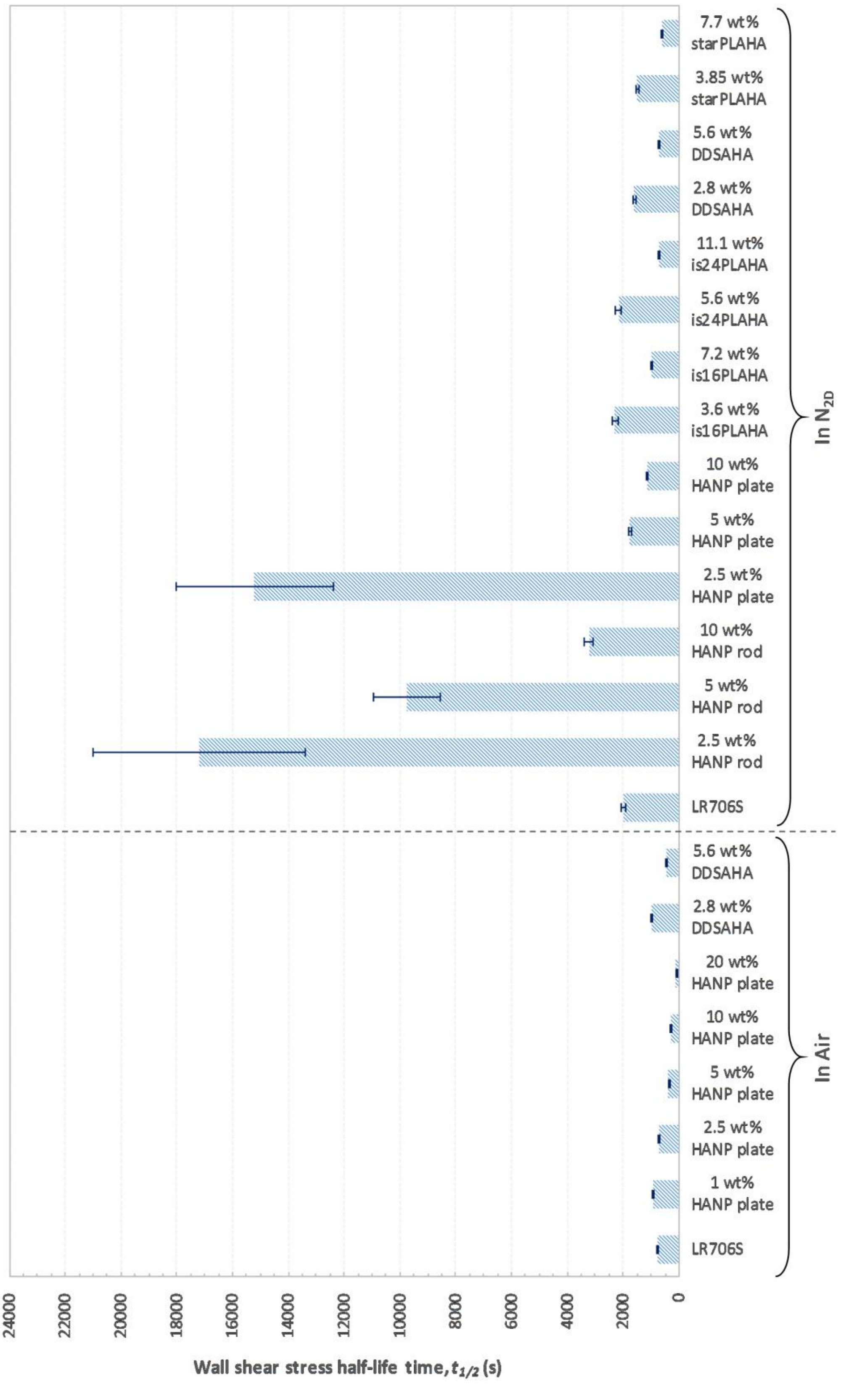

Figure 4.17. Dependence of $t_{1/2}$ on loading content of various HANP compounded with LR706S in Air and N_{2D}. For all coated HANP lower wt% is equivalent to 2.5 wt% HANP and higher value to 5 wt%.

Additionally, nanocomposites with coated particles, namely 3.6 wt% is16PLAHA and 5.6 wt% is24PLAHA in N_{2D} (both wt% equivalent to 2.5 wt% of uncoated HANP), had longer $t_{1/2}$ than neat LR706S by 13.6% and 8.6%, respectively. However, $t_{1/2}$ decreased for 3.6 wt% is16PLAHA by 84.9% and by 85.7% for 5.6 wt% is24PLAHA, along with a decrease in τ_{w0} and E_{mix}, when compared with 2.5 wt% HANP plates. This implies that at HANP loadings up to 2.5 wt% under N_{2D}, uncoated plates enhanced melt properties to a greater extent when compared with coated particles.

4.7. Influence of HANP shape

The effect of HANP morphology on LR706S melt properties is investigated in this section. Figure 4.18 shows 2.5 wt% rod and plate HANP to illustrate the effect of particle morphology on compounding in Air. HANP rod yielded a greater $\tau_{w0,}$ $t_{1/2}$ and E_{mix}, summarised in Table 4.11. In particular, $t_{1/2}$ was longer by 20% for HANP rods when compared with HANP plates, which may imply that a better particle dispersion was achieved limiting matrix degradation.

A similar trend was observed for the compounding of 2.5 – 10 wt% of HANP rods and plates with LR706S in N_{2D} as summarised in Table 4.10. HANP rods again displayed greater $\tau_{w0,}$ $t_{1/2}$ and E_{mix} values when compared to plates for corresponding wt%, e.g. for 5 wt% they were higher by 3.1%, 82% and 19.2% respectively. In principle the greatest changes were observed for $t_{1/2}$, where for HANP plates above 2.5 wt%, it decreased below the magnitude for neat LR706S in N_{2D}. For 10 wt% HANP rods, $t_{1/2}$ decreased by 81.2% when compared with 2.5 wt% yet it was still 38.7% higher than that for polymer only. This infers significantly less matrix decomposition when compounded with HANP rods. A probable explanation is the occurrence of delayed thermal degradation of PLA due to superior dispersion of HANP rod particles. Additionally, HANP plate agglomerates would be expected to act as micro-sized clusters due to the relatively large dimensions of a single particle as mentioned in Section 3.1.2. Furthermore, increasing agglomeration of plates with the loading content of HANP would change properties of the material from nanocomposite to microcomposite which was most likely exhibited in Figure 4.15.

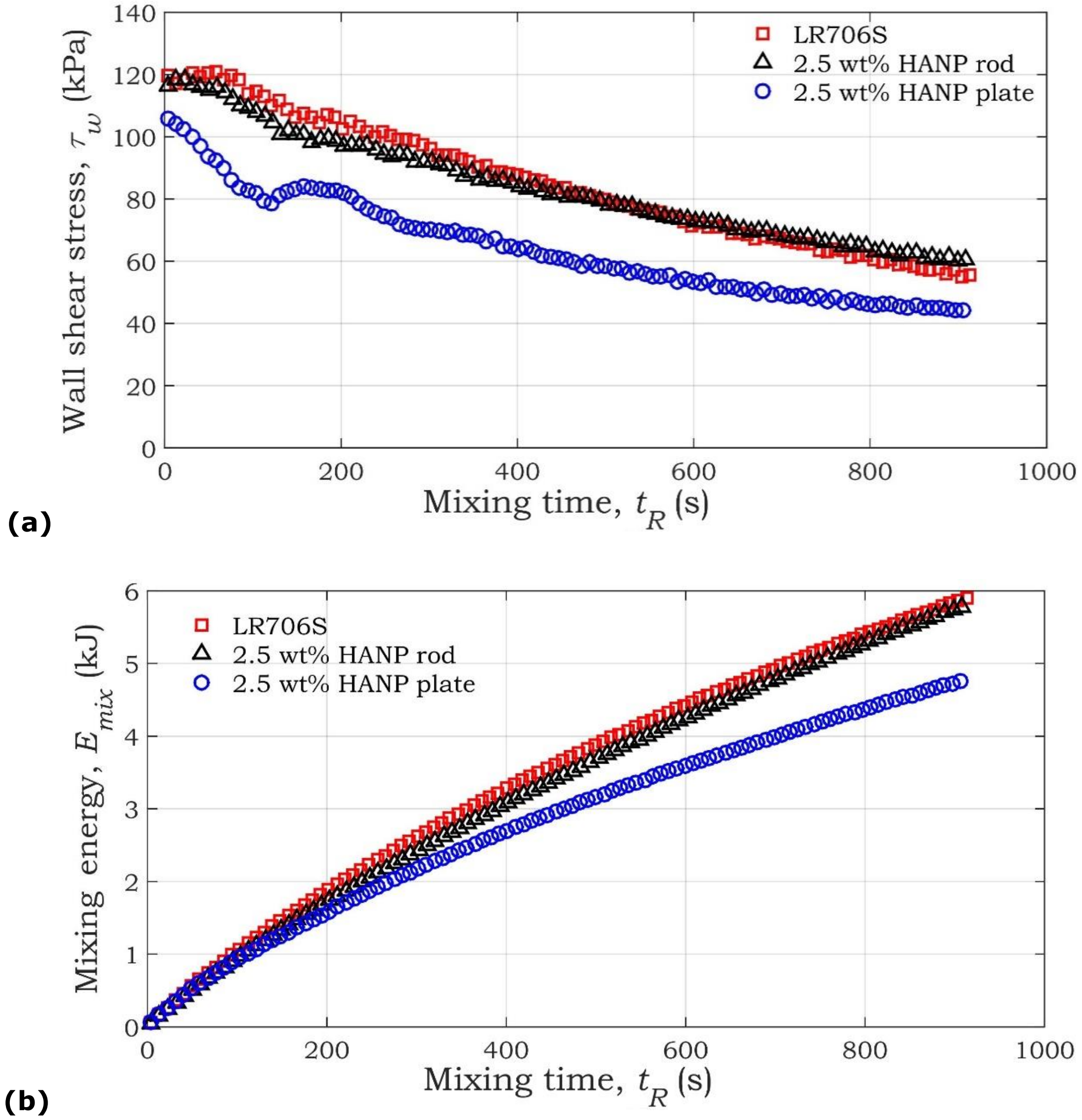

Figure 4.18. Compounding of rod and plate HANP with LR706S in Air at 210 °C and 50 rpm for 15 min presented as (a) τ_w and (b) E_{mix}.

Table 4.11. Compounding of various shapes of HANP with LR706S in Air at 210 °C and 50 rpm for 15 min.

Gas	Material	HANP [wt%]	τ_{w0} [kPa]	$t_{1/2}$ [s]	E_{mix} [kJ] at t_R = 10 min
Air	LR706S	**-**	124.3 ± 0.8	782 ± 13	4.43
Air	HANP rod	**2.5**	116.1 ± 0.8	908 ± 19	4.25
Air	HANP plate	**2.5**	96.1 ± 0.7	727 ± 14	3.60

4.8. Melt rheology and extruder analysis

Capillary rheometry measurements, described in Section 3.2.8, were carried out with PLA and PS to obtain viscosity of the materials and low speed degradation tests were performed to investigate sample viscosity degradation over time. From parameters obtained from power law fitting of the viscosity results, volumetric flow rate in the MiniLab was calculated and used to approximate the number of times material was recirculating in the extruder.

4.8.1. Power-law and Carreau model

Only simple fluids have a constant Newtonian viscosity. Polymers are often modelled as power-law fluids whose relationship is given by

$$\tau = C\,\dot{\gamma}^{n} \tag{4.10}$$

where *C* is the flow consistency index (in Pa.s^n) and *n* is the power law index. Substituting Equation (4.10) into Equation (3.6) gives the viscosity as a power law function of $\dot{\gamma}$:

$$\eta = C\,\dot{\gamma}^{n-1} \tag{4.11}$$

Substitution of Equation (3.2) into Equation (4.10) gives:

$$\frac{h_{ML}\,\Delta P}{2\,l_{ML}} = C\,\dot{\gamma}^{n} \tag{4.12}$$

As $\dot{\gamma}$ is a function of velocity *v*:

$$\dot{\gamma} = \frac{dv}{dy} \tag{4.13}$$

the following relation is obtained:

$$\frac{h_{ML}\,\Delta P}{2\,l_{ML}} = C\left(\frac{dv}{dy}\right)^{n} \tag{4.14}$$

which is integrated for power law fluids to find the relation between *Q* and *ΔP* [139]:

$$\frac{h_{ML}\,\Delta P}{2\,l_{ML}} = C\left(\frac{2n+1}{3n}\,\frac{6Q}{w_{ML}\,{h_{ML}}^{2}}\right)^{n} \tag{4.15}$$

Subsequently, the following equation for Q (in cm^3.s^{-1}) is obtained:

$$Q = \frac{n\,w_{ML}\,{h_{ML}}^{2}}{2\,(2n+1)}\left[\frac{h_{ML}\,\Delta P}{2\,C\,l_{ML}}\right]^{\frac{1}{n}} \tag{4.16}$$

Substituting Equation (4.16) with *C* and *n*, acquired experimentally from rheometry, enables the calculation of *Q* within the back-flow channel which finally can be used to approximate the number of times material is recirculating in the extruder, *N*:

$$N = \frac{Q\;60\;t_R}{V_L} \tag{4.17}$$

To obtain the required power law coefficients, firstly, viscosity measured in the capillary rheometer is fitted with the Carreau-Yasuda model [158] across the whole range of acquired data:

$$\frac{\eta - \eta_\infty}{\eta_0 - \eta_\infty} = [1 + (\lambda\,\dot{\gamma})^2]^{\frac{n-1}{2}} \tag{4.18}$$

where η_0 is the viscosity at zero shear rate, η_∞ is the viscosity at infinite shear rate and λ is the relaxation time in seconds. As η_∞ is generally very low in magnitude and difficult to determine experimentally it is assumed that $\eta_\infty = 0$. The Carreau-Yasuda model then simplifies to the Carreau model:

$$\eta = \eta_0\,[1 + (\lambda\,\dot{\gamma})^2]^{\frac{n-1}{2}} \tag{4.19}$$

Secondly, using Equation (4.19) along with τ_w values obtained from the MiniLab, the viscosity is calculated for material recirculating in the back flow channel. For high shear rates, i.e. those satisfying the condition $\lambda\,\dot{\gamma} >> 1$, the Carreau model reduces to the power law model, see Equation (4.11):

$$\eta = \eta_0\;\lambda^{n-1}\;\dot{\gamma}^{n-1} \tag{4.20}$$

with $C = \eta_0\;\lambda^{n-1}$.

Lastly, the calculated power law coefficients are used in Equation (4.17) to obtain N.

4.8.2. Recirculation of polymers in MiniLab

The method outlined in Section 4.8.1 is presented in Figure 4.19 on an example of LR706S at 210 °C. A PLA recirculation test in the MiniLab in capillary mode with increasing n_s (described in Section 3.2.2.2), which caused increase of τ_w, was compared with the viscosity measurement in the capillary rheometer with increasing $\dot{\gamma}$ through the Carreau model. This was optimised with the Solver function in Excel where the error was defined as the square of the difference between the viscosity measured in the capillary rheometer and the viscosity calculated with the Carreau model. This was summed for all acquired points and was set as the minimum value objective for changing Carreau model parameters. Using the line fit in Figure 4.19(a) τ_w at 50 rpm was found, chosen for the main processing screw speed in the MiniLab, which was correlated with respective $\dot{\gamma}$ and η in Figure 4.19(b). Finally, the applied Carreau model was simplified to the power law model using Equation (4.20) to estimate N for LR706S mixed in the MiniLab at 50 rpm. This is acceptable as in the MiniLab the shear rate is high and the assumption that it is always higher than the transition of the Carreau model.

This procedure was also applied to 2003D and PS recirculated in the MiniLab in capillary mode. The measurements were fitted with the Carreau model based on capillary rheometry data, all shown in Figure 4.20. Curves for $\eta(\dot{\gamma})$ were arranged from 2003D to LR706S with growing viscosity according to the increasing molecular weight of polymers. The $\dot{\gamma}$ was increasing with rising n_s applied in the MiniLab and raising pistons speed in the capillary rheometer. As expected, a lower processing temperature of 200 °C for PS resulted in higher viscosity when compared with 210 °C run.

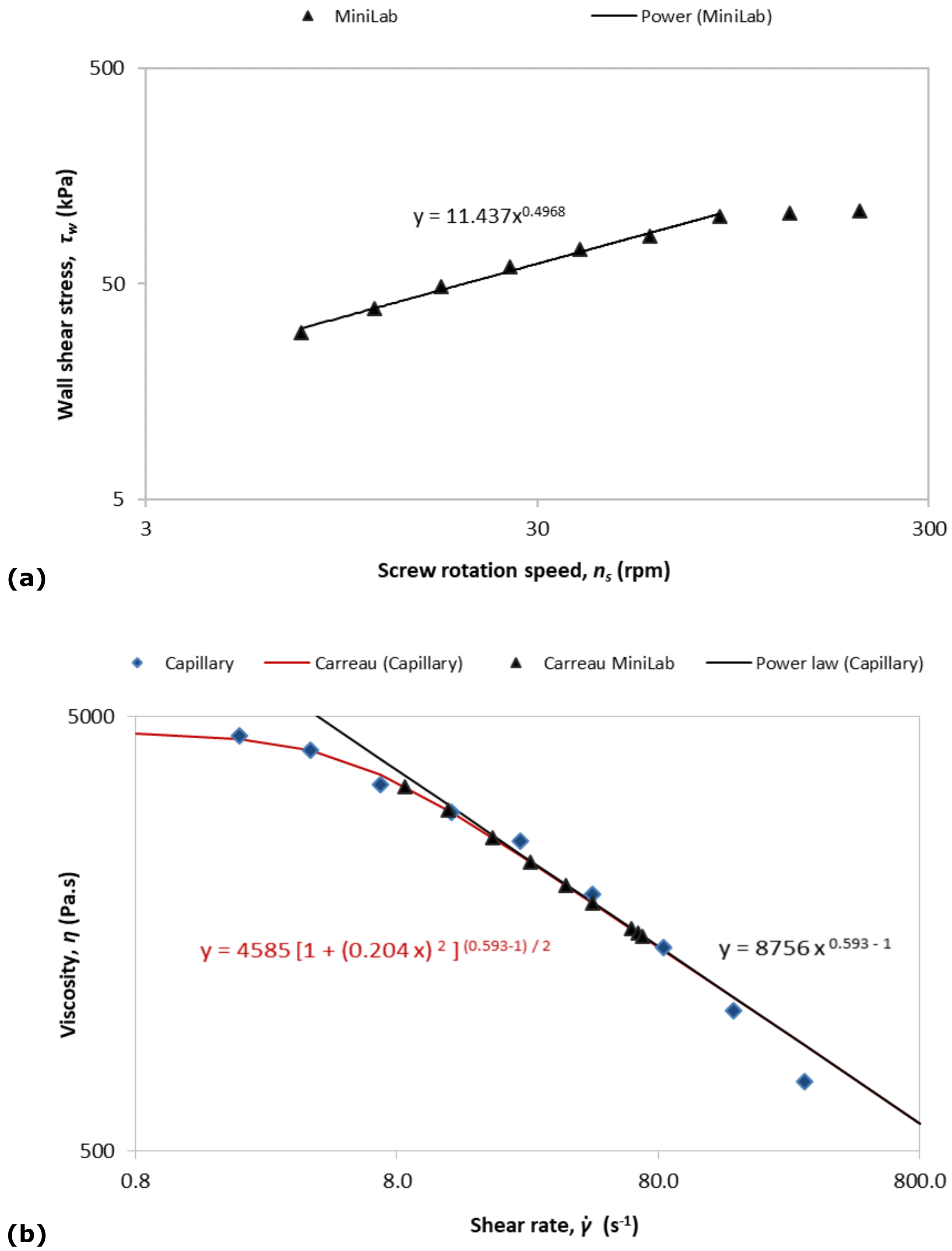

Figure 4.19. Estimation of LR706S viscosity at 210 °C in the MiniLab based on: (a) recirculation in the extruder at increasing n_s and (b) capillary rheometry measurements with increasing shear rate.

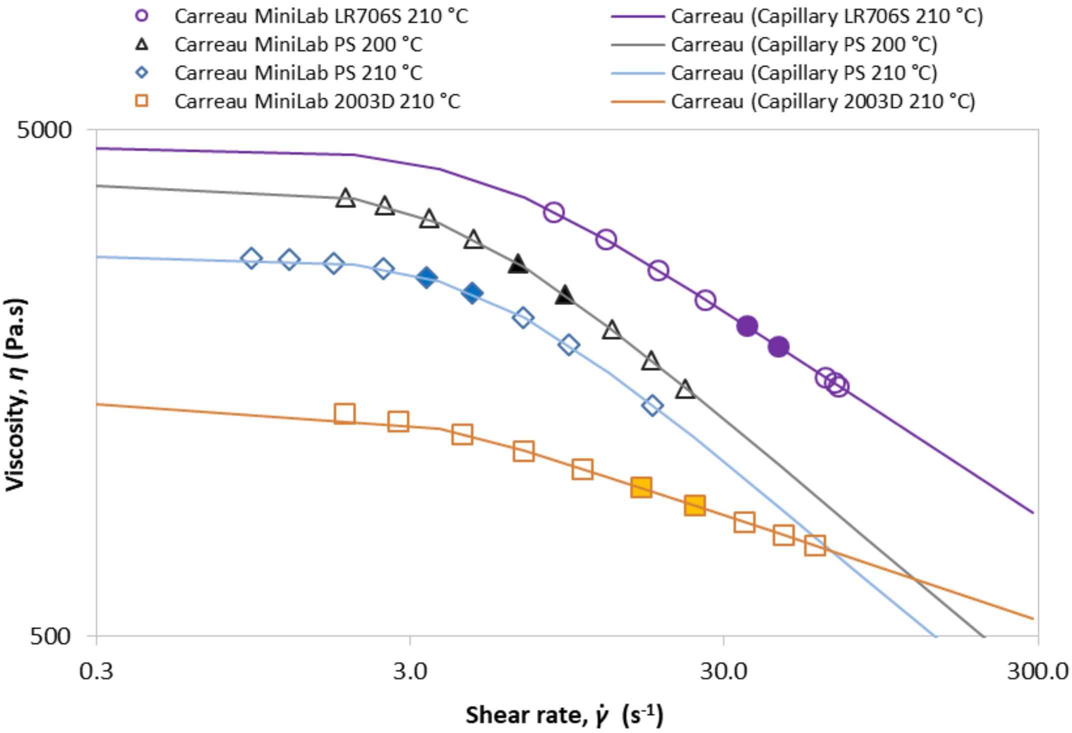

Figure 4.20. Fitting of *η* for polymers recirculated in the MiniLab through the Carreau model based on capillary rheometry measurements, where filled symbols indicate a n_s of 38.5 rpm (left) and 58 rpm (right).

The obtained power law model coefficients, *C* and *n*, and the calculated values of *Q* and *N*, are listed in Table 4.12 and reflect the 50 rpm point for each polymer. This point is positioned between n_s measured in the MiniLab of 38.5 rpm and 58 rpm, marked with filled shape symbols in Figure 4.20. For most of the tested polymers, the 50 rpm point was in the power law region of the $\eta(\dot{\gamma})$ curve with the exception of PS at 210 °C where it shifted to the transition area. For this reason, the applied power law model coefficients (from the simplified Carreau model) reflected *Q* and *N* for PS at 210 °C less accurately.

Table 4.12. *Q* and *N* in the MiniLab for polymers at 50 rpm calculated from power law model applied to capillary rheometry measurements.

Material	Temperature [°C]	*C* [kPa.s^n]	*n*	*Q* [cm^3.s^{-1}]	*N*
LR706S	210	8.76	0.59	0.122	22
PS	200	8.53	0.60	0.021	4
PS	210	8.50	0.60	0.006	1
2003D	210	8.28	0.61	0.073	13

The calculated *N* is directly related to *Q*, as per Equation (4.17), which in turn is proportional to $\dot{\gamma}$ see Equations (4.13) - (4.15). Therefore the lower the shear rate needed to achieve the 50 rpm mark in the MiniLab, the smaller the number of times material is recirculating in the extruder.

4.8.3. Recirculation of nanocomposites in the MiniLab

As *N* is related to the amount of shear experienced by the material in the MiniLab, it can also be a useful measure for both (i) nanoparticle dispersion in the composite and (ii) polymer matrix degradation. Unfortunately, the cost of LR706S and particles and the hire of a larger extruder, which would be used for production of the nanocomposites, and the substantial amount (~60g per run) which is required for capillary rheometry, was a prohibitive factor preventing the performing of direct η measurements of the materials. Therefore an attempt was made to estimate $\dot{\gamma}$ and η of LR706S, 1-10 wt% HANP plate and 2.5 wt% rod nanocomposites mixed in the MiniLab for 15 min at 50 rpm and 210 °C in Air. Note that LR706S capillary rheometry measurements were performed in air only.

For LR706S, for each ΔP point acquired in the MiniLab, $\dot{\gamma}$, *Q* and *N* were calculated using the obtained *C* and *n*, from Table 4.12, and η from the aforementioned Carreau model parameters, see Figure 4.19(b). Following this, average values for *Q* and *N* were calculated for the entire duration of the 15 min run. An assumption was made that for the nanocomposites, *n* remains the same as that for LR706S as the addition of particles would change the material viscosity but not the shear thinning behaviour of the matrix. This was also reflected for PS, were η increased with the decrease of temperature and *C* was different at 200 °C and 210 °C yet *n* remained the same, as quantified in Table 4.12. For all nanocomposites, $\dot{\gamma}$ and η were calculated with the aforementioned power law coefficients obtained for LR706S, e.g. 1 wt% HANP plates in Figure 4.21 which show a good fit within the power law region, and η was also calculated with the Carreau model parameters for LR706S.

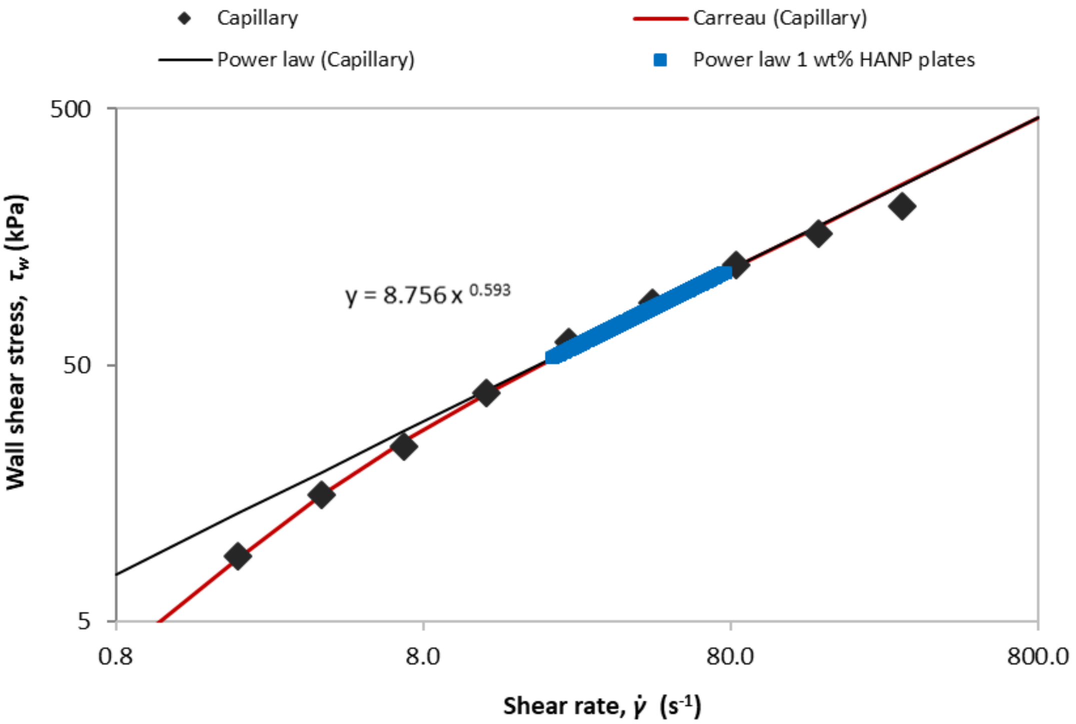

Figure 4.21. Estimation of shear rate for 1 wt% HANP plates based on power law model obtained for LR706S.

New Carreau model parameters *C* and *n* were optimised for the nanocomposites with Solver function in Excel where the error was defined as the square of the difference between viscosity values calculated from both models. This was summed for all acquired points and then set as the minimum value objective for changing *C* and *n*. The $\dot{\gamma}$ and η for nanocomposites were calculated again to correct them by using the new coefficients, see Figure 4.22. The majority of the obtained $\eta(\dot{\gamma})$ curves for nanocomposites lay within the power law range with exception of 5 and 10 wt% HANP plates which partially entered the transition area which made their *Q* and *N* estimation less reliable. Slightly lower η for 5 wt% HANP plates might indicate decrease of $t_{1/2}$ related to viscosity. Substantially lower η for 10 wt% HANP plates, when compared with LR706S and other nanocomposites, suggests further decrease of $t_{1/2}$. This was most likely caused by poorly distributed particles which increased the number of clusters, found in small numbers even at lower wt% of HANP plates, which was observed optically in fractured fragments of the material.

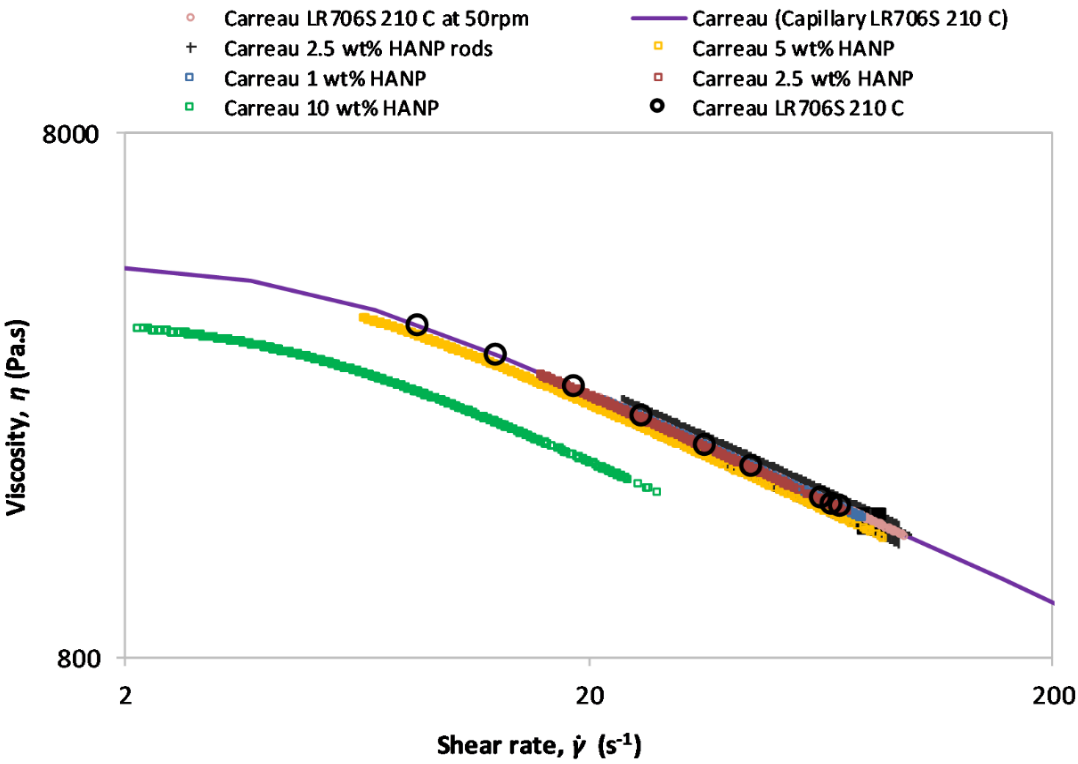

Figure 4.22. Fitting of the Carreau model for estimated viscosity and shear rate of LR706S and 1-10 wt% HANP plate nanocomposites recirculated in the MiniLab for 15 min at 50 rpm.

Table 4.13. *Q* and *N* estimated through power law coefficients for LR706S and nanocomposites compounded in the MiniLab at 50 rpm and 210 °C for 15 min in Air; n was obtained from the unfilled polymer.

Material	HANP [wt%]	*C* [kPa.s^n]	*n*	*Q* [cm^3.s^{-1}]	*N*
LR706S	-	8.76	0.59	0.15	26
HANP rod	2.5	8.72	0.59	0.14	26
HANP plate	1	8.72	0.59	0.13	24
HANP plate	2.5	8.67	0.59	0.09	17
HANP plate	5	8.34	0.59	0.06	10
HANP plate	10	6.46	0.59	0.02	4

Finally, for each nanocomposite, for all *ΔP* points acquired in the MiniLab, *Q* and *N* were calculated, from the obtained *C* and *n*, and averaged for the entire duration of the 15 min run, see Table 4.13. The estimated *Q* and *N* were decreasing with increasing amount of HANP plates that suggests lower pressure drop in the MiniLab due to reduced *η* of nanocomposites (and hence *C*) when compared to pure LR706S which infers less material mixing with more added particles. The obtained parameters for 2.5 wt% HANP rods and 1 wt% HANP plates were similar as their estimated viscosity was also alike, which suggests better dispersion of rods over plates in the polymer matrix.

4.8.4. Low speed degradation

Low speed degradation tests performed for PLA at 210 °C displayed a viscosity change over time e.g. 2003D in Figure 3.13. As η cannot be directly measured in the MiniLab, change of wall shear stress over time was chosen to compare tests carried out in the extruder to those carried out in the capillary rheometer, see Figure 4.23. The τ_w for 2003D at 50 rpm had a similar decay rate over time to the low speed degradation test at a chosen $\dot{\gamma}$ of 18 s^{-1}, reflecting a decline of viscosity measured in the capillary rheometer. In contrast, for LR706S, a decrease of τ_w at 50 rpm was clear yet it was not mirrored in the low speed degradation test at 30 s^{-1}. It was hypothesised that the chosen shear rate of 30 s^{-1} was too low to substantially degrade LR706 to change its viscosity. Another probable explanation was considering air pockets trapped between fine flakes of LR706S, despite packing steps in the capillary rheometer and pressure pre-tests, occasional loud pops were heard, which would explain the unusual fluctuation of τ_w despite a constant $\dot{\gamma}$.

This space is intentionally left blank

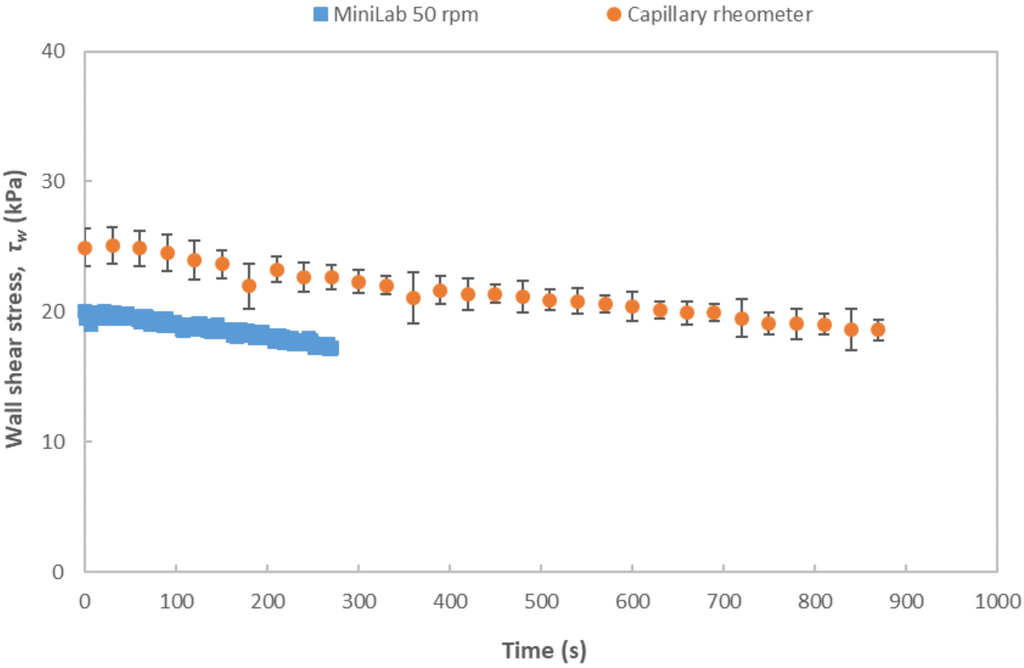

(a)

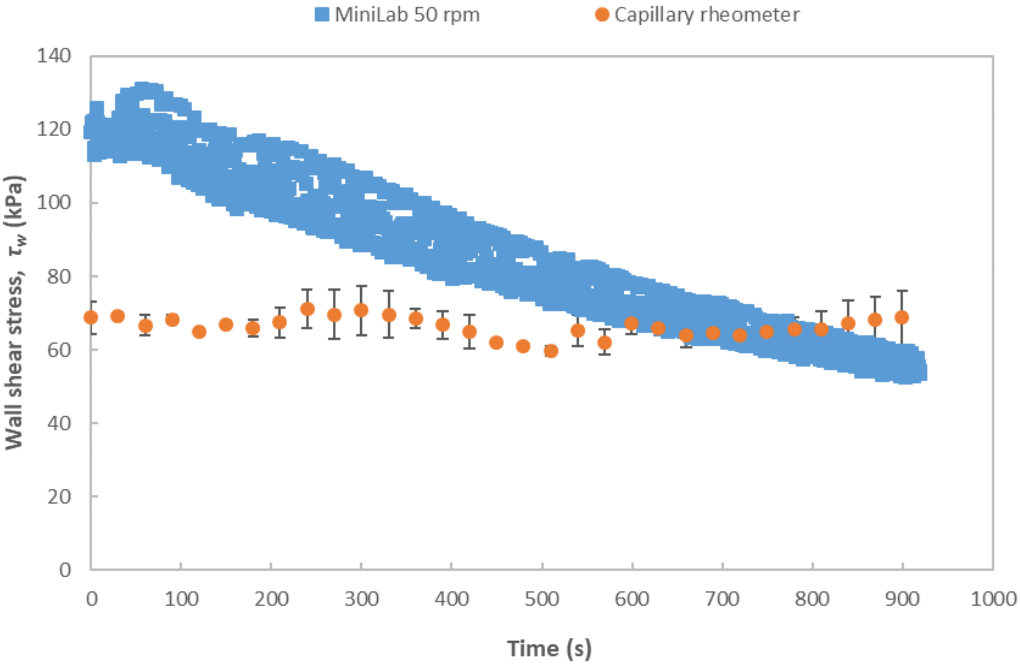

(b)

Figure 4.23. Low speed degradation tests in capillary rheometer at 210 °C for: (a) 2003D at shear rate of 18 s^{-1} and (b) LR706S at 30 s^{-1} compared with respective recirculation in the MiniLab at 50 rpm and 210 °C.

4.9. Conclusions

Nanocomposites were produced by melt compounding coated and uncoated HANP with LR706S. The loading content of HANP and the type of dispersants were varied. Run-to-run variations in the MiniLab extruder occurred predominately due to manual handling and static charge of the nanoparticles. Compounding was mostly carried out for 15 min, in recirculation mode, at 210 °C and 50 rpm due to the MiniLab extruder pressure sensors alarm limits. Note that without this constraint, the optimum speed would be 100 rpm. The experiments which were performed showed that, beyond drying the polymer and fillers, drying of the bottled N_2 was essential to maintain high $t_{1/2}$ during mixing which indicates high molecular weight of PLA. Compounding of HANP and LR706S with shear above 100 rpm led to a shorter half-life, which might infer mechanical degradation of the polymer. This shortening of $t_{1/2}$ could not be compensated by the beneficial influence of inert gas and the addition of dry HANP.

The addition of uncoated HANP plates was found to decrease τ_w, $t_{1/2}$ and E_{mix} during compounding in Air, when compared with LR706S only, with the exception of 1 wt% loading. In contrast, the addition of coated HANP (equivalent to 2.5 wt%) with tailored dispersants was found to increase $t_{1/2}$ during compounding in Air.

The effectiveness of novel tailored dispersants, when coated onto HANP, and nanoparticle morphology was also investigated during mixing under dried bottled N_2. For all 2.5 – 10 wt% rod HANP-LR706S nanocomposites compounded in N_{2D}, $t_{1/2}$ and E_{mix} were greater when compared with respective wt% of uncoated and coated HANP plates.

The Carreau model, which reduced to a power law model for high shear rates, was fitted to capillary rheometry measurements. The model was used to estimate volumetric flow rate and the number of times a material was recirculating in the MiniLab over a 15 min run at 210 °C and 50 rpm. The obtained Q and N were seen to decrease with increasing amounts of HANP plates due to reduced η of nanocomposites, predicted via the model, when compared to pure LR706S. For 2.5 wt% HANP rods and 1 wt% HANP plates, *Q* and *N* were similar as their approximated viscosity was also alike, despite higher quantity of HANP rods in PLA, which suggests better dispersion of rods over plates in the polymer matrix.

In the next chapter molecular weight measurements will correlate the aforementioned results with matrix degradation.

5. Changing Matrix Properties

Melt processing of polylactic acid inevitably compromises properties of the polymer. In this chapter, the influence of extrusion parameters and the inclusion of varying contents of several HANP on LR706S was evaluated through changes in glass transition temperature, degradation temperature (at 5% weight loss), mechanical properties and molecular weight change.

5.1. Molar mass distribution

Changes in the molecular weight of LR706S were measured after melt processing with GPC as described in Section 3.2.6. All plotted results were normalised versus M_w of neat LR706S (M_{w0}) of 405.5 kg.mol^{-1} (±15.6 kg.mol^{-1}). Finally, a rheological model [28] was applied in an attempt to separate thermal and shear effects of melt processing on the polymer matrix.

5.1.1. Influence of HANP on polymer degradation

Compounding of HANP with LR706S altered M_w of the polymer. All materials mixed in the MiniLab at 210 °C with various n_s, t_R in Air or inert gas are summarised in Figure 5.1. Firstly, nanocomposites were ordered according to HANP loading and grouped in relation to compounding atmosphere, shown in Figure 5.1(a), to find their influence on M_w. The lowest molecular weight was found for nanocomposites compounded in Air with 10 wt% HANP, while the greatest M_w was achieved for HANP rod nanocomposites compounded in N_{2D}, particularly at 2.5 wt%.

Next, molecular weight of materials was plotted against the $t_{1/2}$ value, first introduced in Section 4.1, shown in Figure 5.1(b). The $t_{1/2}$ was used as viscosity measurements of the nanocomposites were not conducted due to prohibitively high cost of LR706S and HANP mentioned earlier. A power law trendline was fitted and gave proportion of $t_{1/2} \sim (M_w/M_{w0})^{2.2}$ which resembles the $\eta_0 \sim M_w^{3.4}$ relation discussed further in Section 5.1.3. The power law fit highlighted that all HANP rod and 2.5 wt% HANP plate nanocomposites compounded in N_{2D} had exceptionally high $t_{1/2}$, marked in Figure 5.1 with circles, above all the other materials, which infers improved particle dispersion.

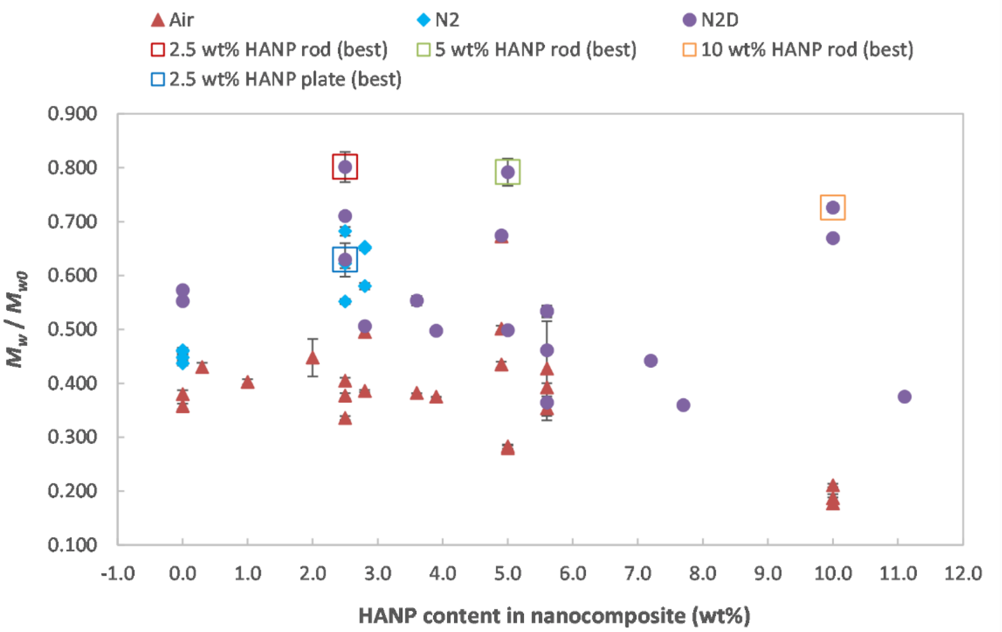

(a)

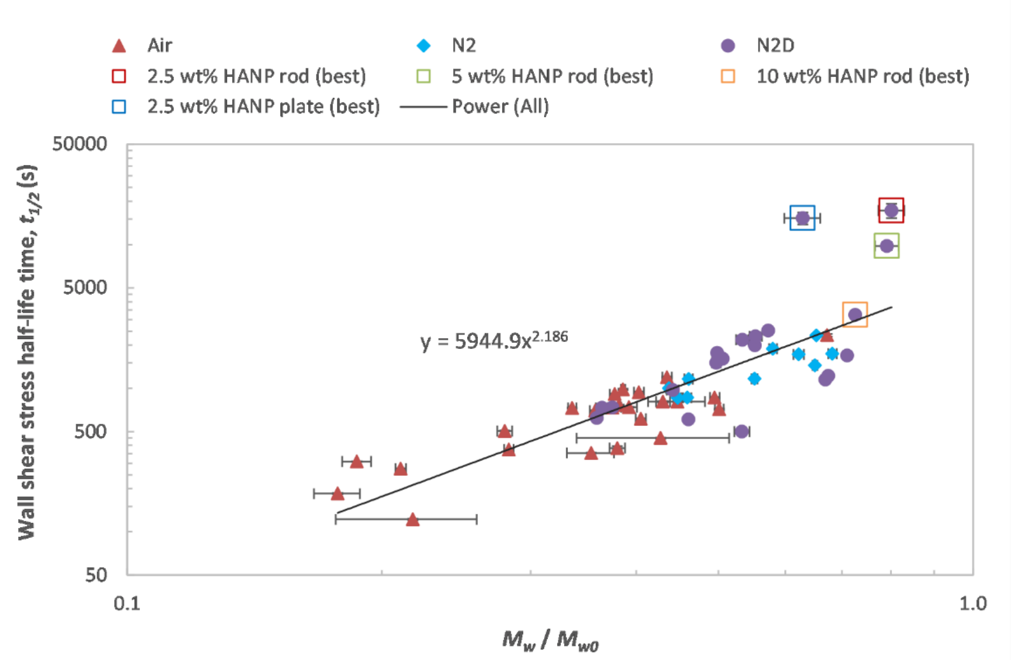

(b)

Figure 5.1. Influence of compounding of HANP with LR706S in the MiniLab at 210 °C on the change in: (a) M_w and b) $t_{1/2}$ in relation to M_w. Where not shown, error bars are smaller than the size of the symbol.

This supports the earlier suggestion in Chapter 4 that $t_{1/2}$ in the MiniLab was not only related to PLA degradation due to decreasing molecular weight but also indicative of HANP dispersion. As the aforementioned nanocomposites exhibited the highest $t_{1/2}$ and M_w they were reviewed separately and compared with materials with coated HANP. The power law trend line fitted in Figure 5.1(b) was reproduced in all subsequent $t_{1/2}$ vs. (M_w/M_{w0}) figures in Sections 5.1.1 and 5.1.2 for comparison purposes.

5.1.1.1. HANP plates

As shown in Figure 5.2(a) processing of 1 wt% HANP plates in Air had a beneficial influence and preserved the M_w of PLA, while increasing loading of particles from 2.5 wt% onwards caused a decline in M_w e.g. for 5 wt% HANP plates M_w decreased by 20.9% in comparison to LR706S extruded in Air. This is consistent with other research on HA-PLA nanocomposites compounded in air where M_w decreased for 5 wt% loadings and above due to increasing particle agglomeration and suspected hydrolytic degradation induced by water in/on the HA [9]. For compounding in N_{2D} an advantageous effect of HANP plates was shown for 2.5 wt% where M_w increased by 9.9% while for 5 wt% M_w decreased by 9.8% versus extruded LR706S. It is therefore hypothesized that, as compounding under N_{2D} substantially decreased the amount of moisture, the M_w of PLA remained higher by inclusion of dry HANP plates with good particle dispersion. Well distributed nanoparticles up to 2.5 wt% possibly had a lubricating effect on polymer melt due to slip between the PLA matrix and HANP plates [159].

For higher filler content, particles were potentially increasingly agglomerated and acted as a microcomposite, which will be further discussed in Chapter 6. This compromised the properties of the PLA, as seen in other research [20]. 10 wt% HANP plates in N_{2D} had unusually high molecular weight to what was expected for this particle loading which even exceeded the molecular weight of 2.5 wt% HANP plates by 6%. The most likely explanation is related to the time of conducting GPC measurements. The majority of material tests were carried out 1-2 years after manufacturing and storage in desiccator, while the molecular weight of 10 wt% HANP plate nanocomposite in N_{2D} was measured a month after extrusion. It is plausible that prolongated storage at room temperature caused further deterioration of molecular weight. This indicates that shelf life of those biodegradable materials needs to be considered during manufacturing of medical devices and their appropriate storage (preferably packed in dry inert gas and kept in a freezer similarly to neat LR706S).

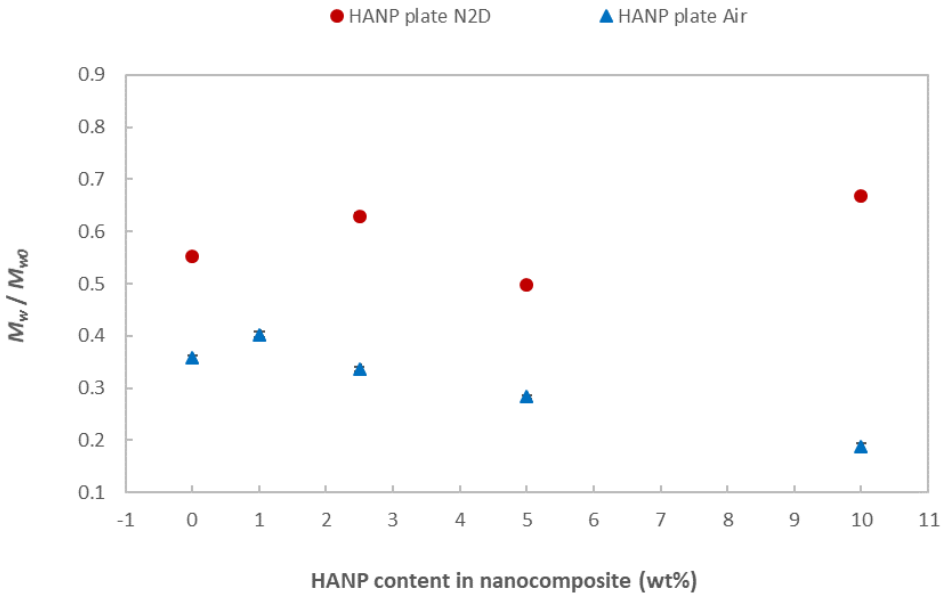

(a)

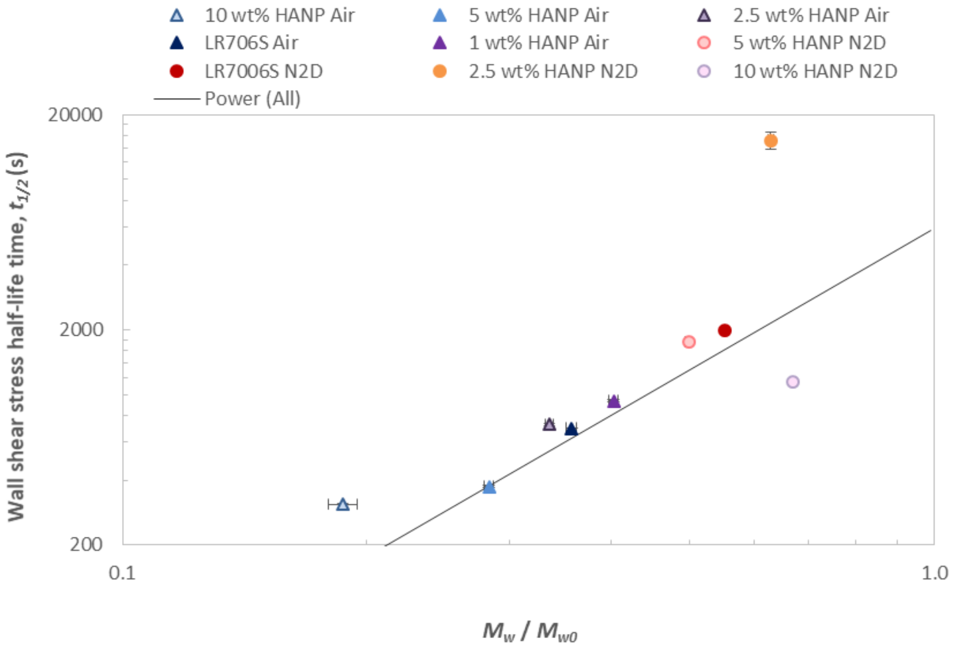

(b)

Figure 5.2. Change in: a) M_w and b) $t_{1/2}$ in relation to M_w of LR706S with addition of HANP plates compounded at 50 rpm, 210 °C in Air and N_{2D} for 15 min. Where not shown, error bars are smaller than the size of the symbol.

HANP plate data in Figure 5.2(b) was plotted along with the power law trend line and a good fit was obtained. The 10 wt% HANP plate nanocomposite in Air had double the $t_{1/2}$ than expected possibly due to improved distribution of particles between shorter polymer chains as M_{w0} reduced by 81.3%. The shorter time span between manufacturing and the GPC measurement meant the M_w of 10 wt% HANP plate compounded in N_{2D} was 1.4 times greater than the trend line value. The $t_{1/2}$ of 2.5 wt% HANP plate nanocomposite in N_{2D} was 7 times higher than the value calculated via the trend line equation which supports a hypothesis of improved particle dispersion when compared with other uncoated HANP plate materials.

Table 5.1. Influence of HANP plates on M_w of LR706S compounded in Air and N_{2D} at 210 °C, 50 rpm for 15 min.

Gas	Material	HANP [wt%]	M_w [kg.mol^{-1}]	M_n [kg.mol^{-1}]	PDI	$t_{1/2}$ [s]
-	LR706S	-	405.5 ±15.6	157.7 ±62.0	3.0 ±1.2	-
N_{2D}	LR706S	-	223.9 ±1.4	91.6 ±2.7	2.4 ±0.1	198 ±35
N_{2D}	HANP plate	2.5	255.1 ±2.2	101.1 ±5.1	2.5 ±0.1	15212 ±1438
N_{2D}	HANP plate	5	202.1 ±1.9	63.5 ±6.7	3.2 ±0.3	1756 ±28
N_{2D}	HANP plate	10	271.3 ±2.2	95.2 ±2.8	2.9 ±0.1	1145 ±17
Air	LR706S	-	145.0 ±2.1	56.0 ±4.0	2.6 ±0.2	698 ±4
Air	HANP plate	1	163.3 ±2.2	62.7 ±3.1	2.6 ±0.2	936 ±10
Air	HANP plate	2.5	136.1 ±1.5	47.3 ±3.1	2.9 ±0.2	727 ±7
Air	HANP plate	5	114.6 ±1.5	38.8 ±0.3	3.0 ±0.1	374 ±4
Air	HANP plate	10	75.8 ±3.0	26.6 ±0.9	2.9 ±0.0	309 ±2

The results plotted in Figure 5.2 for HANP plates are summarised in Table 5.1 along with M_n of the materials. It was observed that M_n decreased at a similar rate to M_w, hence calculated PDI (M_w/M_n) for the majority of materials compounded in the MiniLab for this research had a PDI between 2 and 3. Note that these levels are similar to the 2.6 PDI calculated for neat LR706S.

5.1.1.2. HANP rods

For HANP rods compounded with LR706S in N_{2D}, shown in Figure 5.3(a), M_w of all the nanocomposites remained above the molecular weight of processed PLA regardless of nanoparticle loading and was unquestionably the highest from all materials compounded in the MiniLab. This is consistent with a study by Mathieu et al. [80] about HA-PLA nanocomposites compounded in nitrogen where molecular weight of obtained nanocomposite was higher than of extruded PLA only. For 2.5 wt% HANP rods compounded in Air M_w remained comparable to M_w of processed PLA, while for HANP plates molecular weight already decreased at this particle loading. It demonstrates that HANP rods preserved better molecular weight of LR706S than HANP plates regardless of processing gas. A potential explanation is that HANP rods retain the molecular weight of LR706S more effectively due to greater specific surface area, shown in Table 5.2, and expected improved dispersion, possibly even rods longitudinal alignment with the direction of extrusion [160], protecting polymer chains through increased interactions between HANP and PLA. This infers that well dispersed HANP rods efficiently removed residual moisture, better than HANP plates, and neutralised acidic degradation products of PLA, decreasing reduction of polymer chain length [161].

The data for 2.5 wt% HANP rod nanocomposite in Air and 10 wt% in N_{2D} plotted in Figure 5.3(b) followed the power law trend line together with the respective LR706S reference, while smaller filler loadings in N_{2D} deviated significantly from the fitted regression. The $t_{1/2}$ of 2.5 wt% HANP rod nanocomposite in N_{2D} was the highest from all compounded in the MiniLab materials and it was 4.7 times greater than the $t_{1/2}$ value calculated via the trend line equation. For 5 wt% HANP rod in N_{2D} $t_{1/2}$ achieved a value 2.7 times higher than the calculated one. This supports the earlier assertion that better dispersion of rods, above other compounded HANP, preserved the molecular weight of LR706S. The results plotted in Figure 5.3 for HANP rods are summarised in Table 5.3 along with M_n of the materials.

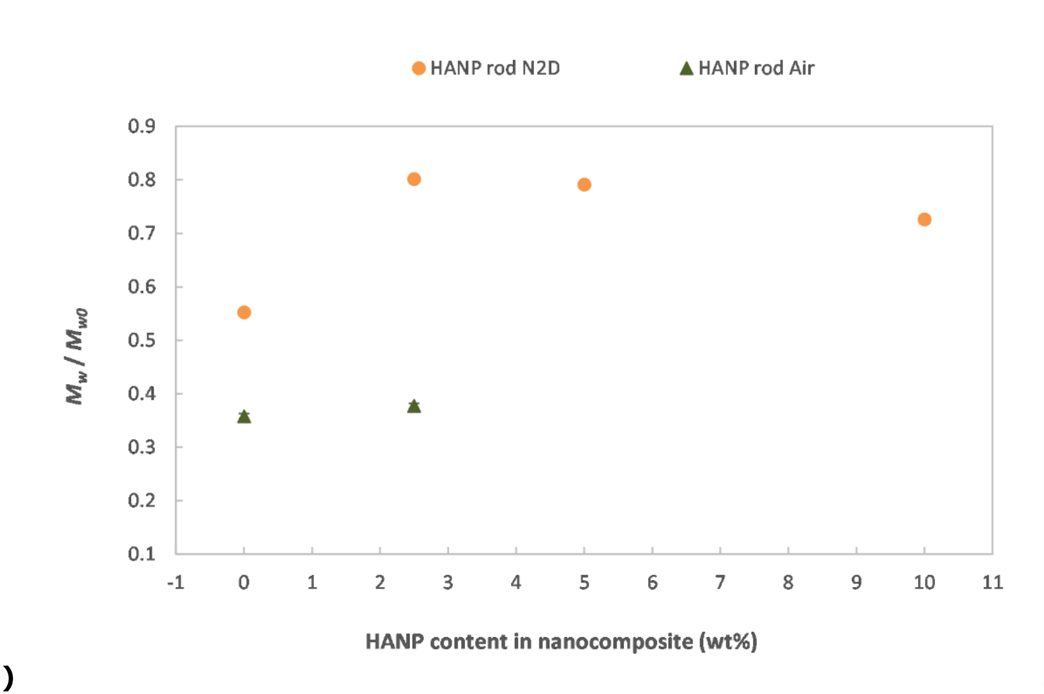

(a)

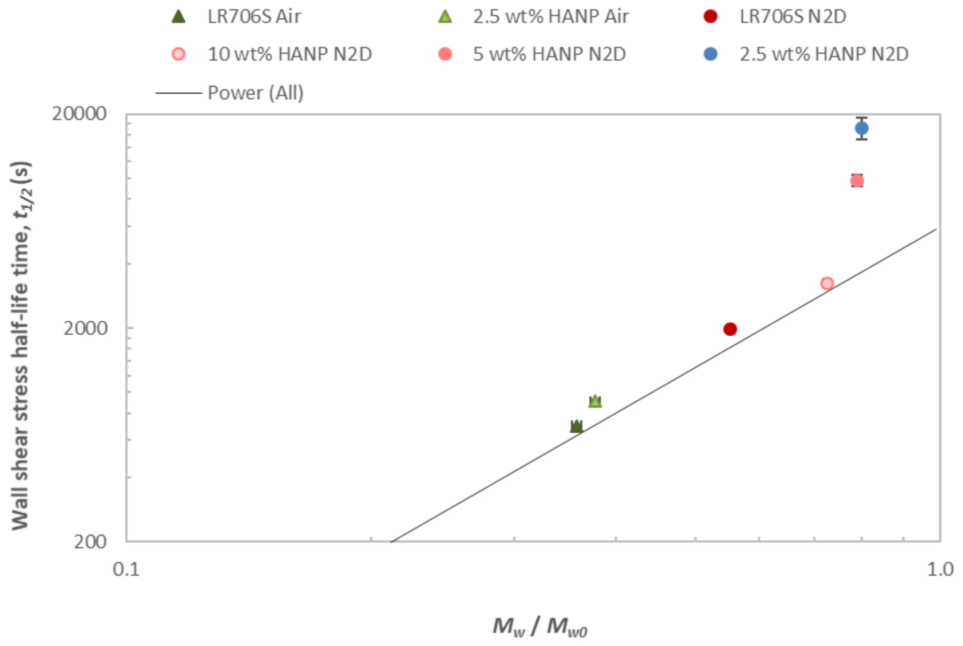

(b)

Figure 5.3. Change of: a) M_w and b) $t_{1/2}$ in relation to M_w of LR706S with addition of HANP rods compounded at 50 rpm, 210 °C in Air and N_{2D} for 15 min. Where not shown, error bars smaller than the size of the symbol.

Table 5.3. Influence of HANP rod on M_w of LR706S compounded in Air and N_{2D} at 210 °C, 50 rpm for 15 min.

Gas	Material	HANP [wt%]	M_w [kg.mol^{-1}]	M_n [kg.mol^{-1}]	PDI	$t_{1/2}$ [s]
N_{2D}	LR706S	-	223.9 ±1.4	91.6 ±2.7	2.4 ±0.1	1983 ±35
N_{2D}	HANP rod	2.5	324.8 ±2.0	139.8 ±6.5	2.3 ±0.1	17209 ±1940
N_{2D}	HANP rod	5	320.8 ±1.8	130.9 ±9.4	2.5 ±0.2	9766 ±606
N_{2D}	HANP rod	10	294.2 ±3.0	114.6 ±11.7	2.6 ±0.3	3236 ±82
Air	LR706S	-	145.0 ±2.1	56.0 ±4.0	2.6 ±0.2	698 ±4
Air	HANP rod	2.5	152.9 ±2.0	58.9 ±5.4	2.6 ±0.2	908 ±10

5.1.1.3. Coated HANP plates

Effectiveness of various coated HANP (with 2.5 wt% of uncoated HANP plates plus coating), described in Section 3.1.3, on protecting M_w of LR706S during compounding in N_{2D} was shown in Figure 5.4 and summarised in Table 5.4. Of all coated particles, only is8PLAHA demonstrated a higher M_w than neat PLA. With is8PLAHA the M_w was 22.1% greater than for neat PLA and was even 7.2% higher than for HANP plates. The nanocomposite with is16PLAHA had M_w comparable to processed PLA while for others M_w was lower than for the neat polymer by 3.4% to 10%. As dispersion of all coated particles was expected to be similar or exceeding HANP plates, see Chapter 6 for more on this, a potential explanation for M_w decrease with the majority of the nanocomposites was decomposition of dispersant during melt compounding. For example, yellowing of 2.8 wt% DDSAHA and 4.9 wt% is8PLAHA nanocomposites extruded in Air was noticed which was more pronounced in the subsequently injection moulded samples, shown in Figure 5.5. On the other hand, as mentioned in Section 3.2.2.1., coated HANP could be only dried at 50 °C in a vacuum oven for 3 h so as to avoid thermal decomposition of the dispersants, which could potentially leave residual moisture that lowered M_w of LR706S due to hydrolytic degradation.

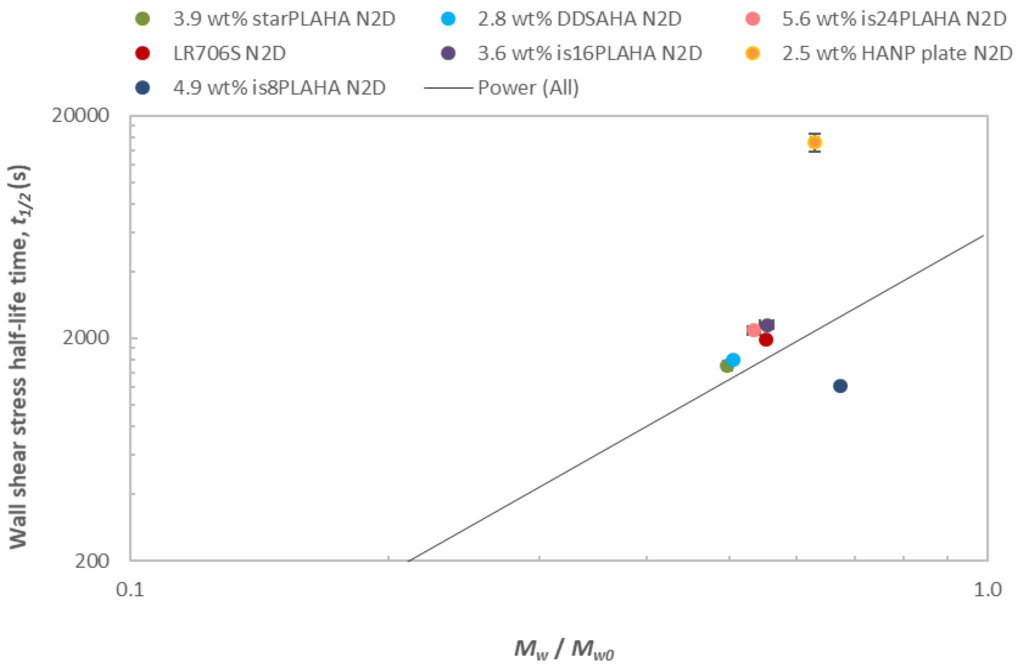

Figure 5.4. Change of $t_{1/2}$ in relation to M_w of LR706S with addition of coated HANP compounded at 50 rpm, 210 °C in N_{2D} for 15 min. HANP wt% was equivalent to 2.5 wt% of uncoated HANP plus coating. Where not shown, error bars are smaller than the size of the symbol.

The $t_{1/2}$ was the greatest for is16PLAHA and is24PLAHA nanocomposites which were 15.8% and 9.4% respectively higher than for processed LR706S, while other listed materials had $t_{1/2}$ lower than PLA by 19.3% to 38.6%. Nevertheless, none of the nanocomposites with coated HANP achieved $t_{1/2}$ comparable to 2.5 wt% HANP plates, even is8PLAHA despite high molecular weight. Table 5.4 also shows, for all coated materials, molecular weight decreases with an increasing amount of particles, similar to the trend seen for uncoated HANP plate nanocomposites.

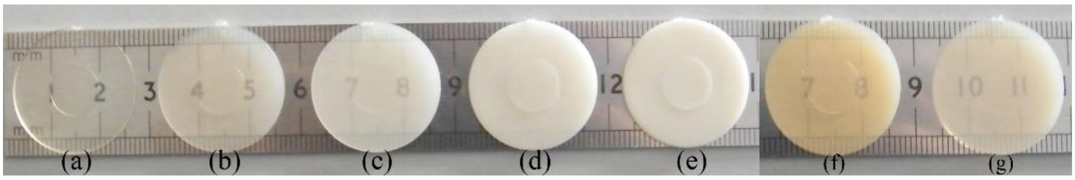

Figure 5.5. IM disc specimens - neat LR706S (a); uncoated HANP-LR706S: (b) 1 wt%, (c) 2.5 wt%, (d) 5 wt%, (e) 10 wt%; coated HANP-LR706S: (f) 4.9 wt% is8PLAHA, (g) 2.8 wt% DDSAHA.

Table 5.4. Influence of HANP on M_w of LR706S compounded in N_{2D} at 210 °C, 50 rpm for 15 min. For all coated HANP lower wt% is equivalent to 2.5 wt% HANP and higher value to 5 wt%.

Material	HANP [wt%]	M_w [kg.mol^{-1}]	M_n [kg.mol^{-1}]	PDI	$t_{1/2}$ [s]
LR706S	-	223.9 ±1.4	91.6 ±2.7	2.4 ±0.1	1983 ±35
is8PLAHA	4.9	273.4 ±1.6	103.6 ±2.7	2.6 ±0.1	1218 ±17
is16PLAHA	3.6	224.3 ±3.8	79.0 ±7.8	2.9 ±0.3	2296 ±48
is16PLAHA	7.2	179.1 ±2.9	54.8 ±3.2	3.3 ±0.2	971 ±10
is24PLAHA	5.6	216.4 ±3.6	72.7 ±10.7	3.0 ±0.4	2169 ±49
is24PLAHA	11.1	151.9 ±1.6	42.6 ±2.1	3.5 ±0.2	735 ±7
DDSAHA	2.8	205.2 ±0.8	75.4 ±1.3	2.7 ±0.1	1601 ±28
DDSAHA	5.6	147.7 ±2.4	40.1 ±1.9	3.7 ±0.2	729 ±7
starPLAHA	3.9	201.6 ±2.3	67.2 ±4.0	3.0 ±0.1	1504 ±23
starPLAHA	7.7	145.6 ±1.4	46.9 ±3.1	3.1 ±0.2	620 ±6

5.1.2. Influence of melt compounding parameters on molar mass

5.1.2.1. PLA

Melt compounding of LR706S in the MiniLab for 15 min at 210 °C decreased M_{w0} by approximately half. Notably, processing in N_{2D} preserved molecular weight of PLA better than in bottled nitrogen or ambient air, where M_w decreased only by 44.8% in comparison to 54.1% in N_2 and 64.2% in Air, as illustrated in Figure 5.6(a). This demonstrates that minimal moisture content is critical during PLA melt processing to minimise decrease of molecular weight, as has been observed in other studies [144]. It also verifies the formerly stated hypothesis that the smaller $t_{1/2}$ of LR706S mixed in Air for 15 min indicates greater degradation of PLA during processing when compared to N_2 and N_{2D}, as shown in Figure 5.6(b). The original power law trend line was applied to $t_{1/2}(M_w/M_{w0})$ data plotted for LR706S with a good fit regardless of n_s.

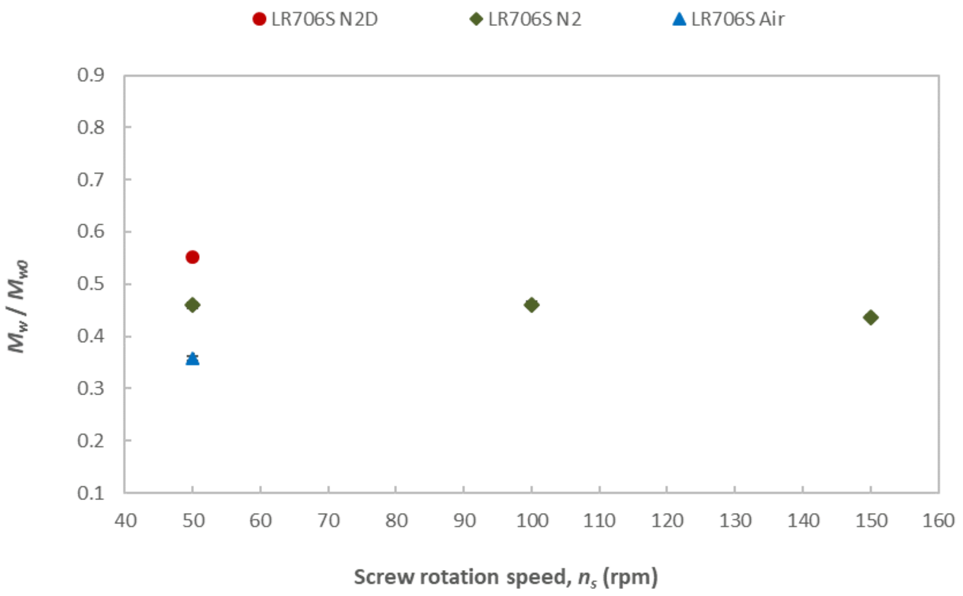

(a)

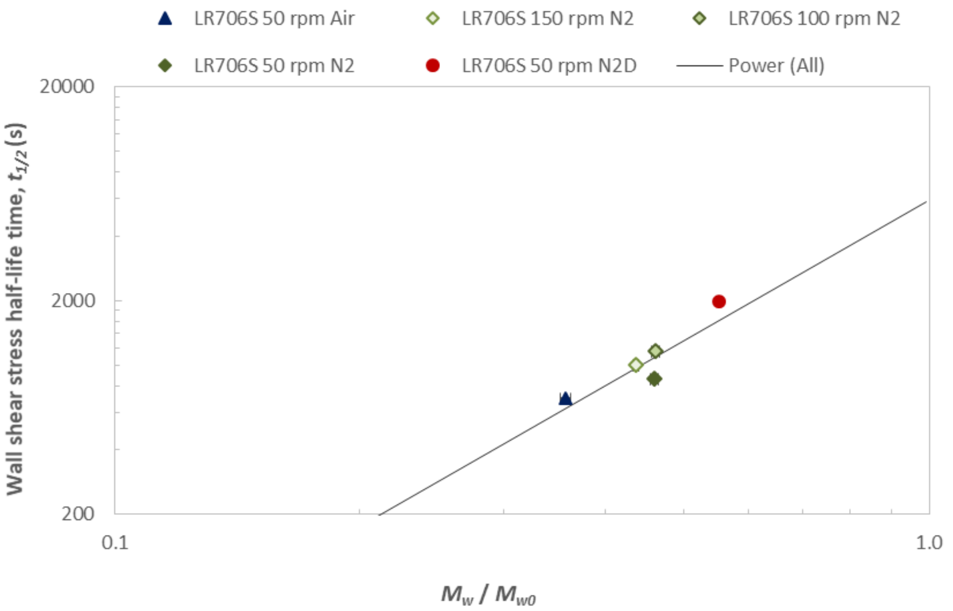

(b)

Figure 5.6. Influence of mixing of LR706S for 15 min with various screw speeds and in Air or inert gas on: a) M_w and b) $t_{1/2}$ in relation to M_w. Where not shown, error bars smaller than the size of the symbol.

Figure 5.6(a) also shows that mixing of LR706S in N_2 at increasing screw speed from 50 to 150 rpm (which was expected to give more homogenous nanocomposite blend [80]) did not have a major impact on M_w, which decreased by only 9 kg.mol^{-1} (4.9%). Yet, as reported beforehand, wall shear stress half-life time shifted for PLA with change of n_s, see Figure 5.6(b), i.e. $t_{1/2}$ increased 26% from 50 to 100 rpm while M_w remained the same. This supports earlier hypothesis that $t_{1/2}$ is partially dependent on n_s and implies that degradation of the polymer did not accelerate from 50 to 100 rpm. However, when n_s raised further to 150 rpm it was reflected in $t_{1/2}$ and M_w decrease due to increased shearing.

5.1.2.2. Nanocomposites

A similar trend followed as well for nanocomposites: 2.5 wt% HANP and 2.8 wt% DDSAHA, in Figure 5.7(a), where M_w decreased by 19.1% and 10.8% respectively when n_s changed from 50 to 150 rpm. Those results are comparable to other research [9] that shown a small rate of M_w decrease for PLA at 180 °C and screw speeds 50-150 rpm which only declined faster for 200 and 250 rpm. Figure 5.7(b) supported the earlier suggestion that changing $t_{1/2}$ was not only related to n_s and PLA degradation, manifested through decreasing M_w with increasing n_s, but also to nanoparticle dispersion in the polymer matrix. Otherwise, if particle presence would only alter molecular weight of the polymer matrix, the relation of $t_{1/2}$ from M_w/M_{w0} would be linear for each studied n_s. Yet, increase of $t_{1/2}$ and M_w from LR706S through uncoated HANP plates up to DDSAHA nanocomposite, along 100 rpm and 150 rpm, was not linear (as per dashed lines) and infers better dispersion of coated HA. At 50 rpm M_w and $t_{1/2}$ of both nanocomposites was similar – only 4.9% and 20.4% higher respectively for 2.5 wt% HANP plate nanocomposite than for 2.8 wt% DDSAHA.

Next, compounding of both types of particles with LR706S can be traced in Figure 5.7(b) with increasing screw speed against the power law trend line. The M_w of 2.5 wt% HANP plate decreased slightly by 24 kg.mol^{-1} (7%) with n_s changing from 50 rpm to 100 rpm yet $t_{1/2}$ remained the same which suggest some improvement of particle dispersion due to further shortening of the polymer chains. At 150 rpm greater mechanical degradation caused both M_w and $t_{1/2}$ to decrease for the 2.5 wt% HANP plate nanocomposite, by 11.3% and 33.1% respectively when compared with 100 rpm, which infers that particle mixing was dominated by decreasing molecular weight.

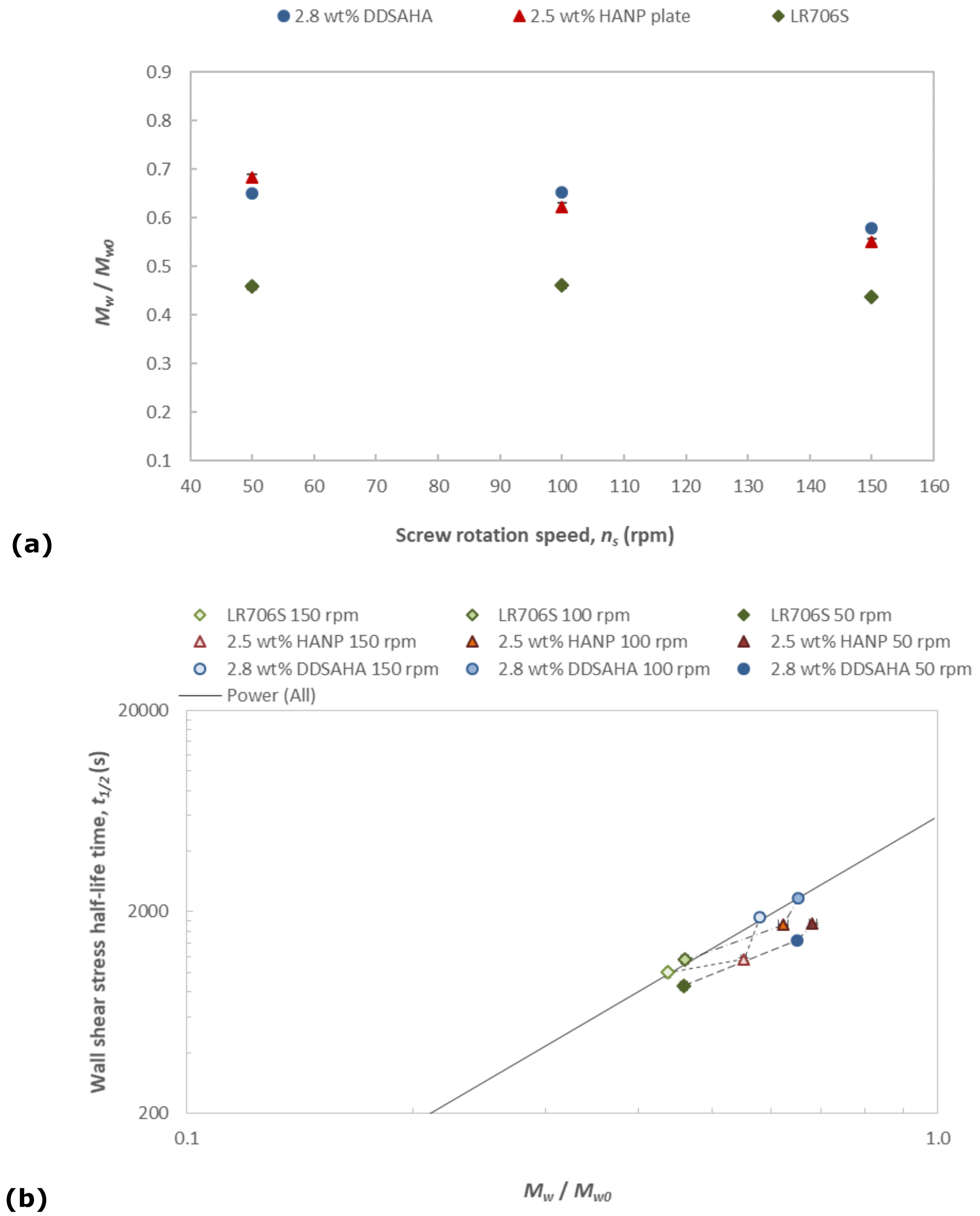

Figure 5.7. Change of: a) M_w, and b) $t_{1/2}$ in relation to M_w, of LR706S, 2.5 wt% HANP plate and 2.8 wt% DDSAHA compounded in N_2 at 50-150 rpm. Where not shown, error bars are smaller than the size of the symbol. Dashed lines are a guide to the eye for each n_s.

For 2.8 wt% DDSAHA $t_{1/2}$ dependence on M_w was similar to that for LR706S. The M_w remained the same with n_s raised from 50 rpm to 100 rpm when $t_{1/2}$ increased by 61% which indicates enhanced dispersion of particles. When n_s increased further up to 150 rpm both M_w and $t_{1/2}$ of 2.8 wt% DDSAHA decreased, by 11.1% and 19.1% respectively when compared with 100 rpm, which implies a detrimental shear effect on the melt overshadowing particle dispersion. However, $t_{1/2}$ of 2.8 wt% DDSAHA at 150 rpm was still 30.5% higher than at 50 rpm which, despite 10.8% lower molecular weight, suggests better particle dispersion at 150 rpm due to increased shearing for this particular nanocomposite. The results plotted beforehand for PLA and 2.5 wt% HANP plate and 2.8 wt% DDSAHA nanocomposites were summarised in Table 5.5 along with M_n of the materials.

Table 5.5. Change of molecular weight and $t_{1/2}$ of materials with varying compounding conditions in the MiniLab.

Gas	Material	HANP [wt%]	n_s [rpm]	M_w [kg. mol^{-1}]	M_n [kg. mol^{-1}]	PDI	$t_{1/2}$ [s]
N_{2D}	LR706S	-	50	223.9 ±1.4	91.6 ±2.7	2.4 ±0.1	1983 ±35
Air	LR706S	-	50	145.0 ±2.1	56.0 ±4.0	2.6 ±0.2	698 ±4
N_2	LR706S	-	50	186.2 ±2.2	81.7 ±2.5	2.3 ±0.0	859 ±5
N_2	LR706S	-	100	187.0 ±2.1	84.6 ±1.7	2.2 ±0.0	1157 ±6
N_2	LR706S	-	150	177.2 ±1.5	78.3 ±3.0	2.3 ±0.1	997 ±6
N_2	DDSAHA	2.8	50	263.8 ±1.7	104.6 ±4.8	2.5 ±0.1	1441 ±22
N_2	DDSAHA	2.8	100	264.7 ±0.2	107.5 ±7.2	2.5 ±0.2	2325 ±45
N_2	DDSAHA	2.8	150	235.2 ±2.5	94.5 ±8.7	2.5 ±0.2	1880 ±33
N_2	HANP plate	2.5	50	276.6 ±3.2	106.5 ±2.5	2.6 0.1±	1735 ±26
N_2	HANP plate	2.5	100	252.3 ±3.6	98.8 ±2.2	2.6 ±0.1	1717 ±29
N_2	HANP plate	2.5	150	223.7 ±1.9	89.1 ±2.0	2.5 ±0.2	1161 ±18

5.1.2.3. Mixing time

Influence of mixing time at 210 °C on molecular weight of materials is presented in Figure 5.8(a). 5.6 wt% DDSAHA was compounded at increasing time from 5 to 15 min at 50 rpm in N_{2D} compared with LR706S at 50 rpm mixed for 15 min in N_{2D}. Also change of M_w of LR706S in Air was studied for PLA mixed for 15 min at 50 rpm and for 4 min at 100 rpm.

The dependence of M_w from t_R was found to be linear for 5.6 wt% DDSAHA nanocomposite with the molecular weight reduced by 13.6% from 5 to 10 min and further 13.3% at 15 min due to extended exposure of polymer to processing temperature [162]. However, more homogenous filler dispersion was expected with longer mixing time [80] for DDSAHA, which was reflected in Figure 5.8(b), by increase of $t_{1/2}$ despite decrease of M_w, where after 15 min of compounding 5.6 wt% DDSAHA nanocomposite $t_{1/2}$ raised by 53.9% from 5 min and reached the fitted power law trend line.

Although fitting an exponential decay to less τ_w data from shorter runs is subject to greater error it was hypothesised that longer t_R gave particles opportunity to mix better with PLA facilitated by shortening polymeric chains due to thermal degradation from prolonged exposure to heat. However, good particle dispersion should be coupled with high molecular weight of LR706S to produce desirable materials for medical devices.

The molecular weight of 5.6 wt% DDSAHA nanocomposite compounded for 15 min at 50 rpm in N_{2D} was 34% lower than for LR706S mixed in the same conditions, shown in Figure 5.8(a), and reached M_w of LR706S mixed for 15 min at 50 rpm in Air. As their $t_{1/2}$ shown in Figure 5.8(b) was also comparable this infers that shear exerted during compounding of dried 5.6 wt% DDSAHA with LR706S for 15 min in N_{2D} had a similar degrading effect on the polymer matrix to moisture uptake during 15 min mixing of PLA in Air.

The M_w of LR706S mixed in Air for 4 min at 100 rpm was 6.2% higher than for 15 min at 50 rpm (and it was not expected to be greater for 4 min at 50 rpm as per Figure 5.6(b)) as it was exposed to heat for shorter time. The $t_{1/2}$ for the shorter PLA recirculation was 45.1% lower than for the longer one, most likely due to the initial transient period after sample loading which had the greatest effect on short time experiments, coupled with greater uncertainty in fitting an exponential decay to less τ_w data. The results plotted in Figure 5.8 were also summarised in Table 5.6.

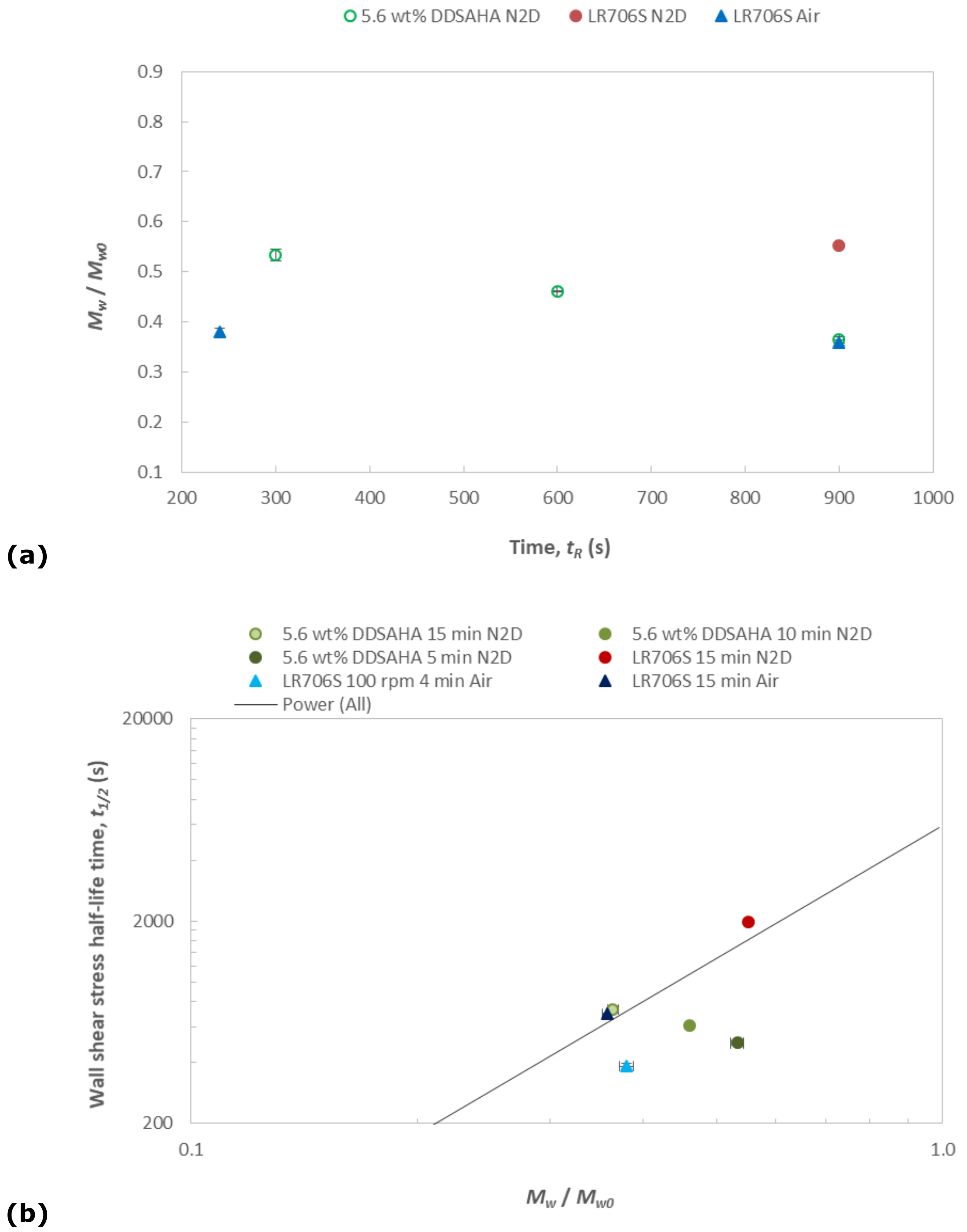

Figure 5.8. Change of: a) M_w and b) $t_{1/2}$ in relation to M_w of 5.6 wt% DDSAHA mixed at 50 rpm for 5-15 min and LR706S at 50 rpm for 15 min and at 100 rpm for 4 min. Where not shown, error bars smaller than the size of the symbol.

Table 5.6. Change of molecular weight and $t_{1/2}$ of 5.6 wt% DDSAHA mixed at 50 rpm in N_{2D} and LR706S in Air with varying compounding time.

Gas	Material	n_s [rpm]	t_R [min]	M_w [kg. mol^{-1}]	M_n [kg. mol^{-1}]	PDI	$t_{1/2}$ [s]
Air	LR706S	100	4	154.0 ±3.2	58.7 ±5.3	2.6 ±0.2	383 ±13
Air	LR706S	50	15	145.0 ±2.1	56.0 ±4.0	2.6 ±0.2	698 ±4
N_{2D}	LR706S	50	15	223.9 ±1.4	91.6 ±2.7	2.4 ±0.1	1983 ±35
N_{2D}	DDSAHA	50	5	216.2 ±4.5	72.4 ±2.0	3.0 ±0.1	499 ±26
N_{2D}	DDSAHA	50	10	186.9 ±0.7	66.3 ±0.8	2.8 ±0.0	606 ±11
N_{2D}	DDSAHA	50	15	147.7 ±2.4	40.5 ±1.9	3.7 ±0.2	729 ±13

5.1.3. Thermal and shear degradation of polymer

Viscosity and molecular weight of a polymer can be described via the Mark-Houwink equation for polymer solutions where intrinsic viscosity is related to viscosity averaged molecular weight (M_V) [163]:

$$\eta = K\, M_v{}^a \tag{5.1}$$

where: *a* is the Mark–Houwink exponent and *K* the characteristic material constant.

For melt viscosity the Equation (5.1) modifies to:

$$\eta_0 = K\, M_w{}^a \tag{5.2}$$

where a = 3.4 for PLA, same for both temperatures of 150 °C and 180 °C [93, 164].

For oscillatory rheometry it was found experimentally [164] that the longest relaxation time of the polymer is related to its molecular weight via a similar exponent expression:

$$\lambda = M_w{}^{3.4} \tag{5.3}$$

Equation (5.3) can be applied to compare the measured molecular weight with the relaxation time, for specific degradation time and temperature during small amplitude oscillatory shear tests in ambient air. Such a study was conducted by Choong et al. [28] to correct for quiescent thermal degradation of LR706S during rheometry. This would allow for the separation of thermal and shear effects of melt processing in the MiniLab on the polymer matrix and possibly indicate improved particle dispersion for the nanocomposites. The function proposed by Choong et al. [28] describes the degradation shift factor *D* at elapsed degradation time t_{deg} at the given test temperature T_t as:

$$D = \frac{\lambda_{deg}}{\lambda_0} = \left[1 + \left(\frac{1}{t_{trans}} \int_0^{t_{deg}} \frac{dt}{\alpha_D}\right)^b\right]^{\frac{c}{b}} \tag{5.4}$$

where: $t_{deg} = t_{ML}$ for each produced material in the MiniLab, λ_{deg} is relaxation time of the degraded polymer at T_t; and experimentally determined by Choong et al. [28] parameters for LR706S at the reference degradation temperature T_D = 170 °C are: relaxation time of the undegraded polymer λ_0 = 4.29 s, transition time t_{trans} = 2761 s for change from plateau to power-law region of the degradation mastercurve with transition speed constant *b* = 1.36 and transition slope constant *c* = -1.00. Degradation shift factor, α_D, used in the above equation, allows for correlation of the utilised reference temperature with the actual temperature during compounding in the MiniLab, and was described as [28]:

$$\ln \alpha_D = \frac{E_a}{R}\left(\frac{1}{T_t} - \frac{1}{T_D}\right) \tag{5.5}$$

where: $R = 8.31$ J.mol^{-1}.K^{-1} is the universal gas constant, $T_t = T_{ML}$ = 210 °C, and calculated activation energy for LR706S: E_a = 131 kJ.mol^{-1} [28] which is in agreement with experimentally measured values for PLA [165].

Combining of Equation (5.3) and (5.4) gives:

$$\sqrt[3.4]{D} = \sqrt[3.4]{\frac{\lambda_{deg}}{\lambda_0}} = \frac{M_w{}^*}{M_{w0}} \tag{5.6}$$

and allows to apply D in calculation of theoretical weight average molecular weight M_W^* of the materials affected only by thermal degradation (TD). The obtained M_W^* can be compared with the actual measured M_w which decreased further due to mechanical degradation (MD) in the MiniLab as a result of shearing, shown in Figure 5.9. The molecular weight loss between M_{w0}=1 and M_W^*, depicted in the plot as the black line, was expected to occur only due to TD and further decrease between the trend line and the actual measured M_w was estimated as effect of MD. The t_{ML} differs from time quoted in the data point labels, which refer to t_R only. The plotted examples of LR706S processed in the MiniLab firstly show how greatly shear affected their degradation, especially for PLA mixed in Air where M_w decreased 53% below M_W^*. Secondly they indicate the addition of HANP rod preserved molecular weight better than the calculated M_W^* would suggest, thus decreasing the impact of TD on the polymer.

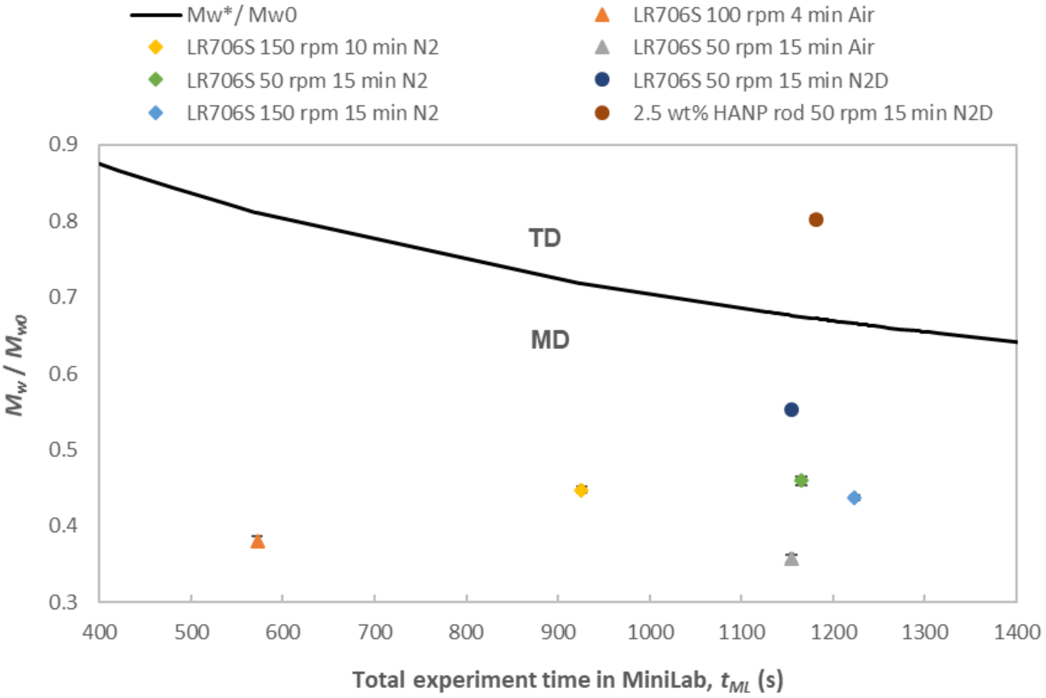

Figure 5.9. Comparison of theoretical and actual M_w of the materials, compounded in the MiniLab with various parameters at 210 °C, affected by thermal and mechanical degradation. Where not shown, error bars are smaller than the size of the symbol.

5.1.3.1. PLA

The impact of TD and MD was estimated for LR706S processed in the MiniLab based on calculated M_W^* and measured M_w of PLA. This analysis allows for greater understanding of degradation mechanisms during compounding of LR706S with various mixing parameters in the MiniLab. In Figure 5.10 comparison of the recirculation of LR706S in different gases showed practically identical TD as M_W^* for PLA mixed for 15 min in all three gases was similar, however the influence of MD decreased from Air to N_{2D} by 62.5% with increasing measured M_w. This infers that processing PLA in dry N_2 can decrease the polymer decomposition due to shearing through limiting hydrolytic and oxidative degradation.

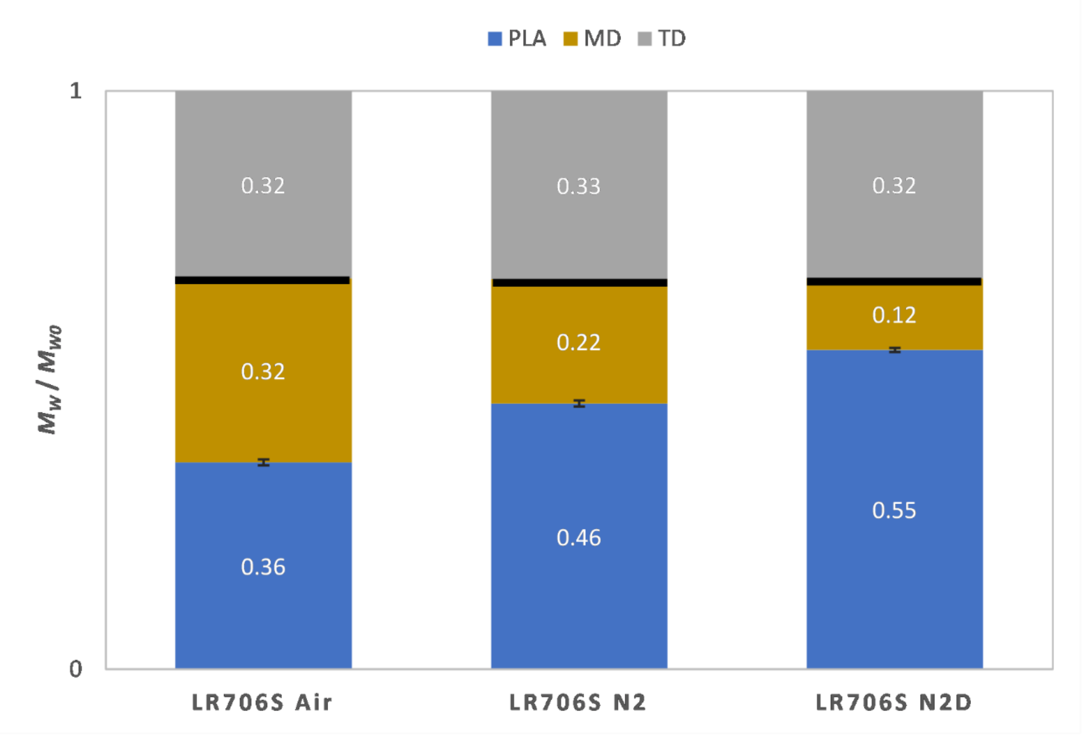

Figure 5.10. Degradation of LR706S compounded in the MiniLab at 50 rpm, 210 °C for 15 min in Air, N_2 and N_{2D} normalised versus M_{w0}, where: MD - mechanical degradation, TD - thermal degradation. The black line on the bars indicates M_W^* for each sample.

Influence of mixing LR706S with various compounding parameters on degradation of PLA was confirmed in Figure 5.11. Firstly, mixing in N_2 at 150 rpm for 10 min decreased M_{w0} by 55% due to MD and TD in nearly even proportion and after 5 more min of recirculation in the MiniLab M_{w0}

declined further only by 1% while the ratio of TD versus MD increased to 59%. This did not mean that after 15 min of mixing in N_2 PLA was sheared less but, as n_s remained the same and M_w of both samples was comparable, TD had greater influence on LR706S decomposition due to longer residence at 210 °C. Secondly, mixing in Air had greater impact on decrease of molecular weight of the polymer as M_{w0} reduced by 62% after only 4 min at 100 rpm mostly due to MD in 69% ratio to TD. For LR706S mixed in Air at 50 rpm for 15 min M_{w0} declined further only by 2% due to MD and TD in even proportion. Therefore, for mixing in both atmospheres it was shown that for shorter mixing times, MD had a larger influence on reduction of M_{w0} than TD.

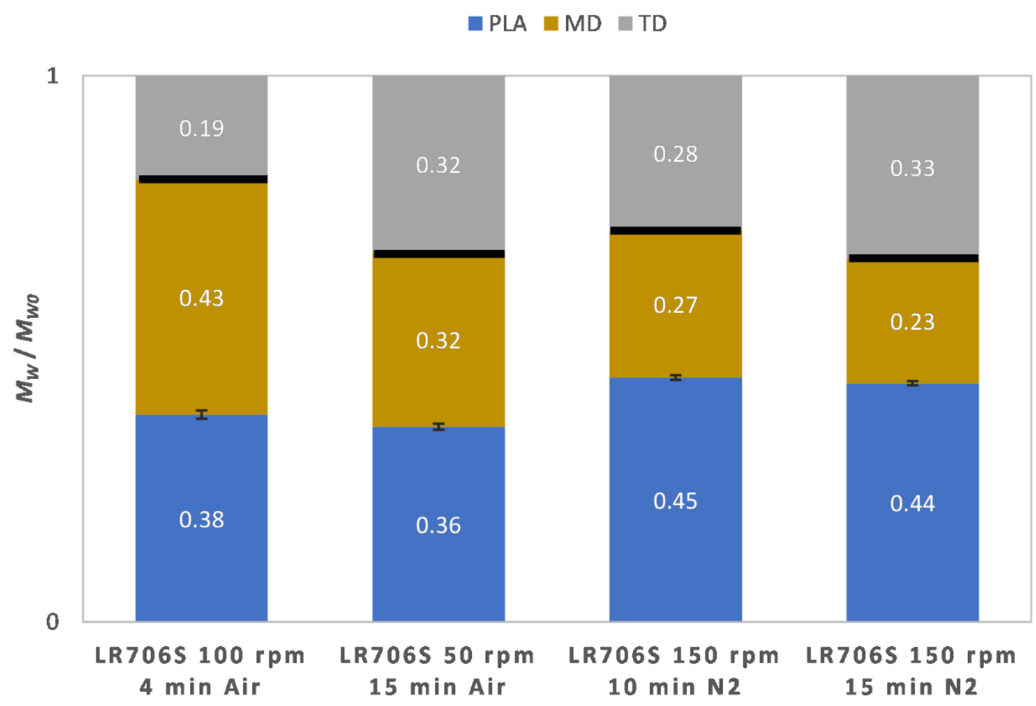

Figure 5.11. Degradation of LR706S mixed in the MiniLab at 210 °C with various compounding parameters normalised versus M_{w0}, where: MD - mechanical degradation, TD - thermal degradation. The black line on the bars indicates M_w^* for each sample.

This relation was also confirmed in Figure 5.12 where molecular weight of PLA remained nearly identical after 15 min of mixing in N_2, despite n_s increasing from 50 to 150 rpm, where TD had major influence on decrease of M_{w0} and practically no change in MD and TD level was observed. Those results for LR706S are in line with other research about mixing PLA in a twin screw extruder [162], which showed that at 200 °C the effect of MD due to shearing reduces with growing residence time when TD had increasing contribution and was more pronounced at higher temperatures.

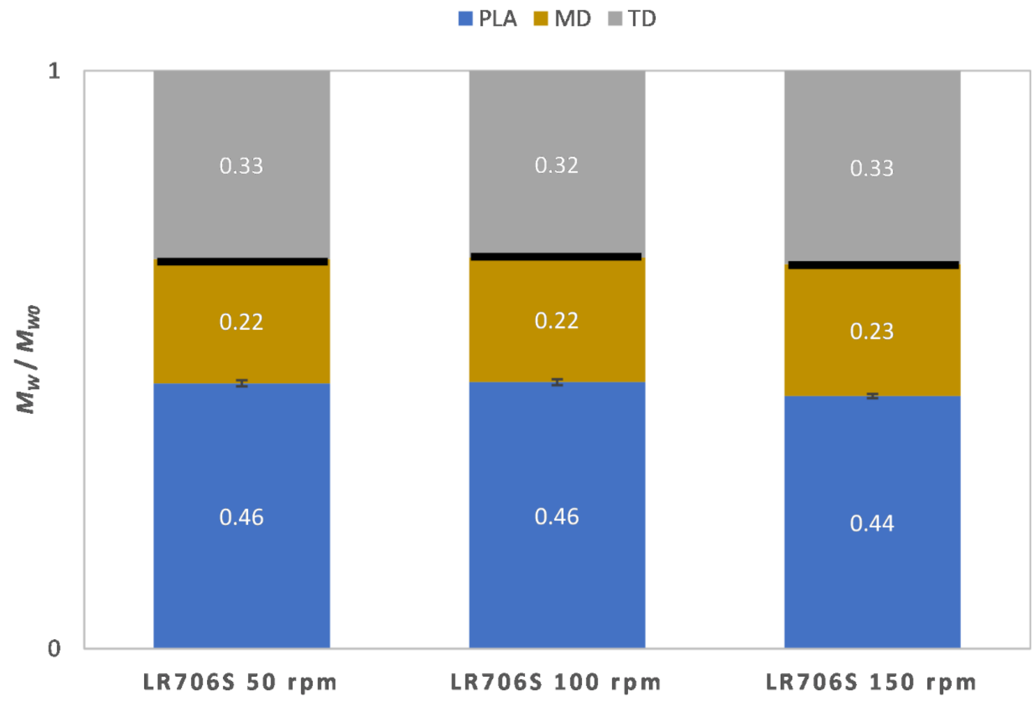

Figure 5.12. Degradation of LR706S compounded in the MiniLab at 210 °C for 15 min in N_2 at 50 -150 rpm normalised versus M_{w0}, where: MD - mechanical degradation, TD - thermal degradation. The black line on the bars indicates M_w^* for each sample.

5.1.3.2. Nanocomposites

Calculated M_w^* of LR706S and measured M_w of all compounded LR706S materials were compared in Figure 5.13 in an attempt to determine the nanocomposites with the best particle dispersion. It was assumed that if a data point lies on the compliance line then the theoretical and actual values for the molecular weight were identical which infers that particles inclusion had a beneficial effect outweighing the effect of MD on PLA. This implies that materials with M_w below M_w^* experienced degradation due to temperature and shear which could not be compensated or was increased by compounding of HANP with LR706S.

For nanocomposites with M_w above M_w^* it was assumed that particle dispersion was improved and preserved M_{w0} above that predicted for TD level, based on an anti-plasticization effect [166]. Nearly all materials compounded in Air and N_2 were severely affected by degradation that brought their molecular weight below M_w^* level, with only one sample from those two groups reaching the theoretical calculated value, which confirmed once again that residual moisture had major adverse effect on M_w of PLA. The M_w of materials compounded in N_{2D} was closer to the compliance line with few nanocomposites having molecular weight exceeding the calculated M_w^*. Those nanocomposites, labelled in Figure 5.13 and marked with circles, were expected to have HANP dispersion greater than for other compounded materials.

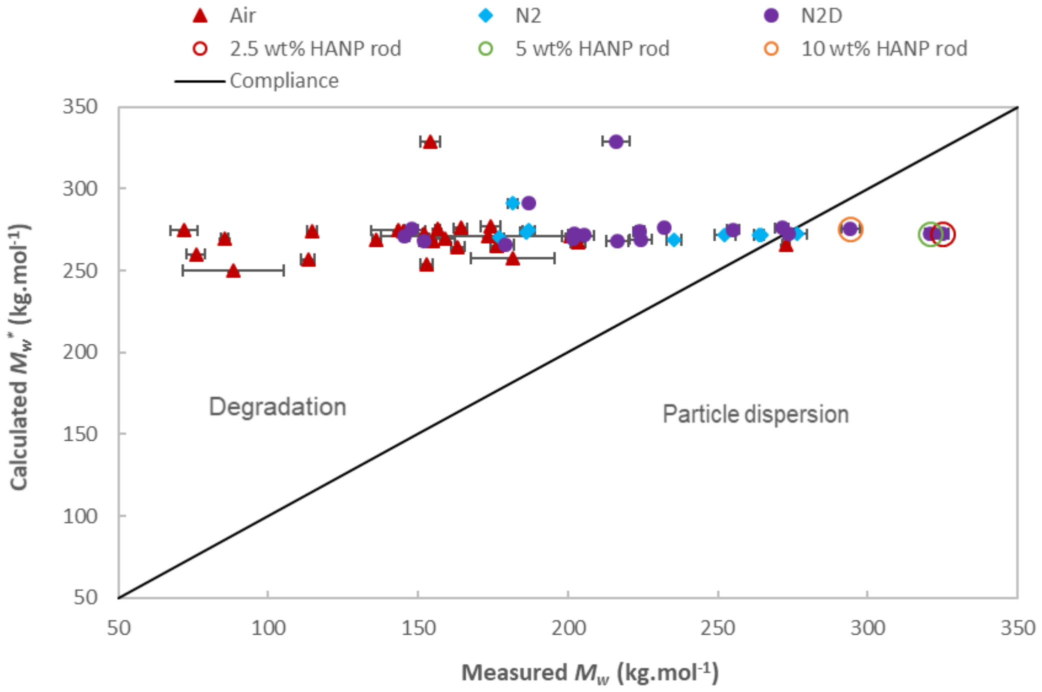

Figure 5.13. Comparison of calculated M_w^* and measured M_w of LR706S materials compounded in the MiniLab.

Examples of materials compounded in Air and N_{2D} were compared separately to further investigate influence of mixing HANP on degradation of LR706S and particle dispersion. Once again it was assumed that the molecular weight loss between M_{w0}=1 and M_W^* was expected to occur only due to TD and further decrease below M_W^* down to the actual measured M_w was estimated as effect of MD, whereas increase of M_w above M_W^* was expected to mark improved particle dispersion (PD).

Firstly, degradation of HANP plate nanocomposites compounded in Air was compared with processed LR706S only. The TD was on average 0.34 for all the materials in Figure 5.14 with slight deviations due to differences in loading time to the MiniLab (as M_w^* is associated with t_{deg} = t_{ML}). The MD decreased 28.6% when M_w increased 11.1% after adding 1 wt% HANP plate to LR706S which implies a beneficial effect of dispersing particles on preserving molecular weight of PLA.

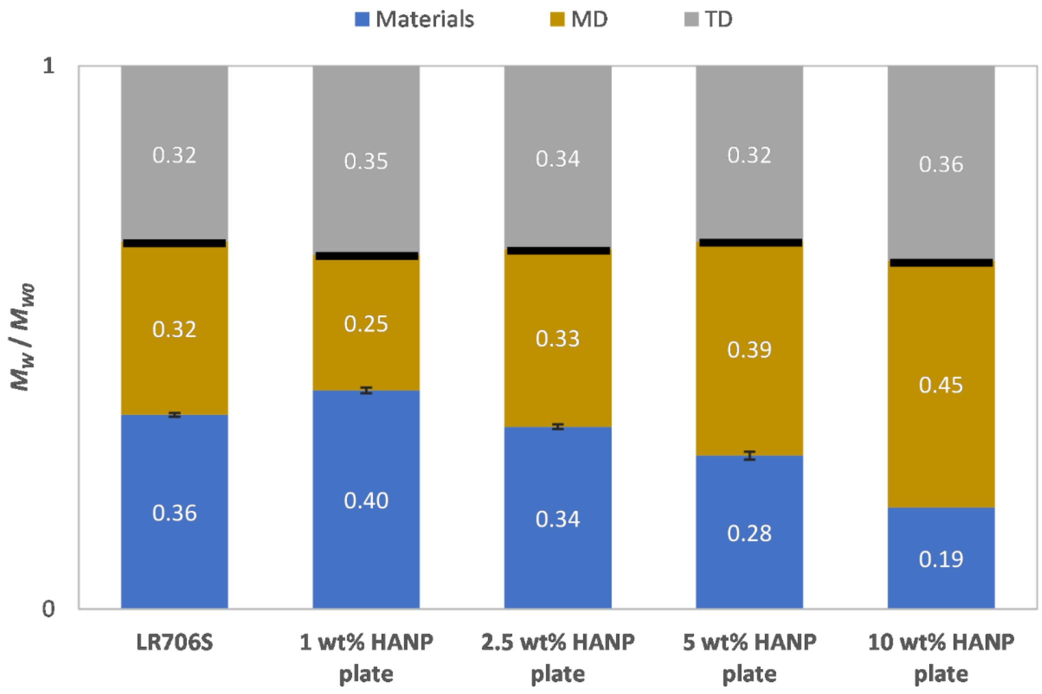

Figure 5.14. Change of degradation of LR706S compounded with 1-10 wt% HANP plates at 50 rpm, 210 °C in Air for 15 min, where: MD - mechanical degradation, TD - thermal degradation. The black line on the bars indicates M_W^* for each material.

Further increase of the amount of HANP plates from 2.5 to 10 wt% resulted in a gradual M_w decrease, down to 19% of M_{w0} for 10 wt% HANP plates, which in turn caused an increase of MD by 40.6% when compared with LR706S only. This infers that HANP plates added above 2.5 wt% to LR706S in Air were not mixed efficiently, and additionally residual moisture present on the particles caused hydrolytic degradation of the polymer during compounding, which further increased the ratio of MD versus TD and had negative impact on M_w of the produced nanocomposites.

Next, the influence of mixing of 2.5 – 10 wt% HANP rods with LR706S in N_{2D} on limiting degradation capacity during compounding was shown in Figure 5.15. The M_w of LR706S was 12% lower than M_w^* due to MD, whereas M_w of all the nanocomposites was above the calculated M_w^* due to beneficial PD which compensated effects of MD and partially of TD.

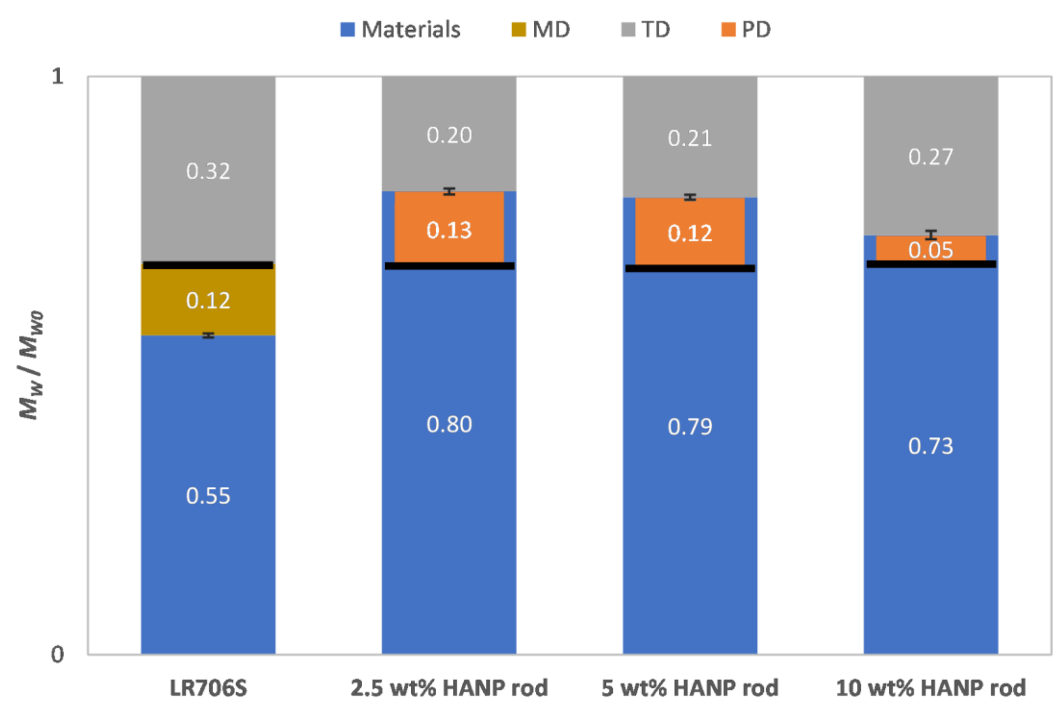

Figure 5.15. Change of degradation of LR706S compounded with 2.5 -10 wt% HANP rods at 50 rpm, 210 °C in N_{2D} for 15 min, where: MD - mechanical degradation, TD - thermal degradation, PD - particle dispersion. The black line on the bars indicates M_w^* for each material.

The smaller TD for the nanocomposite the larger influence of PD on preserving M_{w0} with the greatest M_w and PD for 2.5 wt% HANP rods and the lowest M_w and PD for 10 wt% HANP rods. This would imply that PD decreased for 10 wt% HANP rods due to increasing particle agglomeration and had adverse effect on the nanocomposite M_w.

Finally, the influence of addition of uncoated and coated HANP plates on limiting LR706S degradation during compounding in N_{2D} was shown in

Figure 5.16. The TD was on average 0.33 for all the materials, with slight deviations due to differences in loading time to the MiniLab. For 2.5 wt% HANP plate nanocomposite MD decreased by 58.3%, when compared with LR706S, as M_w was close to M_w^* due to the beneficial influence of the particles.

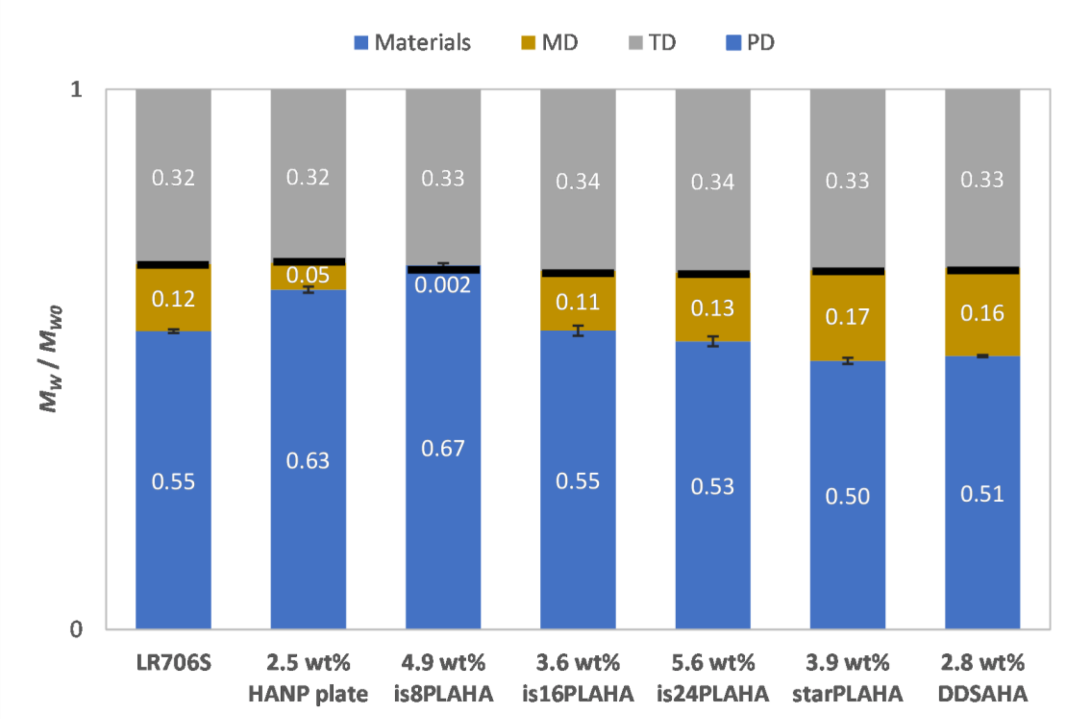

Figure 5.16. Comparison of degradation change of LR706S compounded with uncoated and coated HANP plates at 50 rpm, 210 °C in N_{2D} for 15 min. The wt% of coated HANP was equivalent to 2.5 wt% of uncoated HANP plus coating, where: MD - mechanical degradation, TD - thermal degradation, PD - particle dispersion. The black line on the bars indicates M_w^* for each material.

From all the compared materials with coated HANP, only for 4.9 wt% is8PLAHA the measured and theoretical calculated molecular weight (based on the rheological model applied for tests in Air) matched and fractional PD was shown. This infers that dispersion of is8PLAHA in the polymer matrix was sufficient to compensate for the effect of MD and TD to some extent. For the nanocomposite with 3.6 wt% is16PLAHA M_w and level of MD were comparable with LR706S mixed in the MiniLab and for the other materials M_w and MD decreased even further. This implies that these coated HANP were not mixed efficiently with PLA leaving particle agglomerates exerting shear on the polymer matrix, or/ and that coating degraded due to temperature and shearing, which increased ratio of MD versus TD and had a negative impact on M_w of the produced nanocomposites.

5.2. Thermal characteristics

Differential scanning calorimetry and thermogravimetric measurements, carried out as per methods described in Sections 3.2.7 and 3.2.5 respectively, were used to assess thermal characteristics of PLA changing with processing parameters and particle type and content. The results obtained were correlated with molecular weight of the materials.

5.2.1. Influence of HANP on the glass transition

The effect of melt compounding of HANP with LR7006S on changes of T_g was explored. Preliminary investigation was carried out for HANP plates compounded with PLA in Air and N_{2D}, shown in Figure 5.17. Firstly, a surprisingly low T_g was observed for LR706S mixed in N_{2D} when compared to LR706S mixed in Air or to the polymer as produced. As mentioned in Section 3.2.7 three DSC repeats were carried out for three samples for each material however, due to the unexpected results for LR706S mixed in N_{2D}, extrudates from two separate runs in the MiniLab were tested three times each. The first batch had a T_g of 56.9 °C ±0.6 °C and the second batch 57.6 °C ±0.6 °C, hence the point plotted for LR706S in N_{2D} in all subsequent figures in Section 5.2.1 and 5.2.2 marks the average of the aforesaid two values. It was suspected that the molecular weight for LR706S mixed in N_{2D} dropped below the M_n of LR706S mixed in Air, yet this did not correlate with the GPC findings and further results for M_n will be discussed in Section 5.2.2.

5.2.1.1. HANP plates

In Figure 5.17 it was shown that the T_g for HANP plates mixed with LR706S in Air was lower than for nanocomposites mixed in N_{2D}, where reduced moisture content and dry particles were expected to protect the molecular weight of PLA during melt compounding and as a result minimise the number of the polymer chain ends and free volume. This was hypothesised to increase T_g for nanocomposites compounded in N_{2D} when compared with Air experiments. The T_g of all nanocomposites produced in N_{2D} was comparable to neat LR706S, while for particles compounded in Air T_g decreased with increasing content of HANP plates.

An especially severe reduction in T_g was observed for 10 wt% HANP plates in Air which decreased by 2 °C in comparison to 5 wt% and at a greater rate than in N_{2D} where the T_g decreased by only 0.6 °C from 5 to 10 wt%. A potential explanation of T_g reduction above 5 wt% HANP plates in Air was that an increased number of agglomerates worsened the interface between LR706S and particles, which caused their poor interaction and increased free volume, plasticizing the material [166]. The rise in free volume was most likely amplified in Air due to PLA degradation and an increased number of the polymer chain ends [167], which is further discussed in relation to molecular weight in Section 5.2.2.2. This reduction of T_g with increasing amount of HA nanoparticles compounded with PLA in air was also shown in other research [9], plotted in Figure 5.17 for comparison.

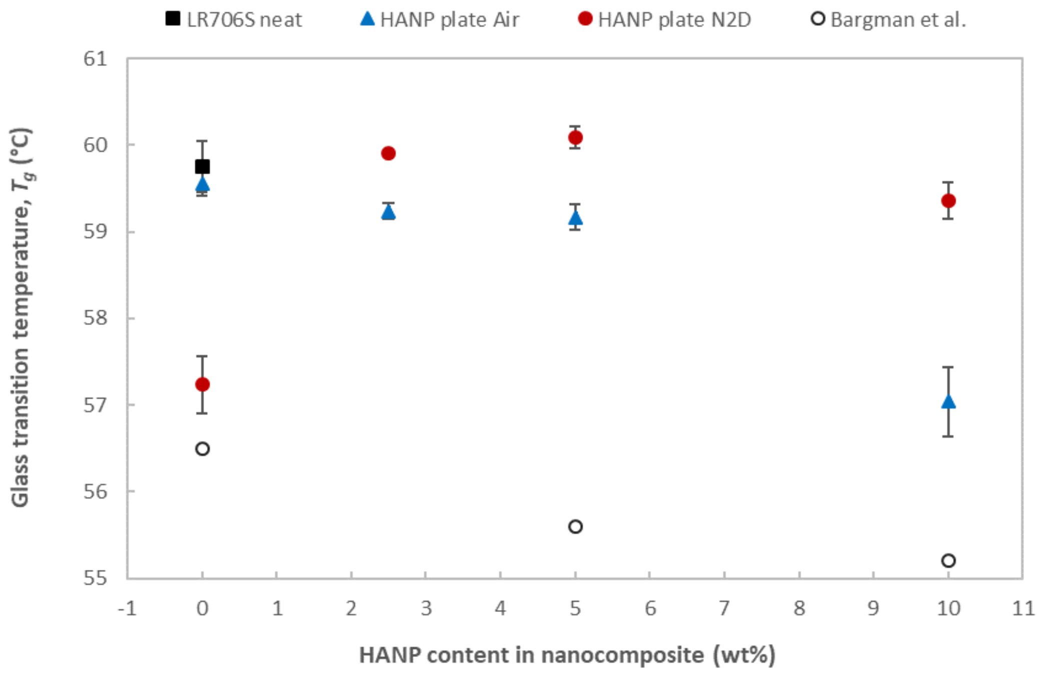

Figure 5.17. Change of T_g with increasing amount of HANP plates compounded with LR706S at 210 °C, 50 rpm for 15 min in Air and N_{2D}. Where not shown, error bars for acquired measurements are smaller than the size of the symbol.

5.2.1.2. HANP rods

Influence of HANP rods on the glass transition of LR706S compounded in N_{2D} is shown in Figure 5.18. The T_g of 2.5, 5 and 10 wt% HANP rod was nearly identical to the T_g of respective nanocomposites with HANP plates in N_{2D}. This would infer similar HA-PLA interface for both types of nanoparticles, despite different shape and surface area of HANP plates and rods, and comparable molecular weight of respective nanocomposites that will be discussed further in the next section.

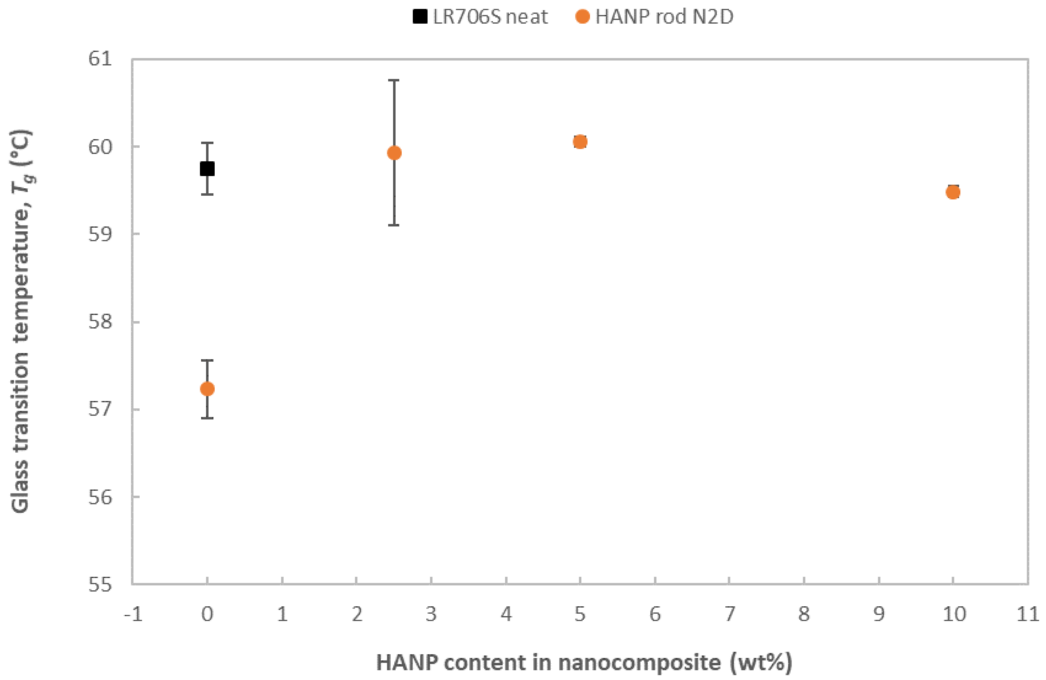

Figure 5.18. Change of T_g with increasing amount of HANP rods compounded with LR706S at 210 °C, 50 rpm for 15 min in N_{2D}. Where not shown, error bars are smaller than the size of the symbol.

5.2.2. Influence of molar mass on the glass transition

5.2.2.1. Flory-Fox equation

Correlation between M_n of PLA and T_g was analysed for samples of three of the Resomer LR series of PLA from Evonik, as well as the 2003D grade from NatureWorks. Resomer LR series is amorphous with an enantiomer proportion of L:D,L 70:30 (so 15% of D-lactide) and high M_w ranging from 242 to 845 kg.mol^{-1} [168]. Natureworks 2003D is also amorphous with an L:D proportion of 95:5 and has lower M_w of 130 kg.mol^{-1} [127]. Figure 5.19 shows the glass transition temperature dependence on the molecular weight of the unprocessed samples. As seen in the literature, T_g decreased for PLA with lower molecular weight due to greater ability of short chains of polymer to relax free volume and reduce T_g [68], which was reflected in this study.

The Flory-Fox equation can be used to relate M_n with T_g:

$$T_g = T_g^{\infty} - \frac{K}{M_n} \tag{5.7}$$

where the T_g^{∞} is T_g at the infinite M_n and K is the characteristic material constant expressed in °C.kg.mol^{-1} [68].

As shown by Saeidlou et al. [169] the K value increases with the D-lactide concentration (X_D) of PLA linearly as:

$$K = 52.23 + 791\,X_D \tag{5.8}$$

And T_g^{∞} is also related with X_D through a following function [169]:

$$T_g^{\infty} = \frac{13.36 + 1371.68\,X_D}{0.22 + 24.3\,X_D + 0.42\,X_D^2} \tag{5.9}$$

Calculated T_g^{∞} and K values for X_D = 0.15 were used in Equation (5.7), despite different L:D proportion for 2003D, and plotted in Figure 5.19 where trend for PLA measurements matches the Flory-Fox equation (F-F) prediction. However, the T_g^{∞} approximation from F-F was 4 °C lower than the temperature of 60.5 °C determined from linear regression for PLA measurements. When the F-F was solved for X_D = 0.002 (not shown in Figure 5.19) the fitted line resembled the linear regression for PLA and T_g^{∞} was 60 °C. The actual T_g measurements [170] were also compared with a plot of T_g against M_n and X_D for PLA which contains data from multiple researchers, summarised by Saeidlou et al. [169]. Once again this comparison suggested that T_g for the PLA samples considered here more closely resembles polymers with D-lactide concentration below 1%. This infers that the crystalline PLLA part of the high molecular weight Resomer LR series polymers and 2003D dominated the influence on their

T_g, raising it 4 °C above the F-F prediction. However, no melt temperature, which occurs for crystalline materials, was found for LR706S or its nanocomposites during the DSC measurements carried out according to methods described in Section 3.2.7. This highlights the fact that F-F is only an empirical rule and the actual T_g depends on many additional factors, e.g. the sample thermal history, DSC measuring technique (temperature ramp) or even different structure of chain ends for the measured PLA and polymers corelated via the Flory-Fox equation.

The actual linear trend line fitted for PLA in Figure 5.19 was copied in all subsequent T_g (M_n^{-1}) figures in Section 5.2.2 for comparison purposes.

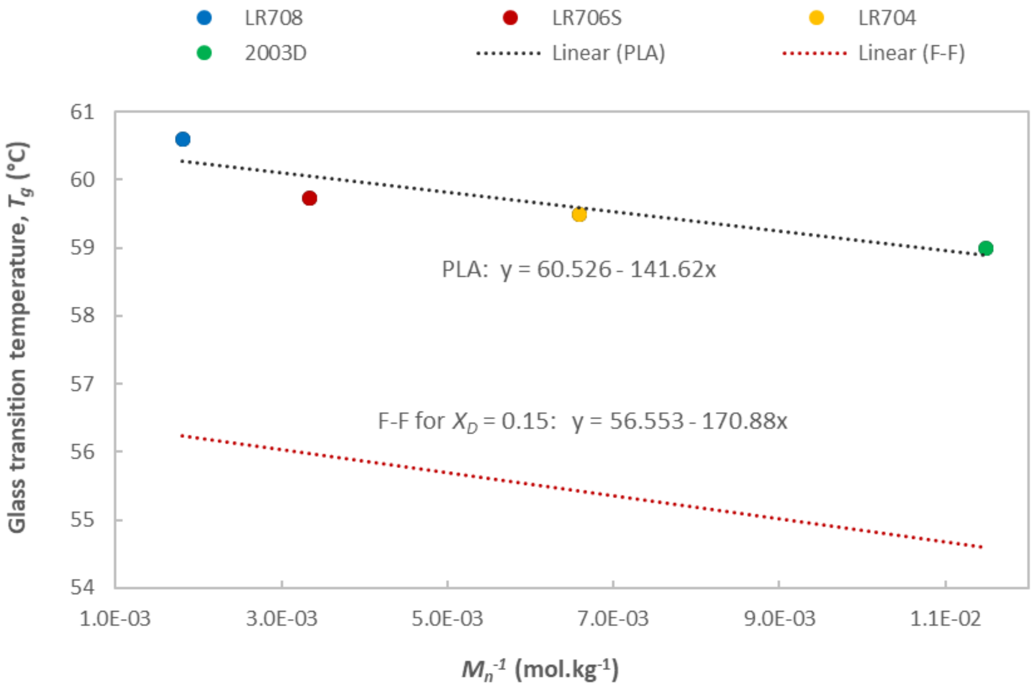

Figure 5.19. Influence of M_n of PLA on the glass transition. Values for 2003D adapted from Choong et al. [127] and Tee et al. [130] and for LR series from Choong [170] and Wiktorska et al. [168].

5.2.2.2. HANP plates

The T_g decreased with declining molecular weight of the materials in Figure 5.20 following the F-F trend. Nanocomposites produced in N_{2D} and PLA processed in Air had T_g comparable to neat LR706S within its error. A noticeable T_g decrease was shown for HANP plate nanocomposites produced in Air when their M_n decreased below 70% in comparison to neat LR706S. This infers that only significant molecular weight loss causes decline of T_g due to the increased number of polymer chain ends.

Unusually low T_g was observed for LR706S in N_{2D} which had high M_n. It was hypothesised that greater N_2 solubility in PLA, due to raised pressure [171] in the MiniLab during mixing under N_{2D}, increased free volume between polymer chains and decreased its T_g. Nanocomposites produced in Air had T_g lower than neat LR706S, which decreased with M_n due to more chain ends, yet their T_g was higher than the F-F linear regression for unprocessed neat PLA. A potential explanation was beneficial interaction between HANP and LR706S, which kept T_g higher than PLA F-F trend would suggest, effecting with similar T_g^∞ but different K for nanocomposites regression fit. However, for 10 wt% HANP-LR706S in Air (with M_n 86% lower than unprocessed LR706S) the T_g declined more rapidly than for other nanocomposites, suggesting larger free volume due to greater particle agglomeration which caused a worse interface between HANP and PLA.

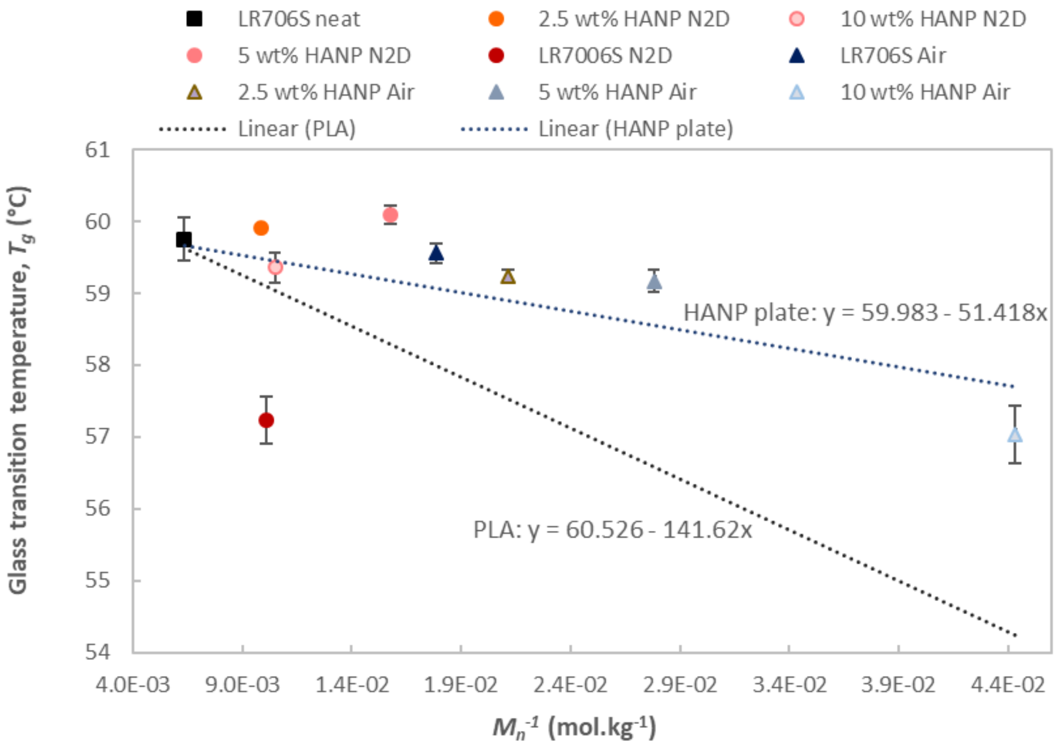

Figure 5.20. Change of M_n and T_g of LR706S with addition of HANP plates compounded at 50 rpm, 210 °C in Air and N_{2D} for 15 min. Where not shown, error bars are smaller than the size of the symbol.

5.2.2.3. HANP rods

The 2.5, 5 and 10 wt% HANP rod compounded with LR706S in N_{2D} had alike glass transition to the respective nanocomposites with HANP plates in N_{2D}, despite lower molecular weight for the latter ones. This might suggest better interface between HANP plates and LR706S due to improved particle dispersion increasing their T_g despite decreased M_n. However, good nanofiller dispersion was also expected to protect molecular weight of PLA as discussed earlier in Section 5.1.1. Therefore, the more likely explanation is that as both types of the nanoparticles had the same chemical composition their HA-PLA interaction was similar, and the 37%-60% M_n decrease for HANP plates materials in N_{2D}, when compared to neat LR706S, was not significant enough to affect their T_g (see Figure 5.20), which finally decreased once M_n reduced by 86% for 10 wt% HANP-LR706S in Air.

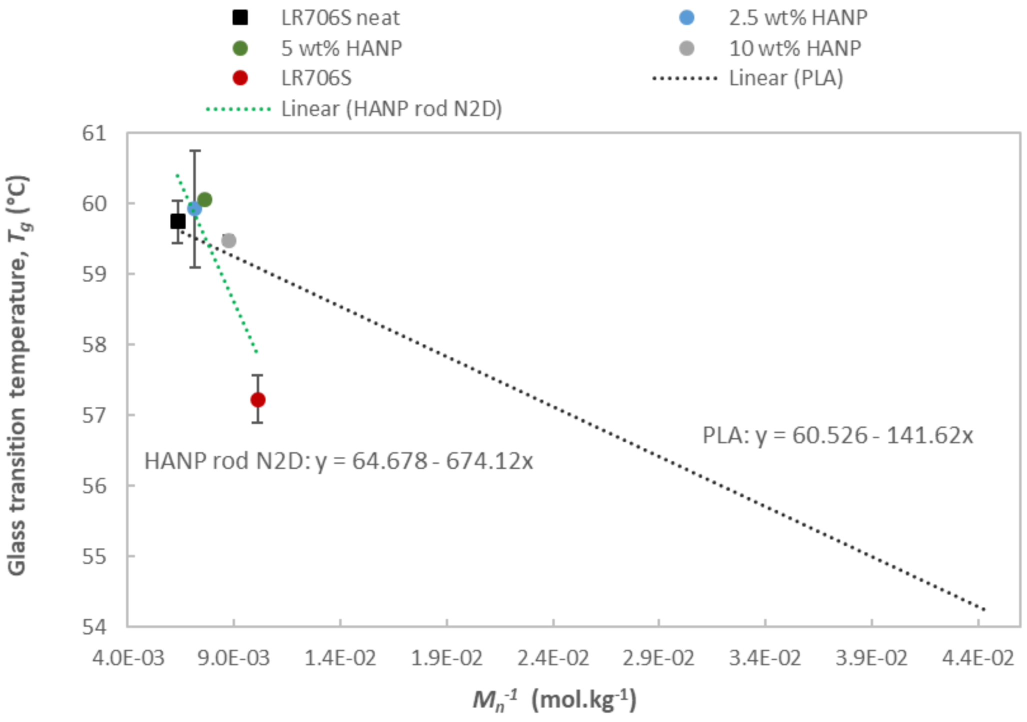

Figure 5.21. Change of M_n and T_g of LR706S with addition of HANP rods compounded at 50 rpm, 210 °C in N_{2D} for 15 min. Where not shown, error bars smaller than the size of the symbol.

The applied F-F regression for HANP rod nanocomposites had greater T_g^{∞} and different K than F-F for PLA only, however the small number of points and T_g error size for 2.5 wt% sample caused a larger degree of uncertainty for the fitted trendline. This infers that comparison of T_g and M_n of HANP plate and rod nanocomposites in N_{2D} is insufficient to relate to their particle dispersion and interface with the polymer matrix, as the molecular weight change was insufficient to alter T_g and both fillers are the same mineral.

5.2.3. Thermal stability

Thermogravimetric measurements were analysed in terms of temperature at 5% weight loss of polymer versus the effect of particle filling, coating and morphology and materials molecular weight to assess their thermal stability.

The temperature at 5% weight loss of the nanocomposites was normalised with respect to only the polymer content ($t_{5\%P}$), including particle coating if present, by subtraction of the final residual weight of the hydroxyapatite after burn off from the original mass of the composite sample as shown in Figure 5.22. This approach was not applied in literature to evaluate $t_{5\%P}$, however in this study focus in given to the polymeric part of the composite, hence the mass adjustment.

As the $t_{5\%P}$ correction is related to the sample mass the greatest difference was shown for high content of HANP, see example in Table 5.7. For nanocomposites with coated HANP, the mass of the dispersant was included in the $t_{5\%P}$ adjustment. All subsequently quoted values of temperature at 5% weight loss for nanocomposites were adapted to $t_{5\%P}$.

Table 5.7. Adjustment of temperature at 5% weight loss e.g. HANP-LR706S compounded in Air at 210 °C, 50 rpm for 15 min.

HANP type	HANP [wt%]	$t_{5\%}$ [°C]		$t_{5\%P}$ [°C]	
HANP plate	2.5	313.2	± 4.0	312.8	± 4.1
HANP plate	10	316.7	± 1.8	315.1	± 1.8
DDSAHA	2.8	314.1	± 3.3	313.9	± 3.3
is16PLAHA	3.6	319.2	± 1.2	319.0	± 1.2

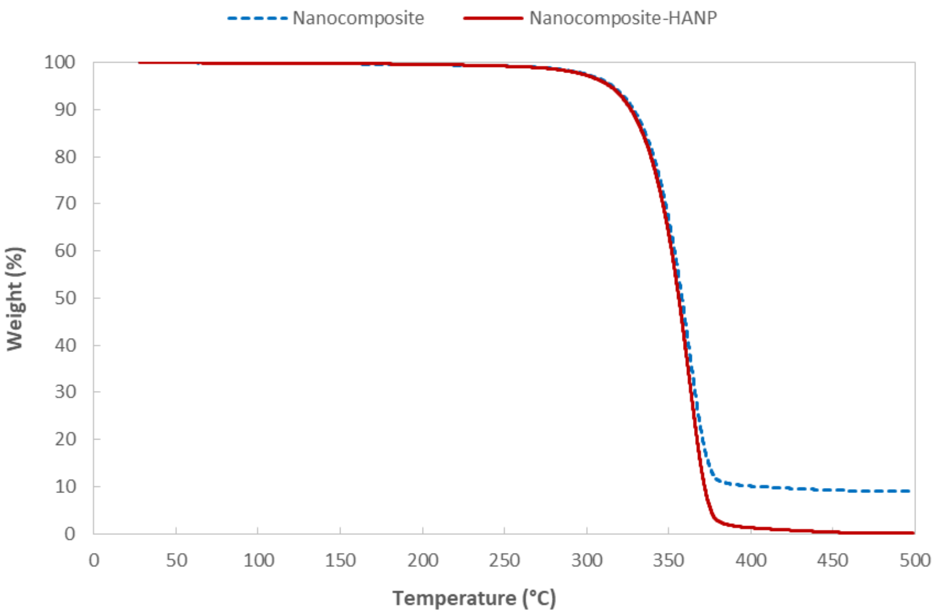

(a)

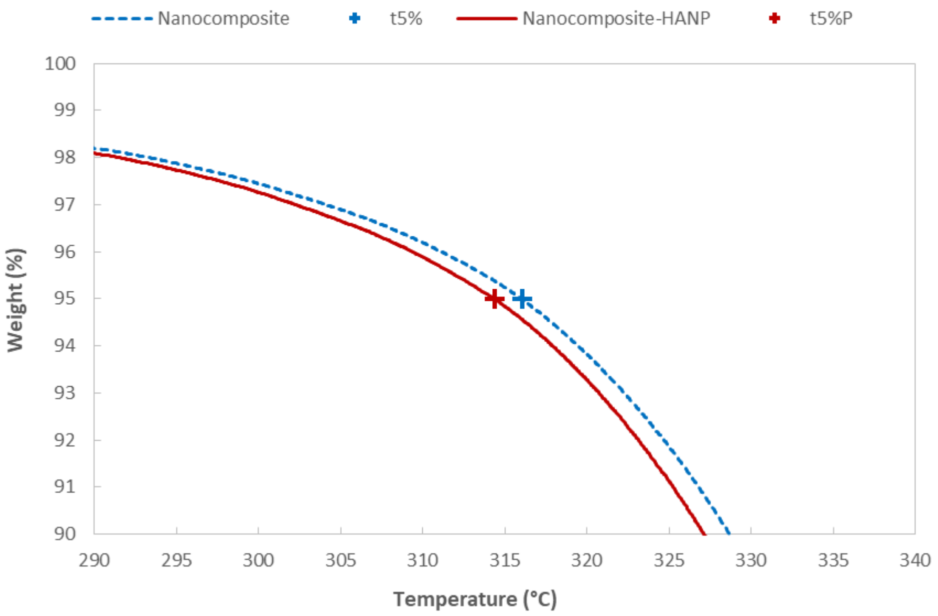

(b)

Figure 5.22. 10 wt% HANP in LR706S (a) subtraction of HANP mass and (b) adjustment of the temperature at 5% weight loss.

5.2.3.1. HANP plates

Figure 5.23(a) compares the effect of HANP plate content on the thermal decomposition at $t_{5\%P}$ for nanocomposites compounded in Air and N_{2D} and values for these materials are listed in Table 5.8. Influence of molecular weight of HANP plate nanocomposites on their $t_{5\%P}$ was investigated versus neat LR706S in Figure 5.23(b).

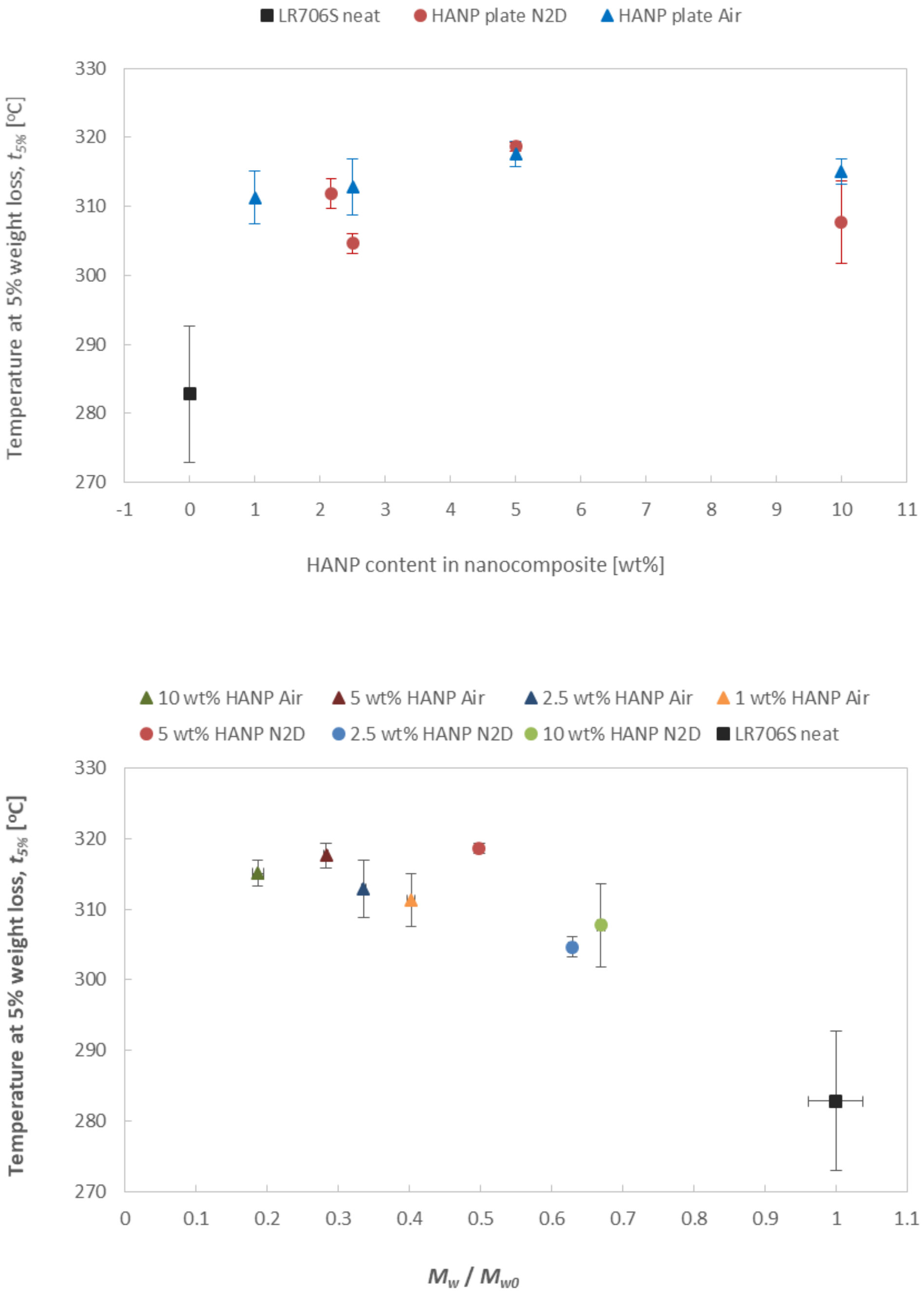

(a)

(b)

Figure 5.23. Change of LR706S $t_{5\%}$ (a) with addition of 1-10 wt% HANP plate compounded at 50 rpm, 210 °C for 15 min in Air and N_{2D} (b) versus their M_w. Where not shown, error bars are smaller than the size of the symbol.

The 5% loss temperature for all HANP plate nanocomposites was 22–36 °C higher than that of the pure polymer regardless of processing gas.

The delay in the initiation of mass loss for the nanocomposites, demonstrated by increase of $t_{5\%P}$, implies that they were more thermally stable than neat LR706S, which was also reported in other studies about HANP-PLA materials [81] and witnessed in different nanocomposite systems e.g. silica-PMMA [120]. Inclusion of HANP plates in the PLA matrix enhances the thermal resistance of nanocomposites in Air and N_{2D} up to 5 wt% e.g. the $t_{5\%P}$ values of 1 wt% and 5 wt% nanocomposites in Air are 9.2% and 11.2% higher than neat LR706S respectively. Above 5 wt% HANP loading the 5% loss temperature decreases slightly, e.g. for 10 wt% HANP in Air $t_{5\%P}$ is only 10.7% greater than neat LR706S, possibly due to particle aggregation in the polymer matrix. However, the $t_{5\%P}$ error bar size for some of the nanocomposite samples caused a large degree of uncertainty for quantitative comparison of the amount of HANP plates with the material's thermal stability.

Despite that a reducing trend emerged for the 5% loss temperature with increasing M_w e.g. for HANP plates in N_{2D}, $t_{5\%P}$ decreased by 4% when M_w increased 26% from 5 to 2.5 wt% HANP plate. For HANP plate nanocomposites when the molecular weight was greater than half of the M_{w0} for the unprocessed PLA the $t_{5\%P}$ transitioned from a relative plateau region to decrease with increasing M_w.

Table 5.8. Influence of HANP plate on $t_{5\%P}$ of LR706S compounded in Air and N_{2D} at 210 °C, 50 rpm for 15 min.

Gas	Material	HANP [wt%]	$t_{5\%P}$ [°C]	
-	LR706S neat	-	282.8	± 9.9
N_{2D}	HANP plate	2.5	304.6	± 1.5
N_{2D}	HANP plate	5	318.6	± 0.7
N_{2D}	HANP plate	10	307.7	± 6.0
Air	HANP plate	1	311.3	± 3.8
Air	HANP plate	2.5	312.8	± 4.1
Air	HANP plate	5	317.6	± 1.8
Air	HANP plate	10	315.1	± 1.8

5.2.3.2. HANP rods

For rod HANP-LR706S nanocomposites compounded in Air and N_{2D}, shown in Figure 5.24(a), $t_{5\%P}$ was greater than that for neat LR706S by 19-25 °C (7-9%) which infers enhancement of thermal stability of the nanocomposites. The magnitudes of $t_{5\%P}$ for all HANP rod materials are listed in Table 5.9. The 5% loss temperature changed slightly in N_{2D} with an increasing amount of particles, however it was statistically insignificant. It is also worth noting that the $t_{5\%P}$ decreased with increasing M_w of nanocomposites as shown in Figure 5.24(b). Using HANP rods in N_{2D} as an example, it is shown that $t_{5\%P}$ of HANP-LR706S nanocomposites depends on both particle loading and effective molecular weight, however the change in $t_{5\%P}$ is minor. For 2.5 wt% HANP rod in Air the size of the measurement error enclosed the spread of $t_{5\%P}$ for all HANP rod nanocomposites in N_{2D}. Therefore, the influence of compounding 2.5 wt% HANP rod with LR706S in Air on $t_{5\%P}$ was difficult to judge beyond severe decrease of M_w by 53% when compared with 2.5 wt% HANP nanocomposite in N_{2D}. The greatest $t_{5\%P}$ difference was observed between neat PLA and the nanocomposites, which for HANP rods was 3-11 °C lower than for HANP plates. This implies that the $t_{5\%P}$ of the nanocomposites depends also on the HANP morphology, which leads to different surface area and varying interface between filler and polymer.

Table 5.9. Influence of HANP rod on $t_{5\%P}$ of LR706S compounded in N_{2D} at 210 °C, 50 rpm for 15 min.

Gas	Material	HANP [wt%]	$t_{5\%P}$ [°C]	
-	LR706S neat	-	282.8	± 9.9
N_{2D}	HANP rod	2.5	302.2	± 1.5
N_{2D}	HANP rod	5	306.1	± 1.5
N_{2D}	HANP rod	10	307.7	± 0.8
Air	HANP rod	2.5	306.3	± 4.0

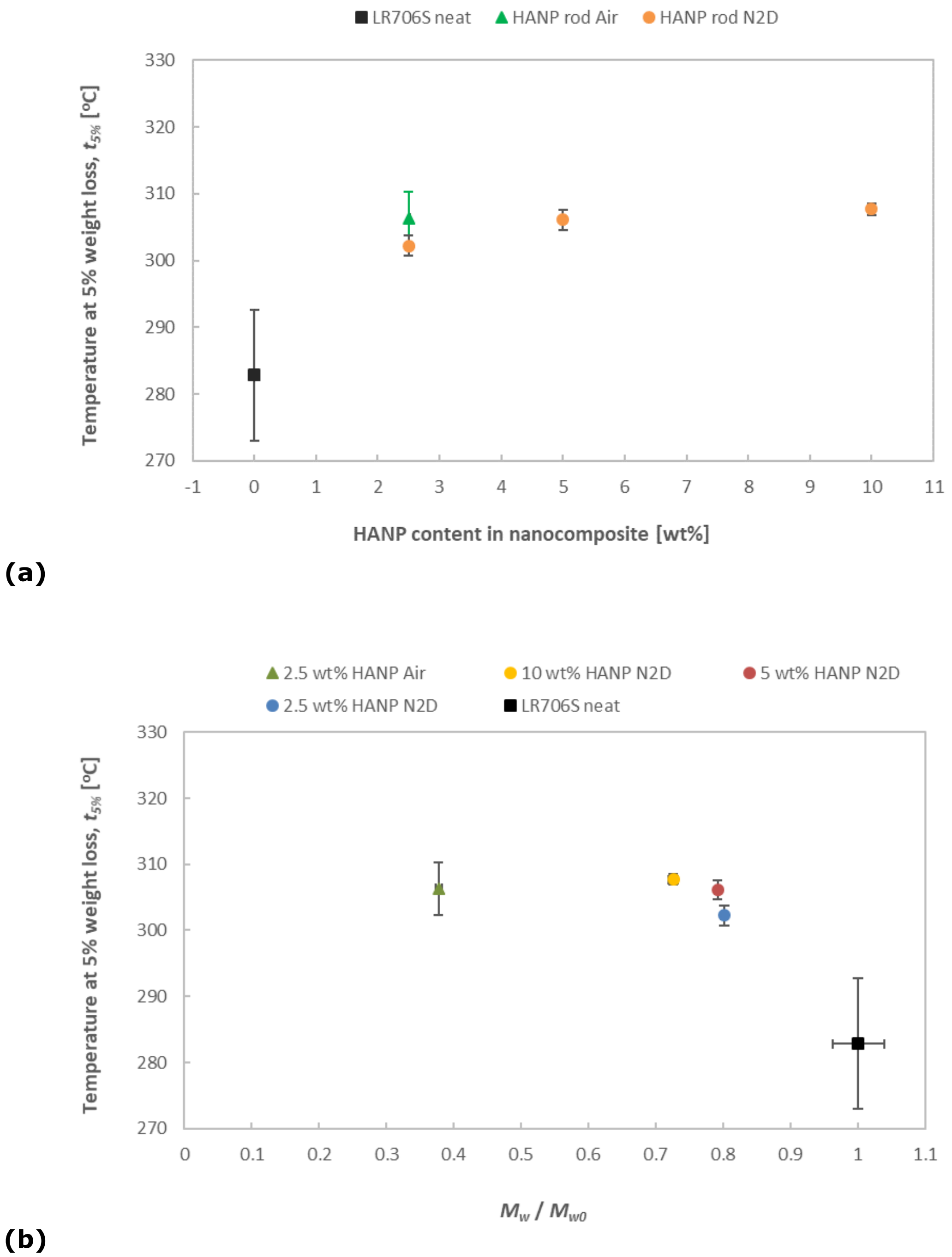

Figure 5.24. Change of LR706S $t_{5\%}$ (a) with addition of 2.5-10 wt% HANP rod compounded at 50 rpm, 210 °C for 15 min in N_{2D} (b) versus their M_w. Where not shown, error bars are smaller than the size of the symbol.

5.2.3.3. Coated HANP

Influence of change of screw rotation speed under N_2 and HANP coating on nanocomposites $t_{5\%P}$ with respect to neat PLA was shown in Figure 5.25(a) and values for these materials were listed in Table 5.10. As demonstrated earlier in Section 5.2.3, the incorporation of HANP results in a delay in the initiation of mass loss resulting in rise of the 5% loss temperature for both coated and uncoated HANP. For 2.5 wt% plate HANP $t_{5\%P}$ continued to slightly raise with increase of n_s i.e. $t_{5\%P}$ increased by 5.4% from 50 to 150 rpm, while for 2.8 wt% DDSAHA $t_{5\%P}$ decreased with increasing n_s i.e. $t_{5\%P}$ decreased by 5.4% from 50 to 150 rpm.

The $t_{5\%P}$ increase for HANP plate nanocomposites infers greater dispersion of particles with increase of n_s, whereas for DDSAHA it suggests the dispersion did not improve with n_s raise or increased shear caused decomposition of DDSA dispersant which had an adverse effect on $t_{5\%P}$. The $t_{5\%P}$ decreased for 2.5 wt% HANP plates with increasing M_w of the nanocomposites from 150 to 50 rpm, as shown in Figure 5.25(b), while for 2.8 wt% DDSAHA $t_{5\%P}$ decreased with decreasing M_w and increasing n_s. This supports the earlier claim that DDSA decomposition accelerated during melt compounding with increasing n_s, as shown in Figure 5.7 in Section 5.1.2.2, therefore lower screw speed would be advised for compounding systems with coated HANP.

For HANP plate nanocomposites increasing $t_{5\%P}$ with increasing n_s, inferring improving particle dispersion, was compromised with a deceasing M_w. This confirmed that compounding at 50 rpm for 15 min in the MiniLab provides an agreeable compromise between particles mixing and preserving the molecular weight of LR706S. At an n_s of 50 rpm 2.8 wt% DDSAHA nanocomposite had 5.4% higher $t_{5\%P}$ than 2.5 wt% HANP.

Figure 5.26 shows the influence of compounding different types of coated HANP with LR706S in N_{2D} on the $t_{5\%}$ and M_w of their nanocomposites. All particles had 2.5 wt% HANP plates with different type and amount of coating which appeared to only marginally change the nanocomposites $t_{5\%P}$ relative to 2.5 wt% of uncoated HANP plates. As listed in Table 5.11 the lowest $t_{5\%P}$ of 300.8 °C was for 3.6 wt% is16PLAHA with the highest result of 306.4 °C for 4.9 wt% is8PLAHA however with the greatest error of 3 °C. Since the $t_{5\%P}$ of the majority of those materials was comparable, and their M_w was lower than for the nanocomposite with uncoated particles, this infers contribution of HANP coating in accelerating polymer matrix degradation. The only nanocomposite with coated HANP which had $t_{5\%}$ and M_w greater than uncoated HANP was 4.9 wt% is8PLAHA, which suggests better thermal stability of that material.

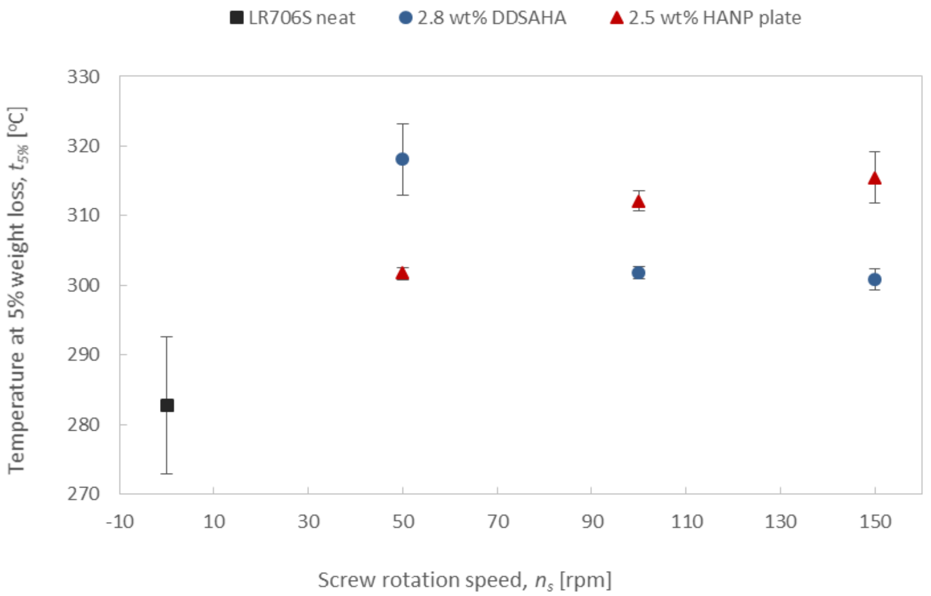

(a)

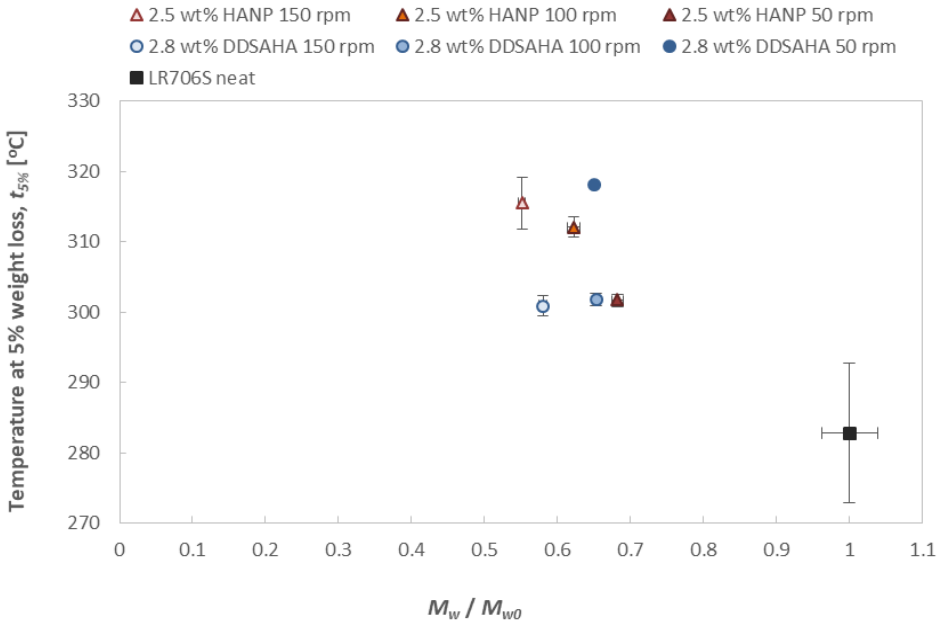

(b)

Figure 5.25. Changing $t_{5\%}$ of (a) 2.5 wt% HANP plate and 2.8 wt% DDSAHA, equivalent to 2.5 wt% HANP plus coating, compounded in N_2 at 210 °C for 15 min at 50-150 rpm (b) versus their M_w. Where not shown, error bars smaller than the size of the symbol.

Table 5.10. Change of $t_{5\%P}$ of 2.8 wt% DDSAHA and 2.5 wt% HANP plate compounded in N_2 at 50-150 rpm.

Material	HANP [wt%]	n_s [rpm]	$t_{5\%P}$	[°C]
LR706S neat	-		282.8	± 9.9
DDSAHA	2.8	50	318.1	± 5.1
DDSAHA	2.8	100	301.8	± 0.9
DDSAHA	2.8	150	300.9	± 1.5
HANP plate	2.5	50	301.7	± 0.9
HANP plate	2.5	100	312.1	± 1.4
HANP plate	2.5	150	315.5	± 3.7

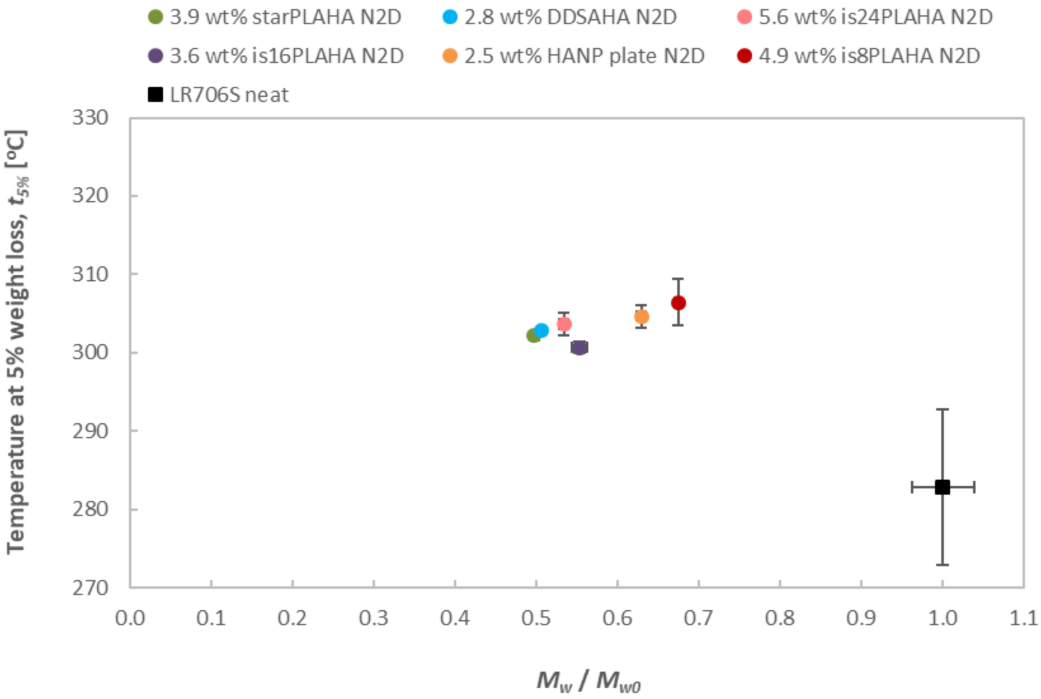

Figure 5.26. Change of $t_{5\%}$ and M_w of nanocomposites with various HANP compounded at 50 rpm, 210 °C for 15 min in N_{2D}. For coated HANP wt% was equivalent to 2.5 wt% of uncoated HANP plate plus coating. Where not shown, error bars are smaller than the size of the symbol.

DDSAHA particles were also utilised to test nanocomposite thermostability versus compounding time in the MiniLab, which was shown in Figure 5.27, where 5.6 wt% DDSAHA was mixed at 50 rpm and 210 °C in N_{2D} for 5 to 15 min. Despite expected thermal degradation of PLA and decrease of molecular weight with increasing compounding time the $t_{5\%P}$ remained at the same level (within the error). This shows that in spite of decreasing properties of polymer matrix with increasing t_R the 5% loss temperature remained the same due to stabilisation with nanoparticles.

Table 5.11. Temperature at 5% weight loss of HANP-LR706S compounded in N_{2D} at 210 °C, 50 rpm for 15 min. For coated HANP wt% was equivalent to 2.5 wt% of uncoated HANP plate plus coating.

Material	HANP [wt%]	Coating [wt%]	$t_{5\%P}$ [°C]	
LR706S neat	-	-	282.8	± 9.9
is8PLAHA	4.9	50	306.4	± 3.0
is16PLAHA	3.6	30	300.8	± 0.7
is24PLAHA	5.6	55	303.9	± 0.1
DDSAHA	2.8	10	303.1	± 0.3
starPLAHA	3.9	35	302.4	± 0.4

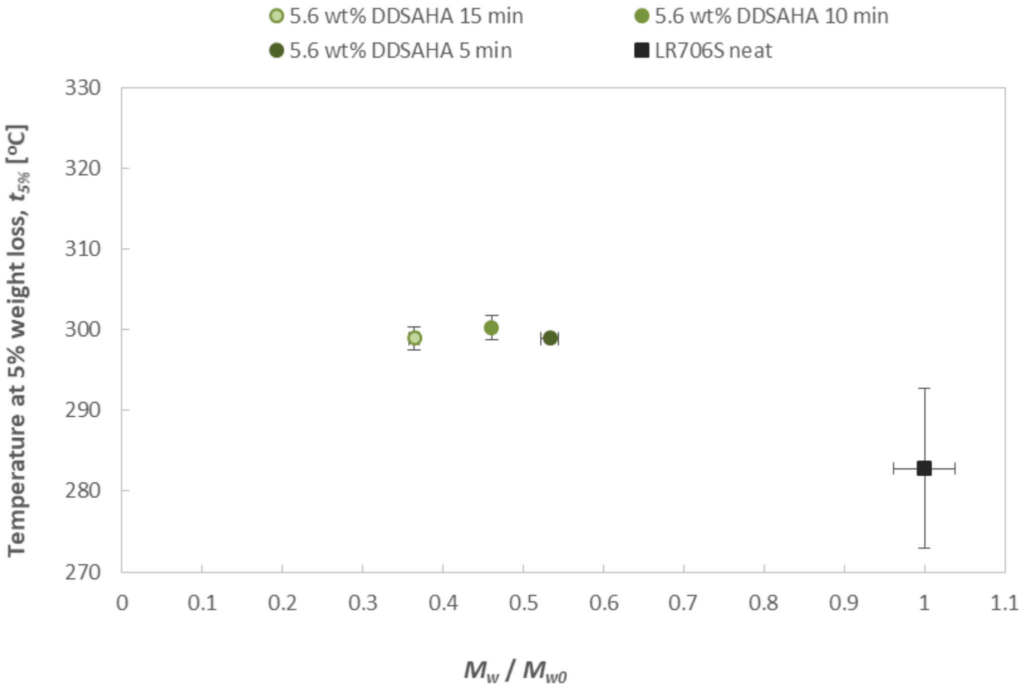

Figure 5.27. Temperature at 5% weight loss and M_w of 5.6 wt% DDSAHA nanocomposites mixed at 50 rpm and 210 °C in N_{2D} for 5-15 min. Where not shown, error bars are smaller than the size of the symbol.

5.3. Mechanical testing

Mechanical properties of LR706S and HANP nanocomposites were investigated after melt processing and measurements were carried out according to methods described in Section 3.2.11. Impact of compounding parameters and mixed particles on materials flexural strength (σ_f) and modulus was assessed. The analysed flexural testing results were adapted from a study by Ward [29] regarding *in vitro* hydrolytic degradation of HANP-LR706S nanocomposites and compared with materials molecular weight. It is worth emphasising that the nanocomposites discussed in [22] were produced by the author of this thesis.

5.3.1. Three-point bending results

Flexural strength and modulus of all the tested materials was compared with their M_w, shown in Figure 5.28(a) and Figure 5.29(a), to assess the influence of molecular weight on the mechanical properties. Results in both plots within the measured molecular weight of the materials appear to be in the plateau area with σ_f inclining slight decrease between 18% - 34% of M_{w0} for samples compounded in Air.

As no materials were produced with lower M_w, the plotted results were compared with the samples degradation study by Ward [29], shown in Figure 5.28(b) and Figure 5.29(b), to demonstrate dependence of mechanical properties of LR706S and HANP nanocomposites on M_w decreasing below 70 kg.mol^{-1} (so less than 17% of M_{w0}). It was shown that at this critical M_w flexural strength and flexural modulus of PLA materials decreased rapidly towards zero. This confirmed that molecular weight had a large influence on decreasing mechanical properties at low M_w (below 70 kg.mol^{-1} for LR706S materials) but at high values had no noticeable effect on E with diminished impact on σ_f, increasing slightly for greater M_w, as per fitted linear regression in Figure 5.28(a) and Figure 5.29(a). The mechanical properties of many materials are dependent on the molecular weight up to a critical value, known as the critical entanglement length. This has previously been shown by both

Fernández et al. [172], for poly (ethylene brassylate), and De Focatiis et al. [173], who demonstrated this dependency with the craze initiation stress of polystyrene at various molecular weights.

The aim of this study was to produce materials with properties comparable to flexural performance of human bones where there is a wide range of modulus values reported from 1 GPa to 20 GPa [82] and bending strength measured for a femur bone of 174 ±84 MPa [174]. As seen in Figure 5.28(a) and Figure 5.29(a) the achieved σ_f was in the range of 96 – 116 MPa, which fits the lower range for human femur, and E reached 3.3 – 5.1 GPa. The flexural properties of the produced materials were encouraging, however their decrease together with reduction of M_w after gamma irradiation sterilisation needs to be considered during design and production of medical devices [175] as even further degradation will occur after implantation. Results of bending tests for uncoated and coated HANP plate and HANP rod nanocomposites were studied separately to investigate influence of particles on the mechanical properties of the materials.

This space is intentionally left blank

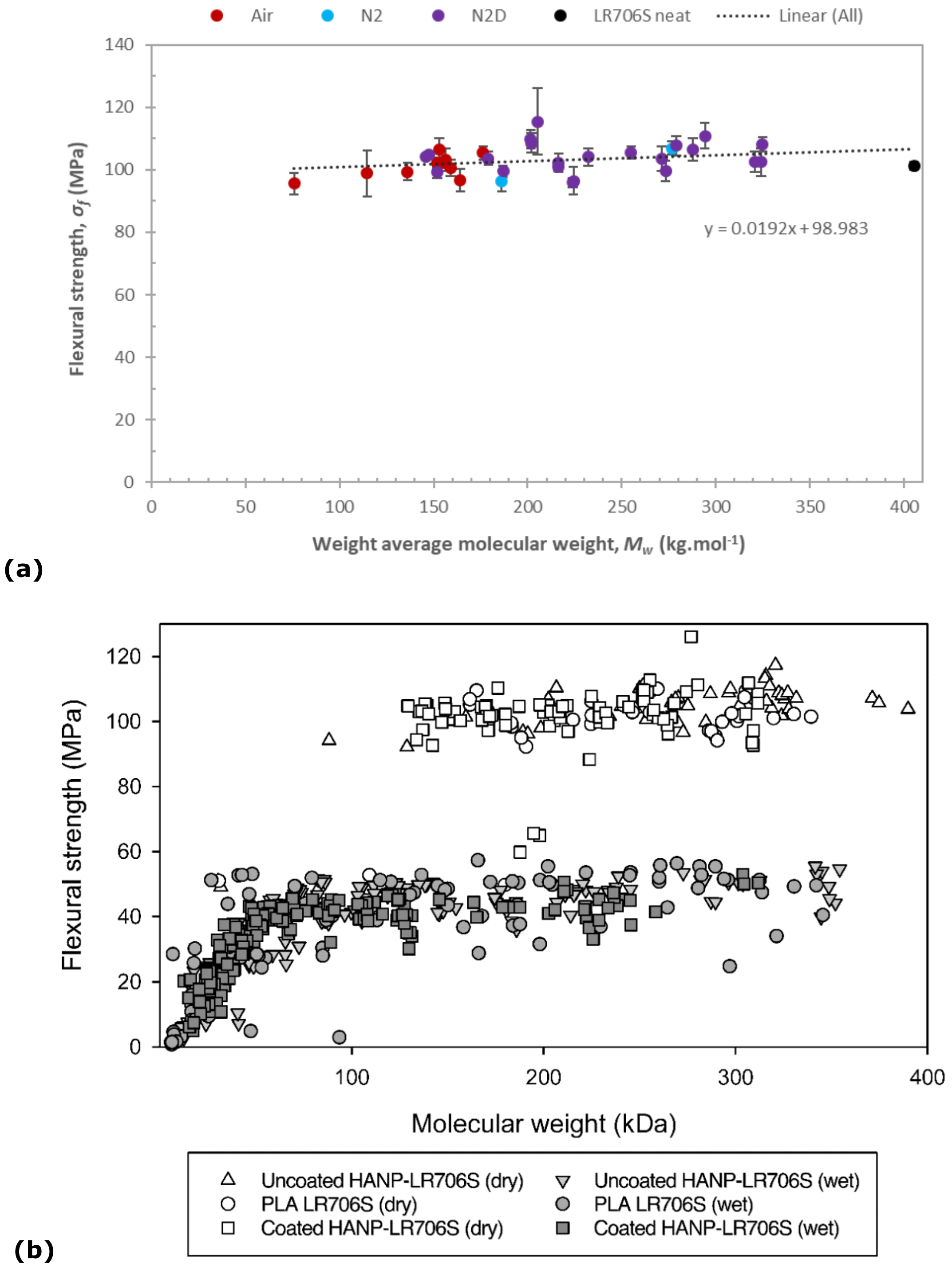

Figure 5.28. Flexural strength of materials after (a) production in Air, N_2 and N_{2D} in the MiniLab compared with (b) results after hydrolytic degradation adapted from Ward [29].

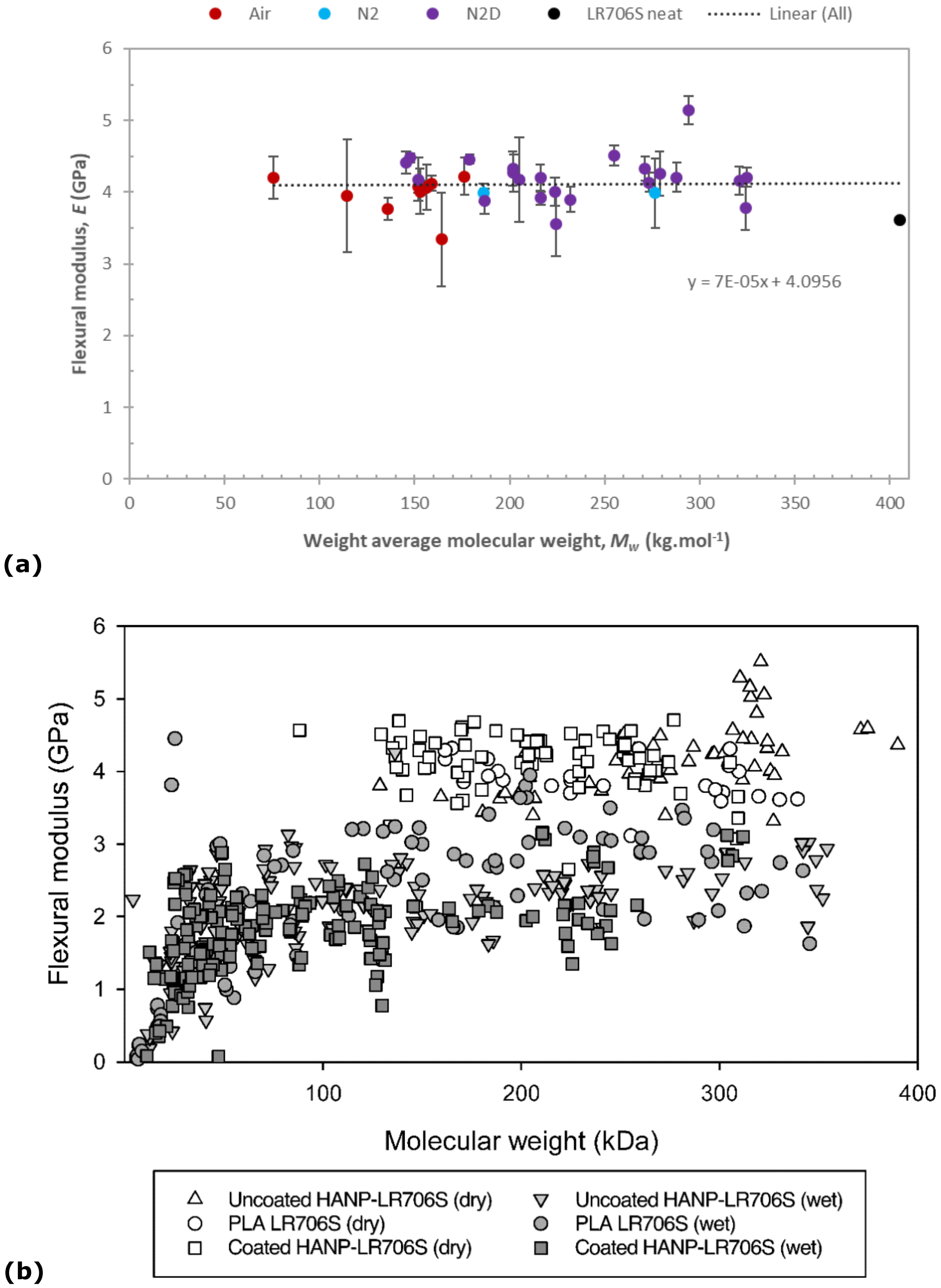

Figure 5.29. Flexural modulus of materials after (a) production in Air, N_2 and N_{2D} in the MiniLab compared with (b) results after hydrolytic degradation adapted from Ward [29].

5.3.1.1. HANP plates

Flexural performance of HANP plate nanocomposites produced in Air and N_{2D} was compared with the amount of particles in the polymer matrix and related to molecular weight, discussed earlier in Section 5.1.

The dependence of σ_f on the amount of HANP was more noticeable for materials compounded in Air, shown in Figure 5.30(a), as it was descending from the plateau area shown earlier with the declining molecular weight. The more HANP plates in Air the lower was M_w and the flexural strength decreased slightly while flexural modulus was increasing. The highest σ_f and the lowest E was recorded for a specimen produced from neat LR706S, with the opposite extreme of values shown for 10 wt% HANP nanocomposite where strength decreased by 6% and modulus increased by 17%. This shows that the strength of the materials was similar while the nanocomposite with the highest amount of filler was stiffest.

Measurements for 5 wt% HANP plate nanocomposite had the greatest level of uncertainty. Additionally, σ_f and E of LR706S recirculated in N_{2D}, shown in Figure 5.30(b), were comparable with the values for the 10 wt% HANP nanocomposite in Air despite its 65% lower M_W. This implies beneficial influence of filler on stiffness of PLA in spite of substantial decrease of molecular weight of the polymer matrix causing decrease in strength which, at 19% of M_{W0}, would be expected to be even lower without HANP presence.

Change of mechanical properties of HANP plate materials, which were marginally dependent of M_w in the plateau region, and PLA compounded in N_{2D} were shown in Figure 5.30(b). Neat LR706S decreased its strength by 5% and increased modulus by 11% after mixing in N_{2D} as the molecular weight practically halved and PLA became stiffer. Once HANP plates were compounded with PLA the flexural strength and modulus increased above values for the nanocomposites in Air. This implies that materials produced in N_{2D} were stronger and stiffer. The greatest E was obtained for 2.5 wt% HANP plate and σ_f for 5 wt% HANP plate nanocomposite which were 25% and 7% higher respectively than neat

LR706S. The lowest *E* was measured for 5 wt% HANP plate which was 20% higher than unprocessed PLA and the lowest σ_f for 10 wt% HANP plate nanocomposite in N_{2D} which was comparable to neat LR706S due to error size.

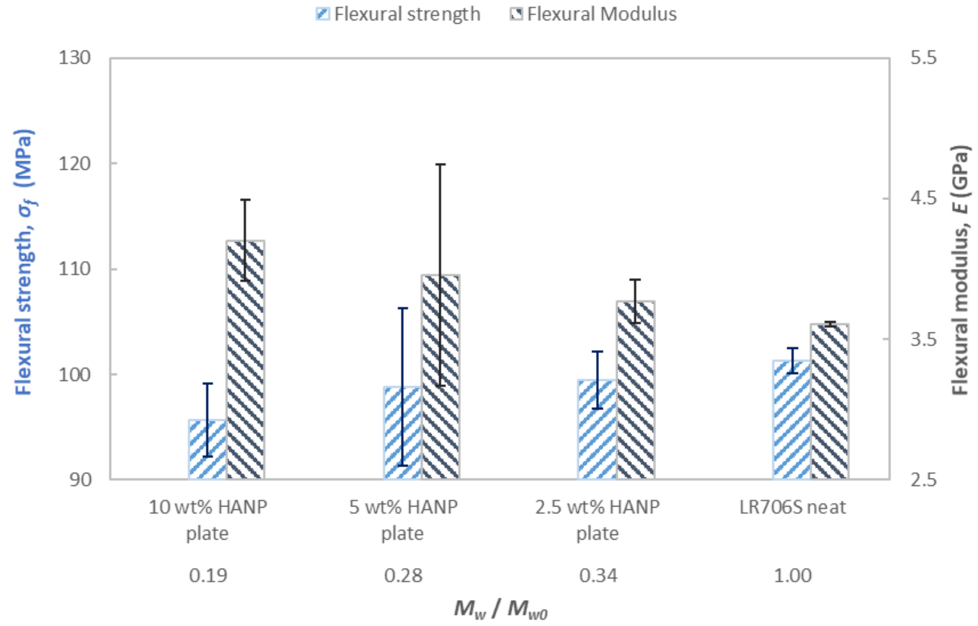

(a)

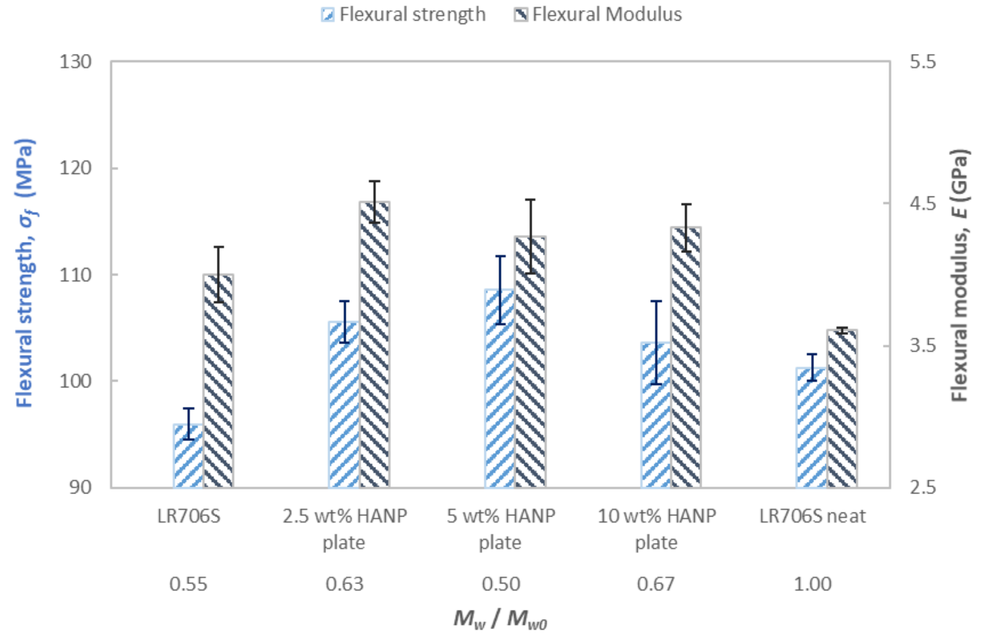

(b)

Figure 5.30. Flexural strength and modulus for 2.5 – 10 wt% HANP plate nanocomposites compounded in (a) Air and (b) N_{2D} versus neat LR706S.

5.3.1.2. HANP rods

The flexural properties of 2.5 wt% HANP rod nanocomposites in N_{2D} and Air were similar due to greater results uncertainty for the later one, as shown in Figure 5.31, despite 48% difference in M_w as in the plateau region. Overall, the modulus of 2.5 and 5 wt% HANP-LR706S was comparable to PLA mixed in N_{2D} while σ_f for 2.5 wt% filler content was 7% higher than neat LR706S and at 5 wt% it came down to level of the unprocessed polymer. The greatest change of σ_f and E was measured for 10 wt% HANP rod nanocomposite which were respectively 10% and 43% higher than for neat LR706S. A similar level of improvement was reported in other research about 10 wt% HA-PLA micro and nanocomposites [109] where greater raise of σ_f and E (relative to PLA only) of 6% and 65% respectively was shown for the composite consisting of 5 wt% micro HA and 5 wt% HANP.

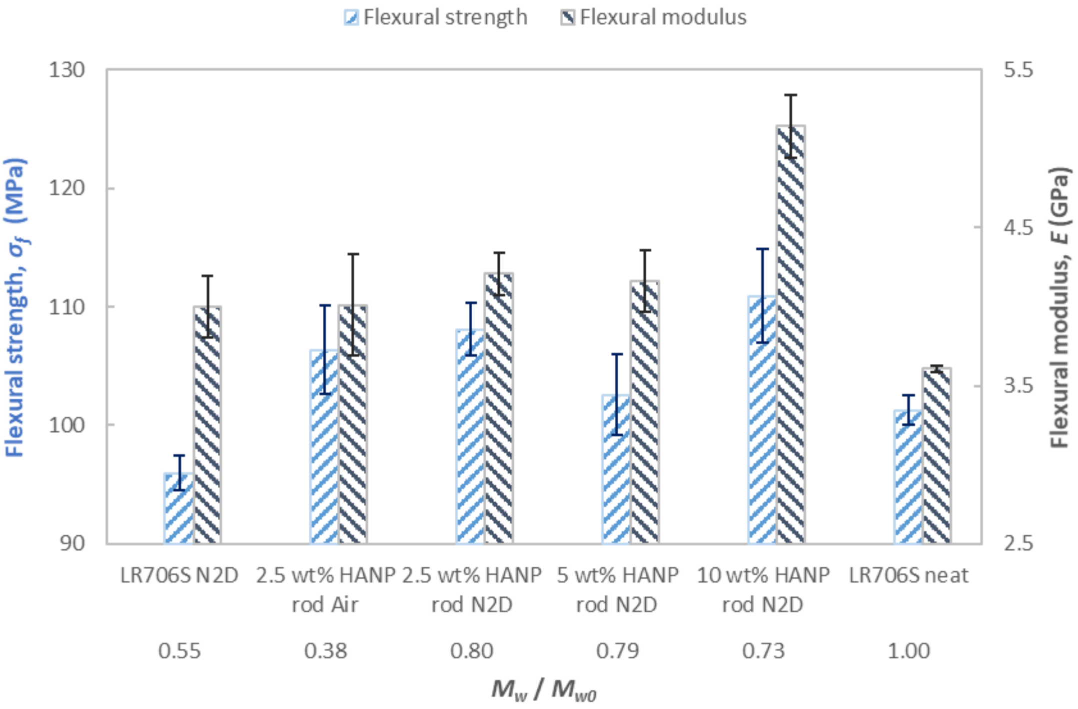

Figure 5.31. Flexural strength and modulus for 2.5 – 10 wt% HANP rod nanocomposites compounded in Air and N_{2D} versus LR706S.

This suggests that at 10 wt% HANP rod loading particles partially agglomerated during compounding in a beneficial proportion which gave a bimodal composite [109] displaying synergistic flexural properties. This effect was not seen for any other tested HANP-LR706S materials, which infers that they were in majority displaying nanocomposite properties at lower particle loadings or behaving like micro composites at higher HA content due to agglomeration. Further investigation of nanoparticles and agglomerates in 10 wt% HANP rod nanocomposite versus other produced materials is required to clarify that hypothesis.

5.3.1.3. Coated HANP

Flexural performance of nanocomposites compounded in N_{2D} with coated HANP plates, which had a marginal dependence on M_w (as in plateau region), was shown in Figure 5.32. The 2.8 wt% DDSAHA nanocomposite had the greatest magnitudes for σ_f and E which were 14% and 16% higher, respectively, than for neat LR706S. However, it is also worth mentioning that the DDSAHA composite had the greatest levels of uncertainty.

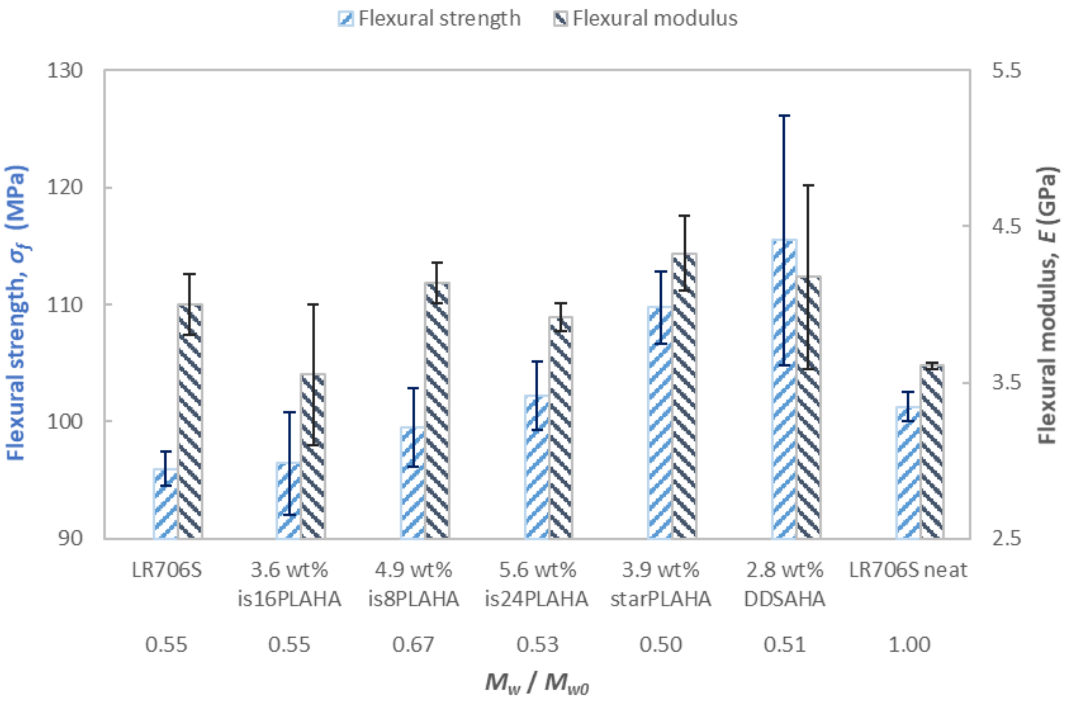

Figure 5.32. Flexural strength and modulus for coated HANP plate nanocomposites, all equivalent to 2.5 wt% uncoated HANP plate, compounded in N_{2D} versus LR706S.

In terms of flexural performance, DDSAHA was seen to be comparable to 3.9 wt% starPLAHA and 2.5 wt% uncoated HANP shown earlier in Figure 5.30(b). Therefore assessing which nanocomposite with coated HANP had the best mechanical properties was challenging. The 3.6 wt% is16PLAHA composite had also high level of uncertainty and its σ_f and E was similar to the remaining two nanocomposites and LR706S mixed in N_{2D}.

Comparison of mechanical properties of 5.6 wt% DDSAHA-LR706S compounded in N_{2D} for 5-15 min was shown in Figure 5.33. The highest values of σ_f and E were achieved after 15 min of mixing, which were 4% and 7% greater respectively when compared with the DDSAHA nanocomposite mixed for 5 min. This infers improved dispersion of the nanoparticles with the increased mixing time, which supports the earlier hypothesis in Section 4.4.2. It also shows that mechanical testing could be a simple method for the optimisation of melt compounding conditions for nanocomposites mixing.

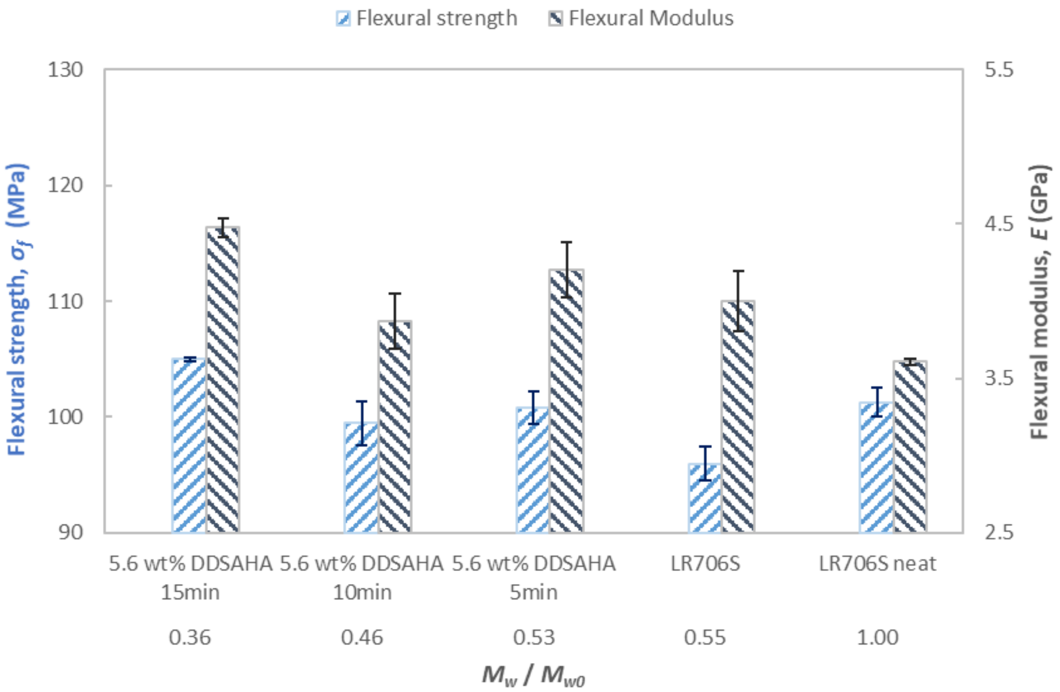

Figure 5.33. Flexural strength and modulus for 5.6 wt% DDSAHA nanocomposites compounded for 5-15 min in N_{2D} versus LR706S.

5.4. Conclusions

Higher molecular weight of materials mixed under dried N_2 and the inclusion of dry HA nanoparticles infers that reduced moisture content in the gas reduces the amount of water in the material which preserved M_w through minimised hydrolytic degradation. The highest range of molecular weights was reported for HANP rod composites in N_{2D} with the greatest M_w at 2.5 wt%. Additionally, molecular weight was decreasing with increasing amount of filler, regardless of the type of HANP, probably due to the polymer shearing with agglomerated particles. The composites loaded with higher amounts of agglomerated nanoparticles most likely acted as microcomposites causing M_w reduction compromising the mechanical properties of PLA, clearly observable for HANP plates in Air.

For coated particles compounded with LR706S in N_{2D} only the nanocomposite with is8PLAHA had M_w 22.1% greater than PLA which was even 7.2% higher than for HANP plate. The is16PLAHA nanocomposite had molecular weight comparable to processed PLA and for other materials with coated HANP M_w was lower than for the polymer.

It was also shown that increasing screw speed from 50 to 100 rpm did not accelerate degradation of the materials and further increase up to 150 rpm had only marginal influence on M_w. Mixing of the nanocomposites with time extending from 5 to 15 min decreased their molecular weight, as expected, due to increased residence time at 210 °C.

The M_w was compared with wall shear stress half-life time during compounding in the MiniLab and power law trendline was fitted for all compounded materials. The $t_{1/2}$ of 2.5 and 5 wt% HANP rod nanocomposites and 2.5 wt% HANP plates was significantly greater than the calculated values which infers improved particle dispersion for those materials. This supports a suggestion of $t_{1/2}$ being also indicative of particle dispersion beyond its relation to PLA M_w. Compounding of HANP at 100 rpm increased $t_{1/2}$ when compared with 50 rpm runs without change in M_w, which suggests enhanced dispersion of particles. Further increasing of the speed to 150 rpm caused a reduction in $t_{1/2}$ and M_w due to shearing effects.

A rheological model was applied to assess thermal degradation of LR706S in Air in relation to residence time at 210 °C, calculated and measured M_w of compounded PLA materials was compared in an attempt to separate thermal and shear effects of melt processing on the polymer matrix. It was found that mechanical degradation had greater influence during shorter mixing of PLA, e.g. 5 min, whereas longer runs of 15 min resulted with dominating effect of thermal degradation. As majority of the materials were compounded for 15 min their thermal degradation would be identical according to the used model (with minor variations due to loading time in the MiniLab) hence decrease of measured M_w below calculated value was expected to occur due to shear. Following this assumption, it was estimated that increase of n_s up to 150 rpm did not increase mechanical degradation while for LR706S and nanocomposites mixed in N_{2D} influence of shear was reduced when compared with compounding in Air.

Higher measured than calculated M_w for HANP rods nanocomposites in N_{2D} once again suggested the greatest particle dispersion in those materials, especially at 2.5 wt%, as the effect of mechanical degradation, and partially thermal degradation, was compensated by the mixed filler. That beneficial effect was diminishing with increasing amount of HANP rods in PLA matrix as the molecular weight of the nanocomposites was decreasing. For HANP plates compounded with LR706S in Air, at 2.5 wt% the measured M_w was 11% higher than for processed PLA hence the influence of the mechanical degradation for the nanocomposite was proportionally smaller. As molecular weight of the HANP plate nanocomposites was decreasing with the increasing amount of filler the influence of mechanical degradation was growing. For nanocomposites with coated HANP compounded in N_{2D} only is8PLAHA had theoretical and measured M_w matching, which infers that effects of mechanical degradation were compensated by the mixed particles.

The remaining nanocomposites with other coated HANP had molecular weight lower than (i) their theoretical M_w and (ii) the M_w of 2.5 wt% HANP uncoated plates, hence their mechanical degradation was greater.

DSC measurements revealed that glass transition temperature for HANP plates compounded in Air was lower than for the nanocomposites produced in N_{2D}. Moreover, T_g of HANP rod nanocomposites in N_{2D} was practically identical to plates, most likely due to identical mineral composition and compounding conditions. The T_g of the materials was compared with their molecular weight in form of M_n^{-1} and linear regression was fitted which reflects Flory-Fox relation. It was shown that measured T_g of polylactic acid from Evonik LR series was higher than calculated values from Flory-Fox equation for PLA with 15% of D-lactide. Furthermore, T_g of the produced nanocomposites was comparable to the one measured for neat PLA and decreased only slightly with increasing amount of HANP plates compounded in Air due to decrease of their M_n by 86% when compared to neat LR706S. This infers that large changes of molecular weight are required to reflect it in the glass transition temperature of the material.

The temperature at 5% weight loss of the nanocomposites was compared to investigate their thermal stability. The $t_{5\%P}$ for the compounded materials was greater than for neat LR706S and for HANP plates it was higher than for rods. Additionally, $t_{5\%P}$ appeared to depend on molecular weight of the nanocomposites once their M_w was above 60% of M_{w0}. Also, $t_{5\%P}$ decreased with lowering amount of filler for the nanocomposites mixed in N_{2D} while their M_w increased. For coated HANP no greater improvement of $t_{5\%P}$ was seen when compared with 2.5 wt% uncoated HANP plates. Influence of screw speed on $t_{5\%P}$ of the nanocomposites compounded in N_2 was assessed. For 2.5 wt% HANP plates $t_{5\%P}$ increased with greater n_s, potentially due to improved particle dispersion, while for 2.8% DDSAHA it declined, affected probably by decomposition of the coating, and M_w was decreasing for both materials with increasing n_s. Compounding time did not have effect on $t_{5\%P}$.

Flexural properties were tested via three-point bending of miniature specimen and showed that modulus was independent of molecular weight of the materials over the considered range, while bending strength showed a small decrease with lowering M_w. Higher values of σ_f and E were found for HANP plate nanocomposites compounded in N_{2D} when compared with mixing in Air. The highest σ_f and E was shown for 10 wt% HANP rods in N_{2D} which suggested that partially agglomerated filler acted as microparticles and created a bimodal composite displaying synergistic flexural properties similar to those shown by Takayama et al. [109]. It was also shown that mechanical testing could be applied as a method for the optimisation of melt compounding conditions for nanocomposites mixing.

Based on the observations in this chapter the following recommendations of particle loading/processing conditions can be made:

- compounding under dried N_2 and the inclusion of dried HANP preserves M_w of PLA,
- screw speed can be increased under N_2 from 50 to 100 rpm to aid particle mixing at no or minimal (7%) decrease of M_w,
- the greatest improvements in PLA properties were shown for HANP mixed under N_{2D} at 2.5 wt%, especially for HANP rods, which exhibited the highest $t_{1/2}$ and M_w.

The main points to take away from this chapter are:

- any amount of particle addition increases the $t_{5\%P}$, but this does not increase further with additional filler,
- in the samples assessed, none experienced sufficient loss of molecular weight during processing to have a significant effect on T_g,
- mechanical degradation was the greater factor at short processing times (5 min), while thermal degradation dominated at higher processing times (15 min),
- flexural modulus was independent of molecular weight of the materials over the considered range, while bending strength showed a small decrease with lowering M_w.

In the next chapter, quantification of HANP dispersion will be estimated and related to the aforesaid results with particle mixing and distribution.

6. Quantifying HANP Dispersion

Measuring the true amount of HANP compounded with LR706S and investigating their dispersion in the polymer provides greater understanding of the results presented for the nanocomposites in previous chapters. Beyond the thermostability analysis reported in Section 5.2.3, TGA tests were carried out to confirm HANP content. TEM was also performed for particle dispersion overview, which was studied further via microcomputed tomography.

All these methods provide an insight into the dispersion found in the produced materials at differing resolutions. TGA sample mass fluctuated between 9 mg and 13 mg, which equates to a volume range of approximately 7.3 - 10.5 mm^3, while the volume of microCT scans ranged from 0.13 mm^3 to 1.33 mm^3. The surface area of the compared TEM images at magnification x26500 was 9.1 μm^2, and assuming the micrograph shows up to 1 nm depth of the ultramicrotomy section, the viewed volume would be 9.1E-6 mm^3. As a result of this, TEM images can only be used as indicators of particle dispersion in the nanocomposite in a very small area, even if many sites are sampled. The microCT scans provide more comprehensive insight into the sample, however microCT is a more time and cost consuming method which requires additional 3D image reconstruction for analysis. Results from both of those complementary imaging techniques are discussed in this chapter along with preliminary micrographs obtained from scanning electron microscopy.

6.1. Establishing HANP content

Thermogravimetric analysis was performed, following the method described in Section 3.2.5, to verify the actual content of HANP in PLA after mixing the desired amount of the materials in the MiniLab. See Figure 6.1 for examples of the results obtained from this analysis. As mentioned in Section 4.3, if loading overpressure occurred during manual feeding of the MiniLab, this led to small amounts of melt moving into free space behind the screws. Additionally, most of the coated HANP had a large static charge which caused small quantities of particles to deposit on surfaces near the extruder feeding tube in an uncontrollable manner. For these reasons, despite the closed recirculation system in the MiniLab, the produced nanocomposites were expected to have HANP content deviating from the exact calculated amounts prepared for compounding. However, possible HANP content variations along the sample extrudate also need to be taken into consideration, which may not be reflected in the TGA results due to the tested sample size.

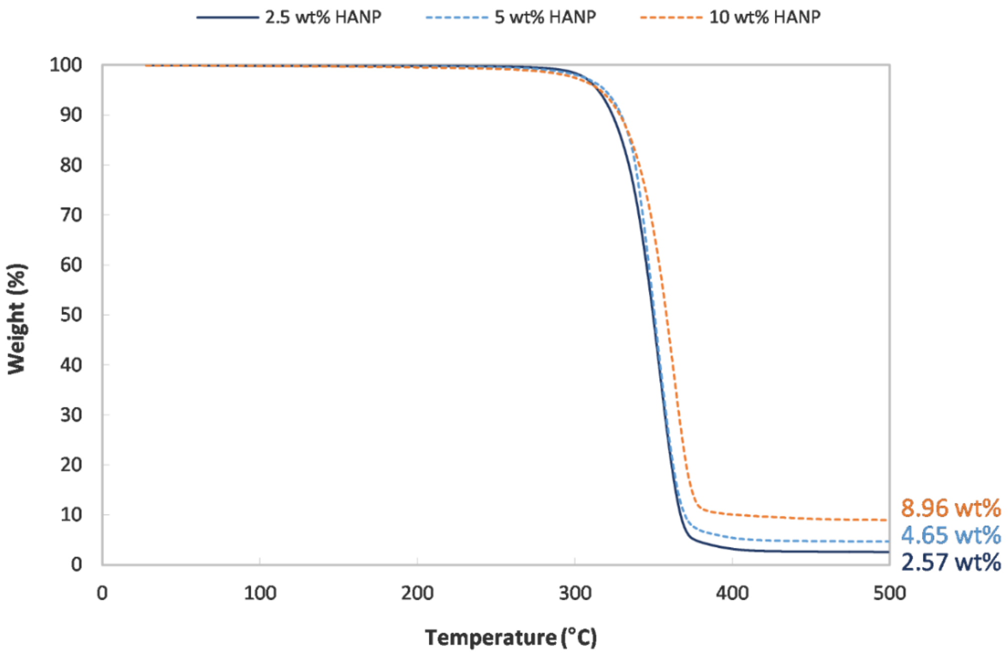

Figure 6.1. TGA measurements of 2.5 – 10 wt% HANP compounded with LR706S in the MiniLab at 50 rpm, 210 °C in Air for 15 min.

6.1.1. HA char residue in TGA measurements

The majority of the nanocomposites were produced nominally at 2.5, 5 and 10 wt% HANP in PLA, or an equivalent of these levels for particles coated with dispersants. A comparison of the calculated amount of filler prepared for compounding of the nanocomposites in the MiniLab versus measured HANP char residue in TGA is shown in Figure 6.2. Most of the nanocomposites had a measured amount of HANP which was less than the calculated loaded amount. From this point onwards, this condition will be termed ‘underloaded’ and the opposite condition termed ‘overloaded’. The underloaded condition was especially true for materials compounded with uncoated HANP in Air, which were manufactured first, and hence more susceptible to run-to-run variations resulting from human input. The variation between the calculated and measured weight percentage for the nanocomposites compounded in the first year with uncoated HANP was on average 12.75% (±6.37%) and in the final year it improved to 5.02% (±2.70), while for the coated HANP it was 11.48 (±8.83) and 11.96 (±8.91), respectively. Unfortunately, despite increasing proficiency of loading materials into the MiniLab, the compliance between the exact calculated amounts of materials prepared for nanocomposites compounding with coated HANP did not improve due to particles susceptibility to static charge.

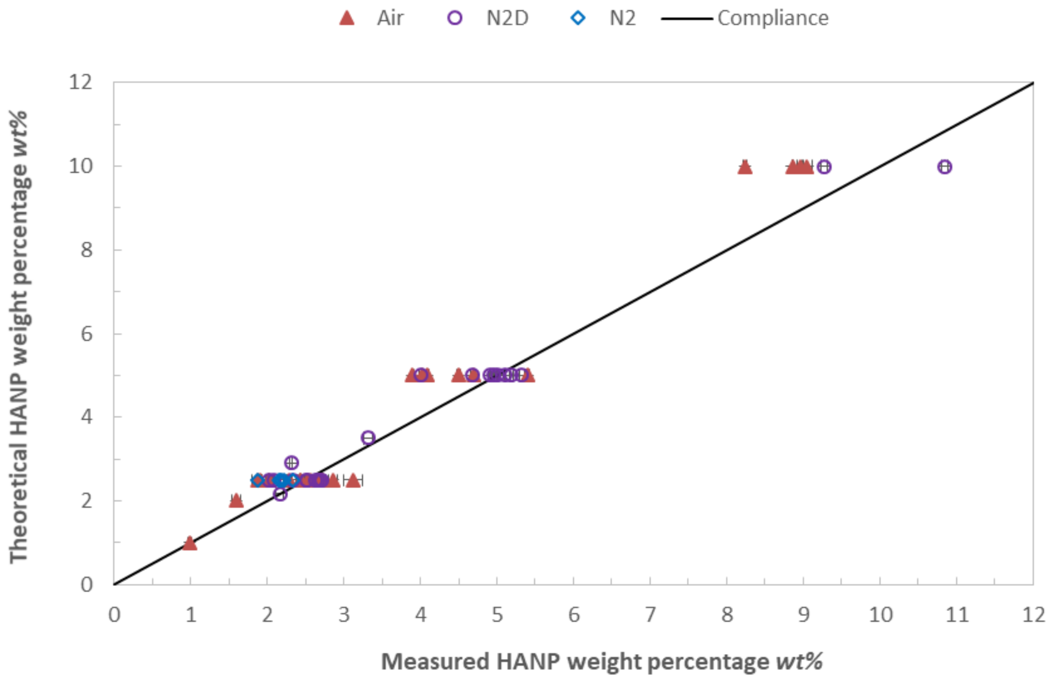

Figure 6.2. TGA measurements of HANP char residue after the nanocomposites burn off versus the calculated wt% of filler for compounding with LR706S in Air, N_2 and N_{2D}. Where not shown, error bars are smaller than the size of the symbol.

TGA results for various materials are reviewed separately in the coming subsections, to further investigate dependence of the properties of the nanocomposites on HANP loading. The measurements presented in previous chapters, i.e. $t_{1/2}$, M_W, T_g, $t_{5\%P}$, σ_f, were compared directly with the nominal calculated value of the particles in the material and so they need to be adjusted according to the determined HANP char residue for exact correlation, for example see Figure 6.3.

6.1.1.1. HANP rods

Char residue for HANP rod nanocomposites compounded in Air and N_{2D} is summarised in Table 6.1 and shows that the produced materials were overloaded (2 - 8%) versus the calculated nominal values of HANP, with the greatest deviation occurring for the sample with the highest filler content. To visualise this offset, the influence of the quantity of HANP rods on the molecular weight of the nanocomposites compounded in N_{2D} is shown in Figure 6.3 where the 8% deviation for 10 wt% HANP rod is noticeable.

Table 6.1. TGA measurements of HANP rod nanocomposites compounded in Air and N_{2D} at 210 °C, 50 rpm for 15 min.

Gas	Name	HA char [wt%]
N_{2D}	2.5 wt% HANP rod	2.64 ±0.01
N_{2D}	5 wt% HANP rod	5.11 ±0.01
N_{2D}	10 wt% HANP rod	10.84 ±0.04
Air	2.5wt% HANP rod	2.69 ±0.07

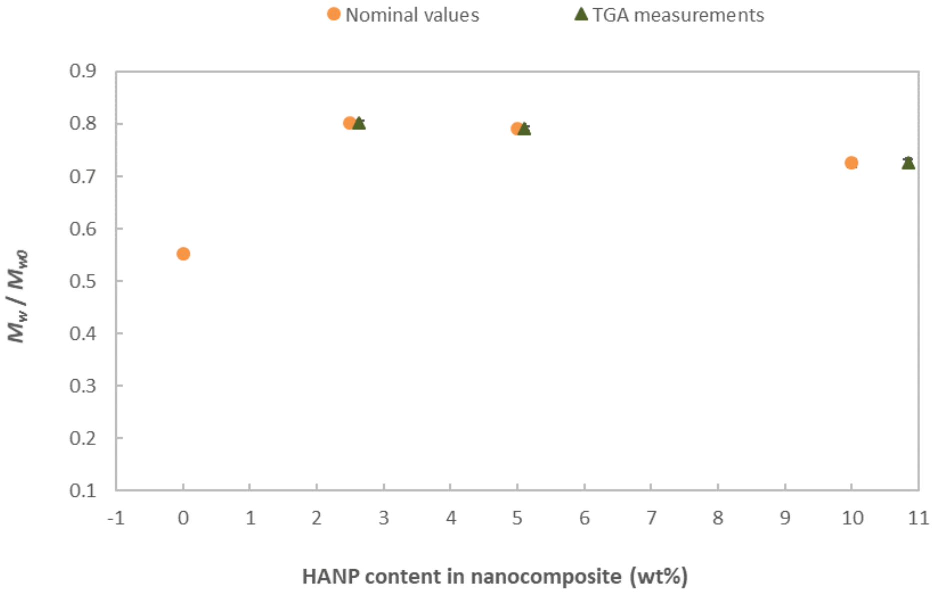

Figure 6.3. Nominal and actual amount of HA nanoparticles versus M_w/M_{w0} of HANP rod nanocomposites compounded at 50 rpm, 210 °C in N_{2D} for 15 min. Where not shown, error bars are smaller than the size of the symbol.

6.1.1.2. HANP plates

Char residue for HANP plate nanocomposites compounded in Air and N_{2D} is summarised in Table 6.2. The materials compounded in Air were underloaded by between 1% and 11% with the most underloading occurring for the nanocomposite with the highest wt% of filler. In contrast, for the HANP plates nanocomposites produced in N_{2D}, the HA char residue for samples with 2.5 - 5 wt% were close to the calculated nominal values (deviation below 1%), whereas for the 10 wt% HANP plate the underloading increased to 7%. This confirms the poorest correlation of calculated and measured amount of filler for 10 wt% HANP plates and rods, which was expected as a thin film of PLA with embedded unmixed HA powder was found adhered on the screws and walls of the extruder after compounding. From this it can be concluded that recirculation in the MiniLab at 50 rpm was insufficient to mix 10 wt% HANP with LR706S effectively.

Table 6.2. TGA measurements of HANP plate nanocomposites compounded in Air and N_{2D} at 210 °C, 50 rpm for 15 min.

Gas	Name	HA char [wt%]
N_{2D}	2.5 wt% HANP plate	2.52 ±0.01
N_{2D}	5 wt% HANP plate	5.01 ±0.01
N_{2D}	10 wt% HANP plate	9.27 ±0.04
Air	1 wt% HANP plate	0.99 ±0.03
Air	2.5 wt% HANP plate	2.44 ±0.05
Air	5 wt% HANP plate	4.50 ±0.02
Air	10 wt% HANP plate	8.86 ±0.01

6.1.1.3. Coated HANP

The content of pure HA in coated HANP was reviewed and results from the TGA measurements for the nanocomposites compounded in Air and N_{2D} are summarised in Table 6.3. The results indicate a reasonable reproducibility in the amount of filler with the same type of coating compounded with LR706S in Air and N_{2D}. The exception to this being is8PLAHA where the materials mixed in N_{2D} had 2.5 times more HA char than in Air. Additionally, is16PLAHA nanocomposites had 19% lower HA content for both runs than the nominal 2.5 wt% calculated for compounding. These exceptions raised questions about actual particle coating level.

The HANP coating level given when the particles were provided for compounding, shown in Table 3.2 in Section 3.1.3, were compared with the TGA measurements listed by Walton [26] for the batches discussed in her work, see Table 6.4. There was a large variation in batch-to-batch coating for is16PLAHA (31.5% - 54.6%). The effect of this was mitigated in the nanocomposite compounding in the MiniLab, as all the samples that were compounded in Air and N_{2D} for a given coating type were made using the same batch of particles. The only exception to this was for the 4.9 wt% is8PLAHA, which clearly suffered from substantial batch-to-batch variation. The first batch had a coating level of 50 wt% and the second batch 18.6 wt%. Other than for is8PLAHA, the residual HA char amounts for the nanocomposites listed in Table 6.3 were close to the nominal 2.5 wt% (deviation between 2% and 8%), indicating correct batch coating analysis.

Table 6.3. TGA measurements of the nanocomposites compounded with coated HANP in Air and N_{2D} at 210 °C, 50 rpm for 15 min. The nominal HANP wt% was equivalent to 2.5 wt% of uncoated HANP plus coating.

Gas	Name	HA char [wt%]
Air	2.8 wt% DDSAHA	2.56 ±0.12
N_{2D}	2.8 wt% DDSAHA	2.67 ±0.02
Air	4.9 wt% is8PLAHA	1.91 ±0.01
N_{2D}	4.9 wt% is8PLAHA	4.80 ±0.10
Air	3.6 wt% is16PLAHA	2.02 ±0.04
N_{2D}	3.6 wt% is16PLAHA	2.02 ±0.03
Air	5.6 wt% is24PLAHA	2.43 ±0.02
N_{2D}	5.6 wt% is24PLAHA	2.71 ±0.05
Air	3.9 wt% starPLAHA	2.53 ±0.02
N_{2D}	3.9 wt% starPLAHA	2.52 ±0.04

The coating levels listed in Table 6.4 and in Table 3.2 differ as they refer to different polylactide coated HANP batches produced during the development of the novel particles.

Table 6.4. The amount of dispersants in coated HANP particles by Walton [26]; (a) produced at lower dispersant concentration in the solution; (b) after 1 year of storage in a glass vial placed in a desiccator under atmospheric pressure at room temperature.

Name	Coating [wt%]
is8PLAHA	18.6 [26]
is16PLAHA[a]	31.5 [26]
is16PLAHA	54.6 [26]
is16PLAHA[b]	41.8 [26]
is24PLAHA	63.8 [26]
starPLAHA	30.8 [26]

Therefore, the production of the nanocomposites with coated HANP was affected by error from several sources including: manual loading of small amounts of static filler, batch-to-batch filler coating level variation and dispersant degradation due to storage. These laboratory scale compounding issues can be mitigated by HANP manufacturing and nanocomposite extrusion at larger scale, which was achieved through scale-up activities discussed further in Chapter 7.

6.1.1.4. HANP loading reproducibility

It was found that the HANP content deviation had an influence on experiment reproducibility discussed earlier in Section 4.3. Properties of the two 10 wt% HANP plate nanocomposites compounded in Air at 100 rpm are compared in Table 6.5. Despite loading the same amount of materials into the MiniLab and processing with identical parameters, experiments had inherent run-to-run variation due to manual handling and the aforementioned issues with mixing high filler content. This resulted in 10 - 18% underloading of particles in the nominal 10 wt% HANP plate nanocomposites which affected $t_{5\%P}$, M_w and $t_{1/2}$. However, this particle loading variation for 10 wt% HANP plate was one of the greatest from all the nanocomposites with uncoated HANP mixed in Air. The majority of the nanocomposites with uncoated HANP had particle loading variation below 11% of the calculated nominal value, see Table 6.1 and Table 6.2.

Table 6.5. Experimental reproducibility of compounding of 10 wt% HANP plate nanocomposite in the MiniLab at 210 °C, 100 rpm for 15 min in Air.

Run	HA char [wt%]	$t_{5\%P}$ [°C]	M_w [kg.mol^{-1}]	$t_{1/2}$ [s]
#1	8.24 ±0.03	308.2 ±6.1	72.0 ±4.5	185 ±3
#2	9.05 ±0.06	309.0 ±5.9	85.4 ±1.2	275 ±4

Table 6.6. Particle amount deviation for coated and uncoated HANP nanocomposites compounded in the MiniLab at 50 - 150 rpm, 210 °C for 15 min in N_2. HANP wt% was equivalent to the nominal 2.5 wt% of uncoated HANP plus coating for DDSAHA.

n_s [rpm]	Name	HA char [wt%]	$t_{5\%P}$ [°C]	M_w [kg. mol^{-1}]	$t_{1/2}$ [s]
50	2.5 wt% HANP plate	1.88 ±0.02	301.7 ±0.9	276.6 ±3.2	1735 ±26
100	2.5 wt% HANP plate	2.19 ±0.03	312.1 ±1.4	252.3 ±3.6	1717 ±29
150	2.5 wt% HANP plate	2.16 ±0.09	315.5 ±3.7	223.7 ±1.9	1161 ±18
50	2.8 wt% DDSAHA	2.33 ±0.05	318.1 ±5.1	263.8 ±1.7	1441 ±44
100	2.8 wt% DDSAHA	2.22 ±0.05	301.8 ±0.9	264.7 ±0.2	2325 ±89
150	2.8 wt% DDSAHA	2.16 ±0.09	300.9 ±1.5	235.2 ±2.5	1880 ±65

TGA measurements deviating from the calculated 2.5 wt% are summarised in Table 6.6 with various n_s. The HANP plate nanocomposites were found to be underloaded by 12 – 25%. Yet, the effect of compounding with different n_s was a dominating factor over the particle amount variation and $t_{5\%P}$ increased for higher n_s while M_w and $t_{1/2}$ decreased. Similarly, for DDSAHA nanocomposites, which were found to be 7 – 14% underloaded, the main cause was changing n_s over deviations in the particle amount.

When compounding with increasing mixing time, t_R was seen to have a dominating effect over the 1 – 7% variation in the particle quantity on the parameters of produced DDSAHA nanocomposites, see in Table 6.7.

Table 6.7. Particle amount deviation for 5.6 wt% DDSAHA nanocomposite mixed at 210 °C, 50 rpm in N_{2D} with varying compounding time. HANP wt% was equivalent to 5 wt% of uncoated HANP plus coating.

t_R [min]	HA char [wt%]	$t_{5\%P}$ [°C]	M_w [kg. mol^{-1}]	$t_{1/2}$ [s]
5	5.33 ±0.03	298.9 ±0.8	216.2 ±4.5	499 ±26
10	4.96 ±0.01	300.3 ±1.5	186.9 ±0.7	606 ±11
15	5.19 ±0.02	298.9 ±1.4	147.7 ±2.4	729 ±13

Table 6.8. Influence of deviation of HA amount for the nominal 2.5 wt% HANP plate nanocomposites mixed in Air, N_2 and N_{2D} at 210 °C, 50 rpm for 15 min. HANP were compounded after a direct transfer from a dry anaerobic glove box or (#) after drying at 300 °C.

Gas	HA char [wt%]	M_w [kg.mol^{-1}]	$t_{1/2}$ [s]	E_{mix} [kJ] at t_R = 10 min
Air	2.44 ±0.05	136.1 ±1.5	727 ±7	4.25
N_2	1.88 ±0.02	276.6 ±3.2	1735 ±26	5.11
N_{2D}	2.09 ±0.01	287.9 ±1.4	1690 ±29	4.80
N_{2D}	#2.52 ±0.01	255.1 ±2.2	15212 ±1438	5.89

Another example on how variations in the amount of particles can influence properties of compounded nanocomposite is shown in Table 6.8, where 2.5 wt% HANP plates (deviation 1 - 25%) were mixed with LR706S in Air, N_2 and N_{2D} at 50 rpm. Materials are listed in the table with a decreasing amount of moisture in the system: the first nanocomposite was compounded in ambient air with dried PLA and HANP and was transferred directly from a dry anaerobic glove box, while HANP for the last composite was dried at 300 °C and mixed with LR706S under N_{2D}.

Therefore, it was expected that M_w, $t_{1/2}$ and E_{mix} would increase in that order with decreasing hydrolytic degradation due to limiting moisture during processing. However, as the intermediate nanocomposites compounded in N_2 and N_{2D} were underloaded by 25% and 16% respectively, their molecular weight was higher than the materials processed in the driest conditions at 2.52 wt% loading due to better particle dispersion with the same screw speed but with less filler. This is in line with previously shown results for plate HANP-LR706S nanocomposites, refer to Table 5.1 in Section 5.1.1.1, where M_w and $t_{1/2}$ are shown to be decreasing with increasing wt% of HANP.

6.2. Preliminary scanning electron microscopy

SEM was utilised to investigate morphology of the nanocomposites and explore application of the method for observing particle dispersion and agglomeration. The approach was applied to the first nanocomposites that were produced; 10 wt% plate HANP-LR706S compounded in Air at 210 °C and 100 rpm for 15 min.

6.2.1. Method

The extruded nanocomposite samples were cryofractured, mounted onto a stub using double-sided carbon tape and sputtered with platinum (at 1.5 kV and 10 mA for 90 s), to obtain around 2 nm of coating to ensure high electrical conductivity.

SEM images were obtained on the fractured surface with a Philips FEI XL30(W) SEM operated at 10 kV, with an additional Energy-Dispersive X-ray (EDX) detector used for elemental analysis.

6.2.2. SEM micrographs

SEM images for a 10 wt% HANP plate nanocomposite are shown in Figure 6.4 and Figure 6.5. Large HANP aggregates, of up to 100 μm in diameter, were observed, see Figure 6.5(a), with poor polymer adhesion illustrated in Figure 6.4(a-c). Beam damage of the nanocomposite sample occurred during measurement as shown in Figure 6.4(d). The applied melt processing parameters for the 10 wt% plate HANP-LR706S nanocomposite were similar to conditions optimised by Mathieu et al. [80] (205 °C and a screw speed of 100 rpm), yet the achieved dispersion was worse than in the HA-PLA nanocomposite compounded by Mathieu et al. [80] (see Figure 2.6(c) in Section 2.2.3). However, this group used PLA with an IV of 1.6 dl.g^{-1}, while LR706S has an IV of 4 dl.g^{-1}, hence the nHA mixed with greater ease as a result of the shorter polymer chains.

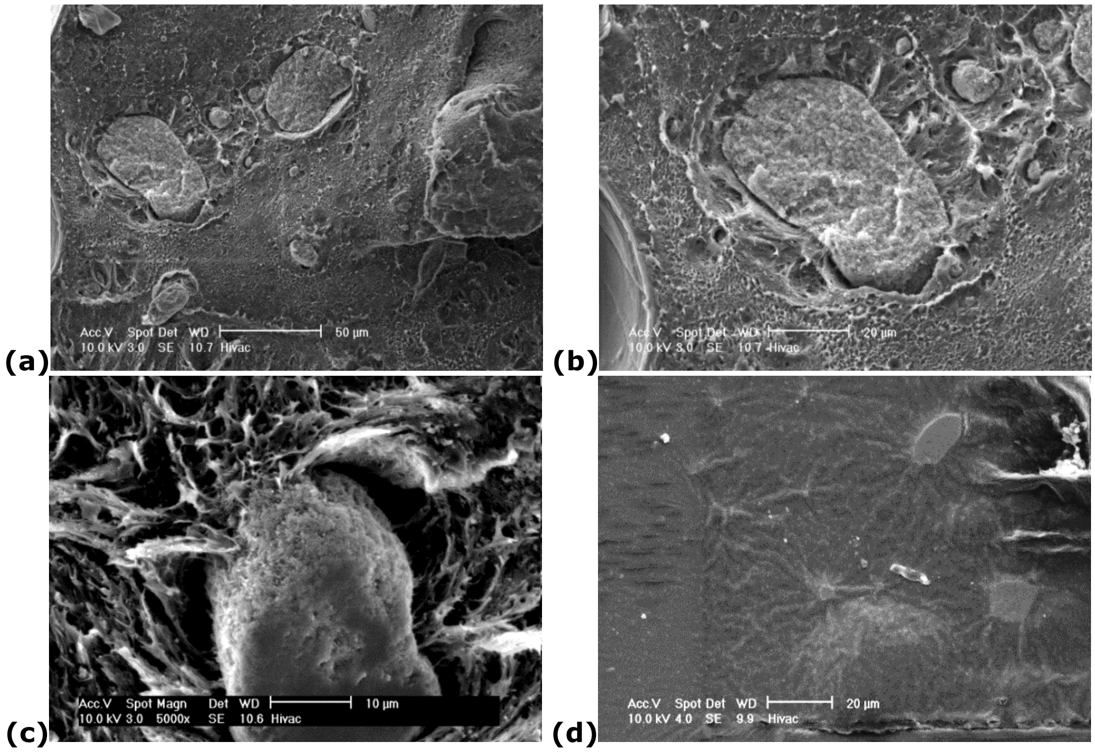

Figure 6.4. SEM images of 10 wt% plate HANP-LR706S mixed in Air: (a) micron size HA agglomerates, scale bar 50 µm, (b) focus on aggregate in section A, scale bar 20 µm, (c) polymer delamination on HANP surface, scale bar 10 µm, (d) beam damage of PLA, scale bar 20 µm.

EDX was used for elemental analysis to confirm that the agglomerates were HANP. Figure 6.5(b) illustrates that relatively high peaks for phosphorus and calcium were recorded for Spectrum 2 marked on Figure 6.5(a), which relates to the chemical composition of HA provided in Section 2.2.2 (for which the expected Ca:P ratio is 5:3). A large amount of carbon was revealed for Spectrum 1, indicating PLA, with some traces of phosphorus and calcium corresponding to the fine dispersion of HANP plates, which will be shown on TEM images in Section 6.3.1.

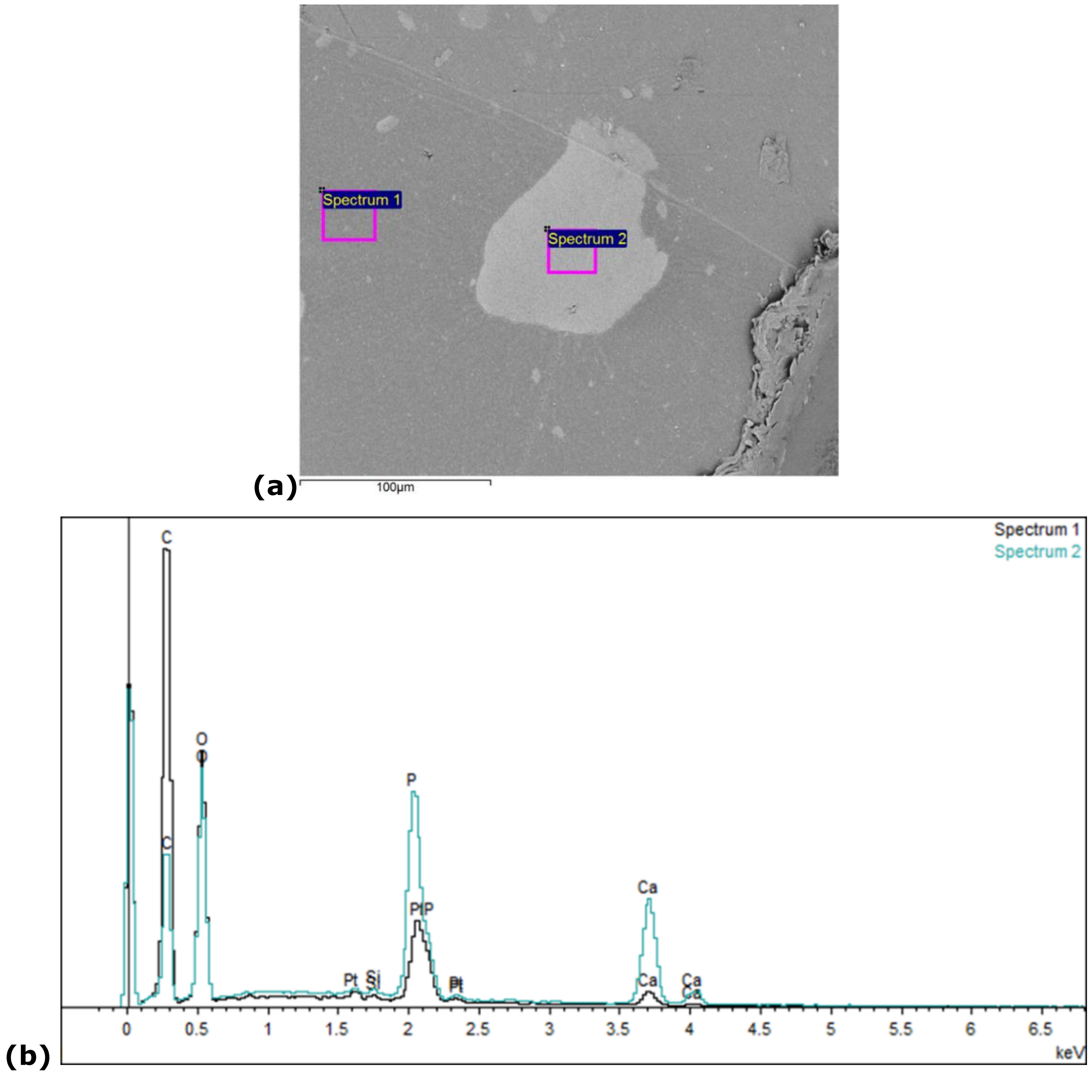

Figure 6.5. (a) SEM micrograph with large micron size HA agglomerate in 10 wt% HANP plate nanocomposite mixed in Air, Spectrum 1 and 2 highlighted for EDX measurement, scale bar 100 μm. (b) EDX graph with distribution of elements for Spectrum 1 and 2.

Measurements of the distribution of elements were performed on relatively small areas of the sample, therefore EDX element maps were recorded on a larger field of 140×140 μm, shown in Figure 6.6. Figure 6.6(a) is a backscattered electron image of the nanocomposite, with brighter areas indicating higher density – the high density HA ceramics can clearly be seen. Figure 6.6(b) shows a carbon rich area related to the polymer (the roughened surface indicates PLA beam damage). Darker circles with less carbon correspond to the HANP agglomerates. Brighter rounded areas on Figure 6.6c and Figure 6.6d represent a high content of calcium and phosphorus respectively, related to the HA structure. Calcium and phosphorus can be seen across the images, reflecting the fine dispersion of HANP platelets in the PLA.

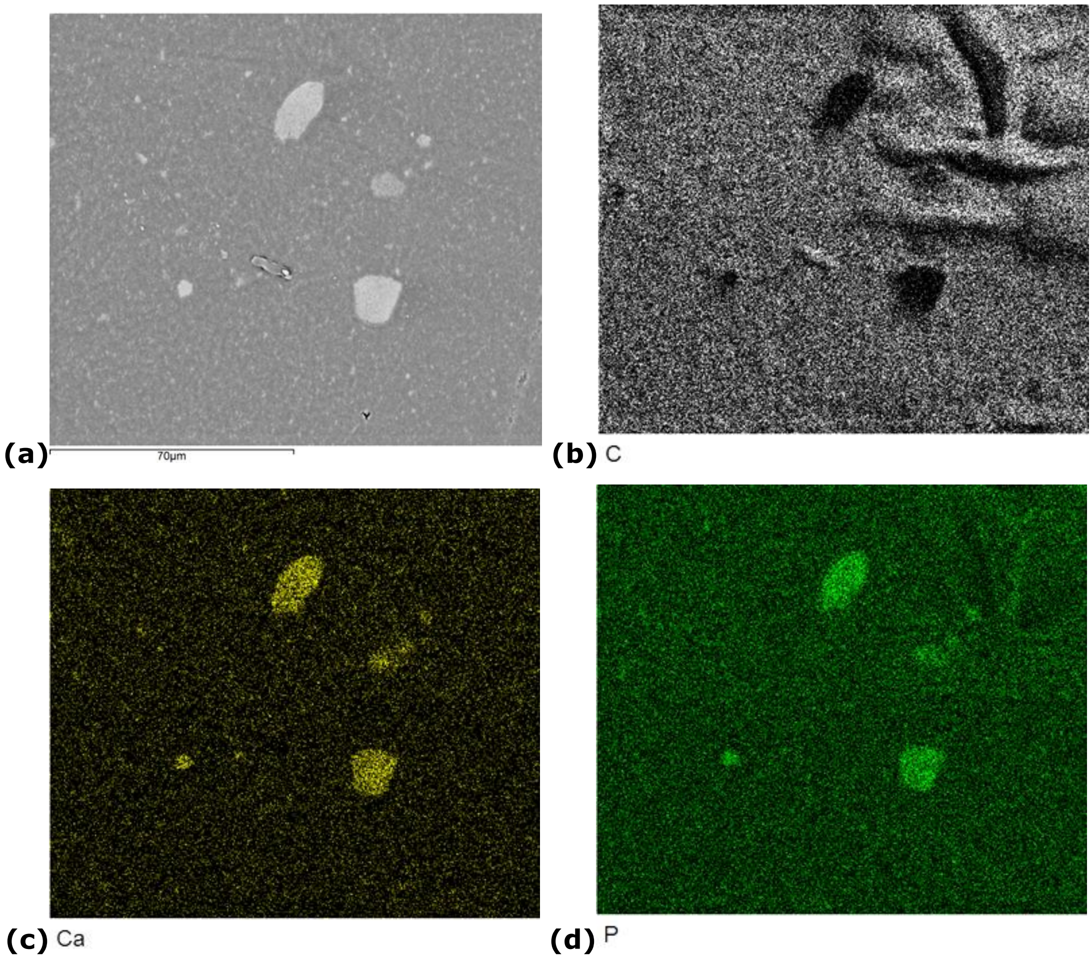

(a) **(b)** C

(c) Ca **(d)** P

Figure 6.6. (a) SEM micrograph of 10 wt% HANP plates in LR706S compounded in Air. EDX maps for elements: (b) carbon (C), (c) calcium (Ca), (d) phosphorus (P).

It was decided that SEM is a sufficient method for viewing HA macro sized agglomerations however nanosized dispersion can be only confirmed via additional lengthy EDX elemental analysis on a large sample area. As it was desirable to observe the particle dispersion at the nanoscale, transmission electron microscopy was employed for imaging which also allows for the viewing of macro sized agglomeration at low magnification, see for example Figure 6.7(e) in Section 6.3.1.1.

6.3. Transmission electron microscopy

The extruded HANP-LR706S nanocomposites were sectioned via ultramicrotomy and TEM images were acquired as per methods described for both in Section 3.2.9. Therefore one microscopy method, requiring single sample preparation, allowed for examining the nanocomposites at macro and nanoscale, which was more efficient.

6.3.1. Quantification of HANP dispersion

A simple semi-quantitative method was employed for TEM image analysis, shown by Khare et al. [125] and described earlier in Section 2.6. Out of all the reviewed image analysis approaches for TEM micrographs, this method was chosen mainly due to its ease of use in manual application for processing multiple images. The method entails determining the largest open square that can be applied on the micrograph without crossing or encapsulating any particle. It was assumed that with decreasing free space on the image (thus decreasing square size) either the dispersion of HANP improves or the wt% HANP increases. Three different micrographs at the same magnification (x26500) and field of view were processed for each imaged nanocomposite and the average side length of a square of free space (l_{sa}) was reported. However, TEM images were acquired from sections cut from the same element of the material, therefore the reported variability only represented a small part of each nanocomposite.

6.3.1.1. HANP plates and rods

TEM micrographs of 2.5% HANP rod and 1-10 wt% HANP plate nanocomposites compounded in Air are shown in Figure 6.7, with increasing magnification from left to right. Figure 6.7 also provides examples of applied squares to estimate the largest free space on the image, which are summarised numerically in Table 6.9. The achieved dispersion of the 10 wt% HANP plate nanocomposite, illustrated in Figure 6.7(e), was comparable with BSE-SEM images of the 10 wt% nHA-PLLA composite presented by Wilberforce et al. [20] shown in Figure 2.7 in Section 2.2.3.

(a) 2.5 wt% HANP rod

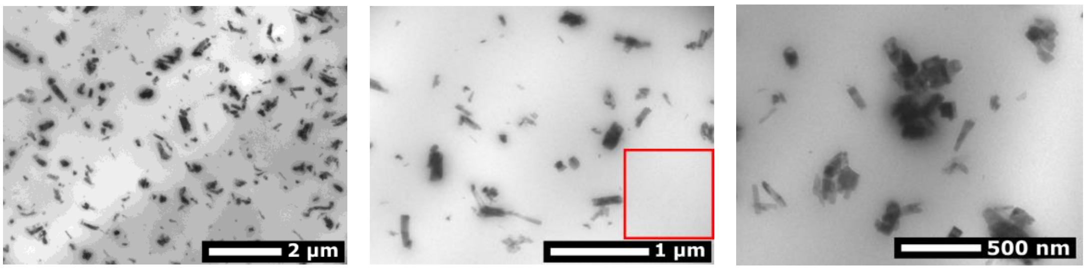

(b) 1 wt% HANP plate

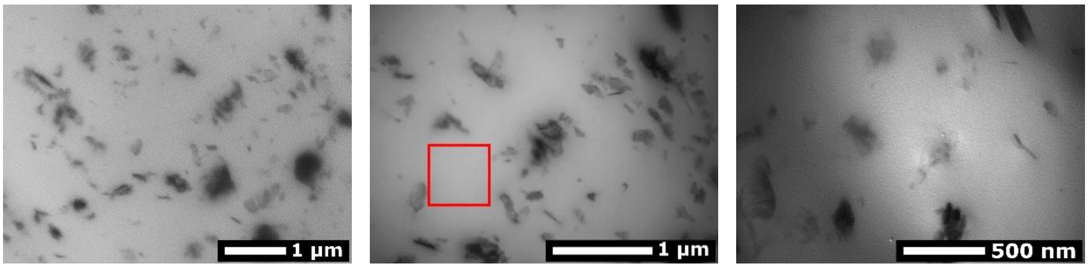

(c) 2.5 wt% HANP plate

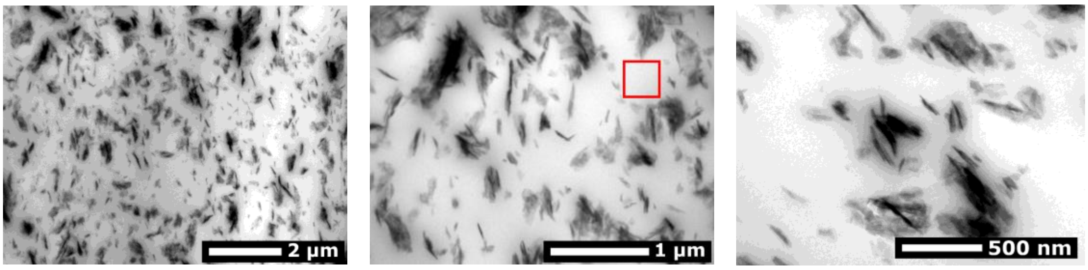

(d) 5 wt% HANP plate

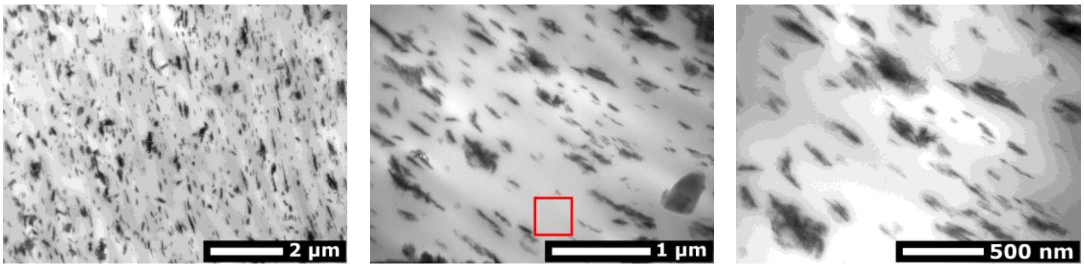

(e) 10 wt% HANP plate

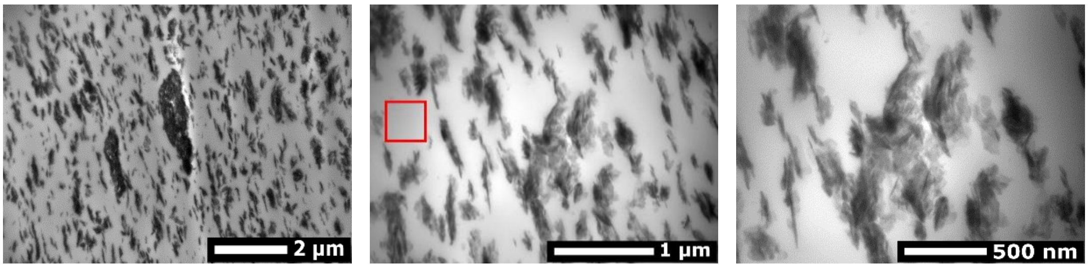

Figure 6.7. TEM micrographs of (a) 2.5 wt% HANP rod and (b-e) 1-10 wt% plate nanocomposites compounded in Air at 210 °C, 50 rpm for 15 min.

The square side length of free space, listed in Table 6.9, decreased with increasing amount of HANP plates as predicted. When 2.5 wt% HANP rod and plate nanocomposites compounded in Air were compared, l_{sa} of the latter was 40% smaller inferring better particle dispersion for plates. The 2.5 wt% HANP rod in Air had also the greatest l_{sa} of all the imaged nanocomposites. This is in contrary to findings reported in Section 5.1.1, specifically in Tables 5.1 and 5.2, where M_w and $t_{1/2}$ for 2.5 wt% HANP rod were greater than for the 2.5 wt% plate nanocomposite in Air (by 11% and 20% respectively), which suggested better particle dispersion of HANP rods in LR706S. However, as mentioned in Section 6.3.1, the TEM images represent a very small area of the produced nanocomposite and therefore they are not a complete representation of particle dispersion in the material.

Table 6.9. Quantification of free space on TEMs of HANP rod and plate nanocomposites compounded in Air at 210 °C, 50 rpm for 15 min.

Name	l_{sa} [nm]
2.5 wt% HANP rod	773 ±106
1 wt% HANP plate	584 ±61
2.5 wt% HANP plate	467 ±94
5 wt% HANP plate	442 ±46
10 wt% HANP plate	398 ±22

6.3.1.2. Coated HANP

TEM micrographs of the nanocomposites with coated HANP (equivalent to 2.5 wt% of uncoated HANP plus coating) compounded in Air are shown in Figure 6.8, and mixed in N_{2D} in Figure 6.9, with increasing magnification from left to right. Figure 6.8 and 6.9 also show examples of applied squares to estimate the largest free space on the image, summarised numerically in Table 6.10.

For the nanocomposites compounded in Air, based on the l_{sa} size, the 2.8 wt% DDSAHA had the best particle dispersion while the 4.9 wt% is8PLAHA had the worst. 2.8 wt% DDSAHA in Air had also the smallest l_{sa} of all the imaged nanocomposites. The other materials listed in Table 6.10 with coated HANP mixed in Air were comparable in l_{sa} to the 2.5 wt% HANP plate (see Table 6.9) as no statistically significant difference was found.

2.8 wt% DDSAHA

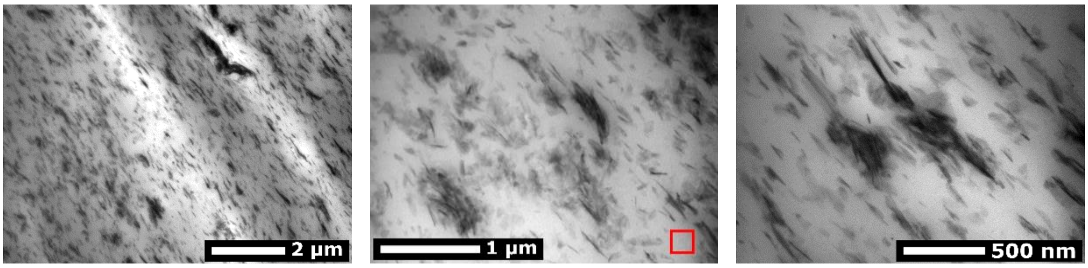

4.9 wt% is8PLAHA

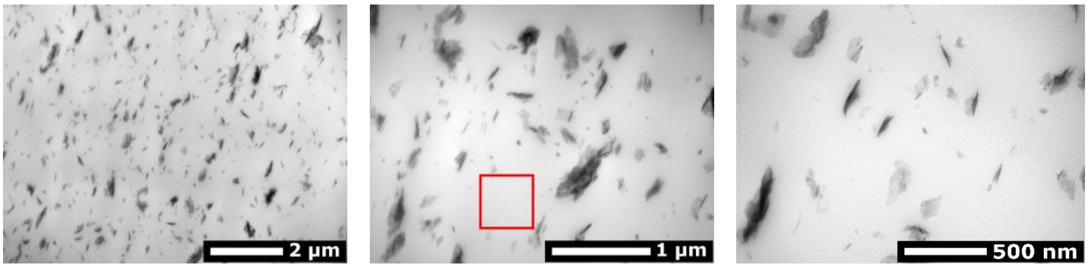

3.6 wt% is16PLAHA

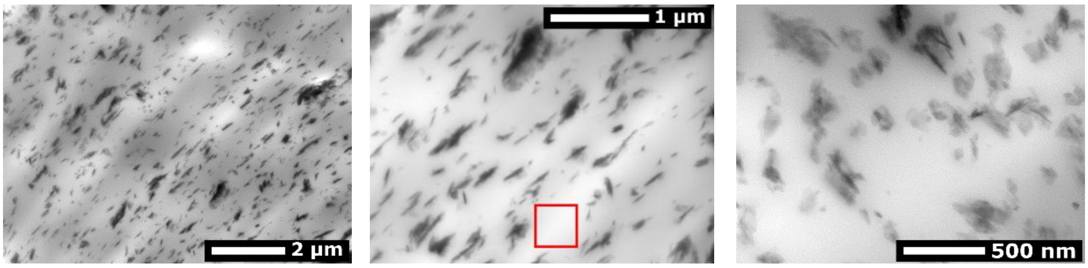

5.6 wt% is24PLAHA

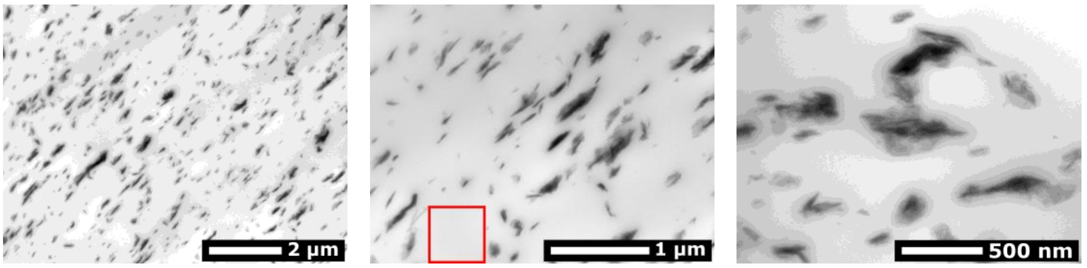

3.9 wt% starPLAHA

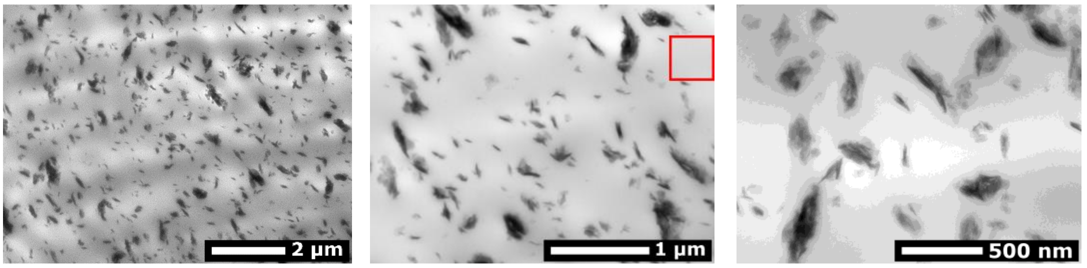

Figure 6.8. TEM micrographs of coated HANP nanocomposites compounded in Air at 210 °C, 50 rpm for 15 min. HANP wt% was equivalent to 2.5 wt% of uncoated HANP plus coating.

2.5 wt% HANP plate

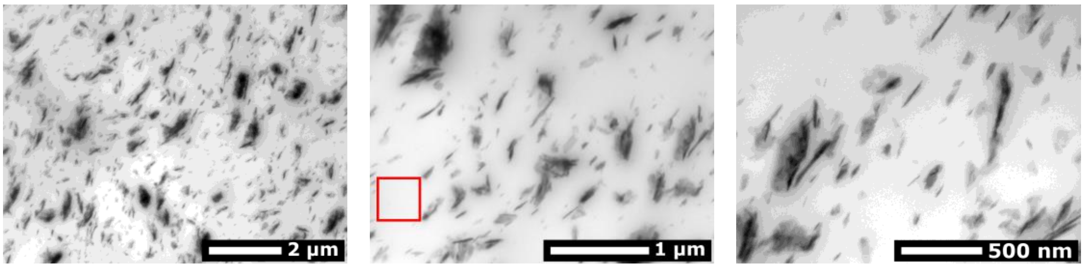

2.8 wt% DDSAHA

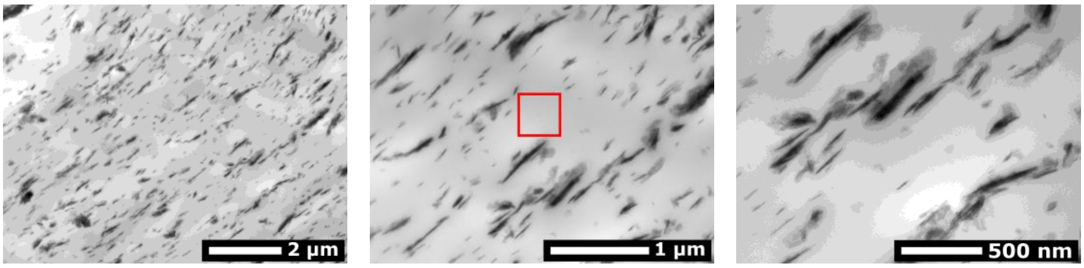

3.6 wt% is16PLAHA

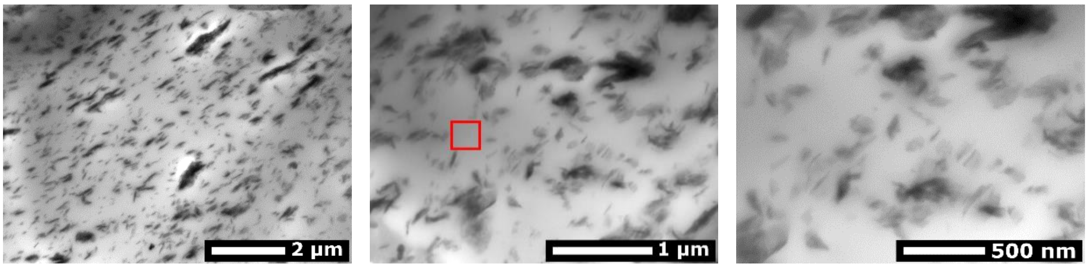

5.6 wt% is24PLAHA

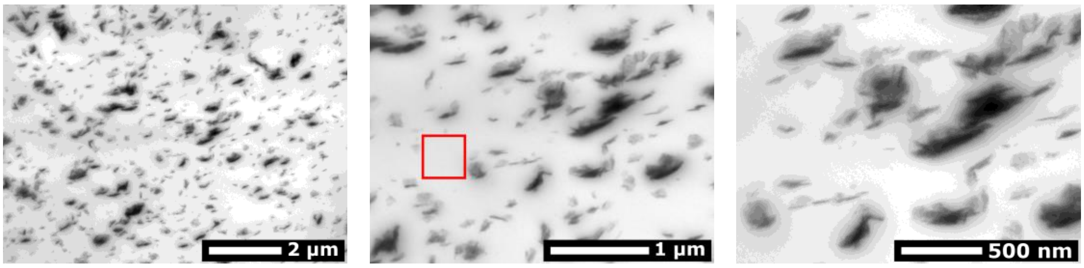

3.9 wt% starPLAHA

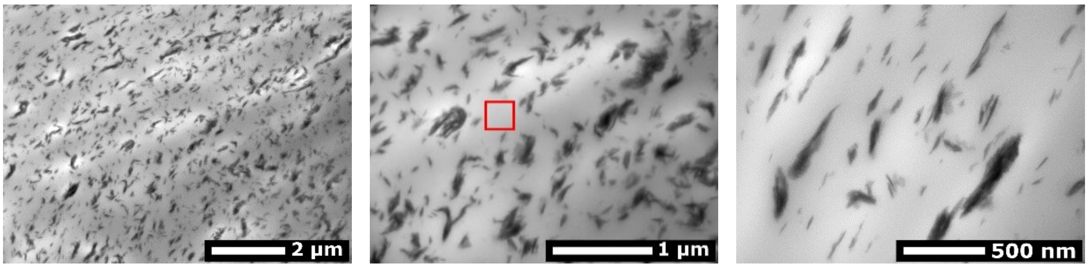

Figure 6.9. TEM micrographs of uncoated and coated HANP nanocomposites compounded in N_{2D} at 210 °C, 50 rpm for 15 min. HANP wt% was equivalent to 2.5 wt% of uncoated HANP plus coating.

For the nanocomposites compounded in N_{2D}, the distinctively smallest l_{sa} was found for 3.6 wt% is16PLAHA suggesting the best particle dispersion.

The rest of the materials listed in Table 6.10 with coated HANP mixed in N_{2D} were comparable in l_{sa} to the 2.5 wt% HANP plate in N_{2D} when taking into consideration the variation in square sizes. Overall, the nanocomposites with coated HANP mixed in N_{2D} had smaller l_{sa} than the materials compounded in Air, with exception of 2.8 wt% DDSAHA, which infers improved nanoparticle dispersion in LR706S in dried nitrogen.

Table 6.10. Quantification of free space on TEMs of the nanocomposites with coated HANP compounded in Air and N_{2D} at 210 °C, 50 rpm for 15 min. HANP wt% was equivalent to 2.5 wt% of uncoated HANP plus coating.

Gas	Name	l_{sa} [nm]
Air	2.8 wt% DDSAHA	221 ±24
Air	4.9 wt% is8PLAHA	603 ±108
Air	3.6 wt% is16PLAHA	426 ±47
Air	5.6 wt% is24PLAHA	537 ±46
Air	3.9 wt% starPLAHA	489 ±39
N_{2D}	2.5 wt% HANP plate	414 ±50
N_{2D}	2.8 wt% DDSAHA	380 ±46
N_{2D}	3.6 wt% is16PLAHA	329 ±18
N_{2D}	5.6 wt% is24PLAHA	352 ±113
N_{2D}	3.9 wt% starPLAHA	368 ±61

Table 6.11. Quantification of free space on TEMs of the nanocomposites with coated HANP compounded in N_{2D} at 210 °C, 50 rpm for 15 min. HANP wt% was equivalent to 5 wt% of uncoated HANP plus coating.

Gas	Name	l_{sa} [nm]
N_{2D}	5 wt% HANP plate	336 ±9
N_{2D}	5.6 wt% DDSAHA	352 ±113
N_{2D}	7.2 wt% is16PLAHA	333 ±65
N_{2D}	11.1 wt% is24PLAHA	389 ±34
N_{2D}	7.7 wt% starPLAHA	343 ±35

The estimate of the largest free space on the images of nanocomposites with coated HANP (equivalent to 5 wt% of uncoated HANP plus coating) compounded in N_{2D} were determined in a similar fashion and are summarised in Table 6.11 by means of l_{sa}. The listed materials with coated HANP were comparable to the 5 wt% HANP plate in N_{2D} when taking into consideration the variation in square sizes.

6.3.1.3. Influence of changing processing conditions

A similar smallest l_{sa} approach was applied to samples with changing compounding parameters. Example images are not provided, since by eye they are indistinguishable.

The average l_{sa} on the TEM image of 2.5 wt% HANP plate and 2.8 wt% DDSAHA nanocomposites, compounded in N_2 at 50 - 150 rpm, is summarised in Table 6.12. Based on the size of l_{sa}, the dispersion of the 2.5 wt% HANP plate nanocomposite was observed to deteriorate with increasing n_s, which is in contrary to findings reported in Table 5.9 in Section 5.2.3.3, where $t_{5\%P}$ increased with increasing n_s inferring improving particle dispersion. The dispersion of the 2.8 wt% DDSAHA nanocomposites were comparable to each other despite increasing n_s.

Table 6.12. Quantification of free space on TEMs of the nanocomposites with coated and uncoated HANP, compounded in the MiniLab at 50 - 150 rpm, 210 °C for 15 min in N_2. HANP wt% was equivalent to the nominal 2.5 wt% of uncoated HANP plus coating for DDSAHA.

n_s [rpm]	Name	l_{sa} [nm]
50	2.5 wt% HANP plate	418 ±61
100	2.5 wt% HANP plate	498 ±13
150	2.5 wt% HANP plate	496 ±34
50	2.8 wt% DDSAHA	453 ±98
100	2.8 wt% DDSAHA	508 ±23
150	2.8 wt% DDSAHA	427 ±76

The average l_{sa} on TEM images of 2.5 wt% HANP plate nanocomposites compounded at 50 rpm in Air, N_2 and N_{2D} (listed with an expected decreasing amount of moisture in the system as explained beforehand in Section 6.1.1.4 for Table 6.8) are summarised in Table 6.13. Taking into consideration the variation in square sizes, the difference in particle dispersion for all those listed nanocomposites is not statistically significant.

Table 6.13. Quantification of free space on TEMs of the 2.5 wt% HANP plate nanocomposites mixed in Air, N_2 and N_{2D} at 210 °C, 50 rpm for 15 min. HANP were compounded after a direct transfer from a dry anaerobic glove box or (#) after drying at 300 °C.

Gas	l_{sa} [nm]
Air	467 ±94
N_2	418 ±61
N_{2D}	537 ±92
N_{2D}	$^{\#}$414 ±50

Similarly, the average l_{sa} on TEM images of 5.6 wt% DDSAHA nanocomposites mixed in N_{2D} for 5 - 15 min, listed in Table 6.14, were comparable (no statistically significant difference).

Table 6.14. Quantification of free space on TEMs of the 5.6 wt% DDSAHA nanocomposites mixed at 210 °C, 50 rpm in N_{2D} with varying compounding time. HANP wt% was equivalent to 5 wt% of uncoated HANP plus coating.

t_R [min]	l_{sa} [nm]
5	360 ±59
10	329 ±63
15	352 ±113

6.4. Microcomputed Tomography

The nanocomposite samples were scanned[3] with parameters described in Section 3.2.10 and the obtained section images were combined into a 3D model and analysed for HANP dispersion in LR706S.

---

[3] X-ray computer tomography scans were performed by Prof Charles Augarde at Durham University in the framework as part of a service provided by the Durham XRCT Facility, which was partially funded by the EPSRC (grants EP/K036084/1 & EP/K024698/1).

6.4.1. MicroCT 3D images analysis

The volume of visible HA and PLA matrix was obtained from the created 3D models of the scanned nanocomposites, examples of which are provided in Figure 6.10, Figure 6.11 and Figure 6.12. The HANP volume percentage was calculated for the scanned materials and converted to weight percentage using material densities. This was then divided by weight percentage of HA measured by TGA for the respective nanocomposites for calculation of visible agglomeration. As the microCT scans were performed at a resolution of 1 µm it was assumed that the HA nanoparticles which were not visible are dispersed while the filler shown in the models represents HANP agglomeration summarised in Table 6.15.

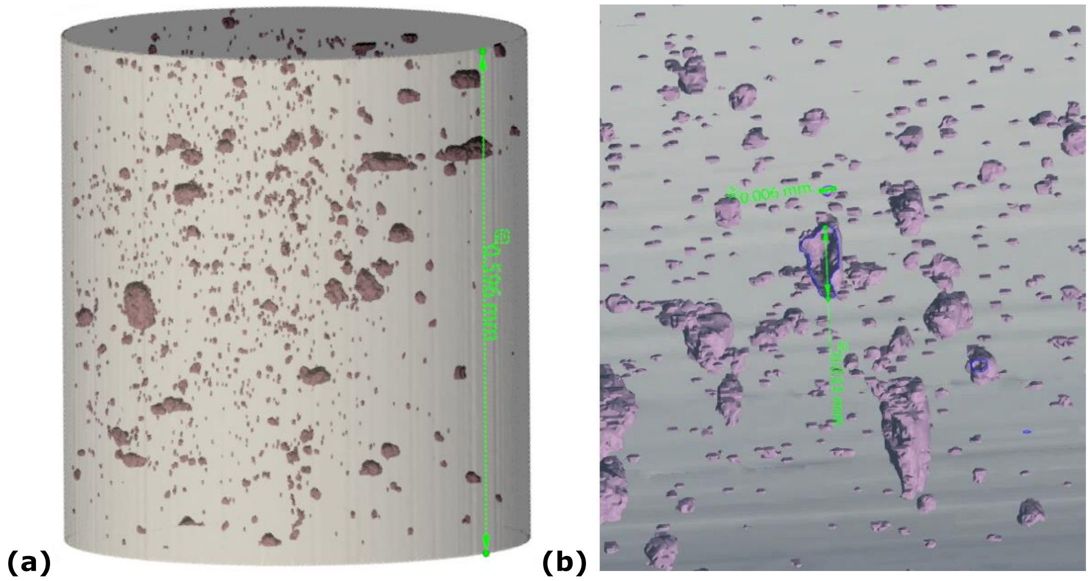

Figure 6.10. MicroCT of 2.5 wt% HANP plate nanocomposite mixed in Air (a) scan overview, measurement of 0.596 mm; (b) section magnification, agglomerates measurement of 33 µm and 6 µm.

Out of all scanned nanocomposites, the least agglomeration was shown for 2.5 wt% HANP rod nanocomposites. Only 2.8% and 0.2% of HA was present in the materials mixed in Air and N_{2D}, respectively, see Figure 6.11. This confirms the greatest particle dispersion above 1 µm for the 2.5 wt% HANP rod compounded in N_{2D} and supports an earlier suggestion in Section 5.1.1 that the exceptionally high $t_{1/2}$ for the material indicated superior HA dispersion. This was also hypothesised in Section 5.1.3.2 where via a rheological model, theoretical and actual molecular weight of the materials was compared and revealed that M_w for 2.5 wt% HANP rod mixed in N_{2D} was greater than the predicted value, which inferred beneficial influence of dispersed particles.

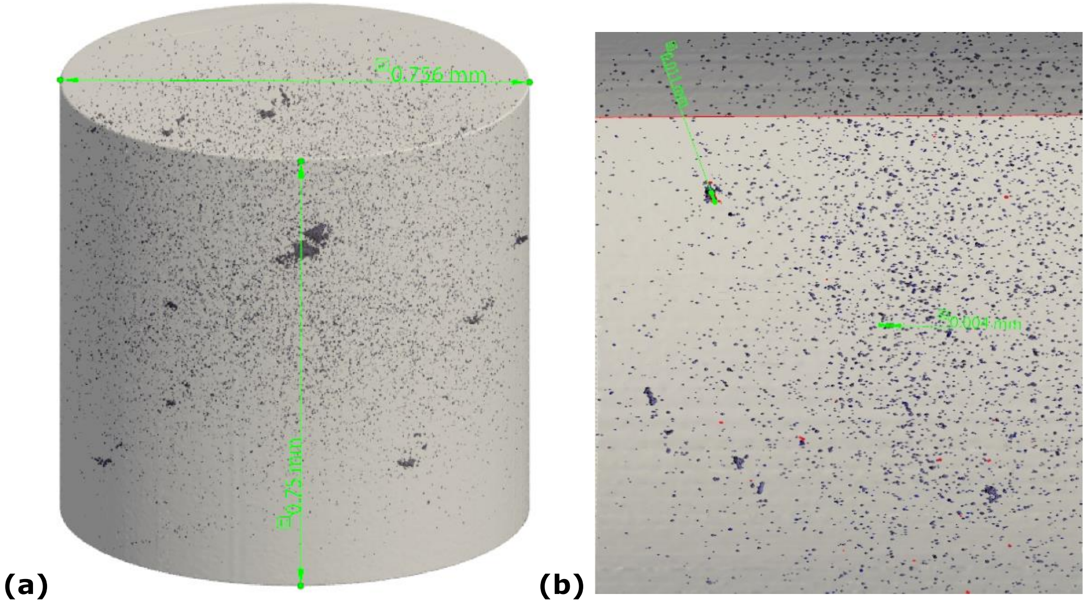

Figure 6.11. MicroCT of 2.5 wt% HANP rod nanocomposite mixed in Air (a) scan overview, measurement of 0.750 mm height and 0.756 mm width; (b) section magnification, agglomerates measurement of 11 µm and 4 µm.

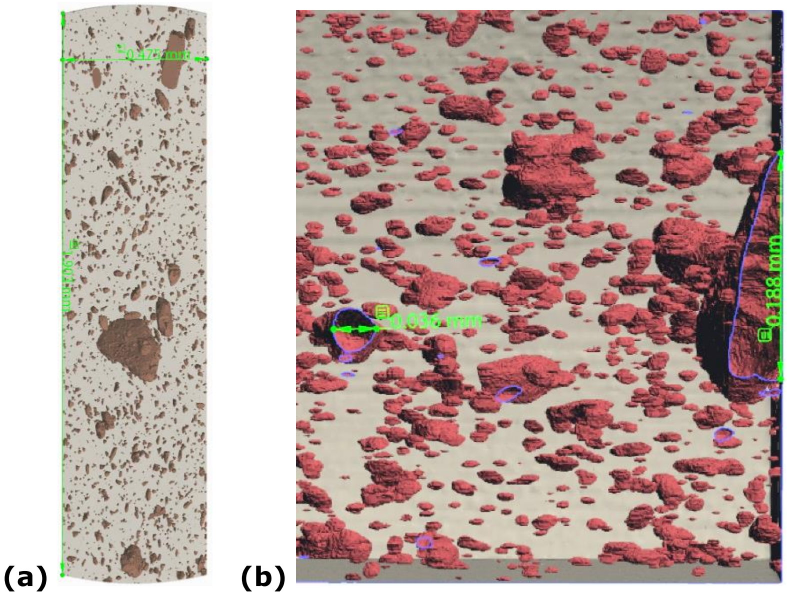

Figure 6.12. MicroCT of 3.9 wt% starPLAHA nanocomposite mixed in N_{2D} (a) scan overview, measurement of 1.903 mm height and 0.475 mm width; (b) section magnification, agglomerates measurement of 188 µm and 36 µm.

Similarly, three times less agglomeration occurred for the 2.5 wt% HANP plate nanocomposite in N_{2D} in comparison to that in Air, which again confirmed beneficial influence of compounding under dried inert gas on particle dispersion. For the HANP plate compounded in Air, agglomeration did not increase with increasing amount of filler from 2.5 to 5 wt%, which suggests that the same proportion of agglomerates is present for both materials.

Table 6.15. HA agglomeration in microCT scans of the HANP-LR706S nanocomposites. For coated HANP the named wt% was equivalent to 2.5 wt% of uncoated HANP plus coating.

Gas	Name	HA char [wt%]	HA in microCT [wt%]	Agglomerates [%]
Air	2.5 wt% HANP rod	2.69 ±0.07	0.08	2.8
Air	2.5 wt% HANP plate	2.44 ±0.05	0.77	31.5
Air	5 wt% HANP plate	4.50 ±0.02	1.39	30.8
Air	4.9 wt% is8PLAHA	1.91 ±0.01	1.77	92.3
N_{2D}	2.5 wt% HANP rod	2.64 ±0.01	0.005	0.2
N_{2D}	2.5 wt% HANP plate	2.52 ±0.01	0.54	21.5
N_{2D}	3.6 wt% is16PLAHA	2.02 ±0.03	1.04	51.5
N_{2D}	5.6% is24PLAHA	2.71 ±0.05	1.71	63.3
N_{2D}	3.9% starPLAHA	2.52 ±0.04	3.52	139.7

The greatest agglomeration for HANP compounded in Air occurred for 4.9 wt% is8PLAHA (92%), which infers that this coating was not efficient in aiding the dispersion of HA nanoparticles in the PLA matrix in Air. Agglomeration of above 100% was calculated for the 3.9% starPLAHA nanocomposite mixed in N_{2D}, illustrated in Figure 6.12. Large aggregates of above 180 μm in diameter were shown which contain high quantities of HA in the scanned part of the material, hence the HA content in the microCT 3D model is greater than that from the TGA measurement due to agglomerated particle distribution. For 3.6 wt% is16PLAHA and 5.6% is24PLAHA nanocomposites compounded in N_{2D} the calculated agglomeration was 51.5% and 63.3% respectively.

6.5. Conclusions

TGA measurements revealed that the nanocomposites compounded in Air had, in the majority, an underloaded amount of HANP versus the nominal calculated amount of filler, while the materials mixed in N_{2D} were better corelated with the theoretical wt% of HA.

The nanocomposites produced with coated HANP were susceptible to additional error originating from the batch-to-batch filler coating level variation and dispersant degradation due to storage. These laboratory scale compounding issues can be mitigated by production of HANP and the nanocomposites at a larger scale, which was achieved through scale-up activities discussed further in Chapter 7.

The preliminarily scanning electron microscopy was found to be an insufficient method to confirm macro and nano dispersion of the HANP particles. Therefore, transmission electron microscopy micrographs of the nanocomposites were acquired at various magnifications. A simple semi-quantitative method was employed for image analysis based on applying the largest open square on the TEM micrograph without crossing or encapsulating any particle. The free space on the image decreased with either increasing HANP content or improving particle dispersion.

The largest square of free space was fitted on micrographs for 2.5 wt% HANP rod nanocomposite compounded in Air while the smallest for 2.8 wt% DDSAHA in Air. Overall, the nanocomposites with coated HANP mixed in N_{2D} had a smaller square size than the materials compounded in Air, with exception of 2.8 wt% DDSAHA, which infers improved nanoparticle dispersion in LR706S in dried nitrogen. Influence of compounding with different parameters could not be detected by TEM due to the small square size deviation between the images for the same material. It should also be mentioned that TEM images represent a very small area of the produced nanocomposite and therefore they are not a complete representation of particle dispersion in the material.

The nanocomposites were also scanned with microCT at a resolution of 1 µm, which represents a substantially larger part of the extruded materials. It was assumed that HA nanoparticles visible in the constructed 3D models represent HANP agglomeration, which can be quantified by comparing the calculated weight percentage with the HA char residue measured by TGA. Out of all the scanned nanocomposites, the least agglomeration was shown for 2.5 wt% HANP rod nanocomposites compounded in Air and N_{2D}. Dispersion of HANP rods and plates improved when mixed with LR706S under dried nitrogen. Coated HANP performed worse than the uncoated particles as they had a substantially higher percentage of agglomerates.

7. Scalable Manufacturing

Scalable manufacturing was performed in cooperation with industrial partners to achieve transferrable processing and production methods of novel bioresorbable HANP-LR706S nanocomposites for next generation medical devices.

7.1. Methodologies optimisation for scalability

7.1.1. Materials

The HANP rod and plate nanocomposites used for scale up activities were produced by Promethean Particles, UK, in their commercial counter-current hydrothermal reactor. They followed the manufacturing route described in Section 3.1.2. A single large batch was produced for each type of nanoparticle. Similarly, is16PLA coated nanoplates were synthesised as a single large batch, using the facilities of Promethean Particles, following the manufacturing route described in Section 3.1.3.1.

Demonstrator components produced at TESco Associates (TESco), USA, used a single batch of LR706S PLA. Demonstrator components produced at Evonik Industries AG (Evonik), Germany, were also produced using a single batch of LR706S PLA. The two batches were different but were of the same material and made to a stringent specification by Evonik.

7.1.2. Nanocomposite stock production

7.1.2.1. Materials for TESco Associates

The HA and PLA utilised for the production of proof of concept orthopaedic medical devices at TESco were processed in a cleanroom environment, using facilities at the University of Bradford. The materials were prepared to obtain 5 wt% HANP-LR706S nanocomposites; in each batch the following was allocated:

(i) at least 520 g of LR706S with HANP plates and rods each in excess of 28 g HA

(ii) at least 520 g of LR706S with is16PLAHApp in excess of 40 g.

The extruder hoppers had to be loaded with larger amounts of materials than desired for compounding to ensure continuous feeding until the extrusion of the batch was complete.

Prior to loading, materials were dried in the following conditions:

(i) LR706S – overnight in a vacuum oven at 50 °C
(ii) is16PLAHApp – for 2 hours in a vacuum oven at 50 °C
(iii) HANP plates and rods – overnight in a conventional oven at 110 °C with the fan disabled.

After opening the oven, to seal and transfer the materials in a secure manner to the hoppers for immediate extrusion, PLA and HA were placed in polypropylene screw capped jars.

Compounding was carried out under N_{2D} using a Thermo Fisher Pharma 11 HME twin-screw extruder (Pharma 11), shown in Figure 7.1, with a 3 mm die and integrated volumetric feeders. A dried nitrogen line was connected to the Pharma 11 at 4 bar and 0.3 $l.min^{-1}$ via the first sensor port on the extruder barrel located directly after the feeding funnel. The extruder and feeders with hoppers, sealed with the main feeding orifice via a set of tight-fitting concentric funnels, were purged with N_{2D} for 10 min prior to compounding.

Also, prior to compounding, the volumetric feeders were calibrated against the extruder screw speed to simultaneously discharge the desired amount of materials, for the required weight percentage of HANP and LR706S, directly through the feeding funnel to the extruder.

A standard screw configuration was provided by Thermo Fisher with two mixing areas, shown in Figure 7.2. The screws each had an 11 mm diameter, with L/D of 40. Compounding was performed at 100 rpm (torque ranging from 4.5 Nm to 7.2 Nm). The extrudate residence time in the extruder was approximately 90 s with throughput of 5.6 – 6 $g.min^{-1}$ (0.33 – 0.36 $kg.h^{-1}$).

Since the Thermo Fisher Pharma 11 HME has a higher torque than the MiniLab, it was expected that compounding would be possible at a lower temperature. However, due to the high molecular weight of LR706S and the increase in viscosity after including the filler, melt processing was still torque limited and required at least 210 °C to operate. Heating zones, numbered 1-8 from the feeding funnel to the discharge area, had the following profile: 1-2 at 150 °C, 3-4 at 200 °C, 5-8 and die at 210 °C. The extrudates, opaque with a rough surface resembling shark skin, were air cooled and collected directly as strands then pelletised with a Pharma VariCut strand pelletiser. Pharma 11 throughput was checked every ~5 min, via weighing the material extruded during one minute, due to instability of the volumetric feeding. Around 560g of pellets were produced for each batch of materials. These batches were sealed in a N_2 atmosphere in moisture barrier bags for transportation.

Figure 7.1. (a) Thermo Fisher Pharma 11 HME twin-screw extruder, adapted from ThermoScientific [176], (b) with disassembled equipment, adapted from Bottom [177].

After compounding was finished, the extruder was purged with a cellulose based cleaning compound (Asaclean Velox Grade GL2), brushed off, washed with hot water and dried. The initial 12 g section of the compound was always discarded to allow for removal of any potential cellulose residue present on the mixing part of the screws.

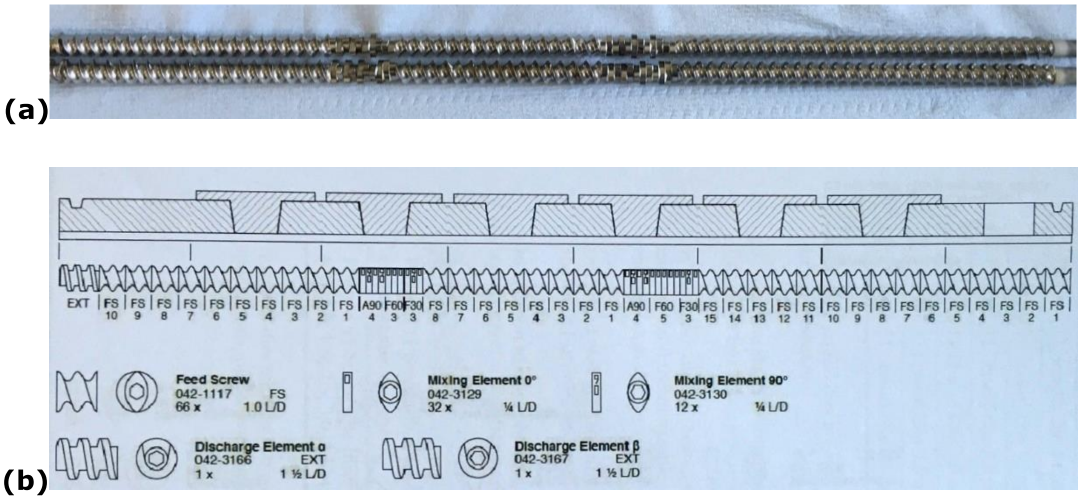

Figure 7.2. (a) Standard mixing screw for Thermo Fisher Pharma 11 HME with main feeding area to the right and (b) elements assembly - adapted from the extruder manual.

The nanocomposite pellets were subsequently dried at UoN in a vacuum oven at 50 °C overnight, vacuum packed, placed in moisture barrier bags in a N_2 atmosphere and frozen before shipment to TESco. Samples were retained for TGA and GPC testing, which will be discussed in Section 7.3.1.1 and 7.3.2.1. A strand of LR706S extruded without particles was also retained, to analyse the influence of melt compounding on PLA only.

7.1.2.2. Comparable materials produced in the MiniLab at UoN

Once TGA measurements were carried out for the materials extruded with the Pharma 11, which will be discussed in Section 7.3.1.1, nanocomposites with equivalent wt% were compounded in the MiniLab with LR706S and HANP from the same batches that were used at the University of Bradford. The processing conditions were 210 °C, mixing at 50 rpm and recirculation for 15 min under N_{2D} so the obtained materials are comparable to the nanocomposites discussed in Chapters 4-6. The materials produced with the MiniLab were analysed via TGA and GPC, which will be discussed in Section 7.3.1.2 and 7.3.2.2.

7.1.2.3. Materials extruded at Evonik Industries AG

The HA and PLA utilised to produce dogbones at Evonik were processed in a cleanroom environment. The materials were prepared to obtain 5 wt% HANP-LR706S nanocomposites. In each batch the following was allocated:

(i) at least 790 g of LR706S with HANP plates and rods each in excess of 42 g HA
(ii) at least 565 g of LR706S with is16PLAHApp in excess of 60 g.

The extruder hoppers had to be loaded with larger amounts of materials than desired for compounding to ensure continuous feeding until the extrusion of the batch was complete.

Prior to loading, materials were dried in the following conditions:

(i) LR706S – overnight in a vacuum oven at 50 °C
(ii) is16PLAHApp – for 2 hours in a conventional oven at 105 °C with the fan disabled, in contrary to the standard procedure of drying coated particles at UoN in vacuum oven at 50 °C for 2 hours, due to risk of Evonik’s vacuum oven contamination with HA particles during decompression
(iii) HANP plates and rods – overnight in a conventional oven at 200 °C with the fan disabled.

After opening the oven, to seal and transfer the materials in a secure manner to the hoppers for immediate extrusion, PLA and HA were placed in glass screw capped jars.

Compounding was carried out under N_{2D} using a Thermo Fisher Pharma 16 twin-screw extruder (Pharma 16) at Evonik, shown in Figure 7.3, with a 3 mm die and integrated Brabender Technologie gravimetric feeders. A dried nitrogen line was connected to the Pharma 16 at 4 bar and 0.3 $l.min^{-1}$ via the second feeding port on the extruder barrel after the feeding funnel. The extruder and feeders with hoppers, sealed with the main feeding orifice via a set of tight-fitting concentric funnels, were purged with N_{2D} prior to compounding.

The gravimetric feeders were set to simultaneously discharge the desired amount of materials, for the required weight percentage of HANP and LR706S, directly through the feeding funnel to the extruder. The extrusion throughput was 1 $kg.h^{-1}$. The screws shown in Figure 7.4 were used for compounding at 120 rpm (torque ranging from 3.8 Nm to 8.5 Nm). They had a configuration tailored to the requirements of Evonik and consisted of feeding elements with varying pitch and one mixing area. Each screw had a diameter of 16 mm, with L/D of 40.

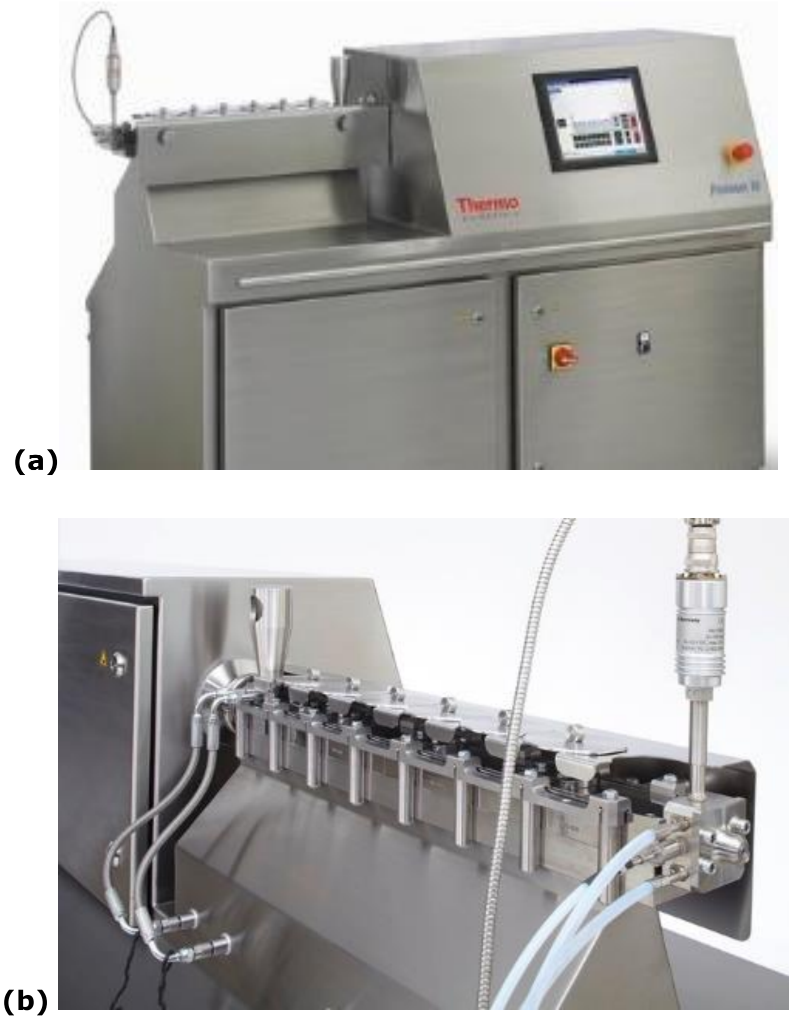

Figure 7.3. (a) Thermo Fisher Pharma 16 twin-screw extruder, (b) barrel equipment and die with transducer. Adapted from ThermoScientific [178].

Heating zones numbered 2-8 from the feeding funnel to the discharge area had the following profile: feeding zone 10 °C, 2 at 50 °C, 3 at 150 °C, 4 at 200 °C, 5 at 210 °C, 6-8 and die at 215 °C. The extrudates, opaque with a rough surface resembling shark skin, shown in Figure 7.5, were air cooled on a conveying belt running at 45% of the maximum torque with high cooling air flow. Solidified strands were directly pelletised with a Pharma VariCut strand pelletiser at 32% of the maximum torque. Around 500 g of each batch, with an average pellet size of 2 x 1.5 mm, was sealed in sample bags for shipment to UoN while the reminder was kept for injection moulding of dogbones which will be discussed in Section 7.2.2.

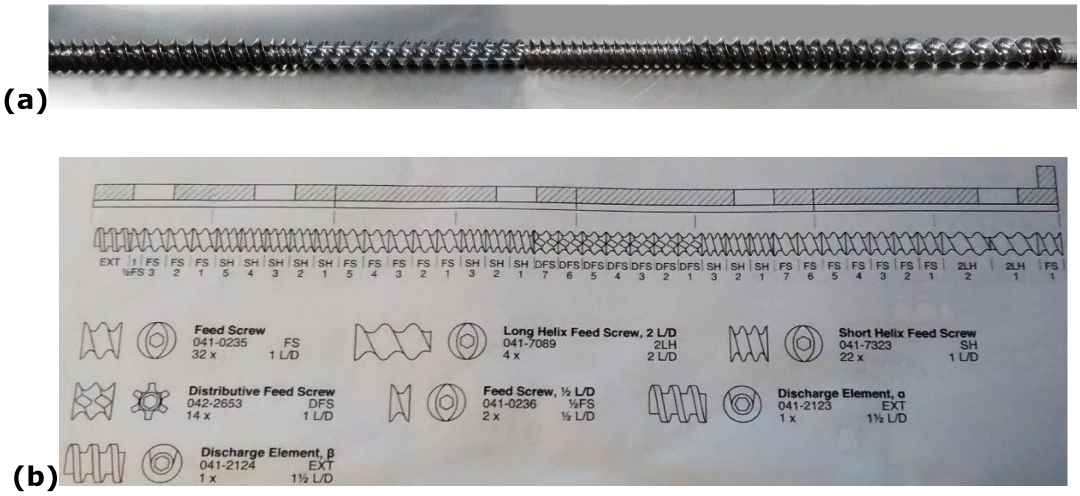

Figure 7.4. (a) Thermo Fisher Pharma 16 mixing screw setup at Evonik, main feeding area to the right and (b) elements assembly - adapted from the extruder manual.

After compounding was finished, the extruder was purged with a cleaning compound (Asaclean Velox Grade U), brushed off, washed with hot water and dried. Compounding was always started with neat PLA (which would then be discarded) to purge out any potential cleaning compound residue present on the mixing part of the screws.

Samples were analysed via TGA and GPC, which will be discussed in Section 7.3.1.3 and 7.3.2.3. A strand of LR706S extruded without particles was analysed to assess the influence of melt compounding on PLA only.

Figure 7.5. Shark skin on HANP-LR706S nanocomposite extrudate produced at Evonik.

7.2. Manufacturing of demonstrator components

7.2.1. TESco Associates

Injection moulded tensile bars (dog bones) and proximal pins were produced by TESco in a cleanroom environment. They were made using the feedstock extruded at the University of Bradford (see Section 7.1.2.1). Examples of the components are shown in Figure 7.6. TESco utilised a proprietary set of processing conditions, which cannot be disclosed. They are highly experienced in the processing of PLA and the conditions were chosen to minimise process-induced degradation.

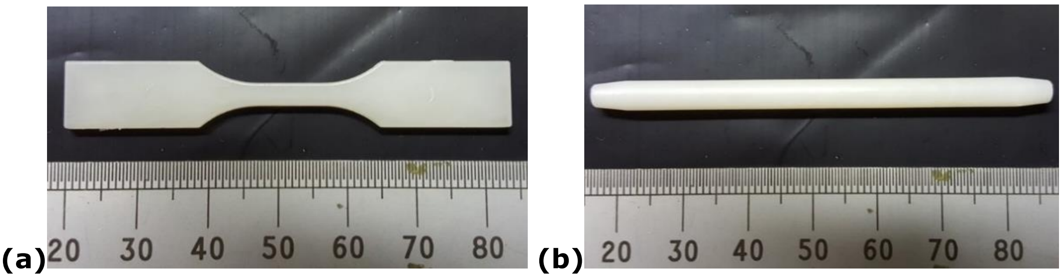

Figure 7.6. (a) HANP plate - LR706S nanocomposite dogbone and (b) proximal pin injection moulded at TESco.

7.2.2. Evonik Industries AG

Injection moulded dog bone samples were produced in a cleanroom environment by Evonik, using an Arburg Allrounder 170S 180-30 injection moulder with a 15 mm screw (Figure 7.7). They were made using the nanocomposites feedstock extruded at Evonik (see Section 7.1.2.3). Examples of the components are shown in Figure 7.8. Prior to injection moulding the pelletised materials were dried at 50 °C for at least 6 h using a compressed air Helios Jetboxx dryer attached directly above the hopper of the injection moulder.

Heating zones numbered 1-4 from the feeding funnel to the discharge area had the following profile: feeding zone 40 °C, 1 at 190 °C, 2 at 198 °C, 3-4 at 200 °C. Materials were injected with a speed of 20 $cm^3.s^{-1}$ and a pressure of 1800 bar into a dog bone mould at 30 °C with a clamping force of 100 kN. They were then cooled for 35 s with a holding pressure of 1600 bar. The entire cycle time for one injection moulded dog bone was 42 s.

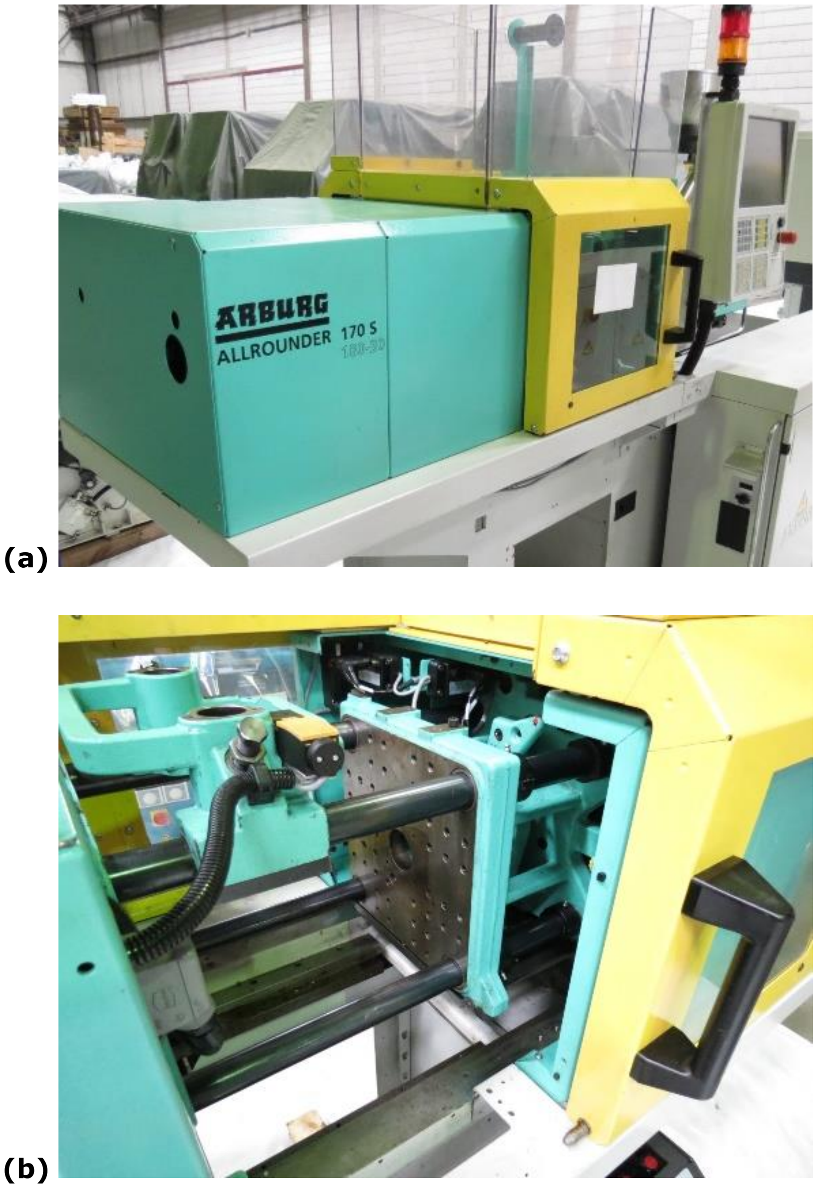

Figure 7.7. (a) Arburg Allrounder 170S 180-30 (b) mould mounting platen. Adapted from Schulz [179].

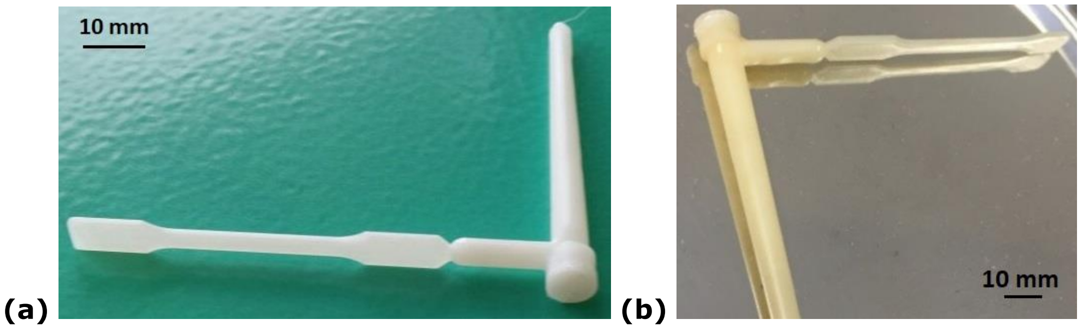

Figure 7.8. Nanocomposite (a) HANP plate and (b) is16PLAHApp dogbone with attached sprue, both injection moulded with the Arburg Allrounder 170S 180-30 at Evonik.

7.3. Product characterisation

Pelletised materials and fragments of injection moulded sprues of the manufactured products were used for TGA, GPC, IV and microCT characterisation. Mechanical testing was carried out (i) with compression moulded rectangular bars produced from the pelletised materials and (ii) directly on the manufactured dogbones and pins.

7.3.1. TGA

TGA measurements performed at UoN were carried out according to the methods described in Section 3.2.5. The char residue, and the temperature at 5% weight loss normalised for the nanocomposites with respect to only the polymer content (see Section 5.2.3), will be discussed in this section.

For the measurements carried out at TESco, details on the equipment and method utilised were not provided.

7.3.1.1. TESco products

The nanocomposite stock compounded for TESco with the Pharma 11 was tested with TGA together with the extruded reference strand of LR706S. For each nanocomposite, 8 samples were taken during extrusion at time intervals of approximately 12 min. For the extruded LR706S, only one sample was tested. The results obtained on these samples are provided in Table 7.1.

Table 7.1. TGA measurements for the LR706S materials extruded with the Pharma 11.

Filler	Char residue [wt%]	$t_{5\%P}$ [°C]
-	0.28 ±0.02	305.0 ±1.7
HANP plate	2.17 ±0.14	313.0 ±3.9
HANP rod	3.45 ±0.17	313.7 ±4.2
is16PLAHApp	2.95 ±0.13	317.0 ±4.5

Based on the measured HA char residue listed in Table 7.1, a total 5.67 wt% for is16PLAHApp was calculated including 48% particle coating (as per the batch details provided in Table 3.2 in Section 3.1.3). The $t_{5\%P}$ increased with the addition of HANP to the PLA when compared to the sample of extruded LR706S without particles. $t_{5\%P}$ was greatest for is16PLAHApp which infers improved thermal properties for the nanocomposites.

As stated in Section 7.1.2.1, the particle loading in the nanocomposites produced with the Pharma 11 was targeted at 5 wt% (without coating for is16PLAHApp), however this was not achieved. Gravimetric feeders were not available for this particular extrusion line and the volumetric feeders had to be utilised. The volumetric feeders required a manual increase of the discharge speed, due to the decreasing amount of PLA and HA in the hoppers, with delayed feedback via throughput measurements. Additionally, a build up of LR706S fines was experienced on the concentric funnels, sealing the feeding area, which had to manually be removed periodically. This build up was potentially due to static electric charge on the LR706S or too high of a temperature in the initial zone. It was also observed that HANP particles floated inside the Pharma 11 from the feeder towards the cavity of the first sensor port, used for feeding N_{2D}, creating some build up. Moreover, is16PLAHApp is a highly static electrically charged powder which persists despite connecting the feeder to active earth. Due those challenges the compounded materials were 31-57% underloaded.

Fragments of sprues from the tensile bars injection moulded at TESco were also tested, these TGA measurements were carried out in triplicate and the average values are provided in Table 7.2.

Table 7.2. TGA measurements for the HANP-LR706S samples injection moulded at TESco.

Filler	Char residue [wt%]	$t_{5\%P}$ [°C]
HANP plate	2.07 ±0.14	315.5 ±3.3
HANP rod	3.55 ±0.12	316.7 ±4.1
is16PLAHApp	2.89 ±0.09	324.5 ±2.1

Based on the measured HA char residue listed in Table 7.2, a total 5.56 wt% for is16PLAHApp was calculated including 48% particle coating. The greatest $t_{5\%P}$ was achieved for the material injection moulded with is16PLAHApp nanocomposite which is 7.5 °C higher than for the pelletised stock batch. This infers further particle dispersion during melt processing which improved thermal properties of the material. The HANP content variation for the respective materials between TGA results, shown in Table 7.1 and Table 7.2, was 2 - 5%, which shows consistency between the results.

Lastly, TGA measurements carried out at TESco for the injection moulded samples are shown in Table 7.3. Based on the measured HA char residue, a total 5.65 wt% and 6.71 wt% for is16PLAHApp tensile bar and proximal pin was calculated respectively (as per 48% coating). These measurements are seen to have a greater deviation from the values for the nanocomposite pellets, 3 – 17% for HANP plate, 14 - 17% for HANP rod and 0.3 – 18% for is16PLAHApp, however they represent only one measurement each for the bar and pin.

Table 7.3. TGA measurements of HA char residue performed at TESco for the HANP-LR706S samples injection moulded at TESco.

Filler	Tensile bar [wt%]	Proximal pin [wt%]
HANP plate	1.80	2.10
HANP rod	2.87	2.98
is16PLAHApp	2.94	3.49

7.3.1.2. Nanocomposites produced in the MiniLab

TGA tests conducted for the nanocomposites compounded in the MiniLab, which are equivalent to the materials obtained from the Pharma 11, are summarised in Table 7.4.

Table 7.4. TGA measurements for the HANP-LR706S nanocomposites compounded in the MiniLab at 210 °C, 50 rpm for 15 min in N_{2D}.

Filler	Char residue [wt%]	$t_{5\%P}$ [°C]
HANP plate	2.17 ±0.05	311.9 ±2.2
HANP rod	3.32 ±0.06	306.5 ±8.2
is16PLAHApp	2.31 ±0.02	307.9 ±1.4

Based on the measured HA char residue, a total 4.44 wt% for is16PLAHApp was calculated (as per 48% coating). The $t_{5\%P}$ was in good agreement (deviation of 0.4 – 3%) with the values acquired for the pelletised stock batch. The particle content variation for the respective materials between TGA results shown in Table 7.1 and Table 7.4, was 0 - 4% for uncoated HANP, which shows a very good agreement, however this is less so for is16PLAHApp (22%).

7.3.1.3. Evonik dogbones

Fragments of sprues from the dogbones injection moulded with the Arburg Allrounder were tested, these TGA measurements were again carried out in triplicate with average values provided in Table 7.5.

Table 7.5. TGA measurements for the HANP-LR706S dogbones injection moulded at Evonik.

Filler	Char residue [wt%]	$t_{5\%P}$ [°C]
HANP plate	4.47 ±0.06	322.1 ±1.9
HANP rod	4.45 ±0.03	319.8 ±4.2
is16PLAHApp	5.46 ±0.10	327.2 ±1.1

Based on the measured HA char residue a total 10.50 wt% for is16PLAHApp was calculated (as per 48% coating). The highest $t_{5\%P}$ was achieved again for is16PLAHApp, which infers improved thermal properties for this nanocomposite.

As stated in Section 7.1.2.3, the targeted particle loading in the nanocomposites produced with the Pharma 16 was 5 wt% (without coating for is16PLAHApp), and this was successfully achieved. The particle content variation was 11% for uncoated HANP and 9% for is16PLAHApp.

Building on previous experience on compounding with the Pharma 11, the feeding zone was cooled followed by a heating zone at a temperature of only 50 °C which prevented polymer build up at the funnel. The materials were dosed with gravimetric feeders and unmodified throughput was maintained therefore making it easier to achieve nanocomposites with filler content close to the desired 5 wt%.

7.3.2. GPC

GPC measurements performed at UoN were carried out according to the methods described in Section 3.2.6. In this section, the full range of the molecular weights (1) is provided containing the main peak (2) with high molecular weights of the majority of the molecules and the peak with short chained species (3), in accordance with Figure 3.9 in Section 3.2.6.

7.3.2.1. TESco products

The nanocomposite stock compounded for TESco with the Pharma 11 was tested with GPC together with the extruded reference strand of LR706S and compared with unprocessed neat LR706S. For each nanocomposite, 8 samples were taken during extrusion at time intervals of approximately 12 min. For the extruded LR706S, only the one sample was tested. GPC experiments were carried out in triplicate for each sample with results for each material provided in Table 7.6. Melt processing of LR706S in the Pharma 11 considerably decreased M_w for the main peak by 33% and the PDI decreased by 20%, while compounding with the nanoparticles preserved the molecular weight. The best results was observed for 5.67 wt% is16PLAHApp as M_w for the main peak reduced by only 7% when compared with neat PLA and the PDI remained the same.

Table 7.6. GPC measurements for the LR706S materials extruded with the Pharma 11. (1) full range of molecular weights, (2) main peak, (3) peak with short chained species.

Material	(1)		(2)		(3)	
	M_w [kg. mol^{-1}]	PDI	M_w [kg. mol^{-1}]	PDI	M_w [kg. mol^{-1}]	PDI
Neat LR706S	384.3 ±27.8	27.2 ±9.6	405.5 ±15.6	3.0 ±1.2	1.2 ±0.6	1.6 ±0.3
Extruded LR706S	265.2 ±8.9	12.6 ±5.2	271.5 ±5.2	2.4 ±0.8	0.7 ±0.2	1.3 ±0.2
2.17 wt% HANP plate	326.2 ±8.8	23.5 ±6.8	338.4 ±5.7	2.7 ±0.2	0.8 ±0.1	1.4 ±0.1
3.45 wt% HANP rod	329.3 ±4.5	25.1 ±6.6	341.9 ±3.4	2.5 ±0.2	0.7 ±0.1	1.3 ±0.1
5.67 wt% is16PLAHApp	354.8 ±3.8	30.3 ±4.4	377.1 ±1.6	2.4 ±0.2	1.1 ±0.1	1.4 ±0.0

Following this, fragments of the injection moulded sprues from the tensile bars were tested. These GPC measurements were again carried out in triplicate with results provided in Table 7.7. When compared to the pelletised stock, the molecular weight decreased further for the respective materials and the PDI increased due to secondary melt processing. For example, M_w of the main peak for 5.56 wt% is16PLAHApp decreased additionally by 18% and the PDI increased by 21%, yet the bars manufactured from the coated HANP still had the highest molecular weight when compared to other nanocomposites.

Table 7.7. GPC measurements for the HANP-LR706S samples injection moulded at TESco. (1) full range of molecular weights, (2) main peak, (3) peak with short chained species.

Material	(1)		(2)		(3)	
	M_w [kg. mol^{-1}]	PDI	M_w [kg. mol^{-1}]	PDI	M_w [kg. mol^{-1}]	PDI
2.07 wt% HANP plate	263.5 ±0.6	37.8 ±4.0	285.1 ±5.3	2.7 ±0.2	0.8 ±0.1	1.5 ±0.1
3.55 wt% HANP rod	262.8 ±5.9	22.8 ±4.2	275.6 ±6.4	2.8 ±0.2	0.9 ±0.1	1.4 ±0.1
5.56 wt% is16PLAHApp	275.1 ±4.4	48.2 ±4.4	309.3 ±4.1	2.9 ±0.1	1.0 ±0.1	1.5 ±0.1

7.3.2.2. Nanocomposites produced in the MiniLab

GPC tests conducted for the nanocomposites compounded in the MiniLab, which are equivalent to the materials obtained from the Pharma 11, are summarised in Table 7.8. Mixing of LR706S in the MiniLab decreased M_w of the main peak by 45% and the PDI by 17% when compared with neat PLA. Compounding with the nanoparticles preserved the molecular weight e.g. for 3.32 wt% HANP rod the main peak M_w reduced by only 33%. When compared to results for the pelletised stock in Table 7.6, due to extended residence at 210 °C, the M_w decreased further for the MiniLab materials, for example, a further 9% reduction was observed for the main peak M_w of 2.17 wt% HANP plate. For the respective is16PLAHApp nanocomposites M_w of the main peak decreased by only 1%, however this surmised to be due to lower amounts of particles in the material.

Table 7.8. GPC measurements for the HANP-LR706S nanocomposites compounded in the MiniLab at 210 °C, 50 rpm for 15 min in N_{2D}. (1) full range of molecular weights, (2) main peak, (3) peak with short chained species.

Material	(1) M_w [kg. mol^{-1}]	(1) PDI	(2) M_w [kg. mol^{-1}]	(2) PDI	(3) M_w [kg. mol^{-1}]	(3) PDI
Extruded LR706S	215.6 ±2.0	25.5 ±5.1	223.9 ±1.4	2.5 ±0.1	0.5 ±0.1	1.6 ±0.1
2.17 wt% HANP plate	298.3 ±9.1	14.3 ±10.7	308.7 ±1.0	2.8 ±0.5	1.7 ±0.2	1.8 ±0.1
3.32 wt% HANP rod	263.4 ±3.7	10.1 ±3.0	270.9 ±3.1	2.7 ±0.1	1.8 ±0.2	1.8 ±0.0
4.44 wt% is16PLAHApp	357.2 ±4.9	15.1 ±1.8	373.4 ±3.0	2.5 ±0.2	1.6 ±0.1	1.3 ±0.1

The GPC measurements were compared with the compounding parameters shown in Table 7.9. The $t_{1/2}$ and E_{mix} of 3.32 wt% HANP rod were both 20% lower than for extruded LR706S, while the main peak M_w for the nanocomposite was 21% higher. This infers decrease of the material viscosity when compared with PLA only. The $t_{1/2}$, E_{mix} and the main peak M_w of 2.17 wt% HANP plate nanocomposite were greater than for rods which suggests better dispersion due to smaller amounts of

HANP. The greatest $t_{1/2}$, E_{mix} and the main peak M_w was observed for 4.44 wt% is16PLAHApp which implies improved dispersion of the particles for this nanocomposite.

Table 7.9. Summary of compounding of HANP-LR706S nanocomposites in the MiniLab at 210 °C, 50 rpm for 15 min in N_{2D}.

Material	T_{w0} [kPa]	$t_{1/2}$ [s]	E_{mix} [kJ] at t_R = 15 min
Extruded LR706S	119.0 ±0.7	1983 ±69	7.66
2.17 wt% HANP plate	110.3 ±0.4	2893 ±76	7.44
3.32 wt% HANP rod	101.9 ±0.3	1577 ±25	6.12
4.44 wt% is16PLAHApp	115.9 ±0.3	6878 ±341	8.61

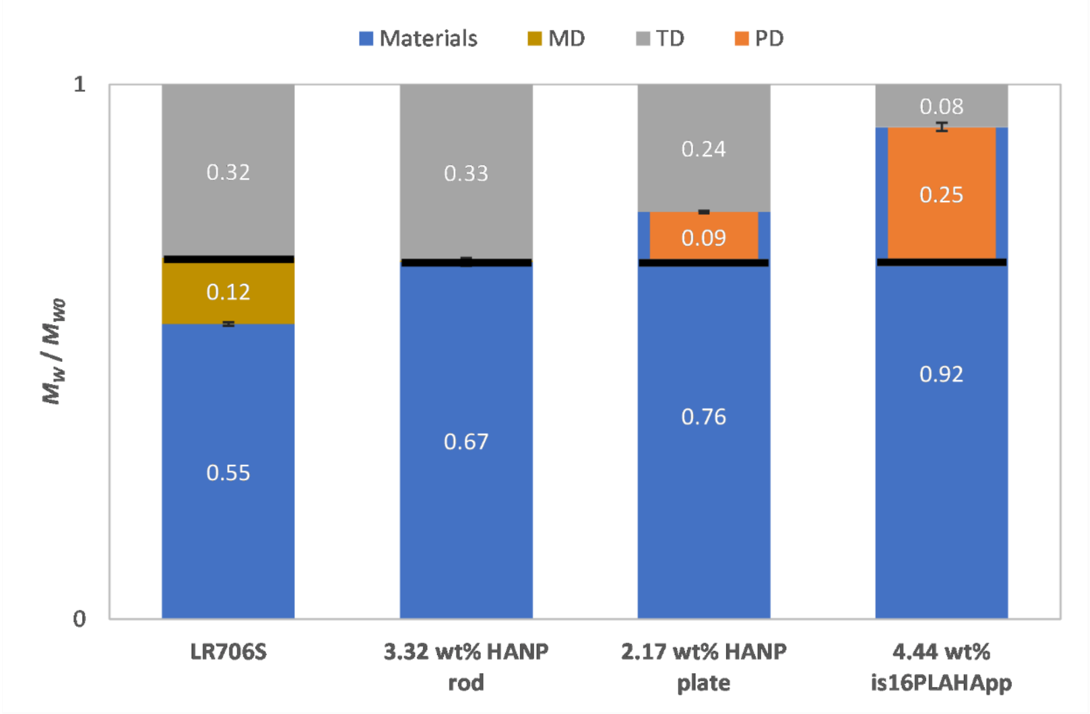

Figure 7.9. Change of degradation of LR706S compounded with various HANP at 50 rpm, 210 °C in N_{2D} for 15 min, where: MD - mechanical degradation, TD - thermal degradation, PD - particle effect.

A rheological model proposed by Choong et al. [28] was applied for molecular weight analysis in an attempt to separate thermal and shear effects of melt processing on the polymer matrix, see Figure 7.9 for the analysis results. The findings infer that the effects of mechanical degradation were compensated by inclusion of the nanoparticles, for example, for 3.32 wt% HANP rod, the theoretical calculated molecular weight matched the measured M_w of the main peak. For 2.17 wt% HANP plate and 4.44 wt% is16PLAHApp nanocomposites, the main peak M_w was above the calculated molecular weight due to beneficial PD which compensated effects of MD and partially of TD.

7.3.2.3. Evonik dogbones

Fragments of sprues from the dogbones injection moulded with the Arburg Allrounder were tested with the GPC measurements carried out in triplicate, see Table 7.10 for the results. As shown previously, compounding with the nanoparticles preserved the molecular weight with the highest values listed for 10.50 wt% is16PLAHApp. The molecular weight of the dogbones injection moulded at Evonik was lower than that of the samples produced at TESco with the respective nanocomposites. However, as the injection moulding parameters at TESco were not disclosed it is not possible to infer if the change in molecular weight between the sample batches originates mostly from different HANP content or if it was also significantly altered by the residence at different processing temperatures.

Table 7.10. GPC measurements for the HANP-LR706S dogbones injection moulded at Evonik. (1) full range of molecular weights, (2) main peak, (3) peak with short chained species.

Material	(1)		(2)		(3)	
	M_w [kg. mol^{-1}]	PDI	M_w [kg. mol^{-1}]	PDI	M_w [kg. mol^{-1}]	PDI
Extruded LR706S	269.6 ±46.0	21.9 ±4.3	281.5 ±48.4	2.8 ±0.2	0.9 ±0.0	1.5 ±0.0
4.47 wt% HANP plate	211.6 ±3.1	32.8 ±2.4	230.8 ±4.0	2.8 ±0.1	0.9 ±0.0	1.5 ±0.0
4.45 wt% HANP rod	235.7 ±5.8	23.0 ±3.2	246.5 ±7.6	3.5 ±0.4	0.7 ±0.0	1.2 ±0.0
10.50 wt% is16PLAHApp	252.9 ±1.8	37.9 ±2.9	278.3 ±3.8	2.7 ±0.1	1.0 ±0.0	1.5 ±0.0

7.3.3. IV

IV measurements were carried out at TESco, with details on the equipment and method utilised not provided.

7.3.3.1. TESco products

IV measurement results are shown in Table 7.11 for (i) the pelletised nanocomposites extruded with the Pharma 11, (ii) which were dried prior to the injection moulding of a (iii) tensile bar and (iv) proximal pin.

A 14 – 16% decrease of IV was apparent due to compounding of material stock for injection moulding, however final values for the produced bars and pins were only 7 – 19% lower than the pellet stock after processing at TESco. This indicates relatively low degradation of the materials due to subsequent processing during injection moulding. The pellet sizes were larger than what would be ideal for the injection moulder utilised, resulting in longer melt times and a likely greater loss in molecular weight. Additionally, the tensile bar mould was not an optimal fit to the process therefore dogbones experienced more degradation during injection which resulted in a lower IV than that for the proximal pins. The nanocomposites with is16PLAHApp exhibited an unusual behaviour after drying, where IV increased, and appeared to have maintained a higher molecular weight.

Table 7.11. IV measurements of the LR706S materials: extruded with the Pharma 11 (as received) and after drying (dried), injection moulded at TESco into a tensile bar (bar) and proximal pin (pin).

Material	IV [dl.g^{-1}]			
	As received	Dried	Bar	Pin
Neat LR706S	4.004	4.015	3.224	3.409
HANP plate	3.418	3.541	3.110	3.342
HANP rod	3.448	3.402	3.197	3.288
is16PLAHApp	3.374	3.633	3.447	3.562

GPC and IV measurements for pellets and tensile bars were compared, shown in Figure 7.10. The same general trend was seen between M_w for full range and the main peak with IV measurements. The post-process assessment of tensile bars revealed, as expected, decreased M_w and IV due to degradation during melt processing.

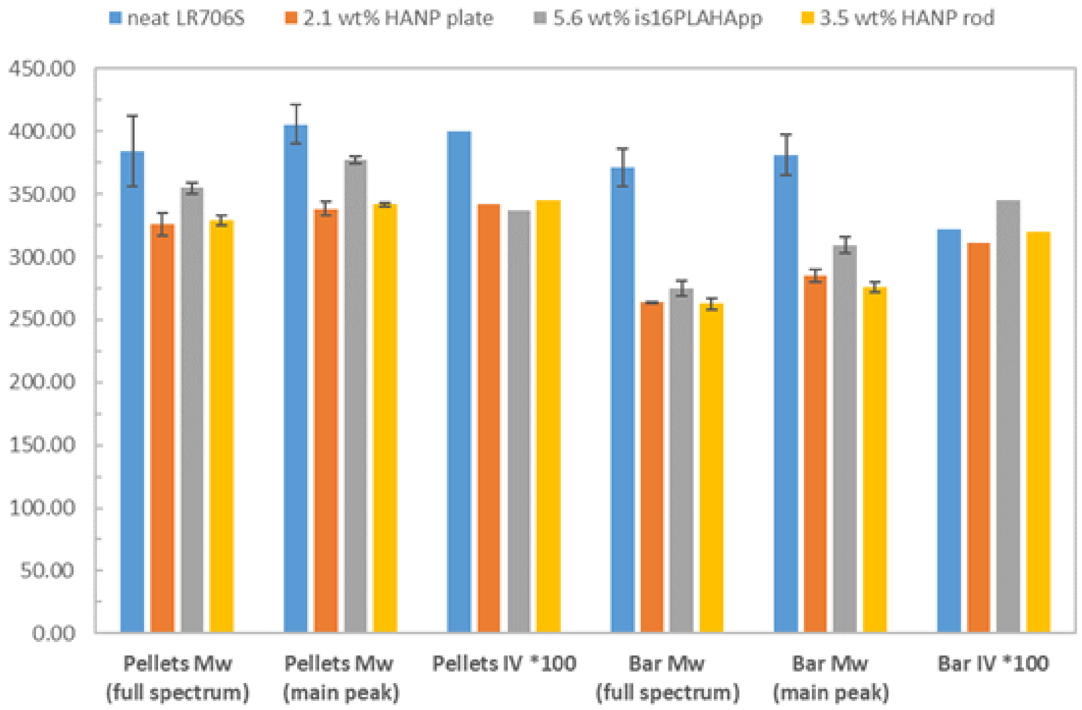

Figure 7.10. Comparison of GPC and IV measurements for pellets and tensile bars.

7.3.4. MicroCT

The nanocomposite samples were scanned with parameters described in Section 3.2.10 and the obtained section images were combined into a 3D model and analysed for HANP dispersion in LR706S. The volume of visible HA and PLA matrix was obtained from the 3D models of the scanned nanocomposites, provided in Figure 7.11 and Figure 7.12. The HANP volume percentage was calculated and converted to weight percentage using densities of the materials. This was then compared with HA char residue measured by TGA.

As the microCT scans were performed at a resolution of 1 μm, it was assumed that the HA nanoparticles which were not visible are dispersed while the filler shown in the models represents HANP agglomeration. The results from the analysis are summarised in Table 7.12.

The least agglomeration (13.5%) was seen for 3.55 wt% HANP rod injection moulded at TESco followed by 5.56 wt% is16PLAHApp. The materials processed at TESco had less agglomeration than at Evonik, most likely due to lower particle loading allowing for better mixing. However, those HANP rod and plate materials processed at TESco had agglomeration which was 98% and 64% worse respectively in comparison to their 2.5 wt% nanocomposites produced in the MiniLab in N_{2D}. The dispersion of is16PLAHApp-LR706S processed at TESco improved by 60% when compared with 3.6 wt% is16PLAHA-LR706S produced in the MiniLab in N_{2D}, however this can be partially attributed to the slightly larger amount of dispersant in is16PLAHApp. The worst dispersion was shown for 4.5 wt% HANP plate nanocomposite injection moulded at Evonik with 77.6% filler agglomeration.

Table 7.13. HA agglomeration in microCT scans of the HANP-LR706S nanocomposites injection moulded at TESco and Evonik.

	Name	HA char [wt%]	HA in microCT [wt%]	Agglomerates [%]
TESco	HANP plate	2.07 ±0.14	1.24	59.80
	HANP rod	3.55 ±0.12	0.48	13.49
	is16PLAHApp	2.89 ±0.09	0.59	20.33
Evonik	HANP plate	4.47 ±0.06	3.46	77.57
	HANP rod	4.45 ±0.03	1.43	32.05
	is16PLAHApp	5.46 ±0.10	1.73	31.75

This space is intentionally left blank

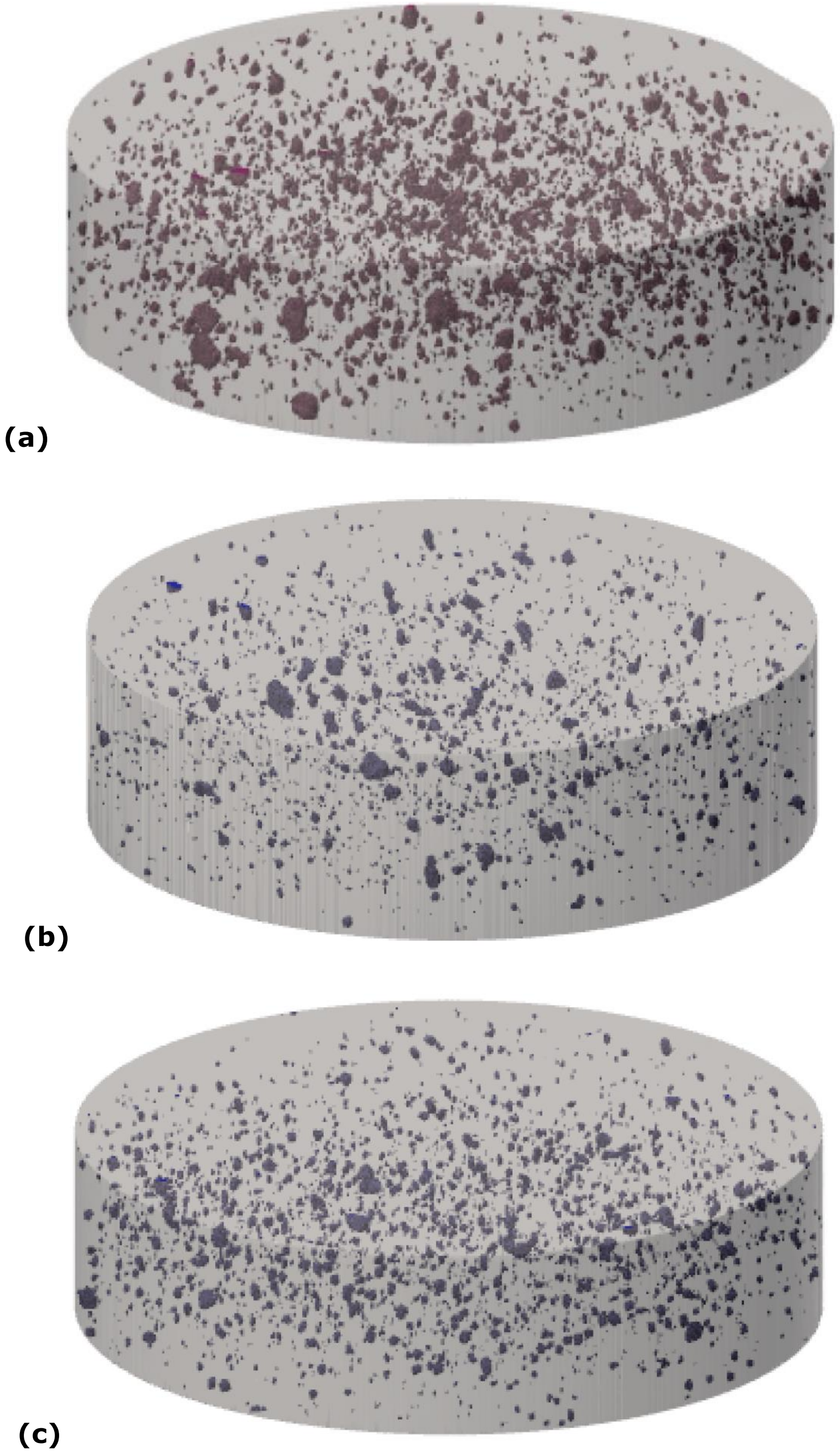

Figure 7.11. MicroCT scan overview of TESco injection moulded nanocomposites with (a) HANP plate, (b) HANP rod, (c) is16PLAHApp. Total volume of each approximately 1.4 mm^3.

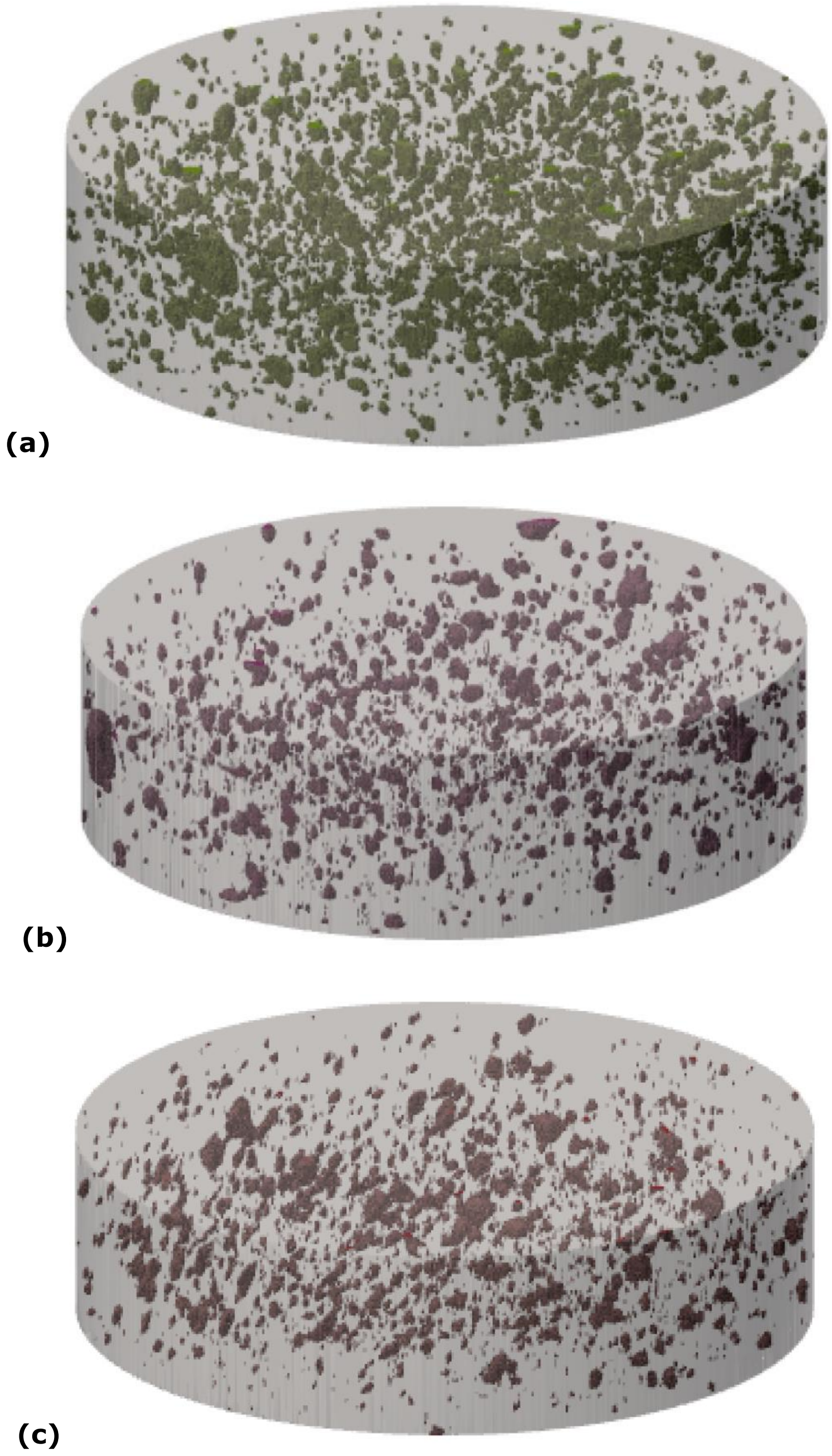

Figure 7.12. MicroCT scan overview of Evonik injection moulded nanocomposites with (a) HANP plate, (b) HANP rod, (c) is16PLAHApp. Total volume of each approximately 1.4 mm^3.

7.3.5. Mechanical testing

Flexural properties were tested with minibar samples, compression moulded from the pellets of nanocomposites extruded with the Pharma 11, accordingly to methods described in Section 3.2.11.

The Instron Tensile Tester 5969 with 5 kN load cell and a speed of 1 mm.min^{-1} with displacement measured via digital image correlation was used for tensile strength measurements of the injection moulded dogbones from TESco.

The torsional tests were carried out with an Anton Paar MCR302 rheometer fitted with an air bearing with integrated normal force sensor and Dynamic Mechanical Analysis adaptor (Solid Rectangular Fixture). Measurements were conducted at 1 Hz and 20 °C, with the oscillatory signal measured by the synchronous EC motor without superposition of a pretension force. Tests were performed on the injection moulded dog bones from Evonik (10 mm length, 2.5 mm width, 1 mm thickness) and the pins from TESco (45 mm length and 4.5 mm diameter).

All experiments were carried out in triplicate.

7.3.5.1. TESco products

Tensile and flexural strength for the samples from TESco are summarised in Table 7.14. No significant differences in values were found. The failure mode showed a definite skin in the injection moulded tensile dogbone specimens.

Table 7.14. Tensile strength and flexural strength measurements with IM dogbone and CM minibars respectively.

Name	IM Dogbones Tensile strength [MPa]	CM minibars Flexural Strength [MPa]
Neat LR706S	59.4 ±0.4	106 ±3
2.1 wt% HANP plate	58.3 ±0.8	109 ±1
3.5 wt% HANP rod	61 ±5	107 ±3
5.6 wt% is16PLAHApp	59.0 ±0.6	102 ±6

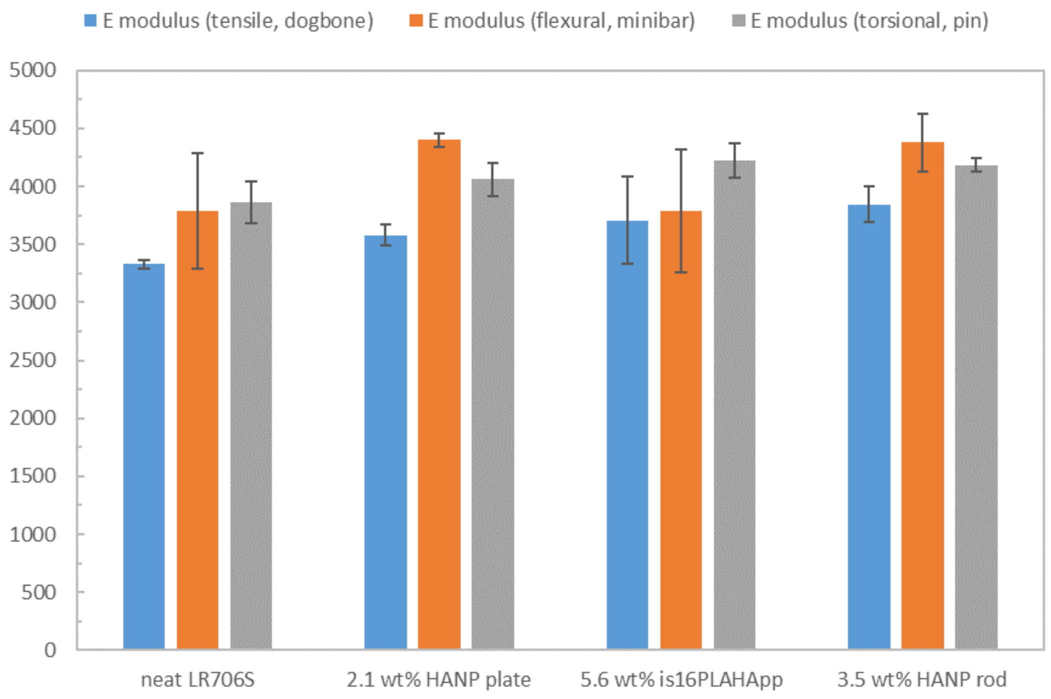

Figure 7.13. Mechanical testing of TESco materials; minibars compression moulded directly from the nanocomposite pellets.

The modulus from the tensile, flexural and torsional tests are compared in Figure 7.13. The lowest modulus was always exhibited by LR706S samples. The tensile modulus of 3.5 wt% HANP rods is statistically higher than that of the neat PLA. The flexural modulus shows no statistical difference between specimens. The torsional modulus of 5.6 wt% is16PLAHApp and 3.5 wt% HANP rod are statistically higher than that of the neat PLA.

7.3.5.2. Evonik dogbones

Torsional testing results were compared for TESco pins and Evonik bars, see Figure 7.14. The shear modulus shows no statistical difference between Evonik specimens, however it is statistically smaller than that for samples from TESco.

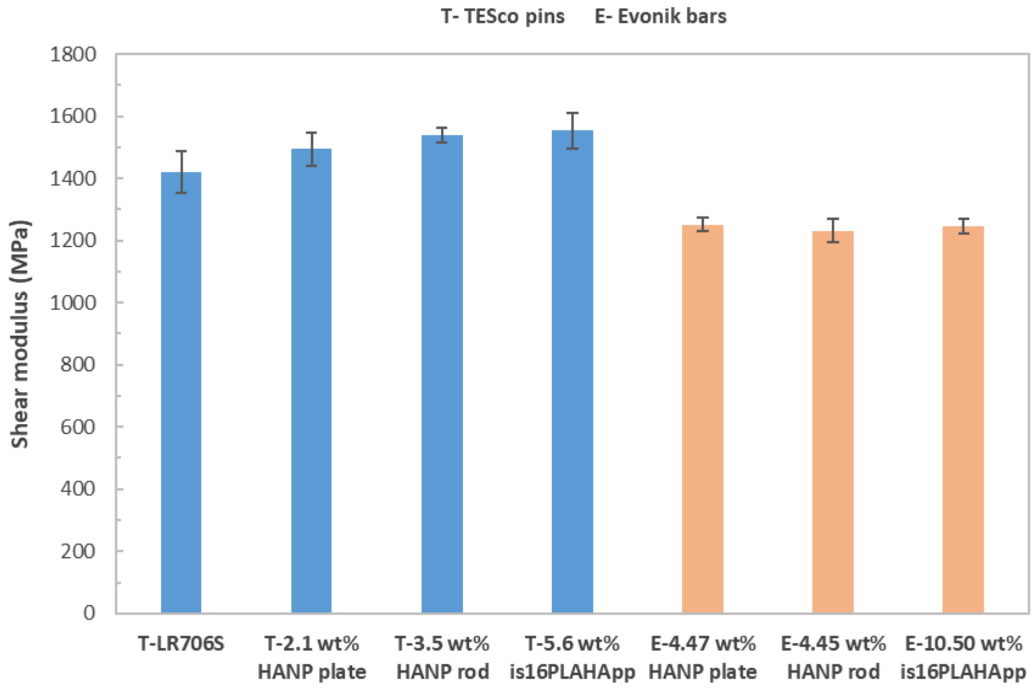

Figure 7.14. Torsional testing of TESco pins and Evonik bars with DMA adaptor on Anton Paar MCR302 rheometer.

7.4. Specific mechanical energy

Screw speed in an extruder controls mixing, polymer melting and generated pressure. It also determines screw flights fill, melt residence time and torque level. Screw speed needs to be optimised to balance improvements in mixing with time in which mixing can occur. Higher screw speeds exert a greater shear rate on the melt, which in turn disperses particles in the matrix, while residence time in the extruder decreases for a given throughput [180]. Twin screw extruders are starve-fed for compounding of composites where the throughput is determined by the feed rate as opposed to screw speed. To produce well dispersed material, where degradation is limited, processing conditions need to be optimised [181].

Specific mechanical energy (SME in kJ.kg^{-1}) can be used for scale up by comparing processing conditions for a given polymeric material in different extruders at the same compounding temperature [182]:

$$\mathrm{SME} = \frac{n_s 2\pi\, T}{m} \tag{7.1}$$

where m is the mass flow rate, also known as throughput (in kg.min^{-1}).

Take two different extruders that share similar characteristics (similar screw geometry, same L/D, outer and inner screw diameter ratio and configuration) but that are of different diameters. If screw speed remains unchanged for constant SME, melt processing can be scaled by adjusting throughput using [177]:

$$m_1 = \left(\frac{\emptyset_1}{\emptyset_2}\right)^3 m_2 \tag{7.2}$$

where $\emptyset$ is the screw outer diameter for the given extruder.

Comparison of the nanocomposites compounded in the Pharma 11 and Pharma 16 was carried out using SME as the metric. This can be linked to recirculation in the MiniLab by substituting Equation (3.3) into Equation (3.1), yielding:

$$\mathrm{SME} = \frac{E_{mix}}{m_{HA} + m_{PLA}} \tag{7.3}$$

using m_{HA} and m_{PLA} loaded to the MiniLab for the particular run. However, the compounding scale-up experiments carried out with the three different extruders are not directly comparable via SME due to:

(i) different screw geometry in the MiniLab, in comparison to the other two twin screw extruders, and operation in recirculation mode

(ii) three different screw speeds were utilised

(iii) Pharma 11 and 16 have the same screw geometry however, due to different HANP loading, the temperature gradient had to be altered for the larger extruder and temperature in the final zones and at the die was 5 °C higher than in Pharma 11 to allow processing.

For these reasons, SME for the three processes is used indirectly in an attempt to qualitatively explain differences between them.

7.4.1. Compounding analysis

Firstly, average *m* and *T* were calculated for each run in Pharma 11 which are summarised in Table 7.15 and used for calculation of SME. Secondly, E_{mix} was calculated for the MiniLab at the end of compounding at 15 min, and at 10 min, which were used to calculate SME at the respective timepoints; summarised in Table 7.16. Finally, SME was calculated for compounding in Pharma 16 with the results summarised in Table 7.17.

Table 7.15. SME for HANP-LR706S nanocomposites compounded in the Pharma 11 at 210 °C and 100 rpm in N_{2D}.

HANP	*T* [Nm]	*m* [kg.h^{-1}]	SME [kJ.kg^{-1}]
2.17 wt% HANP plate	4.72 ±0.49	0.349 ±0.008	510
3.34 wt% HANP rod	4.81 ±0.16	0.334 ±0.021	543
5.67 wt% is16PLAHApp	4.51 ±0.18	0.361 ±0.013	471

Table 7.16. SME for HANP-LR706S nanocomposites compounded in the MiniLab at 210 °C, 50 rpm for 15 min in N_{2D} compared with SME after only 10 min recirculation.

HANP	m_{HA} + m_{PLA} [g]	E_{mix} at 10 min [kJ]	SME at 10 min [kJ.kg^{-1}]	E_{mix} at 15 min [kJ]	SME at 15 min [kJ.kg^{-1}]
2.17 wt% HANP plate	7.73	5.21	674	7.44	962
3.32 wt% HANP rod	7.80	4.41	566	6.12	785
4.44 wt% is16PLAHApp	7.84	5.96	761	8.61	1099

Table 7.17. SME for HANP-LR706S nanocomposites compounded in the Pharma 16 at 215 °C and 120 rpm in N_{2D}.

HANP	*T* [Nm]	*m* [kg.h^{-1}]	SME [kJ.kg^{-1}]
4.47 wt% HANP plate	3.8	1	172
4.45 wt% HANP rod	3.7	1	167
10.50 wt% is16PLAHApp	8.5	1	385

Nanocomposites compounded in the MiniLab for 15 min had the highest SME from all the materials, with the greatest amount of energy used for the production of 4.44 wt% is16PLAHApp-LR706S. Mixing in Pharma 11 used less SME - for the respective materials 31-57% lower than that after 15 min in the MiniLab and still 4-38% lower than at 10 min. The greatest difference was for the nanocomposites with coated HANP.

This suggests that the materials compounded for 90s in the Pharma 11 at 100 rpm and 5.6 – 6 $g.min^{-1}$ throughput experienced less mechanical energy than during 10-15 min compounding at 50 rpm in the MiniLab. Therefore, nanocomposites were sheared more in the MiniLab, providing in effect more mixing. However, this came at a cost of greater matrix degradation due to prolongated residence at elevated temperature.

The molecular weight loss for materials produced in the MiniLab, resulting from the degradation, was compared with M_w measurements for Pharma 11 products in Section 7.3.2.2. Lower molecular weight was found for respective HANP plate and rod nanocomposites produced in the MiniLab, with higher SME, than in Pharma 11. This suggests that consuming more SME causes greater degradation of the polymer resulting in lower molecular weight. In contrast, lower molecular weight and lower SME was found for samples injection moulded at Evonik from the materials produced with Pharma 16 when compared with samples manufactured at TESco from materials produced with Pharma 11. However, the lower M_w is likely caused by the increased amounts of HANP due to increasing particle agglomeration as shown previously in Section 5.1.1.1 for uncoated HANP and Section 5.1.1.3 for coated HANP nanocomposites.

The M_w for is16PLAHApp nanocomposites obtained in the MiniLab and Pharma 11 was practically identical, so one would expect their SME to also be similar. However, since 22% less weight of coated HANP was mixed with PLA in the MiniLab, particles compounded with LR706S could better disperse in the polymer matrix. This is thought to have prevented excessive molecular weight drop which would have occurred from longer residence at 210 °C in the MiniLab.

The throughput from Pharma 11, see Table 7.15, was scaled for Pharma 16, see Table 7.17, according to Equation (7.2). However, due to an increased amount of HANP, the required torque in Pharma 16 to move the screw at 100 rpm was too high. To counter this, barrel temperature was increased in the final zones and die by 5 °C and screw speed was increased to 120 rpm to allow for efficient mixing below alarm thresholds. This highlights that even relatively small weight percentage changes in the nanocomposites significantly influence the torque response which in turn may require adjustments of compounding conditions.

The nanocomposites compounded in Pharma 16 had a SME lower than that of the materials compounded in the MiniLab (65-82% when compared at 15 mins and 49-74% when compared at 10 min) even though they had a higher HANP content. When compared with compounding in Pharma 11, the SME in Pharma 16 decreased by 69% for materials with uncoated HANP and by 18% for nanocomposites with coated HANP.

This infers that less energy was used for particle mixing for the nanocomposites produced in Pharma 16, which in turn suggests inferior HANP dispersion despite increased screw speed and melt temperature. Based on the assumption that the process did not significantly alter the particle dispersion, this hypothesis was confirmed via microCT measurements of samples injection moulded with materials produced with Pharma 11 and Pharma 16, summarised in Section 7.3.4. The presented results showed increased agglomeration for the nanocomposites produced with Pharma 16. Since those materials had more nanoparticles, this suggests that insufficient SME was exerted in Pharma 16 for their compounding to improve dispersion.

7.5. Conclusions

Stocks of nanocomposite pellets were produced using a Pharma 11 extruder at the University of Bradford as three batches: 2.17 wt% HANP plates; 3.45 wt% HANP rods and 5.67 wt% is16PLAHApp. These were shipped to TESco. The produced materials had a HA content lower than the desired 5 wt% HANP due to issues during compounding. Following this, injection moulded parts, namely tensile bars and proximal pins, were successfully manufactured at TESco using industrial processing systems.

Pellets with a higher content of filler, 4.47 wt% HANP plates, 4.45 wt% HANP rods and 10.50 wt% is16PLAHApp, were produced with a Pharma 16 at Evonik and used for injection moulding of tensile bars.

The TGA values were seen to be in a good agreement between the feed material and the final produced parts at TESco (2 – 5% variation for the respective materials).

GPC and IV data showed reasonable consistency. The compounded specimens appear to maintain molecular weight better with the presence of nanoparticles, especially is16PLAHApp. This was also confirmed for equivalent batches produced with the MiniLab. Injection moulded specimens were produced at TESco and Evonik with similar final molecular weight to the processed neat polymer.

No significant difference was observed in yield strength between the samples. However significant differences were observed in modulus values between the samples. The shear modulus for the Evonik specimens was smaller those from TESco.

MicroCT scans revealed that the samples which were injection moulded at TESco had better dispersion than the ones processed at Evonik, most likely due to lower HANP content. Consistently, the worst agglomeration was found for HANP plate materials and the best dispersion was established for 3.5 wt% HANP rods injection moulded at TESco, followed by low agglomeration for the is16PLAHApp nanocomposite.

The developed novel nanocomposites were successfully utilised in the production of demonstrator proximal pins and tensile bars at scale on industrial equipment. However, contrary to what was expected, the achieved HANP rod and plate dispersion was lower than for the equivalent materials produced with the MiniLab in N_{2D}. The dispersion of is16PLAHApp-LR706S processed at TESco improved by 60% when compared with 3.6 wt% is16PLAHA-LR706S produced in the MiniLab in N_{2D}, however this can partially be attributed to the slightly larger amount of dispersant in is16PLAHApp.

Comparison of specific mechanical energy for the nanocomposites produced with the three different extruders revealed that the greatest amount of SME was used to mix materials in the MiniLab. When SME was calculated for the nanocomposites produced with Pharma 16 and Pharma 11 it was found that less energy was consumed for extrusion of the materials produced with the latter extruder. As those materials had more nanoparticles this suggests that insufficient SME was exerted for their compounding to allow for better dispersion.

8. Conclusions

8.1. Major conclusions and research contributions

Novel hydroxyapatite nanoparticles were compounded with LR706S, polylactic acid purchased from Evonik, to develop biodegrable composites for medical devices. The MiniLab twin-screw recirculating extruder was successfully employed for mixing PLA nanocomposites at the laboratory scale. Compounding was mostly carried out for 15 min, in recirculation mode, at 210 °C and 50 rpm due to the MiniLab extruder pressure sensors alarm limits. Those mixing parameters also provide an agreeable compromise between particles mixing and preserving the molecular weight of LR706S. As the extruder was run in recirculation mode the volumetric flow rate could not be measured directly. Therefore, the volumetric flow rate was estimated through comparison of capillary rheometry measurements of PLA with wall shear stress, obtained during compounding, and the number of times recirculation occurred in the MiniLab during a 15 min period was calculated. The obtained Q and N were seen to decrease with increasing amounts of HANP plates due to reduced η of nanocomposites, predicted via the model, when compared to pure LR706S.

From the conducted experiments it was found that compounding under dried N_2 and the inclusion of dried HANP preserves molecular weight of PLA. The screw speed can be increased under N_2 from 50 to 100 rpm to aid particle mixing at no or minimal (7%) decrease of molecular weight. The greatest improvements in PLA properties were shown for HANP mixed under N_{2D} at 2.5 wt%, especially for HANP rods, which exhibited the highest half-life and molecular weight. Any amount of particle addition increases the temperature at 5% weight loss of the polymeric part only, but this does not increase further with additional filler. In the samples assessed, none experienced sufficient loss of molecular weight during processing to have a significant effect on the glass transition temperature. In terms of degradation, mechanical degradation was the greater factor at short processing times (5 min), while thermal degradation dominated at higher processing times (15 min). Flexural modulus was seen to be independent of molecular weight of the tested materials over the considered range, while bending strength showed a small decrease with lowering molecular weight.

TEM images of the sectioned extruded nanocomposites were analysed for HANP dispersion and a simple semi-quantitative method was employed for image analysis based on applying the largest open square on the micrograph without crossing or encapsulating any particle. The free space on the image decreased with either increasing HANP content or improving particle dispersion. Overall, the nanocomposites with coated HANP mixed in N_{2D} had a smaller square size of free space than the materials compounded in Air, with exception of 2.8 wt% DDSAHA, which infers improved nanoparticle dispersion in LR706S in dried nitrogen. However, TEM images represent a very small area of the produced nanocomposite and therefore they are not a complete representation of particle dispersion in the material.

Subsequently, a selection of nanocomposites were scanned with microCT at a resolution of 1 μm. It was assumed that HA nanoparticles visible in the constructed 3D models represent HANP agglomeration, which was quantified by comparing the calculated weight percentage with the HA char residue measured by TGA. Out of all the scanned nanocomposites, the least agglomeration was shown for 2.5 wt% HANP rod nanocomposites compounded in Air and N_{2D}. Dispersion of HANP rods and plates improved when mixed with LR706S under dried nitrogen. Coated HANP performed worse than the uncoated particles as they had a substantially higher percentage of agglomerates.

The HANP plate, HANP rod and is16PLAHApp nanocomposites were compounded with larger extruders, with methodologies transferred from the MiniLab, to produce pelletised material for manufacturing of a demonstrator resorbable device. The compounded specimens appeared to maintain molecular weight better with the presence of nanoparticles, especially is16PLAHApp. Tensile bars and proximal pins were successfully injection moulded using industrial processing systems. GPC and IV data for the manufactured devices showed reasonable consistency. MicroCT scans revealed that the worst agglomeration was found for HANP plate materials and the best dispersion was established for 3.5 wt% HANP rods injection moulded at TESco, followed by low agglomeration for the is16PLAHApp nanocomposite.

Work completed in this thesis has shown that scalable polymer processing methodologies can be utilised for the production of novel nHA-PLA biomaterials, based on degradable high molecular weight LR706S and novel bioresorbable HANP, to deliver solvent free nanomaterials for healthcare applications and produce demonstrator orthopaedic implants. The rod HANP-LR706S nanocomposites produced under N_{2D} exhibited superior particle dispersion in the polymer matrix, over other materials with HANP plates. This was especially true for the material with 2.5 wt% HANP rod compounded in the MiniLab as evidenced via microCT. This knowledge was shown to be transferable to the nanocomposites manufactured at industrial scale as samples injection moulded at TESco with 3.55 wt% HANP rods and 4.45 wt% at Evonik again exhibited the best particle dispersion out of all produced materials.

8.2. Recommendations for future work

There are several questions raised from this work that remain to be addressed.

Performing dynamic rotational rheometry measurements to investigate zero shear viscosity allows for the estimation of a relative modification index (RMI). Based on a method shown by Cuadri et al. [162], RMI can be used to quantify the decrease of PLA melt viscosity due to chain scission for differing compounding conditions, where higher RMI indicates more frequent chain scission attributed to exposure to heat and stress. This will allow for separation, and greater understanding, of individual contributions to degradation mechanisms on the produced materials, due to exerted heating, mechanical shearing and varying residence time during processing.

The semi-quantitative method applied to evaluate HANP dispersion on TEM images of the nanocomposites is not ideal due to the simplified approach employed for estimating the size of particle free areas. In order to improve the quantification of HANP dispersion an automated program, which is less dependent on human judgment, is required. The program would use a variable thresholding to compensate for the large lighting background gradients on the micrographs and particle edge detection based on pixel to pixel evaluation of a grey scale gradient.

It would be interesting to carry out a one-year shelf life study for the produced materials stored in: (i) a desiccator under atmospheric pressure at room temperature, (ii) a vacuum desiccator or a dry anaerobic glovebox at room temperature and (iii) a freezer sealed in a N_2 atmosphere in moisture barrier bags. GPC, DSC and TGA ($t_{5\%}$) measurements at uniform time intervals would allow to study temperature and residual moisture influence on the properties of the nanocomposites.

Investigation of various screws speeds and material discharge speed from the feeders for a dedicated scale-up extruder would allow for process optimisation to maximise HANP dispersion in LR706S during production of nanocomposite pellets. Additionally, the attachment of a compressed air dryer directly above the hopper would limit PLA moisture uptake which can be further limited by running the extruder and feeders under a continuous flow of dried nitrogen. Another option is production of well dispersed HANP-PLA masterbatches which could be dosed with PLA directly to the injection moulder. This limits matrix degradation during secondary melt processing.

Additionally, HANP-PLA materials can be further developed to produce orthopaedic implants with active ingredients with delayed extended release during PLA decomposition.

Finally, nHA coated with new dispersants is likely to change nanocomposite properties due to different interactions between the nanoparticles and polymer matrix. In this work, only DDSA and polylactide coated HANP were used for all investigations. By studying materials made with novel coated nHA it may be possible to understand better how the characteristics of the dispersants influence the nanocomposite properties, and hence the scope for medical applications. Therefore it is highly recommended that research in this area be continued to improve HANP dispersion in PLA and to quantify the effects of nanoparticle dispersion on the macroscopic properties of the materials.

Bibliography

1. Langer, R. and Tirrell, D.A. (2004) **Designing materials for biology and medicine**. Nature, 428, pp. 487.
2. Pawar, R.P., Tekale, S.U., Shisodia, S.U., Totre, J.T., and Domb, A.J. (2014) **Biomedical applications of poly (lactic acid)**. Recent Patents on Regenerative Medicine, 4, pp. 40-51.
3. Ong, K.L., Yun, B.M., and White, J.B. (2015) **New biomaterials for orthopedic implants**. Orthop Res Rev, 7, pp. 107-130.
4. Šupová, M. (2009) **Problem of hydroxyapatite dispersion in polymer matrices: a review**. Journal of Materials Science: Materials in Medicine, 20, pp. 1201-1213.
5. Shikinami, Y., Matsusue, Y., and Nakamura, T. (2005) **The complete process of bioresorption and bone replacement using devices made of forged composites of raw hydroxyapatite particles/poly l-lactide (Fu-HA/PLLA)**. Biomaterials, 26, pp. 5542-5551.
6. Shikinami, Y. and Okuno, M. (2001) **Bioresorbable devices made of forged composites of hydroxyapatite (HA) particles and poly L-lactide (PLLA). Part II: practical properties of miniscrews and miniplates**. Biomaterials, 22, pp. 3197-3211.
7. Hasegawa, S., Ishii, S., Tamura, J., Furukawa, T., Neo, M., Matsusue, Y. et al. (2006) **A 5–7 year in vivo study of high-strength hydroxyapatite/poly (L-lactide) composite rods for the internal fixation of bone fractures**. Biomaterials, 27, pp. 1327-1332.
8. Walley, K.C., Hofmann, K.J., Velasco, B.T., and Kwon, J.Y. (2017) **Removal of hardware after syndesmotic screw fixation: a systematic literature review**. Foot & ankle specialist, 10, pp. 252-257.
9. Bargmann, M., Kothe, H., Steinhoff, B., Alig, I., Rode, C., Wyrwa, R., and Schnabelrauch, M. (2013) **PLA-Based Biodegradable and Cytocompatible Implant Materials: Material Development, Processing and Properties**. Journal of Materials Science and Engineering, B 3 (10), pp. 619-632.
10. Srivastava, R.B. and Vishnoi, T. (2012) Biodegradable Polymers and Polymeric Composites. In: Tiwari, A. et al. (eds.) **Biotechnology in Biopolymers: Developments, Applications and Challenging Areas**. Shawbury, UK: Smithers Rapra Technology Ltd, pp. 153-192.
11. Muggli, D.S., Burkoth, A.K., and Anseth, K.S. (1999) **Crosslinked polyanhydrides for use in orthopedic applications: Degradation behavior and mechanics**. Journal of Biomedical Materials Research, 46, pp. 271-278.
12. Hutmacher, D.W. (2000) **Scaffolds in tissue engineering bone and cartilage**. Biomaterials, 21, pp. 2529-2543.
13. Bose, S., Roy, M., and Bandyopadhyay, A. (2012) **Recent advances in bone tissue engineering scaffolds**. Trends in Biotechnology, 30, pp. 546-554.
14. Zong, C., Qian, X.D., Tang, Z.H., Hu, Q.H., Chen, J.R., Gao, C.Y. et al. (2014) **Biocompatibility and Bone-Repairing Effects:**

Comparison Between Porous Poly-Lactic-Co-Glycolic Acid and Nano-Hydroxyapatite/Poly(lactic acid) Scaffolds. Journal of Biomedical Nanotechnology, 10, pp. 1091-1104.

15. Kutikov, A.B. and Song, J. (2013) **An amphiphilic degradable polymer/hydroxyapatite composite with enhanced handling characteristics promotes osteogenic gene expression in bone marrow stromal cells**. Acta Biomaterialia, 9, pp. 8354-8364.
16. Zhang, P., Hong, Z., Yu, T., Chen, X., and Jing, X. (2009) **In vivo mineralization and osteogenesis of nanocomposite scaffold of poly(lactide-co-glycolide) and hydroxyapatite surface-grafted with poly(l-lactide)**. Biomaterials, 30, pp. 58-70.
17. Liu, Y., Lim, J., and Teoh, S.-H. (2013) **Review: Development of clinically relevant scaffolds for vascularised bone tissue engineering**. Biotechnology Advances, 31, pp. 688-705.
18. Rezwan, K., Chen, Q.Z., Blaker, J.J., and Boccaccini, A.R. (2006) **Biodegradable and bioactive porous polymer/inorganic composite scaffolds for bone tissue engineering**. Biomaterials, 27, pp. 3413-3431.
19. MedicalEXPO. (2018) **Ligafix, an anterior cruciate ligament interference screw; SBM, France** [Online]. MedicalEXPO, The Online Medical Device Exhibition. Available at: http://www.medicalexpo.com/prod/sbm/product-96259-605267.html [Accessed 7 May 2019].
20. Wilberforce, S.I.J., Finlayson, C.E., Best, S.M., and Cameron, R.E. (2011) **The influence of hydroxyapatite (HA) microparticles (m) and nanoparticles (n) on the thermal and dynamic mechanical properties of poly-L-lactide**. Polymer, 52, pp. 2883-2890.
21. Grant, D., De Focatiis, D.S.A., Irvine, D.J., and Parsons, A.J. (2012). **The case for support for the BENcH project**. Available: http://www.nottingham.ac.uk/~enzddf/BENcH/uploads/Main/BENCHCase.pdf [Accessed 7 May 2019].
22. Rudd, C.D., De Focatiis, D.S.A., Howdle, S., Grant, D.M., Scammell, B., Alexander, C. et al. (2012) **EP/J017272/1: Integrated Molecular Design of Melt-processable Bioresorbable Engineering Nanocomposites for Healthcare (BENcH)**. Swindon: EPSRC. Available at: http://gow.epsrc.ac.uk/NGBOViewGrant.aspx?GrantRef=EP/J017272/1 [Accessed 7 May 2019].
23. Keaveny, T.M. and Hayes, W.C. (1993) **Mechanical properties of cortical and trabecular bone**. Bone, 7, pp. 285-344.
24. Cancer.org. (2018) **What Is Bone Cancer?** [Online]. USA: American Cancer Society. Available at: https://www.cancer.org/cancer/bone-cancer/about/what-is-bone-cancer.html [Accessed 7 May 2019].
25. Plackett, D. and Södergård, A. (2005) Polylactide-Based Biocomposites. In: Mohanty, A.K. et al. (eds.) **Natural Fibers, Biopolymers, and Biocomposites**. USA: CRC Press, pp. 579-596.

26. Walton, K.E. (2018) **The continuous manufacture of dispersant coated bioresorbable nanoparticles**. PhD Thesis. University of Nottingham.
27. Choong, G.Y.H., Parsons, A.J., Grant, D.M., and De Focatiis, D.S.A. (2014) Rheological techniques for determining degradation of polylactic acid in bioresorbable medical polymer systems. **Proceedings of the 30th Annual meeting of the Polymer Processing Society, Cleveland, Ohio, 8-12 June 2014**. Available at: http://www.nottingham.ac.uk/~enzddf/files/choong_PPS30_b_extendedabstract.pdf [Accessed 7 May 2019].
28. Choong, G.Y. and De Focatiis, D.S. (2016) **A method for the determination and correction of the effect of thermal degradation on the viscoelastic properties of degradable polymers**. Polymer Degradation and Stability, 130, pp. 182-188.
29. Ward, M. (2018) **Mechanical and structural performance of melt-processable bioresorbable engineering nanocomposites**. PhD Thesis. University of Nottingham.
30. Ghosh, S.B., Bandyopadhyay-Ghosh, S., and Sain, M. (2010) Composites. In: Auras, R.A. et al. (eds.) **Poly(lactic acid) : synthesis, structures, properties, processing, and applications**. Hoboken, New Jersey: Wiley, pp. 293-310.
31. Young, R.J. and Lovell, P.A. (2011) Polymer composites. In: Young, R.J. et al. (eds.) **Introduction to polymers**. CRC press.
32. Bartus, S.D., Vaidya, U.K., and Ulven, C.A. (2006) **Design and development of a long fiber thermoplastic bus seat**. Journal of Thermoplastic Composite Materials, 19, pp. 131-154.
33. Oliveira, M., Bernardo, C., and Hemsley, D. (2002) **The effect of flame retardants on the hot‐plate welding of talc‐filled polypropylene**. Polymer Engineering & Science, 42, pp. 146-151.
34. Sinha Ray, S. (2010) Nanocomposites. In: Auras, R.A. et al. (eds.) **Poly(lactic acid) : synthesis, structures, properties, processing, and applications**. Hoboken, New Jersey: Wiley, pp. 311-322.
35. Liu, P. and Guo, J. (2007) **Organo-modified magnesium hydroxide nano-needle and its polystyrene nanocomposite**. Journal of Nanoparticle Research, 9, pp. 669-673.
36. Luo, Z.P. and Koo, J.H. (2008) **Quantification of the layer dispersion degree in polymer layered silicate nanocomposites by transmission electron microscopy**. Polymer, 49, pp. 1841-1852.
37. Traiphol, N., Rungruangviriya, N., Potai, R., and Traiphol, R. (2011) **Stable polydiacetylene/ZnO nanocomposites with two-steps reversible and irreversible thermochromism: the influence of strong surface anchoring**. Journal of colloid and interface science, 356, pp. 481-489.
38. Coleman, J.N., Khan, U., and Gun'ko, Y.K. (2006) **Mechanical reinforcement of polymers using carbon nanotubes**. Advanced materials, 18, pp. 689-706.
39. Choong, G.Y.H., Lew, C.Y., and De Focatiis, D.S.A. (2015) **Role of processing history on the mechanical and electrical behavior of melt‐compounded polycarbonate‐multiwalled**

carbon nanotube nanocomposites. Journal of Applied Polymer Science, 132.

40. Tyan, H.-L., Leu, C.-M., and Wei, K.-H. (2001) **Effect of reactivity of organics-modified montmorillonite on the thermal and mechanical properties of montmorillonite/polyimide nanocomposites**. Chemistry of materials, 13, pp. 222-226.
41. Gao, F. (2004) **Clay/polymer composites: the story**. Materials today, 7, pp. 50-55.
42. Donnet, J.-B. and Voet, A. (1976) **Carbon black: physics, chemistry, and elastomer reinforcement**, M. Dekker.
43. Fukahori, Y. (2007) **Generalized concept of the reinforcement of elastomers. Part 1: Carbon black reinforcement of rubbers**. Rubber chemistry and technology, 80, pp. 701-725.
44. Howald, J.A., Garber, G.B., and Nowacki, M.C. (1999) **Tire with outer carbon black reinforced rubber strip for static reduction**. Google Patents.
45. Murariu, M. and Dubois, P. (2016) **PLA composites: From production to properties**. Advanced drug delivery reviews, 107, pp. 17-46.
46. Sinha Ray, S., Yamada, K., Okamoto, M., and Ueda, K. (2003) **New polylactide-layered silicate nanocomposites. 2. Concurrent improvements of material properties, biodegradability and melt rheology**. Polymer, 44, pp. 857-866.
47. Villmow, T., Poetschke, P., Pegel, S., Haeussler, L., and Kretzschmar, B. (2008) **Influence of twin-screw extrusion conditions on the dispersion of multi-walled carbon nanotubes in a poly(lactic acid) matrix**. Polymer, 49, pp. 3500-3509.
48. Armentano, I., Dottori, M., Puglia, D., and Kenny, J. (2008) **Effects of carbon nanotubes (CNTs) on the processing and in-vitro degradation of poly(dl-lactide-co-glycolide)/CNT films**. Journal of Materials Science: Materials in Medicine, 19, pp. 2377-2387.
49. Poggi, G., Toccafondi, N., Melita, L.N., Knowles, J.C., Bozec, L., Giorgi, R., and Baglioni, P. (2014) **Calcium hydroxide nanoparticles for the conservation of cultural heritage: new formulations for the deacidification of cellulose-based artifacts**. Applied Physics A, 114, pp. 685-693.
50. Kang, I.-G., Park, C.-I., Lee, H., Kim, H.-E., and Lee, S.-M. (2018) **Hydroxyapatite Microspheres as an Additive to Enhance Radiopacity, Biocompatibility, and Osteoconductivity of Poly (methyl methacrylate) Bone Cement**. Materials, 11, pp. 258.
51. Thatcher, G.L. (2009) Product realization: The processing of bioabsorbable polymers. In: Wuisman, P.I.J.M. et al. (eds.) **Degradable polymers for skeletal implants**. Nova Science Publishers.
52. Woodruff, M.A. and Hutmacher, D.W. (2010) **The return of a forgotten polymer—Polycaprolactone in the 21st century**. Progress in polymer science, 35, pp. 1217-1256.
53. Suzuki, S. and Ikada, Y. (2010) Medical Applications. In: Auras, R.A. et al. (eds.) **Poly(lactic acid) : synthesis, structures,**

properties, processing, and applications. Hoboken, New Jersey: Wiley, pp. 445-456.

54. TÖrmälä, P., Pohjonen, T., and Rokkanen, P. (1998) **Bioabsorbable polymers: Materials technology and surgical applications**. Proceedings of the Institution of Mechanical Engineers, Part H: Journal of Engineering in Medicine, 212, pp. 101-111.
55. Turvey, T.A., Bell, R.B., Tejera, T.J., and Proffit, W.R. (2002) **The use of self-reinforced biodegradable bone plates and screws in orthognathic surgery**. Journal of oral and maxillofacial surgery, 60, pp. 59-65.
56. Strobel, M., Weiler, A., and Timmermans, A. (2007) **Biodegradable interference screw and tool for attaching a transplant to a bone**. Google Patents.
57. Middleton, J.C. and Tipton, A.J. (2000) **Synthetic biodegradable polymers as orthopedic devices**. Biomaterials, 21, pp. 2335-2346.
58. Soppimath, K.S., Aminabhavi, T.M., Kulkarni, A.R., and Rudzinski, W.E. (2001) **Biodegradable polymeric nanoparticles as drug delivery devices**. Journal of controlled release, 70, pp. 1-20.
59. Fredenberg, S., Wahlgren, M., Reslow, M., and Axelsson, A. (2011) **The mechanisms of drug release in poly(lactic-co-glycolic acid)-based drug delivery systems-A review**. International Journal of Pharmaceutics, 415, pp. 34-52.
60. Miyazaki, H., Kinoshita, M., Saito, A., Fujie, T., Kabata, K., Hara, E. et al. (2012) **An ultrathin poly(l-lactic acid) nanosheet as a burn wound dressing for protection against bacterial infection**. Wound Repair and Regeneration, 20, pp. 573-579.
61. Okamura, Y., Kabata, K., Kinoshita, M., Miyazaki, H., Saito, A., Fujie, T. et al. (2013) **Fragmentation of Poly(lactic acid) Nanosheets and Patchwork Treatment for Burn Wounds**. Advanced Materials, 25, pp. 545-551.
62. Cooper, M.L., Hansbrough, J.F., Spielvogel, R.L., Cohen, R., Bartel, R.L., and Naughton, G. (1991) **In vivo optimization of a living dermal substitute employing cultured human fibroblasts on a biodegradable polyglycolic acid or polyglactin mesh**. Biomaterials, 12, pp. 243-248.
63. Chen, C.C., Chueh, J.Y., Tseng, H., Huang, H.M., and Lee, S.Y. (2003) **Preparation and characterization of biodegradable PLA polymeric blends**. Biomaterials, 24, pp. 1167-1173.
64. Kalfas, I.H. (2001) **Principles of bone healing**. Neurosurgical focus, 10, pp. 1-4.
65. Lunt, J. (1998) **Large-scale production, properties and commercial applications of polylactic acid polymers**. Polymer Degradation and Stability, 59, pp. 145-152.
66. Henton, D.E., Gruber, P., Lunt, J., and Randall, J. (2005) Polylactic Acid Technology. In: Mohanty, A.K. et al. (eds.) **Natural Fibers, Biopolymers, and Biocomposites**. USA: CRC Press, pp. 527-577.
67. Jiang, X., Luo, Y., Tian, X., Huang, D., Reddy, N., and Yang, Y. (2010) Chemical Structure of Poly(lactic acid). In: Auras, R.A. et al. (eds.) **Poly(lactic acid) : synthesis, structures, properties,**

processing, and applications. Hoboken, New Jersey: Wiley, pp. 69-82.

68. Fambri, L. and Migliaresi, C. (2010) Crystallization and thermal properties. In: Auras, R.A. et al. (eds.) **Poly(lactic acid) : synthesis, structures, properties, processing, and applications**. Hoboken, New Jersey: Wiley, pp. 113-124.
69. Lim, L.T., Auras, R., and Rubino, M. (2008) **Processing technologies for poly(lactic acid)**. Progress in Polymer Science, 33, pp. 820-852.
70. Ayoubi, A. (2011) **Sculptra** [Online]. London. Available at: http://www.lmaclinic.com/sculptra.asp [Accessed 7 May 2019].
71. Gunze. (2013) **Products - Bioabsorbable materials** [Online]. Tokyo, Japan. Available at: http://www.gunze.co.jp/e/medical/product/product_02.html [Accessed 27 May 2014].
72. Conmed. (2004) **IMPACT™ suture anchor** [Online]. Largo, USA. Available at: http://www.conmed.com/products/shoulder-impact.php [Accessed 27 May 2014].
73. von Burkersroda, F., Schedl, L., and Göpferich, A. (2002) **Why degradable polymers undergo surface erosion or bulk erosion**. Biomaterials, 23, pp. 4221-4231.
74. Chen, Y., Zhou, S., and Li, Q. (2011) **Mathematical modeling of degradation for bulk-erosive polymers: Applications in tissue engineering scaffolds and drug delivery systems**. Acta Biomaterialia, 7, pp. 1140-1149.
75. Parsons, A.J. (2013) BENcH Project Overview: Introduction of project background and deliverables. **BENcH project kick off meeting, 9-10 May 2013, Nottingham.** Nottingham: UoN. Available at: http://www.nottingham.ac.uk/~enzddf/BENcH/uploads/Main/BENcH_kickoffmay2013_overview_AndyParsons.pdf [Accessed 7 May 2019].
76. Lester, E., Tang, S.V.Y., Khlobystov, A., Rose, V.L., Buttery, L., and Roberts, C.J. (2013) **Producing nanotubes of biocompatible hydroxyapatite by continuous hydrothermal synthesis**. Crystengcomm, 15, pp. 3256-3260.
77. Kumar, A. and Tripathi, A. (2012) Biopolymeric Scaffolds for Tissue Engineering. In: Tiwari, A. et al. (eds.) **Biotechnology in Biopolymers: Developments, Applications and Challenging Areas**. Shawbury, UK: Smithers Rapra Technology Ltd, pp. 233-285.
78. Qiu, X., Chen, L., Hu, J., Sun, J., Hong, Z., Liu, A. et al. (2005) **Surface-modified hydroxyapatite linked by L-lactic acid oligomer in the absence of catalyst**. Journal of Polymer Science Part A: Polymer Chemistry, 43, pp. 5177-5185.
79. Hong, Z., Qiu, X., Sun, J., Deng, M., Chen, X., and Jing, X. (2004) **Grafting polymerization of L-lactide on the surface of hydroxyapatite nano-crystals**. Polymer, 45, pp. 6699-6706.
80. Mathieu, L.M., Bourban, P.E., and Manson, J.A.E. (2006) **Processing of homogeneous ceramic/polymer blends for bioresorbable composites**. Composites Science and Technology, 66, pp. 1606-1614.

81. Wan, Y., Wu, C., Xiong, G., Zuo, G., Jin, J., Ren, K. et al. (2015) **Mechanical properties and cytotoxicity of nanoplate-like hydroxyapatite/polylactide nanocomposites prepared by intercalation technique**. Journal of the Mechanical Behavior of Biomedical Materials, 47, pp. 29-37.
82. McManus, A.J., Doremus, R.H., Siegel, R.W., and Bizios, R. (2005) **Evaluation of cytocompatibility and bending modulus of nanoceramic/polymer composites**. Journal of Biomedical Materials Research Part A: An Official Journal of The Society for Biomaterials, The Japanese Society for Biomaterials, and The Australian Society for Biomaterials and the Korean Society for Biomaterials, 72, pp. 98-106.
83. Talal, A., McKay, I.J., Tanner, K.E., and Hughes, F.J. (2013) **Effects of hydroxyapatite and PDGF concentrations on osteoblast growth in a nanohydroxyapatite-polylactic acid composite for guided tissue regeneration**. Journal of Materials Science-Materials in Medicine, 24, pp. 2211-2221.
84. Wiria, F.E., Chua, C.K., Leong, K.F., Quah, Z.Y., Chandrasekaran, M., and Lee, M.W. (2008) **Improved biocomposite development of poly (vinyl alcohol) and hydroxyapatite for tissue engineering scaffold fabrication using selective laser sintering**. Journal of Materials Science: Materials in Medicine, 19, pp. 989-996.
85. Shikinami, Y. and Okuno, M. (1999) **Bioresorbable devices made of forged composites of hydroxyapatite (HA) particles and poly-L-lactide (PLLA): Part I. Basic characteristics**. Biomaterials, 20, pp. 859-877.
86. Furukawa, T., Matsusue, Y., Yasunaga, T., Shikinami, Y., Okuno, M., and Nakamura, T. (2000) **Biodegradation behavior of ultra-high-strength hydroxyapatite/poly (L-lactide) composite rods for internal fixation of bone fractures**. Biomaterials, 21, pp. 889-898.
87. Du, K. and Gan, Z. (2014) **Shape memory behaviour of HA-g-PDLLA nanocomposites prepared via in situ polymerization**. Journal of Materials Chemistry B, 2, pp. 3340-3348.
88. Delabarde, C., Plummer, C.J.G., Bourban, P.-E., and Manson, J.-A.E. (2011) **Accelerated ageing and degradation in poly-L-lactide/hydroxyapatite nanocomposites**. Polymer Degradation and Stability, 96, pp. 595-607.
89. Liu, X.X., Wang, T.X., Chow, L.C., Yang, M.S., and Mitchell, J.W. (2014) **Effects of Inorganic Fillers on the Thermal and Mechanical Properties of Poly(lactic acid)**. International Journal of Polymer Science.
90. Liu, Z., Chen, Y.H., Ding, W.W., and Zhang, C.H. (2015) **Filling behavior, morphology evolution and crystallization behavior of microinjection molded poly(lactic acid)/hydroxyapatite nanocomposites**. Composites Part a-Applied Science and Manufacturing, 72, pp. 85-95.
91. Danoux, C.B., Barbieri, D., Yuan, H., de Bruijn, J.D., van Blitterswijk, C.A., and Habibovic, P. (2014) **In vitro and in vivo bioactivity assessment of a polylactic acid/hydroxyapatite composite for bone regeneration**. Biomatter, 4.

92. Dorgan, J.R., Lehermeier, H., and Mang, M. (2000) **Thermal and rheological properties of commercial-grade poly(lactic acid)s**. Journal of Polymers and the Environment, 8, pp. 1-9.
93. Dorgan, J.R. (2010) Rheology of Poly(lactic acid). In: Auras, R.A. et al. (eds.) **Poly(lactic acid) : synthesis, structures, properties, processing, and applications**. Hoboken, New Jersey: Wiley, pp. 125-140.
94. Libiszowski, J., Kowalski, A., Biela, T., and Duda, A. (2004) **Thermal stability of poly(L-lactide) prepared by polymerization of L,L-dilactide with Sn(II)-based initiators**. Polimery, 49, pp. 690-697.
95. Taubner, V. and Shishoo, R. (2001) **Influence of processing parameters on the degradation of poly (L-lactide) during extrusion**. Journal of applied polymer science, 79, pp. 2128-2135.
96. Kopinke, F.-D., Remmler, M., Mackenzie, K., Möder, M., and Wachsen, O. (1996) **Thermal decomposition of biodegradable polyesters—II. Poly (lactic acid)**. polymer Degradation and Stability, 53, pp. 329-342.
97. Nishida, H. (2010) Thermal Degradation. In: Auras, R.A. et al. (eds.) **Poly(lactic acid) : synthesis, structures, properties, processing, and applications**. Hoboken, New Jersey: Wiley, pp. 401-412.
98. Lee, S.-H., Hyun Kim, S., Han, Y.-K., and Kim, Y.H. (2001) **Synthesis and degradation of end-group-functionalized polylactide**. Journal of Polymer Science Part A: Polymer Chemistry, 39, pp. 973-985.
99. CONAIR (2010) **Handling, Drying, and Reclaim Considerations for PLA**. CONAIR Technology Bulletin. Available at: http://www.conairgroup.com/assets/Knowledge-Center/Whitepapers/General/Handling-Drying-and-Reclaim-Considerations-for-PLA-0810.pdf [Accessed 20 May 2014].
100. Lim, L.-T., Clink, K., and Vanyo, T. (2010) Processing of Poly(lactic acid). In: Auras, R.A. et al. (eds.) **Poly(lactic acid) : synthesis, structures, properties, processing, and applications**. Hoboken, New Jersey: Wiley, pp. 191-216.
101. Xu, J. (2010) Process for Microcellular Injection Molding. **Microcellular Injection Molding**. Hoboken, NJ, USA: John Wiley & Sons, pp. 227-313.
102. Bozzelli, J. (2010) **Don't neglect cooling... There's money to be made** [Online]. Cincinnati, USA: Plastics Technology. Available at: http://www.ptonline.com/columns/don't-neglect-cooling-there's-money-to-be-made [Accessed 7 May 2019].
103. Kimerling, T. (2002) **Injection molding cooling time reduction and thermal stress analysis** [Online]. Amherst, USA: University of Massachusetts. Available at: http://www.ecs.umass.edu/mie/labs/mda/fea/fealib/Tom%20Kimerling/TKimerling_injection_molding.pdf [Accessed 7 May 2019].
104. Park, S.-D., Todo, M., and Arakawa, K. (2004) **Effect of annealing on the fracture toughness of poly(lactic acid)**. Journal of Materials Science, 39, pp. 1113-1116.

105. Kolstad, J.J. (1996) **Crystallization kinetics of poly(L-lactide-co-meso-lactide)**. Journal of Applied Polymer Science, 62, pp. 1079-1091.
106. Fang, Q. and Hanna, M.A. (1999) **Rheological properties of amorphous and semicrystalline polylactic acid polymers**. Industrial Crops and Products, 10, pp. 47-53.
107. Perego, G. and Cella, G.D. (2010) Mechanical Properties. In: Auras, R.A. et al. (eds.) **Poly(lactic acid) : synthesis, structures, properties, processing, and applications**. Hoboken, New Jersey: Wiley, pp. 141-154.
108. Detyothin, S., Kathuria, A., Jaruwattanayon, W., Selke, S.E.M., and Auras, R. (2010) Poly(lactic acid) Blends. In: Auras, R.A. et al. (eds.) **Poly(lactic acid) : synthesis, structures, properties, processing, and applications**. Hoboken, New Jersey: Wiley, pp. 227-271.
109. Takayama, T., Todo, M., and Takano, A. (2009) **The effect of bimodal distribution on the mechanical properties of hydroxyapatite particle filled poly(L-lactide) composites**. Journal of the Mechanical Behavior of Biomedical Materials, 2, pp. 105-112.
110. Aït Hocine, N. (2009) Mechanical property enhancement of polymer nanocomposites. In: Mittal, V. (ed.) **Optimization of polymer nanocomposite properties**. John Wiley & Sons, pp. 123-138.
111. Hong, Z., Zhang, P., He, C., Qiu, X., Liu, A., Chen, L. et al. (2005) **Nano-composite of poly (L-lactide) and surface grafted hydroxyapatite: mechanical properties and biocompatibility**. Biomaterials, 26, pp. 6296-6304.
112. Di, Y., Iannace, S., Maio, E.D., and Nicolais, L. (2005) **Poly (lactic acid)/organoclay nanocomposites: thermal, rheological properties and foam processing**. Journal of Polymer Science Part B: Polymer Physics, 43, pp. 689-698.
113. Singh, S., Ghosh, A.K., Maiti, S.N., Raha, S., Gupta, R.K., and Bhattacharya, S. (2012) **Morphology and rheological behavior of polylactic acid/clay nanocomposites**. Polymer Engineering and Science, 52, pp. 225-232.
114. Song, Y. and Zheng, Q. (2015) **Linear rheology of nanofilled polymers**. Journal of Rheology (1978-present), 59, pp. 155-191.
115. Sabzi, M., Jiang, L., Atai, M., and Ghasemi, I. (2013) **PLA/sepiolite and PLA/calcium carbonate nanocomposites: A comparison study**. Journal of Applied Polymer Science, 129, pp. 1734-1744.
116. Wu, F., Lan, X.R., Ji, D.Y., Liu, Z.Y., Yang, W., and Yang, M.B. (2013) **Grafting polymerization of polylactic acid on the surface of nano-SiO2 and properties of PLA/PLA-grafted-SiO2 nanocomposites**. Journal of Applied Polymer Science, 129, pp. 3019-3027.
117. Zhang, Y., Deng, B., and Liu, Q. (2014) **Rheology and crystallisation of PLA containing PLA-grafted nanosilica**. Plastics, Rubber and Composites, 43, pp. 309-314.
118. Ghorbani, F.M., Kaffashi, B., Shokrollahi, P., Akhlaghi, S., and Hedenqvist, M.S. (2016) **Effect of hydroxyapatite nano-**

particles on morphology, rheology and thermal behavior of poly (caprolactone)/chitosan blends. Materials Science and Engineering: C, 59, pp. 980-989.

119. Pluta, M. (2006) **Melt compounding of polylactide/organoclay: structure and properties of nanocomposites**. Journal of Polymer Science Part B: Polymer Physics, 44, pp. 3392-3405.
120. Hu, Y.-H., Chen, C.-Y., and Wang, C.-C. (2004) **Viscoelastic properties and thermal degradation kinetics of silica/PMMA nanocomposites**. Polymer Degradation and Stability, 84, pp. 545-553.
121. Kasaliwal, G., Göldel, A., and Pötschke, P. (2009) **Influence of processing conditions in small-scale melt mixing and compression molding on the resistivity and morphology of polycarbonate–MWNT composites**. Journal of Applied Polymer Science, 112, pp. 3494-3509.
122. Pegel, S., Pötschke, P., Villmow, T., Stoyan, D., and Heinrich, G. (2009) **Spatial statistics of carbon nanotube polymer composites**. Polymer, 50, pp. 2123-2132.
123. Sahu, T.P. and Jain, Y.K. (2015) **Improved Simplified Novel Method for Edge Detection in Grayscale Images Using Adaptive Thresholding**. Journal of Advances in Computer Networks, 3.
124. Sleit, A., Saadeh, M., and Al Mobaideen, W. (2016) **An Edge Detection Technique for Grayscale Images Based on Fuzzy Logic**. British Journal of Applied Science & Technology, 17, pp. 1-13.
125. Khare, H.S. and Burris, D.L. (2010) **A quantitative method for measuring nanocomposite dispersion**. Polymer, 51, pp. 719-729.
126. Taylor, A., Bray, D., Gilmour, S., Guild, F., and Masania, K. Quantifying the dispersion of nanoparticles in adhesives. **The 2013 Annual Meeting of the Adhesion Society, 2013.**
127. Choong, G.Y., Parsons, A.J., Grant, D.M., and De Focatiis, D.S. (2015) Rheological techniques for determining degradation of polylactic acid in bioresorbable medical polymer systems. **Polymer Processing Society Conference, 2014.** AIP Publishing, pp. 170005.
128. Beltrán, F., Lorenzo, V., Acosta, J., de la Orden, M., and Martínez-Urreaga, J. (2016) Effect of simulated mechanical recycling processes on the properties of poly (lactic acid). **Journal of Environmental Management of the 4th International Conference on Sustainable Solid Waste Management 2016, Cyprus, 23-25 June 2016**.
129. Mark, J.E. and Knovel (2009) **Polymer data handbook [electronic resource] / edited by James E. Mark**, Oxford University Press.
130. Tee, Y.B., Talib, R.A., Abdan, K., Chin, N.L., Basha, R.K., and Yunos, K.F.M. (2013) **Thermally grafting aminosilane onto kenaf-derived cellulose and its influence on the thermal properties of poly (lactic acid) composites**. BioResources, 8, pp. 4468-4483.

131. Lester, E.H. and Azzopardi, B.J. (2005) **Counter current mixing reactor**, Patent W/O 2005077505. Available at: http://www.google.com/patents/WO2005077505A2.
132. Lester, E.H. (2010) **Hydroxyapatite material and methods of production**, Patent W/O 2010122354. Available at: http://google.com/patents/WO2010122354A1.
133. Gimeno-Fabra, M., Hild, F., Dunne, P., Walton, K., Grant, D., Irvine, D.J., and Lester, E. (2015) **Continuous synthesis of dispersant-coated hydroxyapatite plates**. CrystEngComm, 17, pp. 6175-6182.
134. Walton, K.E. (2017) **Personal Communication**.
135. Bard, D., G. Burdett, A. Thorpe, Cooke, J., and Sandys, V. (2015) **RR1068 Summary of work undertaken to assess workplace exposure and control measures during the manufacture and handling of engineered nanomaterials**. Health and Safety Executive Research Report Series. Health and Safety Laboratory, Buxton, UK.
136. UoN. (2012) **Guidance and Safety Requirements for the Creation and Manipulation of Engineered Nanomaterials** [Online]. Safety Office of The University of Nottingham. Available at: http://www.nottingham.ac.uk/safety/documents/nanomaterials.pdf [Accessed 7 May 2019].
137. SAFENANO. (2013) **Are there any workplace safety levels (e.g. OELs) for nanomaterials?** [Online]. Centre of Excellence in Nanosafety, UK Institute of Occupational Medicine. Available at: http://www.safenano.org/knowledgebase/resources/faqs/are-there-any-workplace-safety-levels-(eg-oels)-for-nanomaterials/ [Accessed 7 May 2019].
138. Isaakides, G., Frendel, A., and Bouton, J. (2001) MiniLab - Compounder and Reactor. **Proceedings of PPS 17th intl. Meeting, 2001.** Karlsruhe, Germany: Thermo Haake. Available at: http://www.mcik.co.kr/product/pdf/MicroCompounderReactor.pdf [Accessed 7 May 2019].
139. Son, Y. (2007) **Determination of shear viscosity and shear rate from pressure drop and flow rate relationship in a rectangular channel**. Polymer, 48, pp. 632-637.
140. Tomczynska, M.M., Choong, G.Y., De Focatiis, D.S., Grant, D.M., and Parsons, A.J. Compounding and rheometry of PLA nanocomposites with coated and uncoated hydroxyapatite nanoplatelets. **AIP Conference Proceedings, 2016.** AIP Publishing, pp. 030010.
141. De Focatiis, D.S. (2012) **Tooling for near net-shape compression moulding of polymer specimens**. Polymer testing, 31, pp. 550-556.
142. Su, S., Xu, Y., and Wilkie, C.A. (2011) Thermal degradation of polymer-carbon nanotube nanocomposites. In: McNally, T. et al. (eds.) **Polymer-carbon nanotube composites: Preparation, properties and applications**. Cambridge: Woolhead publishings, pp. 482–510.

143. McCrum, N.G., Buckley, C., and Bucknall, C.B. (1997) Structure of the molecule. In: McCrum, N.G. et al. (eds.) **Principles of polymer engineering**. Oxford University Press, USA, pp. 19-44.
144. Signori, F., Coltelli, M.-B., and Bronco, S. (2009) **Thermal degradation of poly (lactic acid)(PLA) and poly (butylene adipate-co-terephthalate)(PBAT) and their blends upon melt processing**. Polymer degradation and stability, 94, pp. 74-82.
145. Meng, L., Wu, D., Kelly, A., Woodhead, M., and Liu, Y. (2016) **Experimental investigation of the rheological behaviors of polypropylene in a capillary flow**. Journal of Applied Polymer Science, 133.
146. Malvern (2006) **Rosand RH7/RH10 User Manual MAN0362 Issue 1.0**. Worcestershire, UK: Malvern Instruments Ltd.
147. Efimov, A.E., Tonevitsky, A.G., Dittrich, M., and Matsko, N.B. (2007) **Atomic force microscope (AFM) combined with the ultramicrotome: a novel device for the serial section tomography and AFM/TEM complementary structural analysis of biological and polymer samples**. Journal of microscopy, 226, pp. 207-216.
148. Michler, G.H. (2008) Preparation of Thin Sections: (Cryo)ultramicrotomy and (Cryo)microtomy. **Electron microscopy of polymers**. Springer Science & Business Media, pp. 199-217.
149. De Focatiis, D.S. and Buckley, C.P. (2008) **Determination of craze initiation stress in very small polymer specimens**. Polymer testing, 27, pp. 136-145.
150. Ward, M. (2018) **Mechanical and structural performance of melt-processable bioresorbable engineering nanocomposites**. PhD Thesis. University of Nottingham.
151. Al-Itry, R., Lamnawar, K., and Maazouz, A. (2012) **Improvement of thermal stability, rheological and mechanical properties of PLA, PBAT and their blends by reactive extrusion with functionalized epoxy**. Polymer Degradation and Stability, 97, pp. 1898-1914.
152. Maxwell, A., Broughton, W., Dean, G., and Sims, G. (2005) **Review of accelerated ageing methods and lifetime prediction techniques for polymeric materials**. NPL Report DEPC MPR.
153. Witzke, D.R. (1997) **Introduction to Properties, Engineering, and Prospects of Polylactide Polymers**. PhD Thesis. Michigan State University.
154. Coltelli, M.-B., Toncelli, C., Ciardelli, F., and Bronco, S. (2011) **Compatible blends of biorelated polyesters through catalytic transesterification in the melt**. Polymer Degradation and Stability, 96, pp. 982-990.
155. Tomczynska, M.M., Ward, M., Choong, G.Y., Walton, K., De Focatiis, D.S., Grant, D.M. et al. Processing and properties of PLA-HA nanocomposites: The effect of particle morphology and dispersants. **AIP Conference Proceedings, 2017.** AIP Publishing, pp. 150004.

156. Miller, E. and Rothstein, J.P. (2004) **Control of the sharkskin instability in the extrusion of polymer melts using induced temperature gradients**. Rheologica acta, 44, pp. 160-173.
157. Kanev, D., Takacs, E., and Vlachopoulos, J. (2007) **Rheological evaluation and observations of extrusion instabilities of biodegradable polyesters**. International Polymer processing, 22, pp. 395-401.
158. Kennedy, P. and Zheng, R. (2013) Material Properties of Polymers. **Flow analysis of injection molds**. Carl Hanser Verlag GmbH Co KG.
159. Cho, J.W. and Paul, D.R. (2001) **Nylon 6 nanocomposites by melt compounding**. Polymer, 42, pp. 1083-1094.
160. Rangari, V.K., Shaik, M.Y., Mahfuz, H., and Jeelani, S. (2009) **Fabrication and characterization of high strength Nylon-6/Si3N4 polymer nanocomposite fibers**. Materials Science and Engineering: A, 500, pp. 92-97.
161. Ara, M., Watanabe, M., and Imai, Y. (2002) **Effect of blending calcium compounds on hydrolytic degradation of poly (DL-lactic acid-co-glycolic acid)**. Biomaterials, 23, pp. 2479-2483.
162. Cuadri, A.A. and Martín-Alfonso, J.E. (2018) **Thermal, thermo-oxidative and thermomechanical degradation of PLA: A comparative study based on rheological, chemical and thermal properties**. Polymer Degradation and Stability, 150, pp. 37-45.
163. Dorgan, J.R., Janzen, J., Knauss, D.M., Hait, S.B., Limoges, B.R., and Hutchinson, M.H. (2005) **Fundamental solution and single-chain properties of polylactides**. Journal of Polymer Science Part B: Polymer Physics, 43, pp. 3100-3111.
164. Othman, N., Acosta-Ramírez, A., Mehrkhodavandi, P., Dorgan, J.R., and Hatzikiriakos, S.G. (2011) **Solution and melt viscoelastic properties of controlled microstructure poly(lactide)**. Journal of Rheology, 55, pp. 987-1005.
165. Dumazert, L. and Sonnier, R. (2017) **An Insight into the Flammability of Some Bio-Based Polyesters**. Polymers, 9, pp. 706.
166. Oh, H. and Green, P.F. (2009) **Polymer chain dynamics and glass transition in athermal polymer/nanoparticle mixtures**. Nature Materials, 8, pp. 139.
167. Immergut, E.H. and Mark, H.F. (1965) Principles of Plasticization. In: Platzer, N.A. (ed.) **Plasticization and plasticizer processes**. ACS Publications, pp. 1-26.
168. Wiktorska, B. and Stępień, M. (2013) **GPC measurements**. Łódz, Poland: Polish Academy of Science.
169. Saeidlou, S., Huneault, M.A., Li, H., and Park, C.B. (2012) **Poly (lactic acid) crystallization**. Progress in Polymer Science, 37, pp. 1657-1677.
170. Choong, G.Y.H. (2017) **Personal Communication**.
171. Li, G., Li, H., Turng, L., Gong, S., and Zhang, C. (2006) **Measurement of gas solubility and diffusivity in polylactide**. Fluid Phase Equilibria, 246, pp. 158-166.
172. Fernández, J., Amestoy, H., Sardon, H., Aguirre, M., Varga, A.L., and Sarasua, J.-R. (2016) **Effect of molecular weight on the**

physical properties of poly (ethylene brassylate) homopolymers. journal of the mechanical behavior of biomedical materials, 64, pp. 209-219.

173. De Focatiis, D.S., Buckley, C.P., and Hutchings, L.R. (2008) **Roles of chain length, chain architecture, and time in the initiation of visible crazes in polystyrene**. Macromolecules, 41, pp. 4484-4491.
174. Keller, T., Mao, Z., and Spengler, D. (1990) **Young's modulus, bending strength, and tissue physical properties of human compact bone**. Journal of Orthopaedic Research, 8, pp. 592-603.
175. Daniels, A., Chang, M.K., Andriano, K.P., and Heller, J. (1990) **Mechanical properties of biodegradable polymers and composites proposed for internal fixation of bone**. Journal of applied biomaterials, 1, pp. 57-78.
176. ThermoScientific. (2018) **Pharma 11 Twin-screw Extruder** [Online]. Thermo Fisher. Available at: https://www.thermofisher.com/order/catalog/product/553-0600 [Accessed 20 November 2018].
177. Bottom, R. (2014) **Hot melt extrusion and continuous wet granulation in the pharmaceutical industry** [Online]. Thermo Fisher. Available at: https://assets.thermofisher.com/TFS-Assets/CAD/Reference-Materials/Hotmelt-extrusion-wet-granulation-pharm-ind.pdf [Accessed 20 November 2018].
178. ThermoScientific. (2018) **Pharma 16 Twin-Screw Extruder** [Online]. Thermo Fisher. Available at: https://www.thermofisher.com/order/catalog/product/553-1040 [Accessed 20 November 2018].
179. Schulz, R. (2018) **Machines** [Online]. Schulz & Partner International, Germany. Available at: https://www.schulz-partner-international.de/en/machines.html?cat=&item=5549&order=new&action=details&suchbegriff= [Accessed 20 November 2018].
180. Morris, B.A. (2016) Effect of Process on Properties. **The science and technology of flexible packaging: multilayer films from resin and process to end use**. William Andrew, pp. 515-538.
181. Giles Jr, H.F., Mount III, E.M., and Wagner Jr, J.R. (2004) Processing Conditions. **Extrusion: the definitive processing guide and handbook**. William Andrew, pp. 141-150.
182. Villmow, T., Kretzschmar, B., and Pötschke, P. (2010) **Influence of screw configuration, residence time, and specific mechanical energy in twin-screw extrusion of polycaprolactone/multi-walled carbon nanotube composites**. Composites Science and Technology, 70, pp. 2045-2055.

Appendix

A.1. Scale up: production of the nanocomposites and dog bones at Evonik

Video footage was provided for (i) the HANP-LR706S nanocomposites compounded with a Thermo Fisher Pharma 16 twin-screw extruder and (ii) injection moulding of dog bones with an Arburg Allrounder 170S 180-30, both carried out at Evonik Industries AG.

HANP-LR706S extrusion

Injection moulding of HANP-LR706S